Coherent Diffraction Imaging and Ptychography of Human Metaphase Chromosomes

by Laura Shemilt

Submitted for the requirements for the degree of Doctor of Philosophy at University College London.

Supervised by Prof. Ian K. Robinson

London Centre for Nanotechnology & Department of Physics and Astronomy

University College London

September 2014

Declaration

‘ I, Laura A. Shemilt confirm that the work presented in this thesis is my own. Where information has been derived from other sources, I confirm that this has been indicated in the thesis.’

Laura Shemilt, September 2014

Abstract

Mitotic chromosome structure is highly important in the packing and safe separation of DNA during cell division. The chromatin fibre, the first packaging of DNA around histone proteins, is coiled into a highly condensed state during the metaphase stage of mitosis where the chromosomes form their characteristic 'X' shape in order to be split into two daughter cells on cell division. Accessing the 3D structure of the condensed chromatin could provide high resolution information on the location of the genes inside the chromosome during metaphase and the placement of the proteins used in the packaging mechanism. We apply lensless X-ray imaging techniques to chromosomes in an attempt to access their structure. Coherent Diffraction Imaging and Ptychography have potential to achieve wavelength limited resolution in 3D. The techniques directly measure phase that can be used to map the electron density in the sample.

Sample preparation is highly important to obtain good quality images from any microscopy technique. We start with studying sample preparations with Fluorescence and Scanning Electron Microscopy to observe the suitability and effects of the protocols. We perform lensless imaging on nuclei and chromosomes prepared with newly designed protocols for this type of X-ray imaging.

Images of nuclei were retrieved from the ptychography experiments at 34-ID-C, I-13 and cSAXS. Ptychography was performed with a visible light source on a set of 46 human chromosomes. The images provide a map of electron density that can be used to calculate the mass of chromosomes and nuclei. Mass is a macroscopic structural quantity that can be used to observe the changes to the protein and DNA content in the nucleus during the cell cycle given a high enough resolution. The nuclei measured in this work were in an early mitotic state and gave consistent mass values calculated from the phase measured by ptychography. In the case of chromosomes mass calculated from the ptychography images was used to sort and identify them in a form of karyotyping. This method of identification is novel because it takes into account the whole of the chromosome contents, both protein and DNA, whereas standard methods of karyotyping look at positions of bandsin the chromosomes.

Acknowledgements

This work was made as part of a team effort and would have never been achieved without the significant input of many others. I would like to acknowledge their contributions here and thank them for their support in this undertaking.

Firstly I would like to thank my supervisor Prof. Ian Robinson for his help, ideas and guidance during this project. His expert knowledge of the field as well as his hands on approach to research has taught me many valuable skills about scientific research with synchrotron radiation.

Secondly I am indebtted to Dr. Jörg Schwenke, who has helped me greatly in every aspect of this project. His useful discussions on phase retrieval algorithms and the implementation of ptychography have greatly influenced this thesis. Many of the images shown in this thesis were produced from his ideas and with his ptychography programmes.

I would like to thank Ms. Ana K. Estandarte for her help and input with the electron microscopy experiments and analysis. Also for establishing the staining preparations and synthesizing the dyes used in this work. I would like to thank her for her discussion on stains and staining mechanisms.

I would like to thank Dr. Mohammed Yusuf for his work in sample preparation and establishing the laboratory at the Research Complex at Harwell. All the sample preparations for the X-ray experiments discussed in this work were produced by him.

Thank you to Dr. Jesse Clark who has helped me greatly in the early stages of my PhD. I have learnt a great deal about phase retrieval, inverse problems and programming from him.

To Ms. Ephanielle Verabnis and Dr. Fucai Zhang for their hard work on the optical experiments on chromosomes that make up a great part of this thesis. I would like also thank Fucai for his insightful discussions of phase retrieval.

A huge thanks to the various beamline staff for their indispensible help and guidance in running experiments. I would like to thank them for their determination to see experiments run well and providing support throughout. At 34-ID-C, I would like to thank Dr. Ross Harder. At I-13 I would like to thank Dr. Ulrich Wagner, Prof. Christoph Rau, Dr. Zoran Pesic, Dr. Alberto de Farnis and Dr. Aaron Parsons.

I would like to thank Dr. Graeme Morrison and Prof. Malcolm Howells for their useful discussions about the theory of X-ray microscopy which has influenced parts of this thesis. I would also like to thank Graeme for his STXM images of chromosomes.

To Mark Turmaine, for his technical support with the Scanning Electron Microscopy work. To Neha Parmar, for her technical support with chromosome sample preparation.

And to all the members of the research group, for you help, knowledge and support during my

years working here. It has been a great experience to work with you all.

Lastly to all my friends, no. 46 and my family, for your constant, unwaivering support throughout the (many) years of my studies. This is for you.

Contents

List of Figures

List of Tables

Chapter 1

Introduction

The structure of chromosomes is highly important in the packaging of the genetic material and its safe division in to two daughter cells. The form of the chromosome changes through the cell cycle, existing in long fibres in the interphase to allow transcription and replication of the DNA, to a tightly condensed mitotic 'X' shape that undergoes division. The structure of the chromosome is highly debated above the first unit of DNA wrapped around proteins, the nucleosome. How the nucleosome is then coiled up into chromosome is largely unknown. It has been proposed that the nucleosomes are coiled up into a 30 nm fibre but the existence and structure of this fibre are widely debated.

Imaging has played a large part in discovering the known aspects of chromosome structure. From finding the structure of the DNA double helix from X-ray diffraction patterns [1, 2] to being able to diagnose disease from structural changes in the positions of genes using visible light and fluorescence microscopy . The coiling of the DNA strand into the mitotic chromosome is widely debated, especially at the level of the chromatin fibre said to be 30nm in diameter [3]. There exists a resolution gap between 10-30 nm that cannot be easily accessed by most imaging methods in 3D, it is in this resolution gap that the debated 30 nm fibre sits [4].

Lensless imaging techniques of Coherent Diffraction Imaging and Ptychography have the potential to access this gap. These imaging methods use the coherent properties of X-rays and iterative algorithms to retrieve an image from a diffraction pattern [5, 6]. These techniques avoid the use of objective lenses therefore the resolution is limited by the wavelength of the source.

Coherent Diffraction Imaging and Ptychography can be performed with visible-light, electrons and X-rays providing that the source is coherent and can penetrate the sample. Modern synchrotron facilities can produce highly brilliant X-rays with a sufficient degree of coherence to perform these imaging techniques. X-rays have a large penetration depth and wavelengths in the

region of an angstrom, which allows for high resolution 3D imaging to be performed without sectioning. The techniques of Coherent Diffraction Imaging and Ptychography have been applied to many problems in materials science and biology [7–9].

The motivation for this thesis is to start a preliminary investigation into applying the lensless imaging methods of CDI and Ptychography to probe the 3D structure of chromosomes with high spatial resolution. The images, whether a 2D projection or a 3D representation, will provide a full electron density map of the chromosome structure which can be analyzed for mass and if possible higher order structures inside the chromosome. This imaging will provide a picture that contains contributions from the majority of the chromosomal material, DNA and proteins. Many techniques for looking at chromosome structure are looking for information at the molecular level such as the placement of genes in a chromosome, or digesting out different chromosomal proteins. Looking at the macroscopic scale may provide useful insights on the overall protein to DNA content of chromosomes.

Chapter 2 discusses the fundamental theory behind X-ray interactions with matter and how this is applied in X-ray imaging techniques. When forming an image the phase of the wave passing through the object needs to be conserved, which is usually done by a lens. In the case of lensless imaging methods the phase problem is solved with the use of algorithms which iterate between real and reciprocal space, imposing constraints in both until a solution is found. The algorithms will be presented and discussed in this chapter.

Chapter 3 outlines the considerations when applying these techniques to biology. The greatest problems to overcome when measuring biological samples with X-rays is the weak scattering nature of the sample and the potentially damaging radiation dose that comes with imaging. In order to perform an image some dose must be imparted on the sample, however too large a dose can destroy the structural features of interest. Being able to measure sufficient signal from samples that are not highly scattering is limited strongly by the dose they can withstand. The implications of this are discussed further in this section. Some examples of CDI and ptychography in biology are also presented here.

Chapter 4 looks at chromosome structure from the fundamental DNA level to the mitotic state. This chapter also discusses some basic biological theory about the cell cycle and the changes to the nuclear components during this time. The current debates on the structure of the chromosome are presented along with some experiments that have tried to solve them. Imaging techniques form a strong part of this experimentation work and their strengths and limitations with regards to discovering chromosome structure are discussed.

Sample preparation is extremely critical for obtaining good images of chromosomes but cur-

rently there is not standard protocol for X-ray imaging. Chapter 5 discusses how existing protocols for preparing samples for imaging with fluorescence and Scanning Electron Microscopy can be adapted to make a suitable protocol for X-rays. Staining technique for enhancing the phase contrast of chromosomes are discussed in this section and their potential enhancement to the phase shift is calculated.

The ptychography experiments performed on chromosomes and nuclei are discussed in Chapter 6. The experimental set-up of ptychography and the images obtained from these experiments are presented and analyzed. Results from several different beamlines are compared in attempt to find the best experimental set up. The performance of the phase retrieval algorithms is discussed in terms of the image quality and the obtained resolution.

In chapter 7 the images presented in the previous chapter are analyzed for structural information. The nuclear mass is calculated from the phase images obtained from ptychography for several nuclei measured at different beamlines. A ptychography experiment with a visible light source is used to image a spread of human chromosomes. The mass calculated from the phase image is used to sort the chromosomes in order of mass and the results are compared to other chromosome sorting methods.

Chapter 2

Coherent Diffraction Imaging and Ptychography

X-ray Microscopy and imaging have various different forms from lens based X-ray microscopes, tomography to phase retrieval methods. These techniques all rely on measuring the perturbation of an incident illumination by an object and resolving an image from this using a variety of techniques.

The original form of lensless microscopy is Coherent Diffraction Imaging (CDI), where a sample is coherently illuminated and the intensity of the diffraction pattern is collected in the far field. From this diffraction pattern an image of the object can be retrieved through computed algorithms. The algorithms iterate between real and reciprocal space implementing constraints on each to retrieve the phase lost in the measurement. In the case of CDI the constraint in real space is provided by the spatial extent of the sample requiring that the beam size be larger than the sample. This constraint restricts the field of view to the size of the illumination and does not allow extended samples to be imaged. Ptychography is a lensless imaging method that overcomes the limitation of CDI, by scanning a probe over the sample and recording overlapping diffraction patterns. The overlap is then used to constrain the phase retrieval algorithm which allows for a large field of view. The redundancy of the overlapping information can be used to retrieve both the object and the illumination, and adds a robustness to the reconstructions.

This section discusses the theory of X-ray interactions with matter and their application to Coherent Diffraction Imaging and Ptychography. The need for coherence, overcoming the phase problem and the phase retrieval algorithms are also described. Conditions for the experimental implementations of these methods such as experimental geometry and oversampling criteria are

also discussed.

2.1 X-ray interactions with matter

In order to start a discussion on diffractive imaging it is necessary first to describe the interaction between X-ray and matter. These interactions govern the optical properties of the material which need to be considered when imaging.

X-rays can be described as a classical electromagnetic field propagating in space $\mathbf{r} = x\hat{\mathbf{i}} + y\hat{\mathbf{j}} + z\hat{\mathbf{k}}$ and time t. Just considering the electric field at position $\mathbf{r}$ in space and at time t the wave can be expressed in the following way:

$$E(\mathbf{r},t) = E_0 \exp(i\mathbf{k}.\mathbf{r} - \omega t) \tag{2.1}$$

where E_0 is the amplitude of the electric field, $\mathbf{k}$ is the wave vector , and ω is the angular frequency.

The wave-vector $\mathbf{k}$, and angular frequency ω, are related to the wavelength λ and the temporal frequency ν by:

$$|\mathbf{k}| = \frac{2\pi}{\lambda} \quad , \omega = 2\pi\upsilon$$

These relations are used often throughout this chapter as well as the following energy relations:

$$\mathcal{E} = \frac{hc}{\lambda} = \hbar\omega \tag{2.2}$$

where $\mathcal{E}$ is the energy of the X-rays.

Many of the relations outlined in this chapter are discussed with respect to the intensity of the wavefield. The intensity can be described in terms of the complex amplitude as:

$$I = \frac{cn\epsilon_0}{2} |E|^2 \tag{2.3}$$

X-rays have three main interactions with matter, these are : absorption, scattering and refraction. These processes and their relationship to each other will be discussed in the subsequent sections. Many of the derivations presented here are based on Elements of Modern X-ray Physics, Des Mc Morrow and Jens Als-Nielsen [10].

2.1.1 Absorption

When an X-ray photon is absorbed by an atom its energy is sufficient to expel a bound electron. This creates a hole in the electronic shell that is subsequently filled by the de-excitation of another electron, during which a fluorescent photon with energy equal to the excitation energy is released.

The probability of an absorption occurring is described by the absorption cross section σ_a which is dependent on the energy or wave-vector , k, of the incident photon and on the Z number of the material. For a given wave-vector, σ_a varies with atomic number as approximately Z^4. The absorption process does not change linearly with energy and exhibits discontinuities at absorption edges. These discontinuities occur when the energy of the incident photon is greater than the threshold energy for removing an electron from a certain shell, therefore another level of absorption is opened up. Absorption edges occur at the threshold energies of the K, L, M-shells, for example.

The absorption cross section is often described in terms of the absorption coefficient μ. Consider an X-ray beam incident on a sample of thickness τ, with number of atoms N, distributed uniformly, such that the density can be described as N/τ. As the X-ray beam propagates a distance dz into the sample its intensity is decreased and amount $-dI$ due to the absorption process in the material. The reduction in intensity can be described by the following differential equation:

$$-\frac{dI}{dz} = \frac{I(z)N}{\tau}\sigma_a \tag{2.4}$$

where $I(z)$ is the intensity of the X-ray as a function propagation distance into the material z. Eq. 2.4 can be integrated to gain an expression for the transmitted intensity:

$$I = I_0 \exp(-\mu\tau) \tag{2.5}$$

where μ is the absorption coefficient:

$$\mu = \frac{N\sigma_a}{\tau} \tag{2.6}$$

Eq. 2.6 can be rewritten to remove the dependence on the thickness of the material by putting the number density of the material N/τ in terms of the mass density $N_A\rho/A$, where N_A is Avagadro's number, A is the atomic weight and ρ is the mass density of the sample. By substituting the number density for the mass density and rearranging to make σ_a the subject we get the following expression for the absorption cross-section:

$$\sigma_a = \frac{\mu A}{N_A\rho} \tag{2.7}$$

This expression for the cross section does not seem to explain the absorption process described above as it does not have any explicit dependence on energy and does not give rise to the discontinuities. The absorption coefficient μ is the natural logarithm of the ratio of the transmitted and incident intensities , (eq. 2.5) and it is this quantity that has the energy dependence. At the energy where the absorption edge is reached the transmitted intensity $I \to 0$ and $\mu \to \infty$ therefore σ_a becomes very large over the absorption-edge.

2.1.2 Scattering

2.1.2.1 Scattering from a free electron

The simplest model of X-ray interaction with matter is the scattering of a wave by a single free electron. Like absorption the probability of this process occurring is described the scattering cross-section σ_s. To derive the scattering-cross section for a free-electron we start with the differential scattering cross-section. This quantity describes the amount of photons scattered from an incident beam into a solid angle $d\Omega$ (fig. 2.1), which is easily expressed as:

$$\left(\frac{d\sigma}{d\Omega}\right) = \frac{I_{sc}}{\Phi_0 \Delta\Omega} \tag{2.8}$$

where I_{sc} is the scattered intensity, Φ_0 is the incident beam flux and $\Delta\Omega$ is the angle subtended by the detector at distance R from the sample.

We start by calculating the cross section for scattering of an X-ray wavefield described by eq. 2.1, by a single free electron. The flux, Φ_0 can be expressed as the modulus of the incident electric field squared, $|\mathbf{E}_{in}|^2$. The scattered flux can also be similarly expressed in terms of the radiated electric field $|\mathbf{E}_{rad}|^2$. To get I_{sc} from this quantity the flux has to be simply multiplied by the area of the detector $R^2\Delta\Omega$. If these quantities are then substituted into eq. 2.8 then the differential scattering cross section becomes:

$$\left(\frac{d\sigma}{d\Omega}\right) = \frac{|\mathbf{E}_{rad}|^2 R^2}{|\mathbf{E}_{in}|^2 .} \tag{2.9}$$

The incident electric field $\mathbf{E}_{in}$ can be expressed as a complex magnetic wave describe in eq. 2.1. In the far field, when $\mathbf{r} \to R$, the radiated electric field becomes $\mathbf{E}_{rad} \propto \hat{\varepsilon'} \exp(i\mathbf{k}.R)/R$, where $\hat{\varepsilon'}$ is the polarization of the wavefield. This expression for the radiated electric field shows that the accelerated electron acts as a source and radiates a spherical wave. The observed acceleration of the electron depends on the angle of observer to the polarization of the incident beam. The variation of observed acceleration with observation angle can be described as the magnitude of the

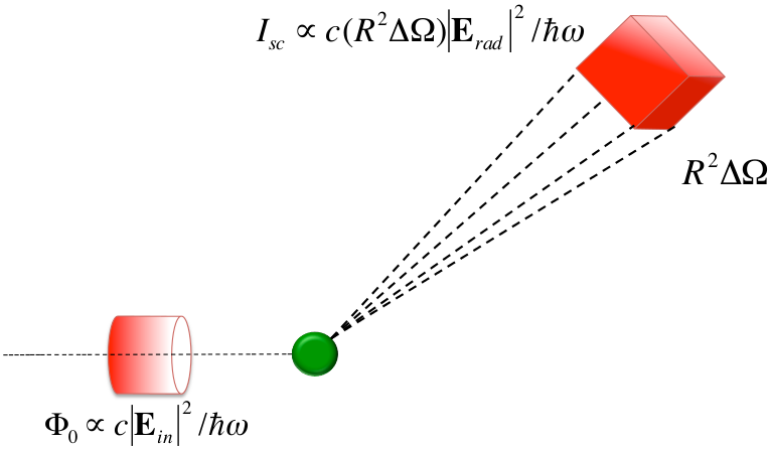

Figure 2.1: Schematic of scattering from a particle. The incident flux Φ_0 is represented by the red cylinder and is proportional to $|\mathbf{E_{in}}|^2$. A proportion of this incident flux is then scattered by the object, represented by the green sphere. The scattered intensity I_{sc} is scattered into a volume given by the solid angle $\Delta\Omega$ and the sample to detector distance R. The scattered intensity is proportional to $|\mathbf{E_{rad}}|^2$.

dot product of the polarization vectors of the incident wave $\hat{\varepsilon}$ and the radiated wave $\hat{\varepsilon'}$.

The radiated field is proportional to the charge, $-e$ and acceleration of the electron at a time $t - R/c$, and can be written in the following form:

$$E_{rad}(R,t) \propto \frac{-e}{R} a(t - R/c)\,|\hat{\varepsilon}.\hat{\varepsilon}'| \tag{2.10}$$

The acceleration of the electron is caused by the force exerted by the incident electric field $\mathbf{E}_{in}$. The acceleration of the electron can be described by the following :

$$a(t - R/c) = \frac{-e}{m_e} E_{in}(0, t - R/c) = \frac{-e}{m_e} E_0 \exp(-i\omega(t - R/c)) \tag{2.11}$$

where m_e is the mass of an electron. Using the dispersion relation $\omega = ck$ and the expression for acceleration eq. 2.11, then we can write eq. 2.10. in terms of the incident electric field and rearrange to get the following ratio between the incident and radiated fields:

$$\frac{E_{rad}(R,t)}{E_{in}} \propto \left(\frac{e^2}{m_e}\right) \frac{\exp(ikR)}{R}\,|\hat{\varepsilon}.\hat{\varepsilon}'| \tag{2.12}$$

The ratio of E_{rad} and E_{in} has to be dimensionless therefore we need a multiplicative factor for eq. 2.12 which has the units of length. The fundamental length scale for the interaction between an electron and an X-ray photon is give by the Thomson scattering length and is defined as:

$$r_0 = \left(\frac{e^2}{4\pi\epsilon_0 mc^2}\right) = 2.82 \times 10^{-13}\text{cm} \tag{2.13}$$

Multiplying the ratio of the incident and scattered electric field by the Thomson scattering

length gives the following expression:

$$\frac{E_{rad}(R,t)}{E_{in}} = -r_0 \frac{\exp(ikR)}{R} \left|\hat{\varepsilon}.\hat{\varepsilon}'\right| \tag{2.14}$$

substituting this result into eq. 2.9, the differential scattering cross-section becomes:

$$\left(\frac{d\sigma}{d\Omega}\right) = r_0^2 \left|\hat{\varepsilon}.\hat{\varepsilon}'\right|^2 \tag{2.15}$$

To obtain an expression for the scattering cross section of the sample we integrate eq. 2.15 over all angles. We find that $\langle|\hat{\varepsilon}.\hat{\varepsilon}'|\rangle$ is 2/3 over a unit sphere and the integration of the spatial angles over a sphere is 4π. The scattering cross-section can be written as:

$$\sigma_s = \frac{8\pi r_0^2}{3} \tag{2.16}$$

Eq. 2.16 shows that the interaction between a free electron and X-rays is governed by the Thompson scattering length. The scattering interaction between X-rays and a free electron is constant and independent of energy. As we consider more complex interactions we will see how the scattering behaviour becomes energy dependent.

2.1.2.2 Scattering from an atom

The next level of complexity is scattering from an atom, which appear to an X-ray beam, as simply a collection of electrons. In the case of an atom the electrons are bound and not free, as in the previous section, therefore their scattering will be effected by their binding energy. An atom has a distribution of charge associated with this binding energy, we can model this as an electron density, $\rho(\mathbf{r})$, which is a function of $\mathbf{r}$, the distance from the nucleus. The scattering from an atom is made up from the scattering contributions of all the electrons which are not all going to scatter in phase. We consider a phase shift $\Delta\phi(\mathbf{r})$, between the wave scattering through one volume element and the neighbouring volume element:

$$\Delta\phi(\mathbf{r}) = (\mathbf{k} - \mathbf{k}').\mathbf{r} \tag{2.17}$$

where $\mathbf{k}$ is the incident wave-vector and $\mathbf{k}'$ is the scattered wave vector. The difference between the wave-vectors is the scattering vector $\mathbf{Q}$ which is equal to:

$$\mathbf{Q} = \mathbf{k} - \mathbf{k}' \tag{2.18}$$

The scattering vector is a very useful quantity when discussing X-ray scattering as it is related to the energy change that occurs during scattering and the scattering angle θ, for $|\mathbf{Q}| = 2k\sin(\theta/2)$. We will discuss scattering from the atom in terms of $\mathbf{Q}$.

The scattering length of an atom is the amount of phase shift through a volume element $d\mathbf{r}$ at position $\mathbf{r}$. This volume element will contribute $-r_0\rho(\mathbf{r})d\mathbf{r}$ to the scattered wavefield. If we consider the scattering of the wavefield to have a phase factor $e^{i\mathbf{Q}.\mathbf{r}}$ then the total scattering length of an atom can be expressed as :

$$-r_0 f^0(\mathbf{Q}) = -r_0 \int \rho(\mathbf{r}) e^{i\mathbf{Q}.\mathbf{r}} d\mathbf{r} \tag{2.19}$$

where $f^0(\mathbf{Q})$ is the atomic form factor. When there is zero phase shift, $\mathbf{Q} = 0$ therefore the atomic form factor becomes equal to the number of electrons in the atom $f^0(\mathbf{Q} = 0) = Z$, conversely, as the phase shift between successive volume elements becomes very large the form factor reduces to zero. It is easy to see from eq. 2.19 that the atomic form factor is Fourier transform of the electron density.

As stated at the start of the chapter the electrons in the atom our bound at different energies which effects their interactions with X-rays. When the binding energy matches closely with the energy of the photon, resonance effects occur reducing the scattering length of atom. This can be described with the complex anomalous dispersion correction $f' + if''$. The complex part comes from the phase lag in response of the harmonic oscillator to the driving field. The atomic form factor can be written in such a way as to include these dependences:

$$f(\mathbf{Q}, \omega) = f^0(\mathbf{Q}) + f'(\hbar\omega) + if''(\hbar\omega) \tag{2.20}$$

These terms are dominant at absorption edges where the scattering length of the atom is reduced by the absorption processes taking place. This dispersion correction plays a large role in the macroscopic properties of a material when acted on by X-rays which will be discussed throughout this thesis.

The behaviour described here does not seem to link to the Thompson scattering behaviour of the free electron. In this part we have only considered the coherent scattering from the atom but another process, Compton scattering, also occurs. If the total scattering from the atom is considered it can be shown that the scattering cross-section is equal to $4\pi Z r_0$, the Thompson scattering cross-section for Z electrons. The ratio for this scattering is split into $1 - f(\mathbf{Q})^2$ for coherent scattering and $f(\mathbf{Q})^2$ for Compton scattering [11] therefore at small scattering angles coherent scattering is dominant. The work undertaken in this thesis is done in the small scattering

angle regime therefore Compton scattering will not be discussed further.

2.1.3 Refractive index

Refraction is related to the processes of scattering and absorption previously discussed but is used to describe the macroscopic X-ray interactions with a material, rather than the atomic or the electronic. The process of refraction, as we know well from visible light, causes the incident radiation to change direction when propagating through a material and is wavelength dependent, causing white light to disperse into its colour spectrum. Unlike light the refractive index for X-rays differs very little from one, typically on the order of 10^{-5}.

The refractive index for X-rays is expressed by the following:

$$n = 1 - \delta + i\beta \tag{2.21}$$

Where the real part δ is related in the following way to the scattering behaviour the material:

$$\delta = \frac{2\pi}{|\mathbf{k}|^2}\rho.r_0 \tag{2.22}$$

where ρ is the average electron density inside the material, and r_0 is the radius of an electron. This expression neglects anomalous and relativistic effects.

The imaginary part β is related to the absorption characteristics of the material and can be expressed in terms of the absorption coefficient:

$$\beta = \mu/2\,|\mathbf{k}| \tag{2.23}$$

The scattering and absorption parts of the refractive index can also be written in terms of the dispersion correction f' and f'' described in section 2.20 . Where δ can be expressed as:

$$\delta = \frac{2\pi N_A r_0}{k^2} f' \tag{2.24}$$

and the absorption factor can be expressed as:

$$\beta = \frac{2\pi}{k^2} r_0 \rho f'' \tag{2.25}$$

The variables δ and β are very powerful in describing the effects of X-ray interactions on a bulk material with relation to atomic variables f' and f''. As β is directly related to the absorption, the value of δ is directly related to the phase shift of the refractive wave caused by the material.

From eq. 2.22 , we can see that δ is also related to the electron density of the material, therefore by gaining quantitative measures of the phase shift the electron density of a material can be found. This will be discussed in later sections for now we give the expression for phase shift $\Delta\phi$ through a material of thickness τ as:

$$\Delta\phi = k\delta\tau = \frac{2\pi}{\lambda}\delta\tau \tag{2.26}$$

The importance of phase shift and absorption in imaging will be discussed further in section 3.1.

2.2 Coherence

The following imaging methods are reliant on the coherence of the illumination to extract phase information from the diffraction pattern. In order to measure phase, which is a retardation or advancement in a wavefront, a comparison with a reference wave must be made. This is achieved by using interference between two waves which requires coherent illumination. The coherent properties of a wave can be separated into spatial and temporal which are also referred to as transverse and longitudinal.

Coherence can be described in a practical way by the visibility V, defined by the difference in intensity between the maxima and the minima in the measured diffraction pattern. Visibility, V, can be expressed as:

$$V = \frac{I_{\max} - I_{\min}}{I_{\max} + I_{\min}} \tag{2.27}$$

where I_{max} is the intensity of the maxima and I_{min} is the intensity at the minima. When the minima of the diffraction pattern are zero, hence $I_{min} = 0$ and $V = 1$, we can assume perfect coherence. When there is no distinction between the maxima and minima of the diffraction pattern, hence $V = 0$, the source is incoherent. In practice most sources are partially coherent which requires a more rigorous mathematical treatment. In the following we will assume a perfect coherent source throughout.

Visibility is a practical measurement of coherence but does not define the spatial and temporal coherence properties of the illumination source.

Longitudinal (temporal) coherence can be thought of as the distance travelled by two waves of different wavelengths from a point where they start in phase to a second point where, again, they meet in phase. A schematic of two waves of wavelengths λ, and $\lambda - \Delta\lambda$ is shown in fig. 2.2. The

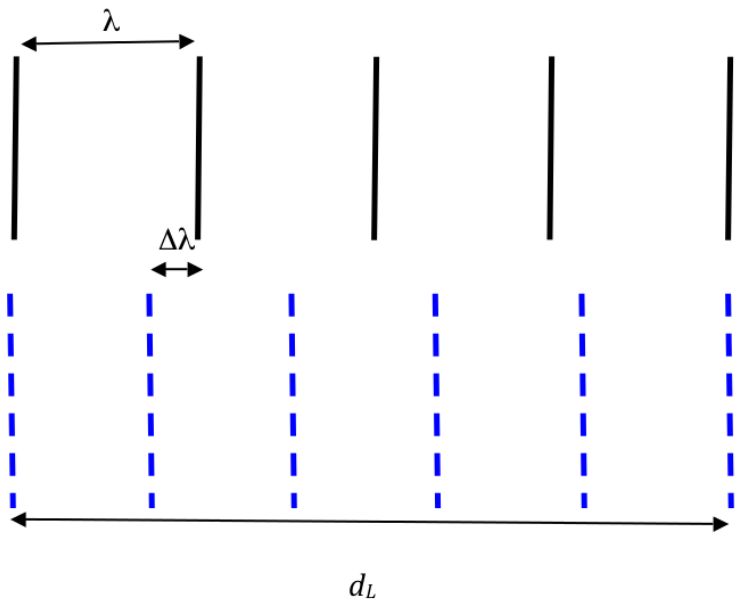

Figure 2.2: Schematic showing longitudinal coherence. Two wavefronts of slightly different wavelengths start off in phase and then meet again in phase at a distance d_L. This distance is the longitudinal coherence length. This diagram has been adapted from reference [10].

two waves start in phase and at distance d_L from this point they are back in phase. It can be shown from the geometry that the longitudinal coherence length is:

$$d_L = \frac{\lambda^2}{2\Delta\lambda} \tag{2.28}$$

The longitudinal coherence is typically set by the bandpass of the monochromator because slight differences in wavelength, $\Delta\lambda$ are introduced by the selecting crystals. The longitudinal coherence of a source can be measured by the visibility in the fringes from crystals of different aspect ratios [12]. With certain designs of monochromators, which select the energy using two crystal pairs, the longitudinal coherence can be varied by altering the bandpass of the monochromator.

The transverse (spatial) coherence is determined by the light path of two rays emanating from the extremities of an extended source. Fig. 2.3 shows waves starting from the edges a source size D, meet in phase at point P at a distance R from the source. The distance from point P to where the waves are completely out of phase is twice the transverse coherence length. It can be seen from fig. 2.3 that the transverse coherence length can be described in terms of the angular relationship between the two waves $\Delta\theta$ or in terms of $\frac{R}{D}$ when the angle is small.

$$d_T = \frac{\lambda}{2\Delta\theta} = \frac{\lambda R}{2D} \tag{2.29}$$

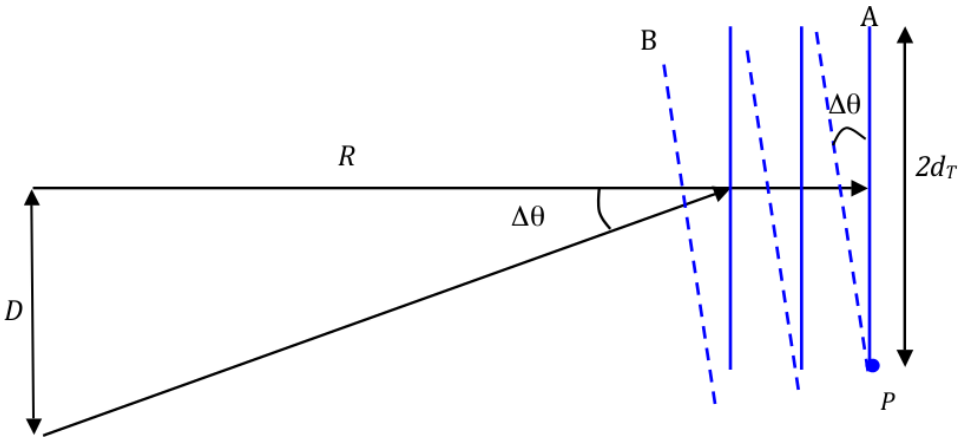

Figure 2.3: Schematic of transverse coherence. Two waves exit from the extremities of an extended source size D and meet in phase at point P, distance R from the source. Travelling along the wavefront from P the waves become out of phase. At twice the transverse coherence length $2d_L$ from point P the waves are completely out of phase. Figure adapted from reference from [10]

Transverse coherence length is set by the source, in this case a synchrotron. A synchrotron source is a Gaussian distribution of incoherent emitters which fall into a space of σ. A sample distance R away from the source will see a coherence length of:

$$d_T = \frac{\lambda R}{2\sigma} \tag{2.30}$$

In most X-ray applications the full coherence length of the synchrotron source is not used and the coherence is set by slits shortly after the monochromator, hence the source size now becomes the slit size. This effects the coherence by having a smaller source nearer to the sample, but depending on the source size used the coherence can be improved.

2.3 The Phase Problem

Coherent Diffraction imaging methods are concerned with solving the phase problem. The phase problem is well known in optics and is described here for a typical X-ray diffraction experiment. The diffracted wavefield exiting from an object, $G(\mathbf{Q})$, can be expressed in the far field as the Fourier transform of its transmission function $\rho(\mathbf{r})$ by:

$$G(\mathbf{Q}) = \int \rho(\mathbf{r}) \exp(i\mathbf{Q}.\mathbf{r}) d^2\mathbf{r} \tag{2.31}$$

Where $\mathbf{r}$ and $\mathbf{k}$ are the real and reciprocal space vectors respectively. Only the intensity of the exiting wave $I(\mathbf{k})$ is measured at the detector which can be expressed as :

$$I(\mathbf{Q}) = aG(\mathbf{Q}).aG(\mathbf{Q})^* = a^2 \left|G(\mathbf{Q})\right|^2 \tag{2.32}$$

where a is a constant factor. In measuring the exit wavefield only the square of the Fourier Modulus is recorded and all the information on the phase of the exit wavefield is lost therefore the object transmission function, $\rho(\mathbf{r})$, cannot simply be recovered by the inverse Fourier transform. This is known as the phase problem.

Whilst the phase is lost in the intensity measurement its information is still encoded in the diffraction pattern providing that the incident illumination is coherent. It can, therefore, be retrieved but on the condition that the diffraction pattern is suitably oversampled. Oversampling will be discussed in detail in section 2.4.

2.4 Oversampling

In a short communication by Sayre [13] he proposed that the solution to the phase problem for crystallography can be solved if the diffraction pattern is sampled at half the unit cell. This is an example of the oversampling criterion defined by Nyquist [14] as sampling at a rate of twice the Shannon frequency. In the case of a crystal the Shannon frequency is the size of the unit cell, a, therefore a sampling rate of twice this in reciprocal space is $\frac{1}{2a}$, half the unit cell size. In a diffraction pattern the Bragg peaks occur at a frequency of $\frac{2\pi}{a}$, Sayre realised that if the pattern could be measured at twice this rate then in theory the phase problem could be solved for the crystal.

Bates extended this argument for diffraction imaging to define the oversampling criteria to be twice the Nyquist sampling rate in each linear direction. Under this definition a 2-D diffraction pattern must be 4× oversampled and a 3-D diffraction pattern 8× oversampled [15]. Miao et al. argued that this sampling criteria was overly restrictive and defined an oversampling rate based on equation counting arguments [16], which is presented here.

Experimentally the diffraction pattern is measured discretely by the detector where the pixels provide sampling points, therefore the diffraction measured at the detector is discrete. Where N denotes the number of pixels in the detector, eq. 2.31 can be written in a discrete as :

$$|G(\mathbf{Q})| = \left| \sum_{x=0}^{N-1} \rho(\mathbf{x}) exp(i\mathbf{Q}.\mathbf{x}/N) \right| \tag{2.33}$$

This expression can be treated as a set of simultaneous equations for $\rho(\mathbf{x})$ at every pixel. Considering that the wavefield is complex, there are two unknown variables at each pixel, requiring

$2N$ equations to solve the phase problem in 1-D, N^2 in 2-D and N^3 in 3D. In this formulation there are two many unknowns therefore in order to solve eq. 2.33 we need to reduce the unknown values. Miao et al. give the following ratio, σ , to determine how many known values are needed to obtain a solution:

$$\sigma = \frac{\text{total pixel number}}{\text{no. pixels with unknown value}} \tag{2.34}$$

We know that the phase problem is undetermined by 2 therefore it should be solvable for $\sigma > 2$. In practice the intensity of diffraction pattern can be measured such that $\sigma > 2$, allowing for the object, $\rho(\mathbf{x})$, to be confined to a defined area of real space, outside of which everything is zero. This region of space is often referred to as a support. As we know the value of our pixels outside this space to be zero we have reduced the number of unknown pixels in eq. 2.34 to be those that lie in the support. In the extension to 2- and 3- dimensions σ need only be greater than $2^{\frac{1}{2}}$ and $2^{\frac{1}{3}}$ in each dimension respectively, less than the $2\times$ oversampling in each direction defined by Bates.

The solution to the phase problem from oversampled data is unique for cases above 1-D except for trivial solution pairs associated with the Fourier Transform. Under a Fourier Transform the complex conjugate $\rho^*(\mathbf{x} + \Delta\mathbf{x})$, multiplication by a constant phase $\rho(\mathbf{x})e^{i\phi_c}$ and the reflection $\rho(-(\mathbf{x} + \Delta\mathbf{x}))$ are indistinguishable from $\rho(\mathbf{x})$ [16]. There are very rare cases where two different image functions will have the same autocorrelation therefore a unique solution is difficult to find.

The oversampling requirement is not as well explored in the case of ptychography. It is assumed from our treatment above that every diffraction pattern in a ptychography set has to be oversampled in the detector plane, however, the redundant information produced by the overlap in a ptychography measurement can be used to compensate for ambiguities caused by undersampling in the data. Edo et al. find that the size of the overlap, set by the size of the scanning step, can be used to compensate for a lack of oversampling as defined by σ [17] . They define a sampling requirement for ptychography $S_{x,y}$ based on the sampling in reciprocal space U and the sampling in real space R:

$$S_{x,y} = \frac{1}{UR} \tag{2.35}$$

The sampling in reciprocal space can be written in terms of σ as $U = (d\sigma)^{-1}$, where d is the size of a fringe. The sampling in real space, can be written also in terms of d, and the overlap between the diffraction patterns $\varpi_{x,y}$, $R = d(\varpi_{x,y} - 1)$. Combining these expressions with eq. 2.35 gives the sampling requirement for ptychography as:

$$S_{x,y} = \frac{\sigma}{1 - \varpi_{x,y}} \tag{2.36}$$

The sampling requirement is fulfilled when $S_{x,y} = 1$ that is when R exactly balances U, and is oversampled in the case $S_{x,y} > 1$ and undersampled when $S_{x,y} < 1$. Therefore it is possible to be undersampled at the detector, in terms of the definition of oversampling presented in eq. 2.33, providing that the scanning step is fine enough. Edo et al. showed that it was possible to reconstruct an image from data that was sampled at $\sigma < 2^{\frac{1}{2}}$ with a complimentary scan step, however quality of the reconstructed images was less than in the correctly oversampled cases. The study showed that in the cases where oversampling $S_{x,y} = 2.6$ the images showed blurred edges and a loss of phase contrast.

2.5 Phase Retrieval Algorithms

The phase retrieval algorithms used in Coherent Diffraction Imaging iterate between real and reciprocal space, imposing constraints in each domain. The Error Reduction (ER), based on the Gerchberg and Saxton iterative method, and Hybrid Input-Output (HIO) are most commonly used [18], however gradient search and steepest descent methods can be used to solve the phase problem. A comprehensive review of all the algorithms can be found in [19].

The ER iterative algorithm (fig. 2.4) is composed of the following steps: firstly, the object guess is propagated to the Fourier plane, here the reciprocal space constraint is applied. The reciprocal space constraint replaces the modulus of the object guess with that of the measured data, whilst retaining the phase from the object guess. For this reason this constraint is sometimes referred to as the modulus constraint. The modified reciprocal space guess is then propagated to the real space plane and the support constraint is imposed. This constraint imposes that the object's density is non-negative in real space and zeros any amplitude that is formed outside the finite size of the object.

The ER algorithm is prone to stagnation because the previous iterate $\rho'_n(x)$ is used as the next starting guess $\rho_{n+1}(x)$. As the algorithm progresses the difference between $\rho'_n(x)$ $\rho_{n+1}(x)$ lessens and reduces convergence speed. The Hybrid Input- Output (HIO) algorithm aims to break this stagnation by using a next iterate, $\rho_{n+1}(x)$, that is composed of both the $\rho_n(x)$ and $\rho'_n(x)$ state. The first three steps of the HIO algorithm follow those of ER, however, the real space modification for the HIO algorithm takes the following form:

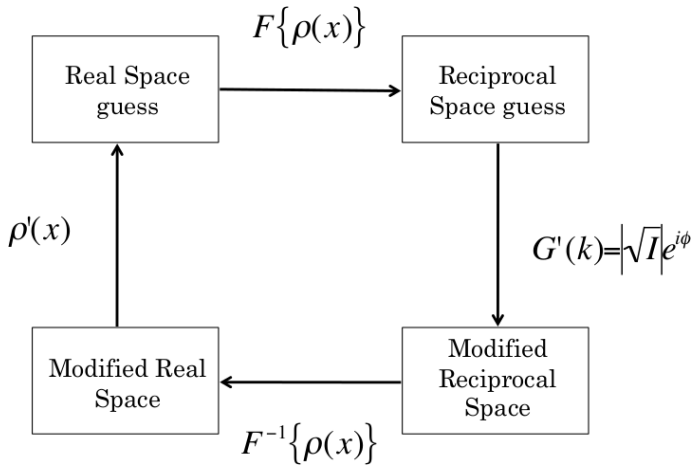

Figure 2.4: Diagram showing path of the Error Reduction phase retrieval algorithm. The algorithm starts with a guess in real space, $\rho_n(x)$ and propagates it to reciprocal space using the Fourier transform. In reciprocal space the guess is updated by retaining the propagated phase but replacing the modulus with the measured diffraction data. This modified reciprocal space guess $G(k)$ is propagated back with the inverse Fourier transform where the support constraint is applied. This updated real space guess, $\rho'_n(x)$, is used as the next iterate in the algorithm.

$$\rho_{n+1}(x) = \begin{cases} \rho_n & x \in \gamma \\ \rho_n - \beta\rho'_n & x \notin \gamma \end{cases} \tag{2.37}$$

where β is a constant and $0 \leq \beta \leq 1$, and γ defines the region of space where the real space domain constraints are violated. From eq. 2.37 when the support constraints are satisfied the object is not updated and where they are violated the value in this regions is driven towards zero by subtracting the output. If $\beta = 1$ then the ER algorithm is recovered.

In practice the ER and HIO algorithms are used in conjunction to get the best possible solution at the quickest convergence rate [20]. The ER algorithm has a very great initial speed of convergence and can be used to drive towards a local minima in solution space [19]. The HIO algorithm is capable of searching the greater solution space not getting trapped in minima, like the stagnation seen in ER. This is discussed further in section 2.6.3. When retrieving the phase from a measured diffraction pattern it is best to use some iterations of ER to drive towards the first solution, then switch to HIO for the majority of the retrieval and finish with ER to locate the nearest minima in solution space. The convergence of the algorithms are monitored with the following error metric:

$$\chi^2 = \frac{\sum(I' - I)^2}{\sum I^2} \tag{2.38}$$

where I' is the current guess at the intensity and I is the measured intensity. The aim is to minimize χ^2 with each consecutive iteration. Fig. 2.5 shows the progress of χ^2 during phase

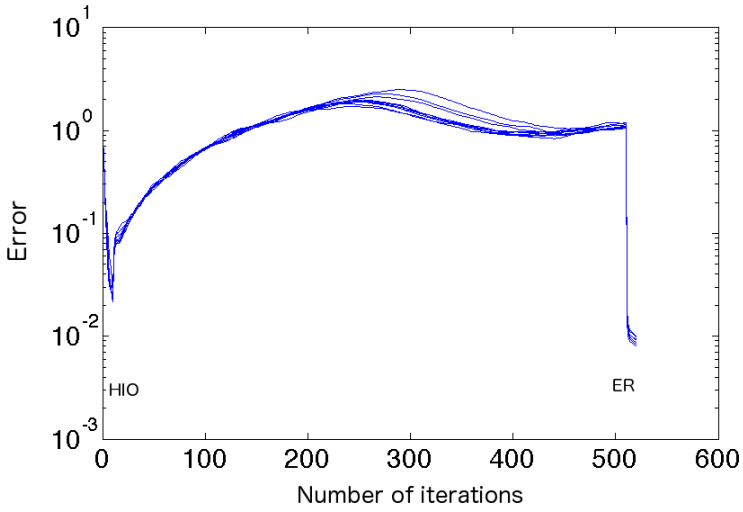

Figure 2.5: Convergence of the algorithms during phase retrieval. The error metric χ^2 is plotted against number of iterations, the onset of each phase retrieval algorithm is marked with either ER or HIO. The first 10 iterations where processed with the ER algorithm.

retrieval with the ER and HIO algorithms, the onset of each algorithms is shown with an arrow. Starting with ER, the value of χ^2 decreases rapidly and then starts to slowly increase with the switch to HIO. During the iterations with HIO the value of χ^2 oscillates slowly until stabilising. The final implementation ER reduces χ^2 as a solution is reached.

2.6 Ptychography Algorithms

A limitation of CDI is that only objects smaller than the spatial extent of the illumination can be imaged, such as metal nanocrystals [8], due to strong real space constraint needed for successful phase retrieval. Ptychography does not use the finite extent of the sample to constrain an object in real space, instead these methods use the overlap of neighbouring diffraction patterns to determine the solution. This overlap constraint provides redundancy in the data that can be used to retrieve the phase and amplitude of both the illumination and the object. Ptychography is based on the assumption that the exit wavefield ψ just after the sample plane can be factorized into the contribution from the illumination $P(\mathbf{r})$ and the contribution from the object $O(r)$:

$$\psi = P(\mathbf{r})O(\mathbf{r}) \tag{2.39}$$

the validity of this assumption is discussed in [21, 22]. The assumption is central for the success of ptychographic algorithms. The two main algorithms used in ptychography are extended Ptychographic Iterative Engine (ePIE) and the Difference Map (DM). There is a third less often used algorithm, translation diversity [23]. The first two algorithms and their implementation will

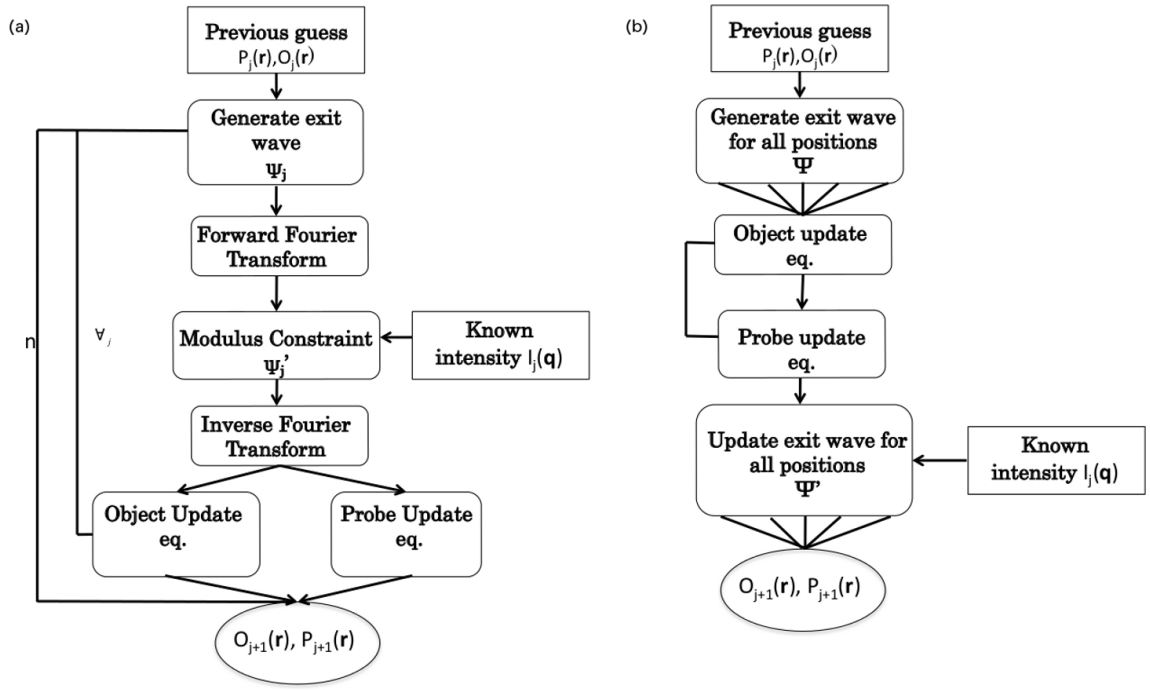

Figure 2.6: A comparison between ePIE and DM algorithms showing each step of the iterative process. (a) Representation of an ePIE loop, this code is updated in sequence therefore an iteration is completed when this loop has been passed for each position. (b) Representation of the Difference Map algorithm, the algorithm follows similar steps to ePIE but updates in parallel. An iteration of DM is completed when this loop has been passed once.

be discussed in this section. Difference Map is often used with the refinement of the Maximum Likelihood method, which improves the reconstructions by minimising a model of the noise during the phase retrieval process [24].

2.6.1 Extended Ptychographic Iterative Engine (ePIE)

In the first ptychography algorithm a known probe was used to reconstruct the object [5] therefore for successful retrieval the probe had to be known very accurately. Experimentally it is very difficult to find a known probe therefore to overcome this problem the algorithm was extended to update both the probe and the object function throughout the reconstruction which increased both the success and rate of convergence of the algorithm. The extended Ptychographic Iterative Engine (ePIE) developed by Maiden et al. [25] uses the following steps to retrieve both the probe and the object function from the overlapping diffraction patterns. The path of this algorithm is displayed in fig. 2.6.

The algorithm starts by multiplying the object at position j, $O_j(\mathbf{r})$, by an appropriate choice of probe position in the sequence $s(j)$, which gives the next guess in the exit wavefield as:

$$\psi_j = O_j(\mathbf{r})P(\mathbf{r} - \mathbf{R_{s(j)}}) \tag{2.40}$$

This guess is propagated to the Fourier plane by a Fourier transform, here the typical modulus constraint of replacing the calculated intensity by the measured intensity is applied, whilst the calculated phase is retained. This updated reciprocal space guess is then propagated back to the sample plane by the inverse Fourier Transform to give an updated exit wavefield $\psi'_j(\mathbf{r})$. From this a new estimate for the wavefield is found by updating the object and the probe functions in the following way:

$$O_{j+1}(\mathbf{r}) = O_j(\mathbf{r}) + \alpha \frac{P^*(\mathbf{r} - \mathbf{R}_{s(j)})}{\left|P(\mathbf{r} - \mathbf{R}_{s(j)})\right|^2_{max}}(\psi'(\mathbf{r}) - \psi(\mathbf{r})) \tag{2.41}$$

$$P_{j+1}(\mathbf{r}) = P_j(\mathbf{r}) + \beta \frac{O^*(\mathbf{r}+\mathbf{R_{s(j)}})}{\left|O(\mathbf{r}+\mathbf{R_{s(j)}})\right|^2_{max}}(\psi'(\mathbf{r}) - \psi(\mathbf{r})) \tag{2.42}$$

where α and β are constants that alter the step size of the update and are chosen to be equal to 1 for most cases. The object and probe guess are updated in a similar way by adding a weighted correction of the wavefield. One ePIE iteration is complete when all the patterns have been updated sequentially from $s(0)$ to $s(j)$. These guesses then provide the next best guess used in the subsequent iteration.

2.6.2 Difference Map Algorithm

The Difference Map algorithm was first demonstrated by Thibault et al. [21], the algorithm follows a similar path of moving between Fourier and real space but its main difference from ePIE is the update of the probe and object functions and that all projections are modified in parallel rather than sequentially.

All the algorithms in this chapter can be described in terms of projections onto sets and we will proceed with a set theory description of the DM algorithm of ptychography. We can think of the following algorithms of having two constraint sets one in reciprocal space and the other in real space. Projection operators are used to map the iterations between the two constraints sets, one of the projections is the modulus constraint p_F and can be written as:

$$p_F(\psi) : \tilde{\psi}(\mathbf{q}) \rightarrow \tilde{\psi^F}(\mathbf{q}) = \sqrt{I(\mathbf{q})}\frac{\widetilde{\psi}(\mathbf{q})}{\left|\widetilde{\psi}(\mathbf{q})\right|} \tag{2.43}$$

The second projection is the real space update, either a support constraint in CDI or an overlap

constraint in ptychography. For the DM algorithm the overlap constraint can be expressed as the following projections :

$$\hat{O}(\mathbf{r}) = \frac{\sum_j \hat{P}^*(\mathbf{r}-\mathbf{r_j})\psi(\mathbf{r})}{\sum_j \left|\hat{P}(\mathbf{r}-\mathbf{r_j})\right|^2} \tag{2.44}$$

$$\hat{P}(\mathbf{r}) = \frac{\sum_j \hat{O}^*(\mathbf{r}+\mathbf{r_j})\psi(\mathbf{r}+\mathbf{r_j})}{\sum_j \left|\hat{O}(\mathbf{r}+\mathbf{r_j})\right|^2} \tag{2.45}$$

These two expressions are coupled providing that there is overlap between the successive diffraction patterns. To get the next iterate according to the difference map we use the following update function which includes the projectors for the overlap and modulus constraints:

$$\psi_{j,n+1} = \psi_{j,n}(\mathbf{r}) + p_F(2\hat{P}(\mathbf{r}-\mathbf{r_j})\hat{O}(\mathbf{r}) - \psi_{j,n}(\mathbf{r})) - \hat{P}(\mathbf{r}-\mathbf{r}_j)\hat{O}(\mathbf{r}) \tag{2.46}$$

The convergence of this algorithm is governed with the following error metric:

$$\chi_{n+1} = \|\psi_{n+1} - \psi_n\| \tag{2.47}$$

which is the norm of the differences between the previous and subsequent iterates. The algorithm is said to converge when this difference becomes sufficiently small that the two constraints can be satisfied and a solution has been found.

In the Difference Map algorithm, all the positions are updated in parallel and not sequentially as in ePIE. The path of the Difference Map is different to that of ePIE (fig. 2.6) as the Object and Probe updates come before the final update of the wavefield in which the modulus constraint is applied.

2.6.3 Comparison of Algorithms as Projections onto Convex Sets

All algorithms in this chapter can be described using the mathematical formalism of projections onto convex sets [26, 27]. Whilst the algorithms where presented here in a different way the projection on to sets description allows us to see the convergence behaviour of the algorithms more easily. The constraint sets of the algorithms lie in Fourier and real space and the solution to the algorithm is where these two constraint sets overlap.

In the case of ER and ePIE the algorithms follow a direct projection onto the two constraint sets (fig. 2.7(a)). The projections move the path from one set to the nearest point on the other set, nearing the solution on each iteration. The progress toward convergence of these algorithms

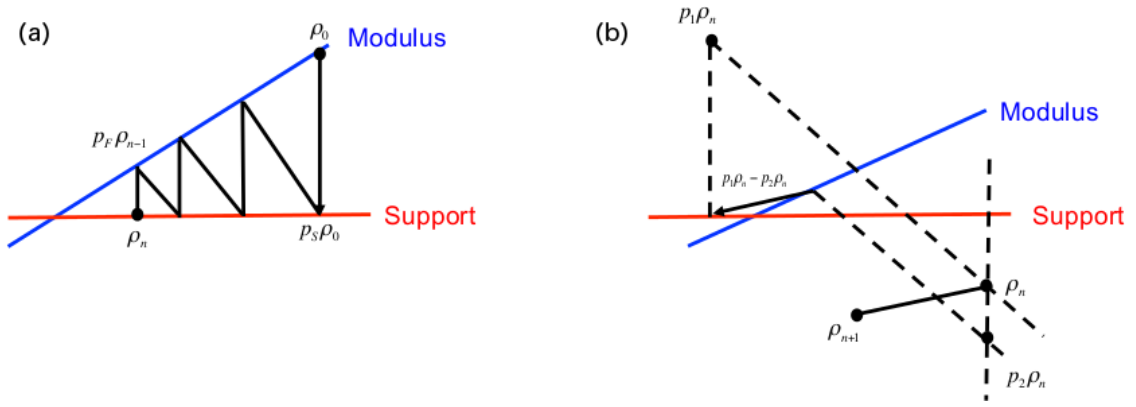

Figure 2.7: Behaviour of ER and DM algorithms as projections onto convex sets. The modulus constraint set is shown as a blue line and the support constraint as the red line, the solution is at the point where the two lines intersect. The path of the algorithm takes is shown as a black line. (a) Geometrical representation of the ER algorithm showing the position of the first iterate, ρ_0, as it has been projected onto the modulus constraint and the position of the final iterate in real space ρ_n. The modulus projector is represented as p_F and the support projection is p_s (b) Geometrical Representation of the HIO algorithm showing the path from the n^{th} iterate to the $n+1^{th}$. Generally a DM algorithm works by taking the difference between two projections labelled here as p_1 and p_2 . The projection of ρ_n with these two operators is shown with a dotted line, and the difference between is represented with an arrow. It can be seen that the path of the algorithm does not always lie on the constraint set. Figure adapted from [19]

is monitored by an error metric. It is easy to see why stagnation occurs in this algorithm, as the solution is approached the difference in space between the iterations becomes very small and the algorithm will indefinitely iterate back and forth between the sets without ever reaching the local solution.

The HIO and DM algorithms do not have the same stagnation problems as ER and ePIE. These algorithms use difference maps to find a solution and do not follow the same projections described above. When using a difference map the update is projected onto both the constraint sets simultaneously and then the next iterate is found from the difference between these solutions. The path that these algorithms take toward the solution is very different from ePIE and ER (fig. 2.7(b)). The difference map methods circle the solution but each update does not necessarily lie in on the constraint set. This allows the DM and HIO algorithms to find different solutions in a global solution space instead of being directed towards a local solution. Using the difference map and error reduction methods in combination as shown in section 1.5 has been used in some cases in this study to achieve convergence using the difference map methods to find a global solution and using the error reduction to move towards it (see section 6.2.1).

2.7 Experimental Geometry

There are two common modes of experimental geometry used in lensless imaging methods. For non-periodic objects that produce speckle patterns from an incident coherent beam the signal is

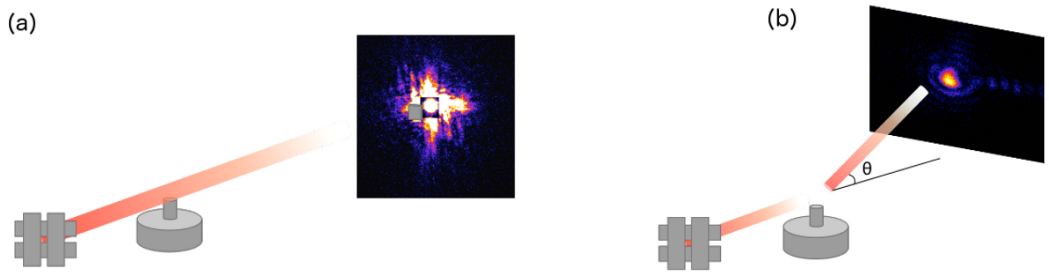

Figure 2.8: (a) Transmission geometry set-up, the illumination size is set by the slits, the detector is in line with the sample. A beamstop protects the detector from the incident illumination. (b) Bragg geometry, the detector is offset from the sample by an angle to catch one of the Bragg reflections from the sample. This can only be used on crystalline samples.

collected in line with the beam axis, this is known as transmission geometry. For periodic objects, CDI can be achieved in reflection geometry, where the coherent diffraction pattern is measured at a single Bragg reflection. Currently, ptychography is being developed to also measure in Bragg geometry [28, 29].

2.7.1 Transmission Geometry

The basic set-up of an experiment in transmission geometry is illustrated in fig. 2.8. (a) . The size of the beam incident on the sample is selected in the schematic by slits but pinholes and focusing optics can be used. The non-periodic sample will produce scattering in the forward direction therefore the detector is placed in the far field in line with the beam axis to collect the signal. A beamstop is placed in front of the detector to block the signal from the direct beam which can be strong enough to destroy the detector, the implications of using a beamstop are discussed further in section 3.5.

In this geometry a 2-D image is a projection of the sample, therefore in order to obtain 3-D image the sample is rotated through 180 degrees and angular projections are taken at fine sampling rate. Each of these angular projections are then reconstructed separately by the algorithms and then a tomography filter-back projection algorithm is used to align the set and retrieve a 3-D image of the sample [30, 31].

2.7.2 Bragg Geometry

Bragg geometry makes use of the crystalline nature of a sample by offsetting the detector at a Bragg reflection and measuring the coherent diffraction pattern around a single Bragg peak (fig. 2.8(b)). This geometry does not use a beamstop as only a portion of the direct beam is reflected

and therefore there is no large signal from the direct beam.

The 3D dataset is achieved by taking a diffraction pattern at fine sampling points through the rocking curve. The entire set of angular projections can be built in 0.5 degrees rather than 180 degrees in the transmission case. These projections are reconstructed using the algorithms to gain an image of the strain in the crystal at that reflection. By imaging multiple reflections in this way and a 3D strain map of the sample can be built up [32].

Chapter 3

Applications of CDI and Ptychography in Biology

Coherent Diffraction Imaging and ptychography can provide three dimensional structural information on the nanometer-scale. Three dimensional information is critical for resolving certain structures, such as helices, where the pitch and chiral information is lost in 2D. A second example is networks, e.g. in neuron systems in brain tissue [33], where there must be information in every dimension the network spans in order to trace the path between joining branches. These types of structures are common in biological materials, and lensless imaging techniques have the potential to access the information needed to solve them.

Since their development lensless imaging techniques have been used to solve a variety of scientific problems in two and three dimensions. There are many examples of the use of CDI and ptychography in materials science, including mapping strain inside objects [8, 29, 34], and obtaining 3D images of industrially useful materials [35, 36]. There are also examples of imaging biological sample with these methods. Here the two main challenges to overcome are the weak scattering from the sample and its degradation due to radiation damage which limits the achievable resolution and the quality of data that can be taken. Despite these boundaries, lensless imaging techniques are optimal for measuring the mesoscale and could be useful in biology where it is currently difficult to observe these scales in thick whole specimens, especially in 3D. The penetration depth of X-rays allows for biological material to be imaged in 3D, without undergoing sectioning process used in other imaging methods. Sectioning methods involve imaging fine slices of a whole object. The sectioning procedure often involves embedding an object in resin then producing fine micron thick slices [37].

Imaging biological materials with X-rays is very challenging due to the ionizing radiation used to illuminate the sample also damages the sample by breaking bonds within the sample [38]. Biological materials have low refractive indices at the energies that lensless imaging techniques are usually performed. This chapter discusses some of the necessary conditions, limitations and technical aspects of imaging biological materials with X-rays.

3.1 Contrast

In X-ray imaging the difference in absorption and scattering cross-sections of the material provide the amplitude and phase contrast in the image. An object that creates contrast to the background by perturbing the amplitude of the wave, either by absorption or reflection, is said to be an amplitude object. An object that does not change the amplitude of the wave and only alters its phase is said to be a phase object. By accessing the phase contrast in an imaging technique, phase objects, which are difficult to visualize in amplitude contrast sensitive techniques, can be easily observed. The likelihood of an object absorbing or scattering a wave is determined by the material's absorption and scattering cross sections.

As discussed in section 2.1 the scattering and absorption cross-sections are linearly proportional to the dispersion coefficients $f'$and f''. The variation of f' and f'' with energy for two common elements in biology, Carbon and Oxygen, is shown in fig. 3.1. The values are taken from the tables calculated by Henke et al. [39]. Starting with the absorption characteristics of the material described by f'' it is clear that at high energies ($\geq$ 1000 eV) the difference in f'' between these materials becomes negligible. For absorption-based microscopy methods the amplitude contrast from biological samples is optimized by using an energy range where the difference between the absorption coefficients of Oxygen and Carbon is the strongest. This energy range lies between the K- edges of Carbon and Oxygen therefore the contrast between oxygen-rich water and carbon-rich proteins is at its highest. It is for this reason that absorption sensitive methods such as tomography, TXM and STXM typically use the soft X-ray energy regime (energies from 100 -2000 eV) when imaging biological samples [38]. Ptychography has been carried out in the water window on a hydrated fossil diatom [40] . The image showed the appearance of fringes at the edges of the diatom, these artifacts are due to the breakdown of the projection approximation in this energy regime.

The difference in f' describes the scattering behaviour of the material so is related to the phase contrast in an image. In fig. 3.1 the scattering of Oxygen and Carbon is reduced at low energies due to the number of absorption processes taking place in this range and is further reduced across

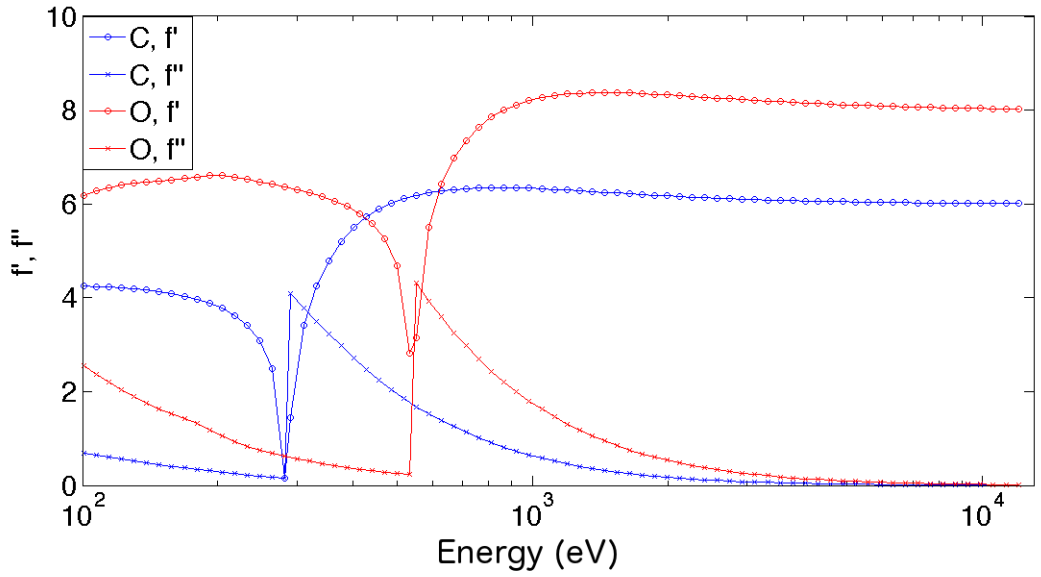

Figure 3.1: f' and f'' for Carbon, blue, and Oxygen red, over the energy range $100 - 10,000$ eV. The water window is the energy range between the absorption edges of C and Oxygen when the difference between the absorption cross-section is the highest. At energies above 1000 eV the absorption cross-section is reduced by the scattering cross-section increases, at these energies the phase contrast is much greater than the absorption contrast. Data from Henke et al. [39]

the K- edges of the materials. At high energy however the scattering processes are dominant in Carbon and Oxygen, so at these energies a biological samples which contain high content of Carbon and Oxygen provide greater phase contrast than absorption contrast. There is a difference in f' between Carbon and Oxygen at high energies, which indicates there is phase contrast between water and protein at high energies. At these energies biological samples become phase objects and in these regimes CDI and Ptychography are performed, measuring directly the phase of the object. It is indicated in fig. 3.1 that biological material become phase objects at these methods could be used to image frozen hydrated samples.

When imaging a biological sample composed of different proteins we wish to see contrast from the different protein regions of the sample. However, proteins have similar electron densities, therefore the difference in phase shift produced from the regions is small, therefore the contrast between the two regions in the images is small which makes the two regions difficult to distinguish from each other.

In order to measure a feature in the background, be it ice, air, or a different protein, the signal from the object must be detectable above the background noise. To investigate how contrast is related to the Signal to Noise Ratio (SNR) we follow a treatment first outlined by Glaser [41] and Sayre [42] and presented by [38]. Here, the sample is subdivided into elements of size d^2 and illuminated with n photons. The signal from feature above background is $n(p_f - p_b)$, where p_f

is the probability of the detecting a scattering event from the feature and p_b is the probability of detecting a scattering event from the background. There will be noise present in this measurement which is given by $\sqrt{np_b}$. The signal from the feature must be recorded with statistical accuracy and an often used measure of this is the Rose criterion. Developed by Rose in order to identify signals on early television screens, the criterion states that in order to resolve a signal with statistical accuracy it must have 5 times greater intensity than the background noise [43]. This limit forms a basis for statistical accuracy used by much of the literature discussed in this chapter.

To measure the signal from the feature it must be detectable above the noise at the level stated by the Rose criterion. This gives the following limit on the detectable signal from the feature as:

$$\frac{n(p_f - p_b)^2}{p_b} > 25 \tag{3.1}$$

From this expression a limit for the exposure the sample must undergo to gain significant contrast can be obtained:

$$np_b > \frac{25}{C^2} \tag{3.2}$$

where C is the contrast defined as:

$$C = \frac{p_f - p_b}{p_b}$$

From eq. 3.2 the exposure needed to produce a certain contrast depends heavily on the scattering power of the object with respect to the background. The relative scattering power is dependent on the size of the object as fewer electrons provide fewer detectable counts, therefore the exposure needed to gain suitable contrast is greater. The relationship between size, contrast and exposure, hence dose, will be explained further in section 3.3.1.

In the case of biological material where the difference between p_f and p_b is small the contrast can be improved by attaching as heavy metal to increase contrast between unstained and stained regions. The heavy metal has a Z number far higher than typical organic molecules and therefore will have a greater scattering cross-section at high energies and increase p_f. There are different mechanisms of inserting heavy metals into a sample which will be discussed in the section 5.2. The area of interest is tagged with the heavy metal will have greater phase contrast than the surroundings making the region easily identifiable. An example of this was staining E. Coli bacteria with MnO which gave strong phase contrast to DNA rich areas in the resulting CDI image [44].

It can be beneficial to exploit both phase and absorption contrast with different microscopy

methods to measure different properties of the specimen. At the Twinmic beamline, Elettra Sincrotrone, Trieste, ptychography and STXM measurements were carried out on a mouse fibroblast sample. The fibroblast was labeled with $CoFe_2O_4$ nano-dots and the energy of the measurement was around the L-edge of iron. The phase contrast image from ptychography does not show a strong contribution from the nano-dots at this energy but the STXM image clearly shows the position of the nano-dots. At this energy range the absorption is the main interaction in the nanoparticles therefore in the absorption-sensitive STXM image there is significant contrast between the nano-dots and the background. Similarly in the ptychography measurement there is not significant phase contrast to see the signal from the nano-dots clearly in the fibroblast due to the absorption processes being dominant in iron at this energy [45].

3.2 Resolution

Lensless imaging techniques should, in theory, offer wavelength-limited resolution. The word resolution can often have an ambiguous meaning due to the varying definitions of this quantity. Definitions of resolution can refer to the limitations of the optical system or simply be the minimum resolvable distance in the resulting image. In lensless imaging techniques the primary measure of resolution comes from the detected signal at largest scattering angle captured by the detector. For small angles the scattering angle is simply related to the distance from the sample to the detector R and the size of the detector D as :

$$\theta = \frac{D}{2R} \tag{3.3}$$

To put this into units of length, the resolution in real space, we simply divide the wavelength by the angles such that $res = \lambda/\theta$. Combining this result with eq. 3.3 we get the following expression for resolution:

$$res = \frac{2\lambda R}{D} \tag{3.4}$$

From this expression we see that the resolution is limited by the geometry of the experiment, wavelength used, detector size and sample to detector distance , which gives the numerical aperture of the detector.

As well as having a sufficient detection aperture to measure diffraction data, the high angle scattering from the sample must be sufficient to provide a statistically accurate signal. For biological samples with small scattering cross-sections it is often difficult to measure a signal at high angles before the structure is damaged. The requirements for gaining a significant signal at high

angles and the damage effects on the reconstruction will be discussed further in section 3.3.

Other losses in resolution come from the experimental apparatus or errors in the reconstructions, this is particularly relevant when going to three dimensions. A 2D image is just a projection through a 3D sample. In order to take a 3D image the sample is rotated and a 2D projection is taken at every angle. These angular projections can be combined to give 3D information in a process called tomography. It technologically difficult to keep alignment of each projection stable on the nanometer scale. Furthermore implementation of Filtered Back Projection algorithms typically used in tomography are difficult for phase images due to the wrapping of the phase and the introduction of phase ramps during the measurement. Often in an image jumps of 2π can be seen in the image, this is known as phase wrapping. To "unwrap" the phase the appropriate multiple of 2π is added to remove the jump. A suitable algorithm has been developed [30] to produce a tomogram from angular projections obtained by ptychography. In this algorithm cross-correlations are used to align projections but positioning errors of several pixels can occur over the 360 degree range. The positioning errors cause artifacts in the 3D image which leads to the spatial resolution of the tomogram being less than the spatial resolution of the 2D projections. Most examples of 3D methods for CDI and ptychography are around 100 nm [7, 31, 46], the current best is at 16 nm [47].

The resolution of the reconstruction can be analyzed by the phase retrieval transfer function (PRTF) [48]. This compares the retrieved diffraction pattern from an average of many phase retrievals $\bar{\gamma}$ to the measured diffraction amplitude over a range of $\mathbf{q}$. The PRTF is defined in the following way :

$$PRTF(\mathbf{q}) = \frac{|\mathcal{F}\{\bar{\gamma}\}|}{\sqrt{I(\mathbf{q})}} = \frac{\langle A(\mathbf{q}) \exp(i\phi_0)\rangle}{\sqrt{I(\mathbf{q})}} \tag{3.5}$$

where $A(\mathbf{q})$ is the diffraction amplitude resulting from the Fourier Transform of the retrieved phases and ϕ_0 is an arbitrary phase offset that is an average of the variations in the total phase over the reconstructions. One ambiguity in the solutions of the phase retrieval is multiplication by a constant phase, under the Fourier transform ρ and $\rho e^{i\phi_0}$ are identical (section 2.4) therefore when taking an average over different solutions the different phase factors must be taken into account. For a perfectly reconstructed diffraction pattern the PRTF would be equal to 1 over the entire range of measured $\mathbf{q}$. The resolution of the reconstruction can be taken to be at the value of $\mathbf{q}$ where the PRTF starts to differ from 1. At this angle the retrieved diffraction pattern no longer shows good agreement to the measured diffraction.

For an image taken with ptychography the Fourier Shell Correlation is used to analyze the

resolution [49]. This analysis was based on a technique used in Electron Microscopy for analyzing image quality [50]. This method takes two images reconstructed from two independent datasets and analysis the cross-correlation over frequency rings (2D) or shells (3D) in Fourier space. The FSC therefore provides a curve of normalised cross-coefficients which shows the consistency between two images at a given resolution. The FSC reduces when the Signal-to-Noise ratio is reduced, therefore a cut off point for agreement can be deduced by using a threshold curve, chosen from an analytical expression separate from the data.

3.2.1 Signal requirements

As we have discussed in the previous sections in order to get sufficient resolution and contrast in an image the number of photons scattered from the sample has to exceed the noise according to the Rose criterion. To achieve this signal requires a certain dose on the sample which ideally should be minimized to avoid damage. Radiation damage causes structural changes in the sample that can lead to errors in the resulting images, therefore damage must be avoided. Damage is discussed further in section 3.3.1. There are many methods to derive the minimum required dose [48, 51, 52] which all follow the basic principle of calculating the coherent scattered intensity from a single voxel of sample size d into a correctly oversampled scattering angle $\Delta\Omega$. The derivation presented here follows that presented by Howells et al. in [53] but we will compare it to the results given in [48, 51, 52].

The scattering signal from a single voxel of size $d \times d \times d$ of material with electron density $\rho(\mathbf{r})$, is derived from the material refractive index to be:

$$\sigma_s = r_e^2 \lambda^2 \left|\rho(\mathbf{r})\right|^2 d^4 \tag{3.6}$$

where r_e is the classical electron radius. The fluence N_0 needed to get the number of photons required to gain a statistically relevant measure P onto the detector from a voxel is $N_0 = {}^{P}/_{\sigma_s}$, substituting eq. 3.6 into this expression gives:

$$N_0 = \frac{P}{r_e^2 \lambda^2 \left|\rho(\mathbf{r})\right|^2 d^4} \tag{3.7}$$

The dose, energy deposited per unit mass, can be expressed in terms of the incident fluence as:

$$D = \frac{\mu N_0 \mathcal{E}}{\epsilon} \tag{3.8}$$

where ϵ is material density , $\mathcal{E}$ is energy, μ is the attenuation coefficient. The minimum required

dose for imaging is the dose needed to get P photons on the detector, therefore we substitute eq. 3.7 into eq. 3.8:

$$D = \frac{\mu P h}{2\pi\epsilon} \frac{1}{r_e^2 \lambda^4 \left|\rho(\mathbf{r})\right|^2 d^4} \tag{3.9}$$

We see from eqs. 3.7 and 3.9 that the fluence, hence the dose scales inversely with d^4. We can check this argument by saying that the contrast (eq. 3.2), C, between the material and the vacuum scales with the voxel thickness d. Hence in order to resolve a feature according to the Rose criterion the dose per unit area $N_0 d^2 > 25/C^2$, as C scales with d, N_0 scales as d^{-4}.

The dose dependence on the wavelength is inversely proportional to λ^2. For the light elements the dose is dominated by the inverse square scaling low energies at becomes almost constant at higher energies. Providing that absorption edges are avoided, this expression argues that measurements should be taken at the lowest energy possible to get the greatest signal for the minimum dose.

The derivation by Howells considers only voxel size and is independent of sample and detector size. Shen et al. derived a set of scaling factors of scattered intensity from the sample depending on the geometry of the object and of the detecting element [52]:

$$I(Q) \propto \begin{cases} d^6 & 2D\,{}^{N}/_{A} = constant \\ d^4 & 3D\,V = A \times d \\ d^3 & 3D\,V = constant \end{cases} \tag{3.10}$$

The scattered intensity for a 3D object where $V = A \times d$ gives a dependence of d^4 which is the same case as derived in eq.3.6. When considering the scattering from the entire object and the intensity depends on d^3. Starodub et al. take these two considerations into account when estimating the minimum required dose to image a biomolecule and find in their calculations a d^{-4} and λ^{-2} dependence but with a different numerical pre-factor to eq. 3.9.

The 3rd and 4th power scalings of voxel size d show that a considerably high number of photons, therefore dose, is needed to image small features. Due to this large dose onset of radiation damage will happen far quicker at high spatial resolutions.

3.3 Dose

Dose is defined as the absorbed ionizing radiation per unit mass, where the S.I. units of dose are Gray [Gy]=[J/kg]. Ionizing radiation is damaging to the structure of the sample, however, some

dose must be imparted on it to produce an image, therefore the object it must be able to withstand the dose required to gain a statistically accurate signal. We discuss the required doses for getting an image and the limitations for imaging with ionizing radiation in biology.

3.3.1 Damage and Dose

Ionizing radiation is ultimately damaging to the sample and causes errors in an image. Radiation damage is difficult to quantify and generalize because it is highly sample dependent. Structural damage however can be monitored through experimentation to find a rough limit of maximum dose a sample can withstand. Firstly we should establish what is damage and when it occurs. As soon as ionizing radiation is absorbed by the sample damage occurs through breaking of chemical bonds, however this level is more important in crystallography, than in imaging of whole objects. In a paper by Kirz et al. the relationship between dose and damage is described as "what determines whether image recorded resembles the true biological structure or the result of changes brought about by exposure" [38]. When imaging with ionizing radiation care must be taken to record the dose delivered to the sample and regard any changes to the object during imaging.

Sample preparation can be used to lessen the damage to the sample or reduce the rate at which the sample is damaged. It is desirable to image most biological samples in a hydrated state as this is the closest to their native environment, however this state shows the quickest damage rates. In order to reduce the rate of damage samples can be chemically fixed or frozen. The review by Kirz et al. outlines some general quantification of dose that can be withstood by sample different sample preparations in an X-ray microscope finding that frozen hydrated samples can withstand $> 10^8$ Gy dose, dehydrated and dried samples $> 10^7$ Gy and wet samples start to show damage at $> 10^4$ Gy [38]. These general statements were from comparing a collection of studies imaging biological samples in different conditions with a variety of sample preparations. Hydrated samples show the quickest structural damage under dose for example, cell ultrastructure being damaged [54] and myofibrils no longer performing their function [55]. Frozen hydrated samples can withstand the greatest dose, but require a greater dose for imaging due to the reduced contrast between ice and protein. The damage mechanism in frozen samples can be seen in crystallography as the fading of spots in the high angles which corresponds to the smallest resolution, (see fig. 3.2) and mass loss [56]. Dehydrated samples cannot withstand as much dose but the contrast between protein and air is considerably higher so they require less dose for imaging. In the dehydrated state, however, chemical fixing is used to prevent radiation damage. The damage effects to chemically fixed samples are likely to be in the form of mass loss [57].

Observation of the diffraction pattern can also indicate the onset of damage to the structure, this

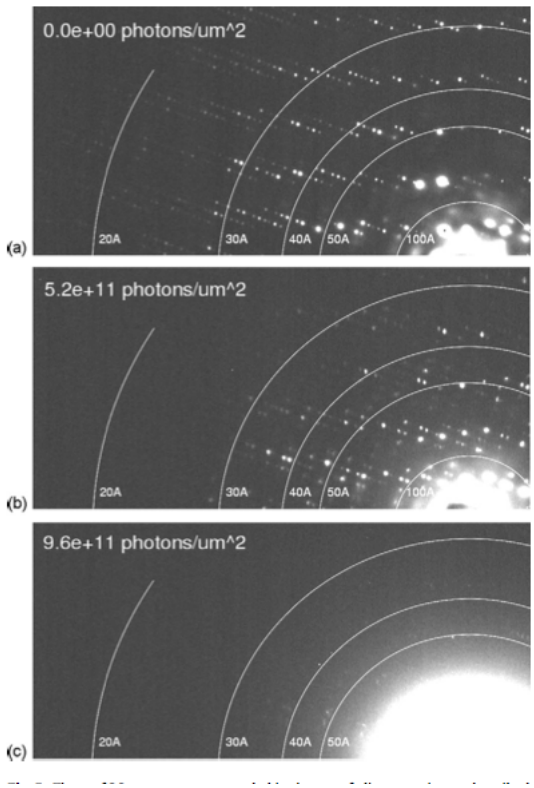

Figure 3.2: Changes to diffraction pattern of a ribosome crystals during exposure to the beam. As the dose increases the high angle diffraction spots start to disappear as features on this length scale are damaged by ionizing radiation. The total flux applied to the crystal is displayed above the diffraction patterns. (a) At zero dose the diffraction spots can be seen to high angles (b) After 5.2×10^{11} photons/μm^2 of flux the diffraction spots start to fade at high angles. (c) After 9.6×10^{11} the diffraction spots have completely faded. Image from [53] Permission from Elsevier.

is important to note for diffraction based imaging methods where the images are not reconstructed in real time therefore damage observed in the image can not be responded to quickly. The changes of the diffraction pattern are illustrated by the fading of high angle intensity spots in the diffraction from an ribosome crystal 3.2. The spots at high angles start to fade after a total incident flux of 5.2×10^{11} photons/ μm^2, then after nearly double this flux most of the mid range spots have faded showing a decrease in resolution with dose [53]. In the final image most of the spots have faded and the central part of the diffraction pattern has increased. This picture directly shows damage per length scale. The high-angle spots disappear when the bonds at smallest lengths scales have been damaged. The damage to short lengths happens more rapidly than large length scales.

A commonly adopted limit of dose in X-ray science is the Henderson limit [58]. This limit states that the amount of dose a frozen macromolecule crystal can absorb before the diffraction pattern decays to half its original intensity is 2×10^7 Gy. In this study by Henderson et al. an incident flux that would impart this dose for 8 keV X-rays is calculated to be 1.6×10^{10} photons/μm^2 . At the time this paper was written, from this flux a crystal could withstand 1 day of beam at the highest performing synchrotrons. This limit has recently been reviewed by Neutze et al. for imaging biomolecules with X-ray free electron lasers, an extremely high flux source [59]. In this review it was found the very large damage caused by the pulse incident on the biomolecule providing the exposure time is short enough that the diffraction is collected before the onset of the damage.

3.3.2 Resolution and Dose

As mentioned in the above sections radiation damage is ultimately resolution limiting. In a paper by Howells et al. the maximum resolution achievable by CDI of a biological object is calculated by equating the minimum required dose for image (eq. 3.9) and the maximum tolerable dose on the sample [53]. The maximum tolerable dose is the amount of dose an object can withstand before the damage is too high to measure at a given resolution. The value at which these these two quantities intersect provides the maximum achievable resolution of CDI before the errors from the damage affect a structure at this length scale.

In the paper by Howells et al. the maximum tolerable dose was estimated from experimental evidence with a variety of different techniques, including crystallography, soft X-ray CDI, electron crystallography, and electron tomography. The curves for the minimum required dose and the maximum tolerable dose, plotted in fig. 3.3, estimate the maximum resolution that can be achieved with these techniques to be 10 nm, the point at which the maximum tolerable dose and the minimum required dose become equal. Biological samples are more susceptible to radiation damage, than for example metals, and ultimately restricts the achievable resolution when imaging these

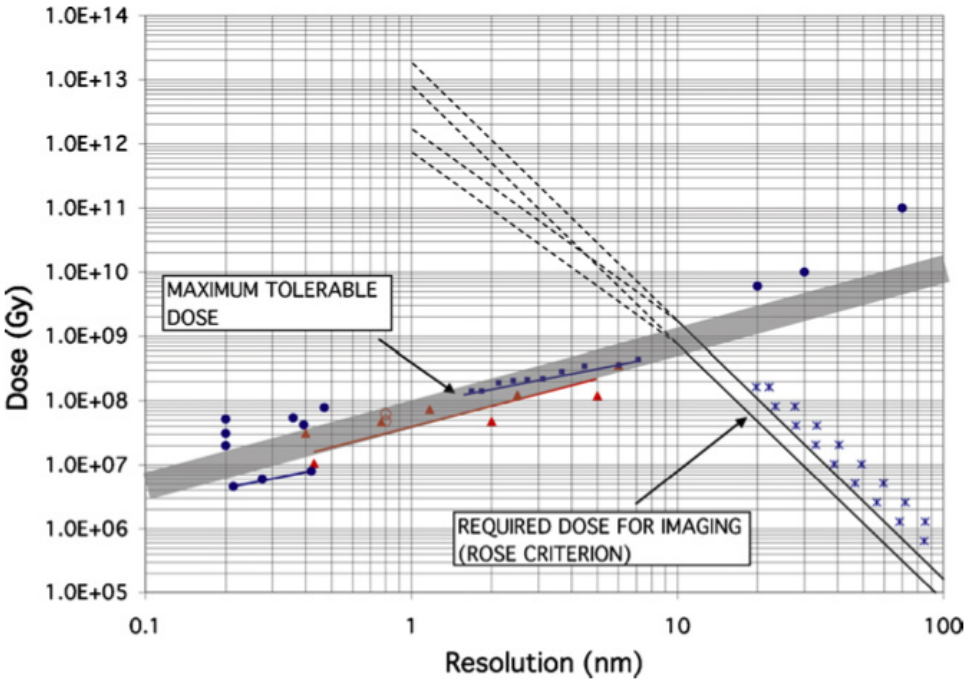

Figure 3.3: Maximum tolerable dose curve and required dose for imaging curve plotted against resolution. The intersection of these two curves at 10 nm its the maximum resolution that could be theoretically achieved by coherent diffraction imaging. Maximum tolerable dose curve is experimentally found from the following: Figure from [53] Permission from Elsevier

objects with CDI.

The maximum tolerable dose calculated here is relevant for a single shot measurement such as CDI , however, ptychography requires multiple overlapping positions which implies that more dose will be needed. However, the dose can be spread over each probe position, therefore the same dose can be applied to a ptychography image as a CDI image. The redundancy of the ptychographic measurement has been used to extract information, seemingly beyond the scope of the data, such as super-resolution and probe positions [60, 61], which may allow for reconstructions from noisy or sparse data. To date most of the successful work done in ptychography on biological samples, are from samples designed to withstand strong radiation (see section 3.6).

A theoretical examination of whether these techniques would be able to achieve atomic resolution was outlined by Schropp and Schroer [62]. They discuss question of the minimum required dose to image an atom or a molecule in its surroundings. The main result of this work finds that a feature can be detected in its surroundings if it provides enough signal to be detectable on its own. They find that the dose required to image an atom is inversely proportional to its atomic mass Z^2. They calculate the required dose density for imaging a Carbon atom $Z = 6$ in a molecule at the correct oversampling and obeying the Rose criterion as 9×10^{10} photons/nm^{2}which is impossibly high for current X-ray sources. A biological molecule could not withstand this dose according to

fig.3.3. In new X-FEL sources a very high flux photon pulse is incident on the sample providing a high dose density. This pulse destroys completely the biological sample but passes sufficiently fast that the diffraction is taken before the damage sets in. This approach is often referred to as "diffract and destroy" and promises higher resolution than is currently obtainable with synchrotrons [63].

3.3.3 Dose Fractionation Theorem

In order to avoid damage we would like to image our sample with the minimum dose possible to still achieve a statistically accurate measurement. For the most part we have been considering dose through a single projection of the sample, however, to produce a 3D image multiple projections of the sample are needed. X-rays have large penetration depth and therefore are capable of resolving structures in the 3D. The dose fractionation theorem states that, "A three-dimensional reconstruction requires the same integral dose as a conventional two-dimensional micrograph provided that the level of (statistical) significance and the resolution are identical" [64]. This statement argues that a 3D image can be made up of statistically insignificant projections providing that the resulting collection has the same statistical significance of a 2D micrograph therefore the dose required for a 3D and 2D image is the same. The mathematics of this statement are not debated however there is criticism of the level of significance needed to create a 3D image. Saxberg and Saxton argue that doses for significance in 3D images remains unreasonably high [65] and that for some cases a 2D micrography is better to see some structures. A counter argument by Hoppe says that the comparison of Saxberg does not use the same definition of significance and compare the density of a 3D image to a 2D projection, which are not physically the same [66]. One test of this theory with numerical simulations for a wide range of biological specimens finds it to be valid [67].

3.4 Detectors

In the previous sections there has been a great emphasis on detectable signal and achieving a statistically accurate signal. The choice of detector in an experiment can greatly influence the success of the imaging technique. In order to choose the correct detector for the experiment there a few basic detector properties that need to be considered a good summary of these properties is found in [11].

The first important property of detectors is the Detection Quantum Efficiency or (DQE) which describes the efficiency at which an event at the detector is recorded. This can simply be described in terms of the SNR of the input signal and the SNR of the output measurement:

$$DQE = \left({}^{S_o}/_{N_o}\right)^2 / \left({}^{S_i}/_{Ni}\right)^2 \tag{3.11}$$

The Quantum Efficiency of a detector is the fraction of incident photons that contribute detectable events. The DQE can be written in terms of the QE, the noise of the detector M, and the Poissonian noise of the photons $\sqrt{N}$:

$$DQE = {}^{(N\times QE)}/_{(N+M^2\times QE)} \tag{3.12}$$

Therefore if the detection noise $M << N$ then $DQE = QE$. For the best detection DQE should be equal to unity. Often DQE is quoted as a single number but it is in fact a function of several variables. Current single photon counting detector technologies have DQE = 0.98 at optimal energies [68].

The second important property is the dynamic range of the detector. The dynamic range is defined as the maximum signal before saturation over the RMS noise of the detector. For a single counting detector the noise of the detector refers to occasional mis-detections or false events measured by the detector. A threshold needs to be set on the detector so that false events are not recorded however this threshold cannot be set arbitrarily high for then true events will not be detected. Saturation is a point at which the detector response no longer follows linearly the count rate. In each detector a dead time is introduced which is the time after a signal is processed before an new signal can be processed. At high count rates this dead time correction limits the response function of the detector and saturation is reached.

Spatial resolution of a detector is the amplitude of response from a given point signal and can be described in terms of the Point Spread Function (PSF). The response of the detector to a point signal is this point convolved with the PSF of the detector. For detectors the PSF can often be modelled with a Gaussian. The spatial resolution can be given in terms of the Modulation Transfer Function (MTF) which is Fourier Transform of the PSF.

For a CDI experiment on a biological sample the ideal detector has a high DQE such as a single photon counting detector and a high dynamic range. From a weak scattering sample it is important that every photon from the sample is detected. The high angle scattering will have on the order of 10^6 fewer counts than the central beam therefore the dynamic range becomes critical to detect to high resolution.

3.5 Beamstops

The geometry of CDI or ptychography setup is typically in the forward scattering direction (see section 1.7.1), when the detector is placed in line with the sample along the beam axis. Measuring in the forward scattering direction often requires the use of a beamstop to protect the detector from the direct beam. In most cases detector pixels become saturated when registering a large number of photon counts, which can lead to poor read out and ultimately permanent damage. The beamstop is typically a piece of highly attenuating material placed in front of the detector face to reduce the intensity of the signal from the direct beam. This region contains the low frequency information of the diffracting object, therefore its removal by a beamstop causes artifacts in the reconstructed image or the phase retrieval algorithms to fail entirely [69]. This is a common problem in CDI and there have been many attempts to solve it both experimentally and in the data processing stage.

In early examples of CDI the missing centre of the diffraction pattern caused by the beamstop was replaced by a calculated Fourier Modulus of an x-ray microscopy image of the sample gained by a lens-based X-ray microscopy [44]. Whilst this technique produced successful reconstructions of E.Coli bacteria, it can cause artifacts in the reconstruction is the calculated centre and the outer diffraction are not correctly matched.

A practical way to reduce the error from the missing data is to minimize beamstop size to cover the fewest pixels possible, preserving most of the low resolution diffraction data. One way of achieving this is to cover a quarter of the detector with an attenuating plate and then replace the missing data with the opposite quadrant using centrosymmetric arguments. With careful alignment this results in only a few central pixels covered by the corner of the quadrant being lost. The values of these pixels can be estimated in the reconstruction stages by the phase retrieval algorithms. However, this only works for real objects where the symmetry arguments are valid. This method has been employed in chromosome [70] and yeast [31] imaging with CDI, in both cases 3D images were successfully reconstructed.

Another treatment of the beamstop problem is to use a semi-transmitting beamstop placed over the central beam. Here instead of blocking the signal from the direct beam it is simply attenuated, allowing information to reach the detector but not to saturate it [71]. This section of the data can then be multiplied by the attenuation factor of the metal in the processing stage to estimate the signal from the direct beam. Wilke et al. analyzed the effect on the reconstructed phase of different attenuation corrections and found that the reconstruction algorithm (ePIE) was quite robust for changes of multiple orders of magnitude. They found that the range of usable low flux increased a hundred times but could not be increased more than this due to the strong scattering from the

star test pattern.

Huang et al. simulated the effects of missing central data on the performance of the phase retrieval algorithms [69]. They observed that if the missing central data contained over 10 speckles there were artifacts in the reconstruction for HIO algorithm, which was the most tolerant algorithm to the missing data. These artifacts occur because they and their Fourier transform both fulfill the real and reciprocal space constraints of the algorithm. The missing data causes a set of very weakly constrained modes that can be estimated using harmonic oscillator modes multiplied by the correct coefficients. If these modes are calculated and given to the algorithm as an extra constraint then the artifacts from the reconstruction can be removed [72]. This application of modes to the constrain the reconstruction was used to obtain an image from a yeast cell [73].

The beamstop remains one of the main challenges in biological imaging even with the advance of new detector systems that have significantly higher dynamic range. These detectors do have a saturation limit and therefore need some protection from the direct beam however, occasionally a beamstop can be removed from the experimental setup with the expense of less incident photons on the sample.

3.6 Examples of Ptychography and CDI in biology

A good example of 3D coherent diffraction imaging in biology was achieved by Jiang et al [31]. Diffraction patterns of a whole unstained yeast cell were taken at several angular projections. Each of the diffraction patterns was reconstructed by CDI forming a series of 2D real space images that were reconstructed by tomography to form a 3D image. The arrangement of the components of the yeast cell can be clearly seen (fig. 3.4) such as the nucleus in orange, the mitochondria in blue, the endoplasm reticulum in green, and the vacuole in white. The image was measured with 50 nm resolution and the average density of the yeast spore was calculated to be 1.14 g/cm^3, providing quantitative information about the size of the elements in the cell and the physical properties of the sample. In comparison to EM tomographic studies of yeast show higher resolution than this allowing for reconstructions of high order structure, e.g. microtubials in yeast [74], however the physical property of density can be calculated from the phase image.

In order to achieve 3D imaging ptychography is combined with tomography, which requires a ptychography dataset at a sufficient number of angular projections to be reconstructed with tomography algorithms. As discussed in section 3.3.3 the dose fractionation theorem means that the tomography need not require more dose, however, this step limits the achievable resolution by tens of nanometers mainly due to stage movements and the data preprocessing before the

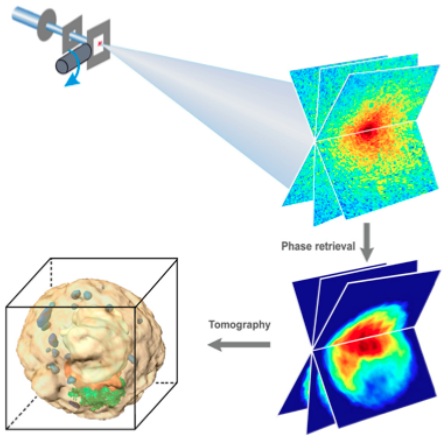

Figure 3.4: Set up of CDI -tomography experiment showing the final result of a 3D yeast cell. In the top left part of the image the experimental set up is shown, the incident beam is selected by a pinhole and scattering from the aperture is blocked by the second square aperture. The figure in the top right shows the diffraction pattern from the incident beam on the sample. The bright centre shows the direct beam and the surrounding speckle is the signal from the sample. The sample is rotated and at each rotation a diffraction pattern is taken to produce a 3D set shown in the top right. This tomographic set is then used to form an amplitude reconstruction in each plane (bottom right) which is finally made into a 3D image (bottom left). Figure from reference [31]. Permission from Proc. Natl. Acad. Sci.

tomography algorithms can be applied [30].

Due to the strong dose imparted by this technique two of the most successful examples of biological ptycho-tomography have been applied to radiation resistant biological materials because of the high minimum required dose. The first example is of a 3D image of a bacterial D. Radiodurans, (fig.3.5), a bacteria which can withstand high levels of ionizing radiation [75], which shows regions of high density DNA inside the eukaryotic cell, shown in red (fig. 3.5). The mass density of 1.6 g/cm^3 was calculated for the DNA rich regions from the phase measured by ptychography.

The second example was of a section of mouse femur, bone is another material that can be exposed to high levels of radiation without damage. This was also studied with ptycho-tomography to produce the first 3D image which showed the passage of osteocyte lacunae (L) and the connecting canaliculi (C) at 150 nm resolution. This example demonstrates the power of these methods when applied to biology, that the networks of fibres can be mapped out in detail in 3D without sectioning. In bone these networks of osteocyte lacunae and canaliculi are thought to be responsible for bone formation and it is critical to have 3D structural information in order to successfully study this process.

3.7 Comparison to other techniques

Strong contenders to Coherent Imaging Methods are other synchrotron methods such as Transmission X-ray Microscopy (TXM) and Scanning Transmission X-ray Microscopy (STXM) which use

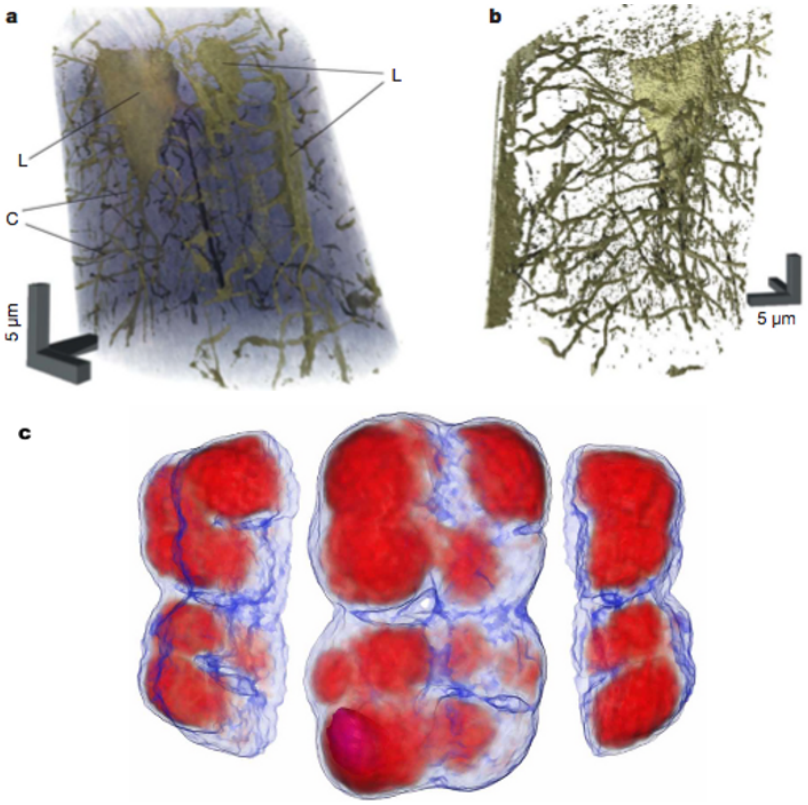

Figure 3.5: (a) Ptychography reconstruction of the phase component of a mouse femur showing the lancunae (L) and the canaliculi (C). The grey area shows the volume of the sample, (b) the lacuno-canalicular network, image obtained by segmentation and isosurface rendering. Images from [46]. Permission from the Nature Publishing Group. (c) Three views of the 3D reconstruction of D. Radiodurans. The red regions show the DNA inside the wall of the eukaryotic cell , shown in blue. Image from [7] Permission from The Optical Society.

zone-plate optics to create an image. These optics are difficult to manufacture and are resolution limiting, the development of Coherent Imaging methods aims to break this limit on resolution by avoiding optics. Electron Microscopy (EM) is a powerful technique routinely used in biological imaging which can obtain similar information to that of X-ray imaging. Transmission Electron Microscopy has very high resolution however the small penetration depth of electrons results in destructive sectioning procedures. Another contender to these methods are new non-linear optical methods such as PALM and STORM. These optical methods, known as "super-resolution" methods can achieve resolution of tens of nanometers,by measuring the , similar to X-ray techniques but can only be applied to samples that can be imaged using fluorescence.

A comparison of the techniques given in table 3.1 summarizes the different methods with respect to the properties described in this chapter: resolution, sample damage and the penetration depth of the sample. Modern EM currently has greater resolution than lensless microscopy methods with High Resolution Transmission Electron Microscopy (HRTEM) being able to achieve atomic [76] compared to the highest achieved resolution of CDI of 2 nm [77]. These resolution limits are for radiation hard samples current limits for biological samples are lower with current cryo-electron tomograph measuring cellular ultrastructure with 0.2 nm resolution [78] in 3D. The penetration depth of electrons is approximately 100 nm limiting the size of objects that can be visualized with tomography. To perform 3D imaging of larger objects a delicate sample preparation procedure is used. This involves embedding the sample in plastic or ice and slicing into sections several nanometers thick. New methods involve Focussed Ion Beam milling to produce ultra thin slices [79]. Each of these sections is then imaged and the images are stitched together to give 3D information. Performing sectioning techniques can impart some damage in the structures of interest. Furthermore the resolution in the direction of the sectioning is limited by the size of the slices. Whole mount sample preparations can be used with cryo-TEM to a resolution of 4-6 nm [80]. The penetration depth of X-rays allows for whole biological samples to be imaged in 3D with tomography.

New super-resolution microscopy techniques, such as PALM and STORM, use matched wavelengths to excite fluorescent dyes in such a way that only molecules at distance greater than the classical diffraction limit are giving a signal at any one time [81]. In this way the diffraction limit is broken as the fluorescence can be tracked to a single binding site, continuous switching of fluorescent markers can be used to build up an image with resolution less than 30 nm [82]. These light microscopy methods have the unique advantage over X-ray and electron methods because they can measure live samples in a wet state [83, 84]. However, the fluorescent dyes that are used a basis for imaging, both disrupt the native state and do not give a faithful representation of structure in the image if dyes do not attach correctly to the binding site.

Method	Resolution	Penetration depth	Damage to sample
Super-resolution optical microscopy	30 nm	—	Application of fluorescent dyes can disrupt native state.
Transmission Electron Microscopy	0.2 nm, Å	Limited to 100 nm	Sectioning to access 3D structure. Radiation damage.
STXM, TXM	50 nm	Whole biological samples	Radiation Damage
CDI and Ptychography	50-120 nm	Whole biological samples	Radiation Damage

Table 3.1: Providing a comparison between the Coherent Diffractive Imaging and ptychography with other imaging techniques that are used to image biological samples. The techniques are compared by typical resolution, sample thickness and damage to the sample.

Atomic Force Microscopy is a surface sensitive technique that scans a tip attached to a cantilever over a sample and measures the force applied to the tip from the sample by detecting the deflections of the cantilever. These deflection measurements can be used to obtain topographical information. The tips can be tailored to produce strong force reactions at points of interest such as using a magnet in Magnetic Force Microscopy or using a molecule with a certain bio-chemical specificity. Chromosome topography has been measured with AFM to high resolution [85, 86] and is especially useful in detecting breakages and translocation points [87]. One advantage of AFM is that chromosomes can be measured in a variety of buffers and does not have to go through extensive sample preparations [88]. With a genetic probe AFM can also be used as a "chromosomes cutter" allowing high precision dissection of parts of the chromosome [89].

X-ray microscopy methods such as Transmission X-ray Microscopy, Scanning Transmission X-ray Microscopy are used to routinely look at biological samples [90, 91]. X-ray microscopes typically operate in the water window and image the differences absorption over the sample. The resolution for STXM and TXM is governed by the quality of the focussing optics and most beamlines can reach below 50 nm resolution in frozen hydrated samples [92] and coupled with tomography are achieving 3D imaging of whole cells [93]. These techniques are several years ahead in development than the lensless based imaging techniques, and have dedicated beamlines [94, 95] which can perform imaging in the frozen hydrated state. The ultimate resolution of lens based methods are limited by the quality of optics, these are difficult and expensive to produce for X-rays. Lensless based imaging is advantageous as by removing the lens has the potential to produce wavelength limited resolution.

3.8 Summary

CDI and Ptychography have the potential to be useful in the imaging of biological samples, by allowing for mesoscale ($\sim$ 10 nm) to be imaged in the 3D, but this is technically challenging to implement. The weak scattering of X-rays from biological materials give low signal to noise so it is difficult to increase resolution and contrast within an image. Better contrast and resolution come at the cost of greater dose applied to the sample which is ultimately damaging to the sample structure. The onset of radiation damage happens quickest at the smallest length scales setting a limit to the maximum resolution that can be achieved with CDI of 10 nm for biological samples. To date there have been few examples of 2D reconstructions with 30-50 nm resolution and in these examples the contrast between different areas of samples have been low. Moving to 3D introduces other difficulties in achieving high resolution such as motor stability and good alignment of projections. Considering the dose fractionation theorem the limit on resolution by radiation damage for 3D images is still the same as in 2D but to date only samples that are radiation hard have been imaged.

Ptychography and CDI has the potential to overcome the resolution limits of lens based X-ray microscopy and image large samples in 3D without sectioning. Both Electron Microscopy and X-ray microscopy have more years development than the lensless imaging techniques, and are producing high resolution images of biological materials. Obtaining these images is technologically difficult requiring stable sample environments which are difficult to implement with freezing capability. When applying lensless imaging to biology there is a need for advanced detector technology to record the very weak high resolution signal as well as the strong central peak. The limitation of the beamstop can be used as an advantage in this case by artificially increasing the dynamic range of the detector but with the expense of artifacts in the reconstructions.

Chapter 4

Chromosome Structure

A set of chromosomes contain all the genetic material in a mito-organism and are important for the safe replication and transferal of this information as the cell divides. There have been many studies on the human chromosome that have provided much information on the functionality and role of the chromosomes, and this chapter aims to summarize some of the work done that is applicable to this thesis. Chromosome structure undergoes many changes in size and form during the cell cycle, to compact the large lengths of DNA into the size of a nucleus without damaging the fibre. There are many studies focusing on different levels of chromosome structure at different times during the cell cycle in which imaging techniques have been essential. In this chapter we will discuss the current knowledge of the chromosome structure and how imaging has made an impact on this. We will also discuss how X-ray imaging techniques, such as CDI and ptychography may be applied to imaging chromosome structure.

Many of the definitions in this chapter and explanations of the basic cellular and nuclear processes follow Essentials of Genetics by W.S Klug et al. [96].

4.1 The Nucleus

Living organisms can be split into two major kingdoms eukaryotic and prokaryotic. There is a third group archea which are a form of prokaryote. Eukaryotic cells contain a nucleus whereas prokaryotes contain the nuclear material in a different way and do not have a nucleus. Prokaryotic cells are typically small organisms such as bacteria. The nucleus is the part of the cell that contains all the genetic information which is coiled up into chromatin fibres. Also present inside the nucleus is the nucleolus where the ribosomal RNA is synthesized.

The nuclear envelope is a 30 nm thick double membrane surrounding the nucleus and has a

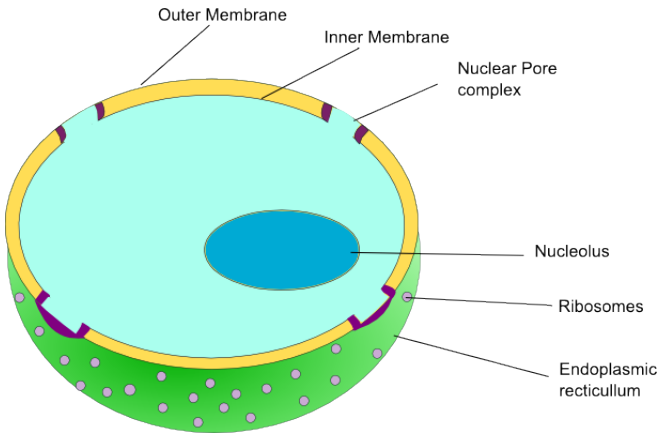

Figure 4.1: Diagram of nucleus structure. The DNA that is contained inside the nucleus in the form of chromatin is protected from the other components of the cell by the nuclear membrane. The outside of the nucleus is dotted with ribosomes that translate proteins which are then secreted in the endoplasmic recticullum.

phospholipid bilayer (see fig 4.1). This membrane separates the nuclear contents from the cell cytoplasm, however the membrane is porous to allow transport between the nucleus and the rest of the cell. There are large proteins needed by the nucleus during different times of the cell life, therefore the nuclear envelope contains large pores, the pore and the complex are 100 nm in size, to accommodate the protein complexes too large to permeate the membrane. On the outside of the nuclear membrane there is the endoplasmic reticullum which is a network of sack like structures called cisternae. On the outer layer of the endoplasmic recticullum membrane sit ribosomes. The role of a ribosome is to synthesize proteins from amino acids as dictated by the messenger RNA (or mRNA). The proteins that are made by the ribosomes are then secreted into the endoplasmic reticullum. The Golgi apparatus are made up of layers cisternae and have the important function of labelling and packaging the proteins so they are then sent to the correct part of the cell.

4.2 The cell cycle

The cell cycle refers to the process of cell duplication (fig. 4.2). For a eukaryotic cell, one with a nucleus, the cell undergoes interphase in which the cell grows and performs its function. After, is mitosis, where the cell duplicates the chromosomes which are then divided into two nuclei. Cytokinesis, part of the mitosis stage, is where the cytoplasm divides and two daughter cells containing exact copies of the DNA are formed.

The interphase stage of the cell cycle can be broken down into three stages that describe the cell's function during interphase: G1, S and G2. During the S (or synthesis) stage the DNA synthesis occurs this is when the cell copies all the genetic material making a second set of DNA.

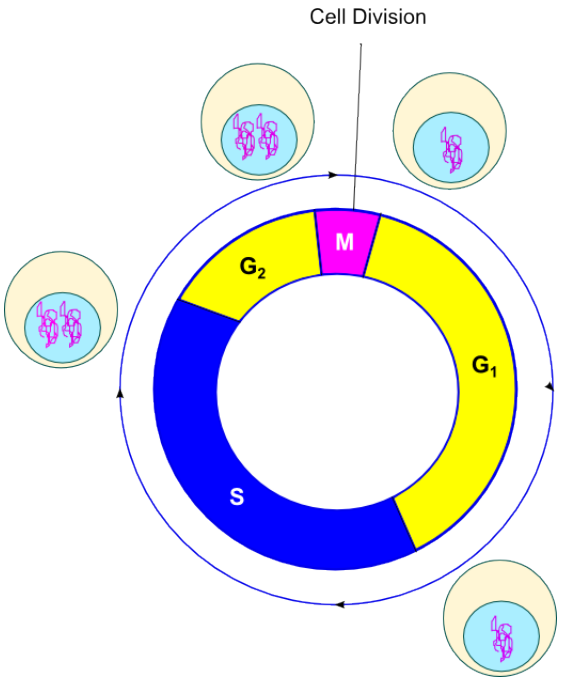

Figure 4.2: Diagram of the cell cycle showing the four stages G1, S, G2 and M (mitosis). The form of the main components of the cell are shown for the G1, S and G2 phases. The G1 phase has all the genetic information in the form of decondensed chromatin fibres, during the S phase the genetic information is replicated so now the cell contains two relative copies. The cell splits in two during cyto-kinesis producing two daughters cells each with containing a copy of the genetic information of the original cell. Figure adapted from [97]

In the G1 and G2 (gap) stages that precede and succeed the S phase (fig. 4.2) no synthesis occurs but damaged DNA is repaired. The G1 stage is where the path of the cell is decided, either the cell continues through synthesis and then on to mitosis or it enters the G0 stage where the cell is still active but will not divide. The cell cycle consists of four main stages G1, S, G2 and M, which stands for mitosis.

During mitosis the cell prepares to divide into two daughter cells containing the genetic material of the parent cell. During interphase the chromosomes are uncoiled, and the genetic information exists in decondensed chromatin fibres to allow synthesis. When mitosis occurs the chromatin condenses to form the mitotic chromosome that have the characteristic X shape. These chromosomes are in homologous pairs- for each chromosome there exists a copy, for the exception of the X,Y sex chromosomes in males. In humans there are 46 chromosomes or 23 pairs. The total number of chromosomes is referred to as the diploid number, half of this number is the haploid number. So for humans 46 is the diploid number and 23 is the haploid number.

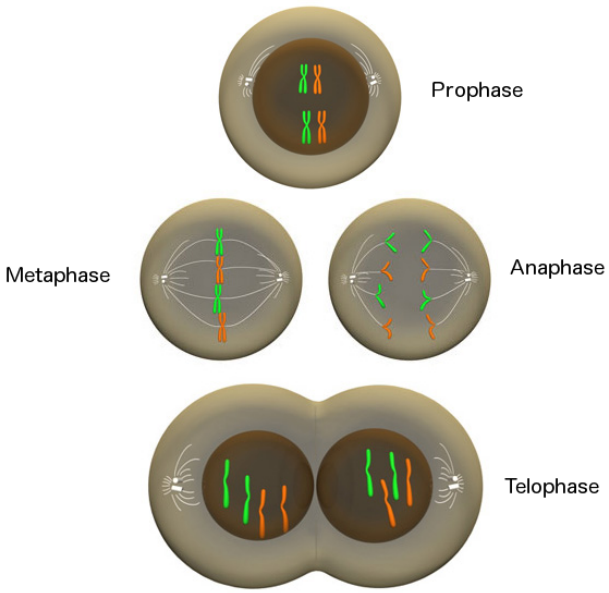

Figure 4.3: Diagram showing the four stages of mitosis: prophase (top), metaphase (centre left), anaphase (centre right) and telophase (bottom). During these stages the nuclear envelope breaks down, the chromatin condenses to form chromosomes and spindles are produced to line up the chromosomes along an axis for successful division. Teleophase is when the chromosomes undergo division. After telophase, the nuclear envelope is rebuilt and the nucleus divides into two. Figure from [98]. Permission from Nature Publishing Group.

4.2.1 Mitosis

In the late G2 stage of the cell cycle, the chromosomes start to condense and prepare for nuclear division that occurs in mitosis. Mitosis can be broken down into the following four stages : prophase, metaphase, anaphase and telophase (fig. 4.3).

The cell typically spends half of mitosis in prophase during which several key processes happen. In prophase a pair of centrioles move to opposite sides of the cell. These centrioles nucleate spindle fibres that are strung between them creating an axis along which the chromosomes will divide at a later stage. During this time the nuclear envelope starts to disappear and the nucleolus breaks down. The chromatin inside the nucleus starts to condense and the chromosomes start to form. Near the end of prophase the chromosomes have formed two distinct arms, called chromatids, which are joined throughout the centromere.

The early period of metaphase (or prometaphase) involves the migration of the chromosomes to the centre of the cell, or the metaphase plate. Metaphase is strictly defined as when the chromosomes have finished moving and are aligned by their centromeres along the metaphase plate. The chromosomes are now ready to be pulled apart by the spindle fibres which happens during the anaphase stage of mitosis.

The key event of anaphase is separation of the chromatids to form to two daughter chromosomes

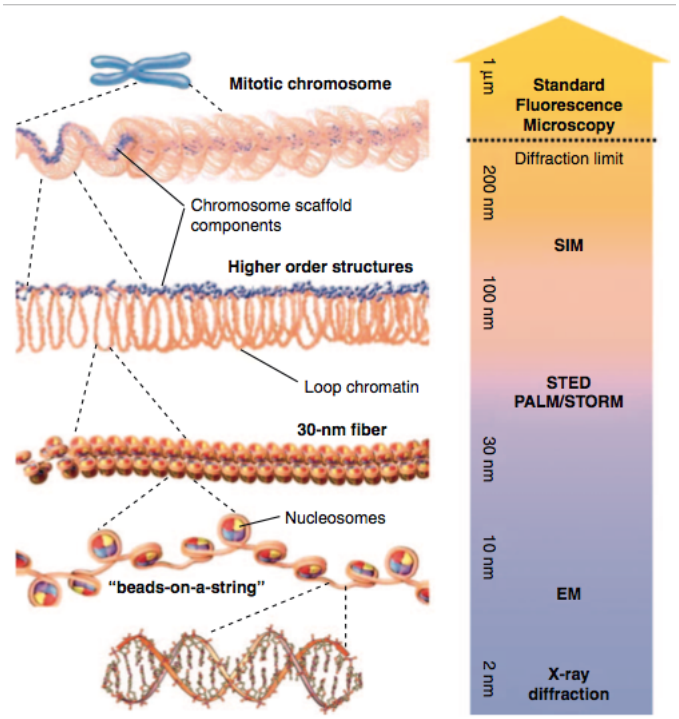

Figure 4.4: The levels of the chromosome structure against the imaging techniques that can be used to observe these length scales. The basic structural unit of chromosomes is the double helix of the DNA fibre. After the coiling around histone proteins to make nucleosomes at the 11 nm scale, little is known about the further packing of DNA in a mitotic chromosome. Figure from [4]. Permission from Elsevier.

which occurs by the division of the centromere. The spindle fibres then pull each the daughter chromosomes to opposite sides of the cell. At the end of anaphase the genetic material has been split and moved to have a set of chromosomes at opposite sides of the cell.

The final stage of the mitosis is telophase during which the cell divides to create two daughters which each contain a copy of the genome. The most important event during telophase is the cyto-kinesis, or the splitting of the cytoplasm in the cell.

4.3 Chromosome structure

The levels coiling of the DNA single fibre into the famous 'X' shape of the metaphase state is little understood. Imaging has contributed strongly to the existing knowledge of chromosome structure, from the double helix of the DNA being found by X-ray diffraction patterns obtained by Rosalind Franklin [1], to the light microscopy experiments that characterized chromosomes and found their anomalies. There is however a gap in spatial resolution between 10-30 nm (see fig.4.4) which cannot be accessed in 3-D by any of the common imaging methods. Theoretically lensless imaging techniques have the ability to access this region in 3D due to their large penetration depth and wavelength limited resolution. The imaging methods that are close in resolution to

CDI and ptychography are PALM/STORM fluorescence methods and electron microscopy. X-ray methods were compared to PALM and STORM and electron imaging methods in section 3.7. PALM/STORM methods have been applied to single chromatin fibres but this structural range is really at the limit of the resolution of the technique [4]. Electron microscopy methods have been used extensively but the small penetration depth of electrons limits the sample thickness that can be measured. Typically high resolution TEM tomography has a thickness limit of 300 nm [99].

The reason the mitotic structure is interesting is to explain the coiling mechanism of the long strand of DNA into the chromosome form. The chromosomes contain all the genetic code which is vital for life so it is important that this information is packaged in a safe way so that it will not be damaged, however the structure cannot be absolutely rigid because the DNA needs to be accessed in the interphase period of the cell to perform its function. To successfully reconstruct a 3-D fibrous structure, where the coiling may have a certain chirality and helicity it is necessary to image in three dimensions to be able to access all the information to construct a model of the fibre packing. Chiral structures are non-identical to their mirror images and helical structures are a curve in 3D space and both these structural properties can only be described in three dimensions. Performing 3-D imaging through sectioning can disrupt the coiling structure, therefore does not provide a true picture of the internal structure. Sample are often fixed in resins before section but this embedding process may also lead to artefacts and damages [100]. It is possible to look at large whole-mount samples , such as cells, with TEM however, these undergo cryo or drying processes [101].

4.3.1 DNA

The smallest structural level in a chromosomes is the DNA, which contains the genetic code essential to life. The structure of DNA was famously found by Crick and Watson [2] from an X-ray diffraction pattern measured from isolated DNA fibres. DNA is a macromolecule formed of four base molecules that form a double helix structure through hydrogen bonding. A double helix structure has a minor groove and a major groove and turns with a certain handedness. In its common B-form, the DNA's minor groove is 12 Å wide and the major groove is 22 Å wide and is right-handed helical. The four molecules that makeup DNA, are: Adenine (A), Guanine (G), Thymine (T) and Cytosine (C). The molecules will only bind A-T and G-C and these configurations of binding is called a base pair, which takes up 3.4 Å along the length of the DNA strand. The sequence of these pairs contain the code which is the genetic information of an organism. Being able to read this code gives information on evolution, genetic disease and functionality of genes. In the 1990s The Human Genome project was launched to find the entire genetic sequence of the

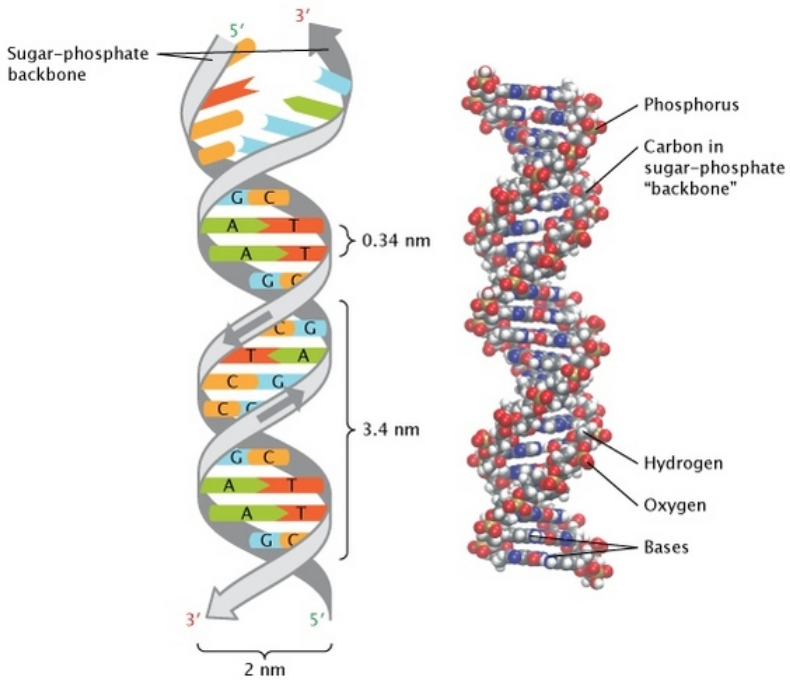

Figure 4.5: On the left a schematic of the structure of DNA in its common B-Form showing the base pairs between the phosphate backbone. The base pairs take up 3.4 Å along the length of the DNA. The DNA is a double helix with a 22 Å major and 12 Å minor groove. The right shows an atomic model of DNA with Hydrogen atoms in white, Oxygen in red and the bases in blue. Fig. from [102, 103] Permission from Nature Publishing Group.

human genome.

There are several methods of performing sequencing but one of the most commonly used methods, and the one that was used in the Human Genome project is shotgun sequencing method. In this method the extracted DNA strand is cloned to form several identical fibres. These fibres are then cut it to many pieces like, the random firing of a shotgun from which the method takes its name. The sequence of base pairs in small fragments of DNA are found. By looking for matches in overlapping sequences between the small DNA fibres, alignments, the large fibre can be pieced together [104].

From sequencing 99 % of euchromatin and some of the constitutive heterochromatin in the human genome has been established, but there are still sections of heterochromatic DNA that remain unsequenced. It is technically difficult to apply shotgun sequencing to heterochromatin because of the large amount of repeating sequences, however it has been achieved in the case of fruit flies [105]. It has been estimated from sequencing results that the human genome in total contains approximately 3 billion base pairs of DNA. The number of base-pairs in chromosome given by sequencing is an estimate based on the sequenced euchromatin and the estimated size of the unsequenced heterochromatin areas.

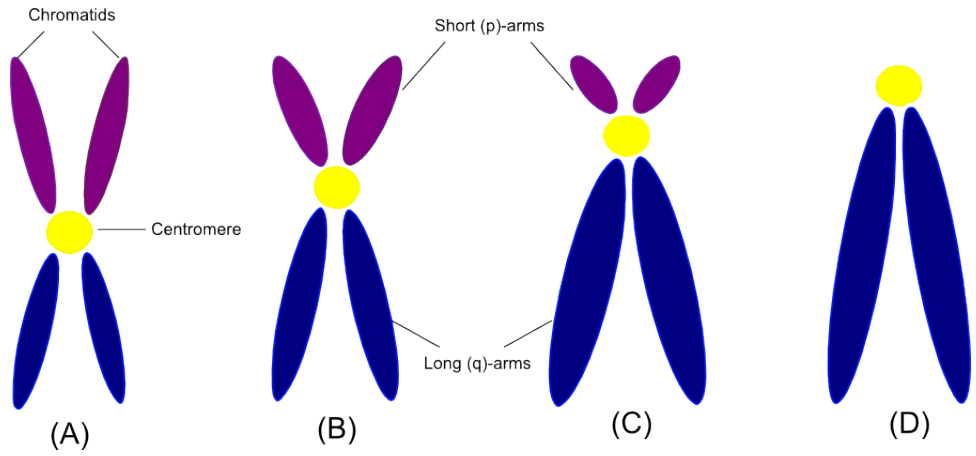

Figure 4.6: Metaphase chromosome structures. The chromosome is formed of two arms, the shorter of the two is the p-arm and the other the q-arm. The arms are joined together by the centromere and stopped at the ends with a telomere. Four chromosomes shapes can be defined from the length of the arms and the position of the centromere, there are (A) metacentric, (B) sub-metacentric, (C) acrocentric and (D) telocentric.. Figure adapted from [106].

4.3.2 Metaphase chromosome structure

We have seen in a previously (section 4.2.1) the chromosomes have a variety of different structures throughout the cell cycle. The chromosomes are most easily visualized under a light microscope in metaphase and their name comes from the greek “chroma” meaning colour and “soma” meaning body. In metaphase the chromosomes form their characteristic ’X’ shape which is composed of two arms a short arm (p-, or petite, arm) and a long arm (q-, or queue, arm) grouped together at the centre by a centromere (see fig. 4.6). The telomere regions are found at the end of the chromosomes arms which protect the ends of the chromosomes and prevents fusion with neighbours.

The gross chromosome structure can be described by the placement of the centromere and the length of the two chromosome arms. There are four structures metacentric, submetacentric, acrocentric and telocentric. In metacentric chromosomes the centromere placement is in the centre of the sister chromatids resulting in p- and q-arms of approximately equal lengths. Submetacentric chromosome have the centromere placed between the middle and the end of the chromatids resulting in two different arm lengths, a short p-arm and a long q-arm. In acrocentric chromosomes the centromere is placed close to one end of the chromatids giving a very short p-arm. Telocentric chromosomes have the centromere placed at the end of the chromosomes therefore there is no distinguishable short arm.

The chromosomes in the human nucleus have different lengths and contain examples of all the four chromosomes above. Different species often show one particular shape, for example mouse chromosomes have majority acrocentric chromosomes and chromosomes from barley are only metacentric [107],[108].

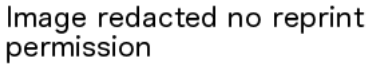

Figure 4.7: Karyotype of a human female produced by G-banding. Chromosomes are first treated with trypsin then Giemsa staining is applied. Giemsa as an affinity for the A-T regions which show up as dark bands. These order of bands are unique for every chromosome therefore can be used to sort them. Image from reference [109]

4.3.2.1 Karyotype

The variation in size and shape with additional structural information from the placement of genes along the chromosome arms can be used to identify and sort the chromosomes. An arrangement of sorted chromosomes is called a karyotype (see fig. 4.7). In the early methods of performing a karyotype chromosomes were identified by this barcode, then sorted by length and each pair of chromosome was identified by a number, for example, chromosome 1 is the longest and number 22, is the shortest. The sex chromosomes, number 23, are mid range in length, with the X chromosome being similar in length to chromosomes 9-12. Diseases can be observed just from changes in the gross chromosomes structure, therefore performing a karyotype is an essential screen when looking at genetic disease and a starting point for studies of chromosomes.

Traditional light microscopy methods are principally concerned with the overall shape of the chromosomes and can be used to identify the positions of genes along the chromosome arm with the help of staining. One of the first methods using the combination of light microscopy and staining is the method of banding, where chromosomes are first treated with a protease and then stained with a light absorption dye which results in a striped pattern emerging along the length of the chromosome arms. The banding pattern gives a unique "barcode" that can be seen under an optical microscope and it is from this pattern that each chromosome can be identified. The unique barcode made up of these stripes is called an ideogram. Depending on the type of banding that is performed the stripes reveal the regions in the chromosome that contain a dense area of a certain type of chromatin (for further details see section 4.3.3). In the technique of G or Q

-banding A-T rich areas of facultative, heterochromatin are stained, whereas the G-C rich regions of euchromatin is shown in R-banding. C- banding stains mainly constitutive chromatin which is located at the centromere of the chromosome. Whilst these methods are not used too heavily in modern research biology, they are routinely used in hospitals as a way of screening chromosomes for diseases which show up as deletions, such as Cri-du-chat syndromes, or repetitions of stripes in the banding pattern or sometimes an extra chromosome as in the case of Down Syndrome.

Modern methods of light microscopy are based on ideas similar to the banding technique. The basic principle is to mark an area of interest in the chromosome with a fluorescent tag or dye to better visualize it under a fluorescent microscope. A dye can be chemically tailored to attach, for example, to a single gene, single chromosomes or the telomere and centromere. This technique does not have sufficient resolution (on the order of 200 nm) to see high order structure of the chromatin fibres but genetically useful information can be gained from the position of certain regions of interest in a chromosome.

The method of Fluorescence In-Situ Hybridization (FISH) allows the selection of a specific DNA sequence of interest in the chromosome to be tagged. This method uses small sequences of DNA that match the sequence of interest in the chromosome. The small sequences of DNA are modified to be able to attach a fluorescent molecule. Both the probes and the DNA in the chromosome are denatured, which allows new hydrogen bonds to form between the probe and the chromosomal DNA strand. The hybridization step mixes the probe with the chromosomal DNA and the probe finds its target, the matching sequence. The fluorescent dyes are then attached to the probes and highlighting the specific sequence in the chromosomal DNA when viewed under a fluorescence microscope. The advantage of FISH over banding methods is that it can detect defects in cancerous chromosomes that traditional banding methods cannot [110]. FISH can also be performed on interphase chromosomes to map positions of genes in the nucleus (see section 4.3.4.1 for further details).

Multicolour (M-)FISH can be used to produce a karyotype in metaphase chromosomes (this process is sometimes also known as spectral karyotyping). This technique uses a number of probes to hybridize to the chromosomes. The different probes are tagged with different fluorescent dyes that are excited at and fluoresce at different wavelengths. These probes are attached to the hybridized metaphase chromosomes and produce a unique colour for each chromosome. The colour is computer generated from the unique fluorescence pattern of the different fluorescent probes attached to the chromosomes by analysing the detector pixel counts and assigning a colour based on the ratio of colours (wavelengths) of the mixture of fluorescent photons from the chromosomes. [111]. For more details on the process of M-FISH please see the methods subsection 5.5.2.

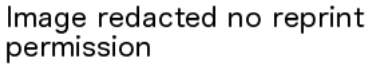

Figure 4.8: Flow karyotype of human chromosomes stained with Hoescht and chromomycin. The numbers identify the chromosomes sorted by their relative fluorescence. Chromosomes 9-12 are difficult to distinguish in this flow karyotype. Figure from [112]

Another way of performing a karyotype is through flow cytometry. In this process chromosomes are stained with two fluorescent dyes that are excited by, and fluoresce at, different wavelengths. Chromosomes are passed individually under a light source by floating them individually in a buffer. The light source excites the dyes and the fluorescence emitted from them is measured. The chromosomes are then sorted by how much fluorescence of each of the dye is emitted. A karyotype of human chromosomes is shown in fig. 4.8, where the chromosomes are stained with Hoescht 33258 (fluoresces at 420 nm) and chromomycin (fluoresces at 480 nm) [112]. The circles represent the histograms of the number of due counts for each of the chromosomes, and the numbers indicated the chromosome numbers. Practically this is a very useful way of sorting chromosomes as the end product is a collection of all of one chromosome, which would allow studies on just that particular chromosome. There are deeper implications of this technique, firstly that fluorescence from a dye can be quantified in this way and secondly that chromosomes from a cell have been karyotyped using all the chromatin, not just the euchromatin as in sequencing. The euchromatin content, however, scales linearly with chromosome size so can be easily used for karyotyping. All chromosomes can be resolved by this karyotyping method except 9-12 and 14-15 which have insufficient variation in the number of base pairs to be sorted by this method. Karyotyping by flow cytometry found that some chromosomes had more base pairs than their position in the karyotype suggested. This ability to detect A-T and G-C rich regions of unsequenced DNA and quantify the total number of base pairs in a chromosome makes it a candidate to be used in evolutionary studies by comparing these basic properties of chromosome structure between species [113].

4.3.3 Chromatin

The long strand of DNA is compacted into a space of a nucleus typically $5-10$ μm. The negatively charged phosphate backbone makes it difficult for DNA to fold upon itself. In the first level of compaction the DNA strand is wound around positively charged proteins called histones to form a nucleosome. Discovered by Olins and Olins looking at decondensed chromatin fibre from chicken with Transmission Electron Microscopy, it was found that the coiling of DNA around histone proteins formed a "beads on a string" model [114]. The unit of histone protein with the turns of DNA is called a nucleosome. The nucleosome disc is 11 nm in diameter and 6 nm thick, and have 1.7 turns of DNA around them. The core histones are composed of 5 proteins : linker H1, H2A, H2B, H3 and H4. The H1 protein structure, is the linker protein that binds the DNA in between the nucleosomes (the linker DNA) to the central histone core. The structure of the nucleosome has been resolved at 1.9 Å through X-ray crystallography [115] but the exact role and placement of the linker histone is still unknown [116].

The non-histone proteins that are included in a chromosome are numerous and still undergoing characterization. Mitotic chromosomes are approximately 2:1 DNA to protein and several thousand of these proteins have been found through various chemical techniques that isolate proteins from chromosomes [117]. A study of proteins in chromosomes suggests that there is a protective layer around chromosomes which is a made up of protein, eight of which were identified in the study [118].

The fibre consisting of DNA, histone and non- histone proteins is called chromatin, of which the beads on the string model is the most decondensed state. The chromatin fibre only exists in eukaryotic cells. Prokaryotic cells have a different arrangement of DNA which is often a single strand of chromatin packet into an area like a nucleus. The role of the chromatin fibre is to package the DNA into a small volume that can be contained inside the nucleus. The coiling of the chromatin is done in such a way that it protects the DNA from damage but allows the processes of replication and transcription to take place in interphase. The chromatin is condensed tightly during mitosis and needs to unravel to allow transcription to take place.

The part of the chromatin that has active genetic code, therefore is transcribed from is called euchromatin and this part undergoes structural changes through the cell cycle, becoming loose in interphase to allow access to the genetic material and recondensing during mitosis. There are some parts of the fibre that remain condensed during the interphase, called heterochromatin. DNA in euchromatin is replicated earlier in the S phase than the DNA in heterochromatin. Heterochromatin can be further separated into two categories constitutive and facultative. Constitutive heterochro-

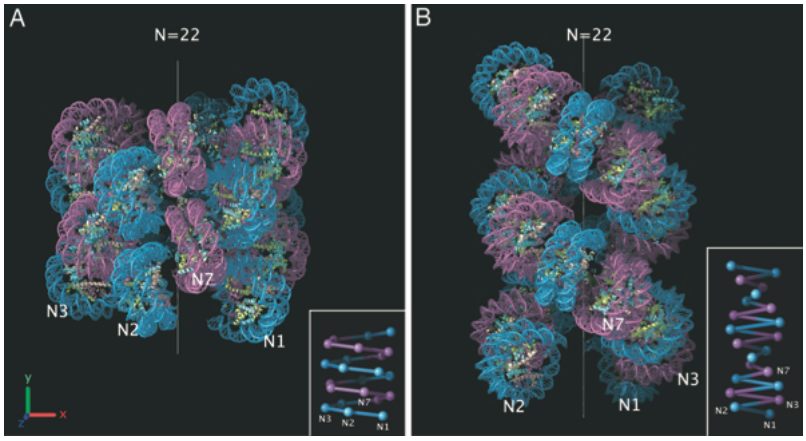

Figure 4.9: Proposed chromatin structures from cyro-electron microscope of mouse chromosomes. (a) One start solenoid model of 30 nm chromatin fibre based on diameter and packing ration measurements from EM images (b) two start zig-zag model where nucleosomes are folded on top of each other in a zig-zag method based on findings of the tetranucleosome. Figure from reference [120] Permission from Elsevier.

matin contains repetitive sequences of DNA, known as satellite DNAs and is predominantly found in the centromere and telomere regions of the chromosome. Facultative heterochromatin is a condensed fibre of genes that do not undergo transcription but can decondensed into euchromatin if triggered by several factors. Facultative heterochromatin is involved in gene silencing in yeast cells and X-chromosome inactivation Constitutive heterochromatin can also part-take in transcriptional silencing, firstly as by preventing gene rearrangements between highly similar genetic sequences and secondly by enforcing chromosomal segregation [119].

The structure of chromatin in a mitotic chromosome is largely unknown despite the body and variation of work that has looked into this problem. It has been suggested that the nucleosome units coil up into a 30 nm fibre, but the existence and the structure of this fibre is much debated.

These models mainly come from chromatin studied as single fibres or reconstituted fibres. In a study by Robinson et al. existence of the 30 nm fibre was found by cryo-EM, however this was from small segments of chromatin not a long isolated strand [120]. This was further supported by experiments by Grigoreyev et al. [121] that found both solenoid and zig-zag could be present in the same fibre under certain conditions. A presence of a 30 nm structure was also detected in stretched chromatin fibres with PALM/ STORM microscopy methods [4].

Two proposed models of nucleosome packing into chromatin are centered on the existence of the 30 nm fibre. These are the solenoid model and the zigzag architecture (fig. 4.4). The zig-zag architecture has been found by X-ray crystallography on a tetranucleosome, but because this only represents a single unit, it is unknown how a ribbon or fibre is constructed from this tetranucleosome block [123]. A key mystery to unravel whether the structure of chromatin fibre adopts a zig-zag or solenoid is the placement of the linker histones (H1) [116].

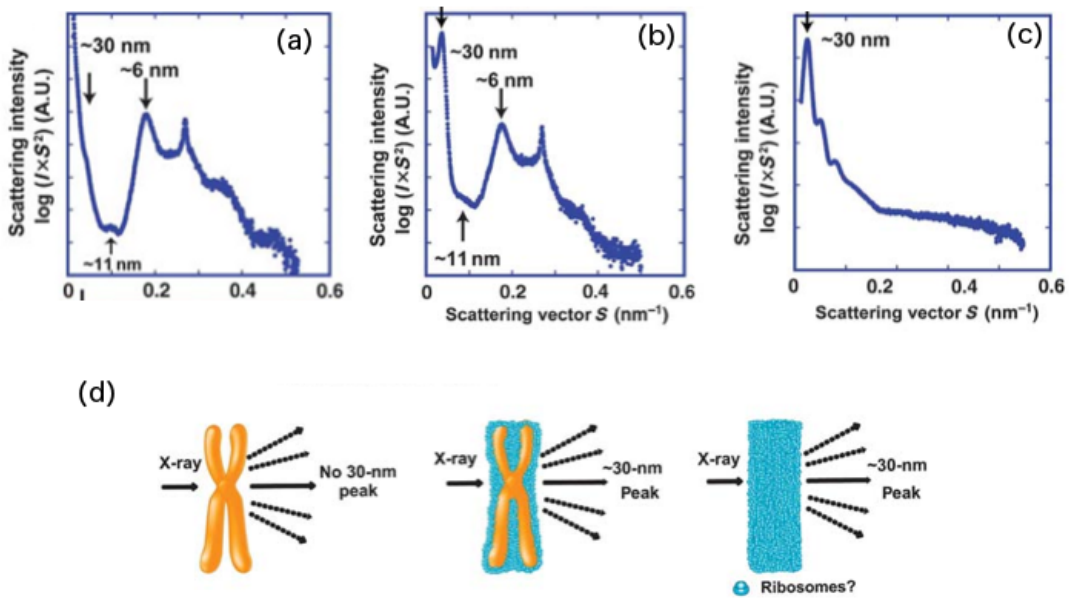

Figure 4.10: (a) SAXS profiles of human chromosome with the ribosomes removed and (b) human chromosomes with ribosomes. The 30 nm peak seen for the human chromosomes cannot be seen when the ribosomes are removed. (c) SAXS profile of a ribosome section of a Xenopus egg shows a narrow 30 nm peak. (d) Diagram showing that the aggregation of ribosomes might be responsible for the 30 nm peak. Figure from [122] Permission from The EMBO journal.

The solenoid model (shown in fig. 4.9(a)) is proposed from EM measurements of chromatin fibres prepared in vitro [120]. In the models that were made from the measurements it was found that the number of base pairs in the linker DNA played a role in the overall shape of the fibre. This is further supported by evidence that the position of the H1 linker histone is critical to the structure adopted by the chromatin fibre. Studies of chromatin folding with depleted H1 proteins find a structural change from reduction of linker lengths [124] to improper folding of chromosomes [125].

There is much controversy and a lack of knowledge surrounding the structure of the chromatin fibre which has only been summarized in this section. For further information see a highly detailed review by Woodcock and Ghosh [3].

4.3.4 Higher order chromatin structure

Currently there is no viable model for how chromatin is organized into a chromosome. To gain such a model, knowledge of the 3D structure of the chromatin and how it is assembled and disassembled must be known, to simplify the argument we can think of the structures as: Primary, a linear arrangement (e.g., beads on a string model), Secondary, structures formed by nucleosomes (e.g. 30 nm fibre) and Tertiary, the higher order interaction of secondary components [128]. There have been a range of studies investigating tertiary structures such as the compaction of chromatin

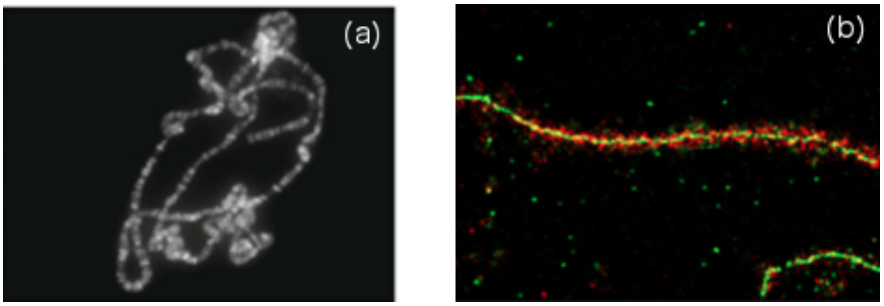

Figure 4.11: (a) Fluorescence microscopy image of a polytene chromosome stained with DAPI. These chromosomes are extremely long and show natural banding. Image from [126] Permission from Cold Spring Harbour Laboratory Press.(b) Super-resolution microscopy image of lampbrush chromosomes, the chromatin loops are shown in red and the central strand shown in green. Image from [127]

inside chromosomes. This sections attempts to detail some of the work investigating higher order chromosome structure.

Some of the most useful insights into higher order chromosome structure do not come from mammalian species. Polytene and lampbrush chromosomes are a more exotic shape than most chromosomes yet provide an insight into the structure of the chromosome. Found in some tissues inside larvae, polytene chromosomes are composed of many strands of DNA as they continually go through replication but without the stages of separation of cytoplasmic division. This produces a very long chromosome with bands running across the diameter of these chromosomes. Each of these bands contains active genes and upon transcription the bands uncoil producing a puff. This shows that the tightly packaged chromatin needs to have a mechanism to decondense during translation and can coil back up after the process.

Lampbrush chromosomes are meiotic chromosomes and consist of many lateral loops, of a single double helix, running along a central axis, composed of two double helical strands. Each of these loops contain active genes. It is thought like the polytene chromosomes these loops decondense during transcription.

Human chromosomes only contain a single strand of duplex DNA and the decondensation and condensation steps have a greater degree of complexity. As with the 30 nm fibre there are studies which look at both the higher order structure of the chromatin inside the nucleus in the decondensed state and in the mitotic chromosome in the highly condensed state.

4.3.4.1 In the nucleus

During interphase chromosomes are in an open state like an unravelled ball of wool to allow replication and transcription to take place. Unlike in mitotic chromosomes, the position of genes and structure in interphase is relatively unpredictable.

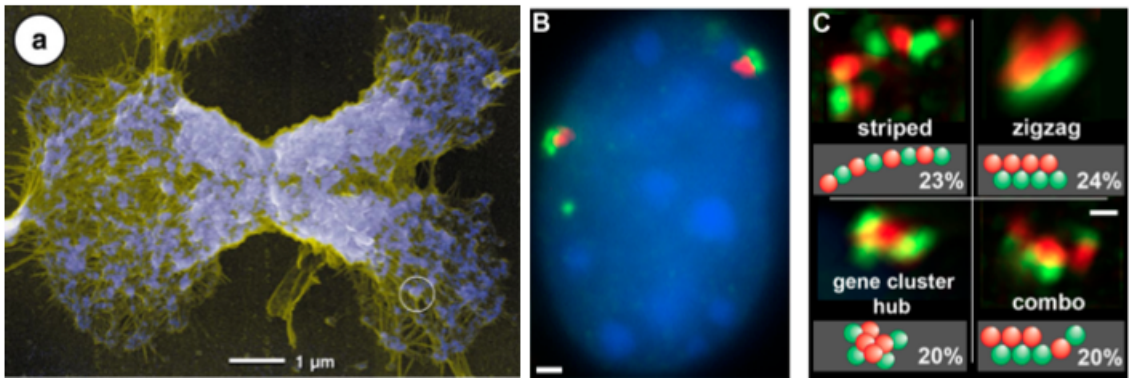

Figure 4.12: (a) SEM image of a decondensed barley chromosome showing parallel matrix fibres in yellow and chromomere globules in blue. The chromomeres are around 100 nm in size and attach to the parallel matrix fibres which compact on condensation. Image from [129] . Permission from Elsevier. (b) Gene rich areas (red) and gene deserts (green) in a mouse nucleus using FISH. The gene deserts are toward the nucleus periphery. (c) The formations of subunits of the gene rich and poor areas inside the interphase nucleus. All scale bars show 1 μm. Image from [130] Copyright The Rockerfeller University Press, maybe reprinted for non-commerical use without specific permission.

Work by Shopland et al. using FISH imaging methods on an area of mouse chromosome studied four active gene areas inside regions where there were no genes, or gene deserts [130]. Fluorescent probes were used to tag the gene rich areas and gene deserts that were then imaged with 400 nm resolution. They classified three interphase chromosomes structures (fig. 4.12(c)): zig-zag, gene-cluster and striped and also saw areas that were combinations of these subunits. They found that these geometric structures were based on the primary gene sequence of those areas and that the position of the inactive genes lay towards the periphery of the nucleus (fig. 4.12(b)).

Fluorescence microscopy does not have the resolution to see if these gene areas interact but can only tell if they are near each other. A chemical approach can be used to find if the interphase structure allows for the interaction of two genes. The chromosome conformation capture (3C) method aims to find this by creating a 3D structural model of genes that are close in interphase [131] using sequencing of cross-linked fragments of DNA. To form the fragments,chromatin is fixed with formaldehyde then cut with restriction enzymes. The fragments are then religated under diluted conditions where they form inter-ligations between themselves. In this way DNA fragments that are far apart in the genetic sequence, but are close in space in the interphase nucleus, can be ligated to each other hence producing a 1-D mapping of the chromosome structure [132]. This method has been successfully used to produce a whole model of the X chromosome in interphase for various cells. It was found that there is a variability in chromosome structures between cells on a large scale [133].

4.3.4.2 In the mitotic chromosome

A study by Earnshaw and Laemelli found that with the removal of histone proteins the chromosome structure fell into loops around a central fibre that had a similar starting shape to that of the original chromosomes. They proposed a model where the chromosome is formed of chromatin loops attached to a central scaffold [134]. Work on separating structural protein complexes has shown that the structure may be more complicated than that proposed by Earnshaw. For example two complexes condensin and cohesin are found to be responsible for structure in different parts of the chromosome. Cohesin, the joining of the two sister chromatids and condensin is responsible for chromosome condensation [135]. Cohesin holds the sister chromatids together through S phase until anaphase. Condensin is has a key role in chromosome condensation, that starts the process of mitosis [136].

In a study by Wanner et al. of barley chromosomes with Scanning Electron Microscopy revealed a new unit of structure, called chromomeres, which are approximately 100-200 nm in size [129]. This was found by doing several decondensation steps of barley chromosomes and noting that they appeared to be composed of parallel matrix fibre with globules attached (see fig.4.12(a)). The decondensation of the chromosome occurred in a linear fashion which suggested the stretching out of fibres rather than the uncoiling of a bound fibre. This picture of central protein matrix fibres is further supported by force-length measurements on chromosomes. When a chromosome was stretch apart with micropipettes the chromosome diameter was preserved to up to five times the original length [137]. This suggests that the structure of chromatin fibres are cross-linked to an elastic protein matrix that contracts in a linear fashion. Wanner et al. argue that there are several advantages to the linear model, over a superhelical model, suggested by their research. Firstly, linear models facilitate easy chromatid separation, and secondly, a linear model can easily explain uneven chromatid lengths (short arm, long arm).

Limited evidence suggests a strictly linear organization in the structure of metaphase chromosomes, yet as discussed in section 4.3.3, the structure of chromatin could be either linear or disordered. There are many models that suggest a disordered or helical compaction of nucleosomes into chromatin plays a role in DNA transcription, replication and repair [138]. Studies on entire chromosomes and not just chromatin show a linear compaction. The banding patterns appear completely sharp at the resolution of light microscopy and are found to map in a strictly linear fashion with the sequence as far as is known. The boundaries between the bands are not known below the resolution of light microscopy, around 200 nm, which corresponds to approximately 600 bp. SEM studies on banding with trypsin and Giemsa show that the trypsin leaves linear cuts

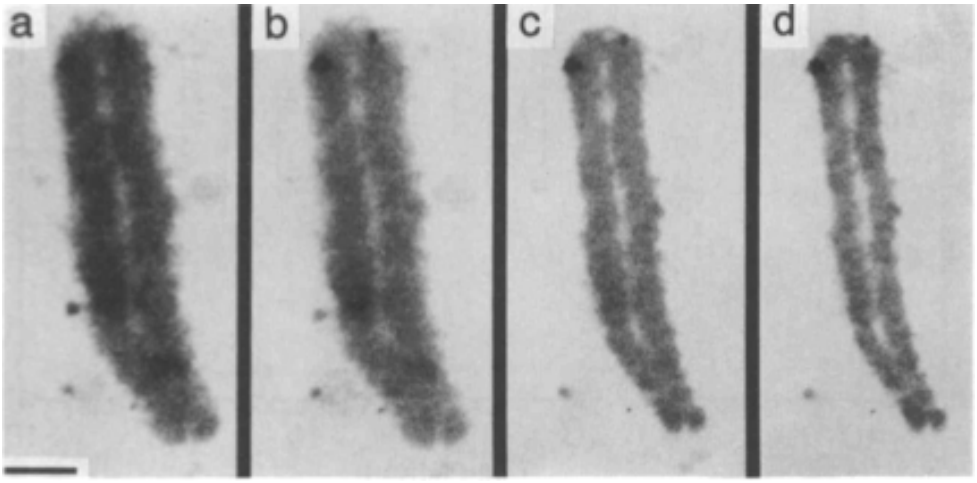

Figure 4.13: STXM images of single Vicia Faba chromosomes after continuous application of dose. (a) 0 Mrad, (b) 35 Mrad, (c) 139 Mrad (d) 240 Mrad. Scale bar = 2 μm. Figure from [57] Permission from John Wiley and Sons.

in the chromosome corresponding to the bands seen in light microscopy [139]. The condensation mechanism appears to be biologically relevant and probably has a packaging role in the preparation of progressively tighter packed bundles of DNA ready for cell division. Condensation can be reversed in vitro by the use of proteases and other chemical agents over a surprisingly large scale. This wide range of sizes of organized material originating from a single fibre of DNA suggests a biological relevance of the process. Many of the ∼150 protein species associated with the self assembly of chromosomes are involved with sequential orchestration, scaffolding and regulation of the process as its length scale diminishes [134]. In vivo decondensation has not been studied as extensively, but presumably involves sequential removal of the proteins used for assembly.

4.4 Imaging chromosomes with X-rays

In this chapter the structural level of chromatin is difficult to access with many imaging methods without damaging chromosome structure either through sectioning or application of fluorescent dyes. When finding structural units through imaging the length scale must be within the range of achievable resolution of the technique (fig. 4.4) and there is a resolution gap between 10-30 nm which is at the limit of resolution for most techniques. Coherent Diffraction Imaging and Ptychography can access this length scale in three dimensions without sectioning the material. This is particularly advantageous when looking at coiled fibres, whose structure can only be determined in 3D as much of information on the higher order structure such as helicity, is lost in 2D projection images. The current practical resolution of CDI and ptychography however is not sufficient to access information on the DNA fibre, which has a 2 nm diameter.

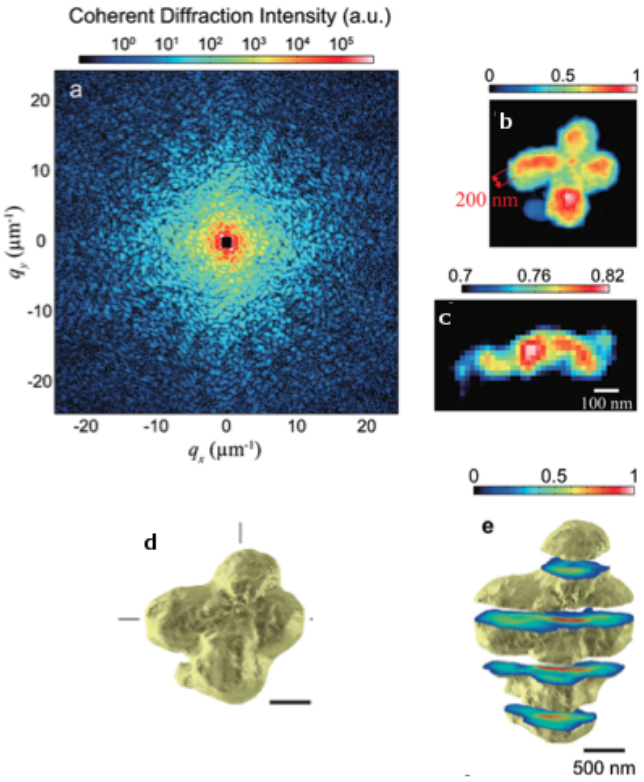

Figure 4.14: (a) Diffraction pattern from a chromosome taken at BL-29-XU, Spring-8, (b) 2D electron density image of a chromosome obtained by CDI at 38 nm resolution, (c) magnified image of chromatin arm marked in red in (b). (d) Isosurface rendering of the chromosome (e) Split isosurface rendering of chromosome showing projections of electron density at that position. Figure from [70] Permission from author, Prof Y. Nishino.

In order to successfully image chromosomes the sample preparation has to be optimized to the imaging method. This makes correlative microscopy very difficult as the sample preparation that gives the best results by one imaging method will achieve poor results in another. Also any sample preparation technique that removes the chromosome from its native state but often more information about the sample can be obtained through intensive methods such as staining.

Vicia Fabia (bean) chromosomes have previously been studied with Scanning Transmission X-ray Microscopy [57]. This study produced 2D projection images of chromosomes which clearly shows the individual chromatids and the centromere (fig. 4.13). The image has sufficient detail to see the difference in mass thickness along the chromatids and some of the winding fibres can be distinguished at the edges of the chromosomes. The images were used to map mass loss due to radiation damage and calculate a mass loss per unit dose applied. This was done for several different sample preparation conditions: hydrated, dried, frozen-hydrated and freeze dried. The freeze dried samples had the lowest mass loss per dose which suggests chromosomes should be imaged in a freeze-dried state to reduce radiation damage during imaging.

The lensless imaging technique of CDI has been applied to human metaphase chromosomes by

Nishino et al. [70]. Using the BL-29-XU coherence beamline at the Spring-8 synchrotron in Japan, diffraction data was taken of a chromosome from a HeLa cell and a 3D reconstruction was obtained. Samples were prepared by gentle centrifuging the chromosomes fixed in a buffer containing 10 mM Hepes-KOH, 5 mM $MgCl_2$ and 0.5% glutaraldehyde onto a 100 nm thick silicon nitride window. The chromosomes were washed with water and left to air dry.

The resolution of the 2D image (fig. 4.14(b)) is 38nm as calculated from the PRTF (see section 3.5), this resolution is on the order of the scale of the chromatin fibre. The image clearly shows the two separated chromatid arms and the area of the centromere. The electron density inside the chromosome was mapped from the retrieved phase and shows clear backbone through the chromatin arms and shows some structure in the magnified image of the chromosome arm (fig. 4.14(c)) . Comparing the electron density maps to images of the chromosomes taken with a fluorescence microscope it can be seen that the region of high electron density corresponds to the concentration of DNA along the chromatid. There is a central spot of strong electron density between the chromatids which the could be the previously reported chromosome scaffold that is present in the centromere [140]. The dose withstood by the chromosome in this experiment was 4×10^8 Gy for a single projection and 2×10^{10} Gy for the entire 3D dataset.

The 3D electron density map of the chromosome shows the surface morphology of the chromosome and internal features (fig. 4.14). In sections through the 3D images there is a core of high electron density around the centromere region which could be attributed to the highly condensed chromatin fibre in this region. This corresponds to the central spot of high density seen in the 2D projections. The resolution of the 3D image was calculated from the PRTF to be 120 nm.

CDI has the sensitivity to measure different regions of electron density within the chromosomes. This investigation shows promise that by further increasing the resolution of the technique more details of the chromosome structure will be revealed.

4.5 Summary

The chromosome structure is highly complex and dynamic. Large changes can be seen in the chromosome structure through the cell cycle from its highly decondensed state in interphase to the 'X' shape of mitotic form. The structure of the mitotic shape can be used as a diagnosis of genetic conditions by looking at the placement of genes along the chromatid arms and the number of chromosomes in a cell. The chromosomes show structural and genetic difference to be sorted by various methods into a karyotype which can be used as a starting point for the study of chromosome structure.

The chromosome is made up of chromatin fibre. The basic structural unit of chromatin is the nucleosome which is DNA coiled around histone proteins. The further coiling of the this fibre inside the chromosome is still largely debated. There has been much experimentation into the further winding of chromatin into a 30 nm fibre. Studies have proposed two different models of the packing of this fibre into the chromosome from the solenoid and zig-zag models to the proposition that chromatin has no further order above the level of the nucleosome.

Lensless imaging techniques have the resolution and penetration depth to obtain high resolution 3D images of the chromosome structure. CDI and ptychography can access the resolution gap between 10-30 nm that is currently difficult to image with other techniques. The first images of the chromosome with CDI show varying electron density over the chromatids and centromere as well as the 3D surface morphology of the chromosome. When applying these techniques to biological samples the radiation dose has to be considered as it damages the sample and is resolution limiting.

Chapter 5

Chromosome Sample Preparation

Sample preparation is critical to obtaining good quality images and is carefully designed to complement the imaging technique. Lensless X-ray imaging techniques are still under development and have been applied in a few biological cases therefore it is necessary to find a sample preparation method by researching existing protocols used in both X-ray and other techniques. As discussed in Chapter 3 procedures during sample preparation can disrupt or modify the native state of the chromosome therefore sample preparation must be trialled and the modifications monitored if possible. Light and fluorescence microscopy provide the standard on which we can base our experimental work and sample preparation. It is used to check the quality and performance of the cell culture and chromosome isolation methods since it captures the density of the yield and the gross morphologies of the chromosomes. Protocols from Electron Microscopy have been studied extensively as they have many key elements that are needed for X-ray methods such as preparing a dehydrated sample and using chemical fixation methods to prevent radiation damage. The EM sample preparation methods have been studied carefully for their effects on structural preservation and damage. We use staining methods to enhance the signal from the DNA in the X-ray images and mechanisms for binding dye molecules to DNA are discussed in this chapter. The protocol for the X-ray experiments is designed from the outcomes of the previous stages and will be detailed at the end of this section.

5.1 Cell Culture and Chromosome Isolation

The chromosomes and nuclei used in the following studies are taken from a cell line that is grown in culture following standard protocols. A cell line is split by taking a small number of cells to provide the initial cell stock in a process that is known as passage. A cell line can be passaged a

certain number of times before it becomes damaged and unsuitable for use.

Cells are cultured in a medium and under a mixed gas which provides an environment for the cells to grow. To remove cells from the medium they are centrifuged. The cells are synchronized in culture to produce a large number of mitotic chromosomes. The aim of the synchronization is to get all the cells to reach the same point in the cell cycle at the same time so when they are harvested there is a high yield of cells in the phase of interest. A common way to do this is with a chemical procedure sometimes known as "arrest and release", which blocks all the cells at the S stage of the cell cycle with an inhibitor. Once the majority of cells have reached this stage the block is released and the cells are allowed to continue to mitosis at which point their growth is arrested with the addition of colcemid which prevents the formation of spindles that pull the chromosomes apart. We wish to study the chromosome in mitosis so the cells are prevented from dividing. For the protocol used to perform cell culture see section 5.5.1. Chromosomes produced from these cultures are then used in the X-ray experiments presented in Chapter 5.

The cells are placed in a hypotonic solution that bursts the membrane leaving only the nuclear material. This material is then washed several times in a fixative, usually 3:1 methanol acetic acid but there are many alternatives. The fixative precipitates the DNA in the mitotic chromosomes preserving its form at the time of addition.

To isolate the chromosomes the nuclear material in the fixative is centrifuged until a pellet is formed and some of the fixative can be removed. To release the chromosomes about 60 μl of suspension is dropped on to a slide from a height to burst the nuclei and release the chromosomes from the nuclear membrane [141] and when observed under a light microscope the chromosomes can be seen clustered together. This is known as chromosome spreading. A full chromosome spread contains all 46 chromosomes close enough together in space to be identified as being from the same cell. Once the chromosomes have been spread on slides dyes and stains can be applied for techniques such as banding and M-FISH (see section 5.5.2).

5.2 Staining

Staining is a useful tool in imaging because it can be used to either enhance contrast, label a region of interest, or identify specific chromosomes. A stain molecule contains a part that will bind to some region of interest and a part that will provide contrast in the imaging technique either through absorbance, fluorescence or scattering. There are many stains used across microscopy methods that bind readily both protein and DNA, here we focus on DNA-specific stains as used to increase the contrast from DNA rich regions.

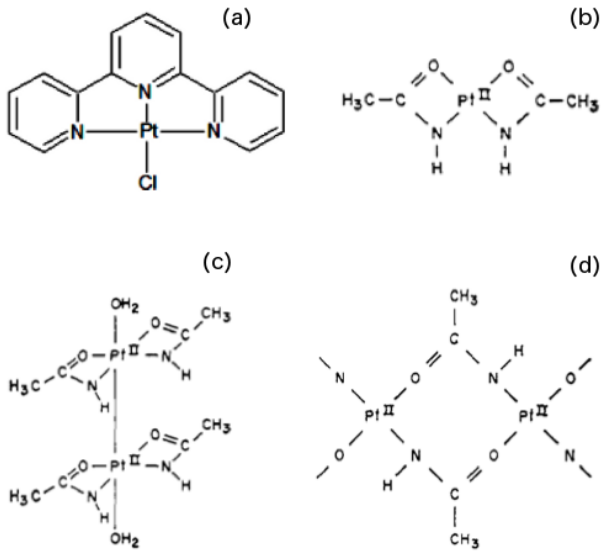

Figure 5.1: (a) Structure of Pt(terp)Cl a heavy metal based stain that binds by intercalation (b)-(c)-(d) Proposed structures of Platinum Blue which binds to DNA through minor groove binding. Both dyes were used during this study. (a) from reference [142], (b) from [143]. Permission from the American Chemical Society.

There are several ways in which a stain can bind to DNA. These are: intercalation, minor-groove, major groove or external binding. In intercalation the dye molecule binds in between the DNA base pairs. Dyes that stain by intercalation are typically small molecules that have planar aromatic groups that bond with the DNA base pair through $\pi - \pi$ bonding. The p-orbitals of the aromatic groups in the stain overlap with the p-orbitals of the aromatic groups of the DNA. Due to the binding of a molecule between base pairs, intercalation causes the DNA to unwind and lengthen [144].

Minor-grove binding and major groove binding occur when the dye attaches along either the minor or major groove in the double helix. Major-groove binding is typically covalent when using a metal stain due to the coordination of the metal with nitrogen atoms of the base pairs. This interaction is common for platinum based stains due to the affinity between platinum and nitrogen [144]. Non-covalent binding methods such as Hydrogen bonding results in minor or major grove binding when an electron negative atom in the stain can bond with the H-donor sites of the base-pairs.

Fluorescent stains are used in the identification of genetic material in the early stages of sample preparation. In order to check the yield of cell culture and identify the efficiency of spreading techniques DAPI and SYBR gold are used. These dyes can be added at many different stages of a protocol and and are easy to apply making them a suitable diagnostic. The emission wavelength of SYBR gold is 537 nm and the emission wavelength of DAPI is 461 nm.

Heavy metal dyes are used in the X-ray methods to enhance the scattering from the object. Scattering contrast increases with Z-number of the atoms so by applying a metal to the DNA region we can successfully increase the scattering of this region. The heavy metal dyes used in this study were platinum(II)-bis-acetimide (Platinum Blue), synthesized by Ana K. Estandarte, and Chloro(2,2´:6´,2-terpyridine)platinum(II) chloride dihydrate (Pt(terp)Cl) from Sigma Aldrich. The structure of the Platinum blue is still unknown due to the difficulty to crystallize it, but it is thought to be a polymer structure that binds along the minor groove, proposed structures are shown in fig. 5.1(b)-(c)-(d). The structure of Pt(terp)Cl is known and binds uniformly along the DNA through intercalation with a binding ratio of 1 dye molecule per 2.5 DNA base pairs.

5.3 Scanning Electron Microscopy of Chromosomes

Scanning Electron Microscopy (SEM) is used to study the effects of sample preparation on chromosomes and establish a protocol for X-rays. With correct sample preparations the surface structure can be observed on the 1 nm scale so we can see features of the chromosome in much greater detail with SEM than fluorescence. The application of metal stains to chromosomes can also be observed in this technique.

There have been many previous studies of the human chromosome with SEM which have mainly been concerned with the changes to the overall shape of the chromosomes [145] and their changes during mitosis [146]. These works have noted a globular surface structure that covers the chromosomes which has also been seen with Atomic Force Microscopy (AFM) [86].

The effects of sample preparation can be observed from the shape and structure of the globule layer. It has been noted that the effects of buffers cause change in the globule structure [147] and careful drying must be implemented in order to get detailed surface information. They observed that surface structure was different between chromosomes prepared in a polyamine buffer and those prepared in a citric acid buffer. For the citric acid preparation the surface was composed of globular chains 50-70 nm in diameter whereas polyamine prepared chromosomes had a flat “scaly” surface with subunits of different sizes.

The globular surface detail of the chromosome can be damaged by harsh drying procedures, it has been noted by us and others to date that the globular structure does not appear in air dried chromosomes [145, 146]. In order to successfully preserve this structure for imaging with SEM the chromosomes must be carefully dried with critical point drying or using chemical drying methods.

So far there has been no identification of the role or composition of the nucleoplasmic layer, however a study of chromosomes done with Small Angle X-ray Scattering (SAXS) suggests that

after standard preparations ribosomes can form some of the surface content of the chromosomes. SAXS profiles of chromosomes prepared with typical isolation methods showed a peak at 30 nm, however chromosomes with the ribosomes removed showed no peaks at this level of structure [122]. This suggests that the ribosomes aggregated to the surface of the chromosome are responsible for the 30 nm structure in chromosomes (see section 4.3.3).

The Back Scattered Electron (BSE) signal comes from typically 5-100 nm inside the sample depending on the incoming energy and can be used to see detail under the surface of the chromosomes [129]. To access information about DNA a heavy metal stain such as Pt(terp)Cl or Platinum Blue are applied. The heavy platinum atom produces strong BSE signal in the areas where DNA is present allowing the structure under the surface to be seen. Other examples of heavy metal stains used in electron microscopy are Uranyl Acetate and Osmium tetroxide, however these stains target both DNA and protein [148] whereas the Pt based stains have affinity to DNA only.

As well as enhancing contrast, osmium impregnation has been used in many studies to improve conductance which prevents charging causing artifacts in the images. The osmium impregnation causes swelling and disruption to the fine structure of the chromosome. A sample preparation developed by Wanner and Formaneck preserves the surface structure of the chromosome and stains with PtBlue avoiding toxic osmium impregnation [149]. The platinum ions provide strong contrast in the backscattered electron (BSE) signal which allows the trace of DNA structure under the surface of the chromosomes to be seen in the BSE images. From these images a new structural model of the chromosome was proposed using this protocol discussed in section 5.3.1.1.

This protocol has not been successfully applied to mammalian chromosomes because of a mesh-like layer over the chromosomes, which is not present in plants, making barley an ideal subject to study chromosome structure with SEM. In studies by Schroeder-Reiter, this nucleoplasmic layer was digested away with certain proteases, however, it is likely that the surface structure of the chromosome is damaged or modified by this treatment [150]. This layer was also reported by Gautier et al. [151] who studied ultra-thin sections of human chromosome spreads with TEM. They observed that this layer was present between chromosomes and had chains of a 'granular-type structure'.

We studied human metaphase chromosomes prepared using the "drop-cyro" method designed to observe chromosomes in the SEM. The chromosomes were stained with nucleic acid specific, contrast enhancing platinum based stains, in an aim to understand the applications of this protocol to human chromosome samples. In one set of preparations Cytoclear, a commercially available mixture of proteases, lipases and detergents was added to the cell culture step to try and remove the mesh-like layer observed in human chromosomes. The surface structure of the Cytoclear

treated chromosomes were compared to preparations that were obtained from standard cell cultures. Secondary Electron (SE) images are analyzed to look at the effects of sample preparation. Back Scattered Electron (BSE) images are analyzed to obtain an estimate of uptake of dyes by the DNA. The suitability of this sample preparation protocol for X-ray microscopy methods is discussed. Calculations of estimate phase shift are made from the images obtained in order to provide an estimation of the suitability of ptychography as an imaging method for chromosomes.

5.3.1 Materials and Methods

5.3.1.1 Sample Preparation for Scanning Electron Microscopy

The chromosomes prepared from culture methods outlined in section 5.5.1, were spread on marked glass slides using the "drop-cryo" protocol established by Wanner et al. [129]. A 60 μl drop of chromosome suspension is spread on a frozen, marked glass slide. A further 3 drops of a 45% acetic acid are dropped on the slide and a coverslip is placed on top. The slide is then immediately transferred to dry ice coverslip down for 15 mins. The coverslip is removed and the slide placed into 2.5% glutaraldehyde in 75 mM cacodylate buffer for 15 minutes then washed in 0.1 M cacodylate buffer. The chromosomes were stained with a platinum based dye Chloro(2,2´:6´,2-terpyridine)platinum(II) chloride dihydrate from Sigma Aldrich (catalogue no. 26420) of 10 mM concentration for 15 minutes. After staining the preparations were washed in water for 5, 10, and 15 minutes. The slides were taken through a dehydration series of ethanol, 5 minutes in 70% solution, 10 minutes in 85% solution, and 15 minutes in 100% ethanol. The chromosomes were finally chemically dried using hexamethyldisilazane (HMDS) from Sigma Aldrich, which has been shown to have a similar effect as critical point drying [152].

This protocol can also be performed using Platinum Blue instead of Pt(terp)Cl. After the wash in cacodylate buffer stain with platinum(II)-bis-acetimide, 5 μM is a recommended concentration, for 30 minutes in the dark. Wash in water for 5, 10 and 15 minutes before proceeding with the ethanol dehydration step.

Chromosomes prepared in this way are going to be different from the native state mainly due to the dehydration process. The "drop-cryo" protocol aims to preserve some of the native structure through freezing and fixing the chromosomes then dehydrating using Critical Point Drying or chemical drying methods.

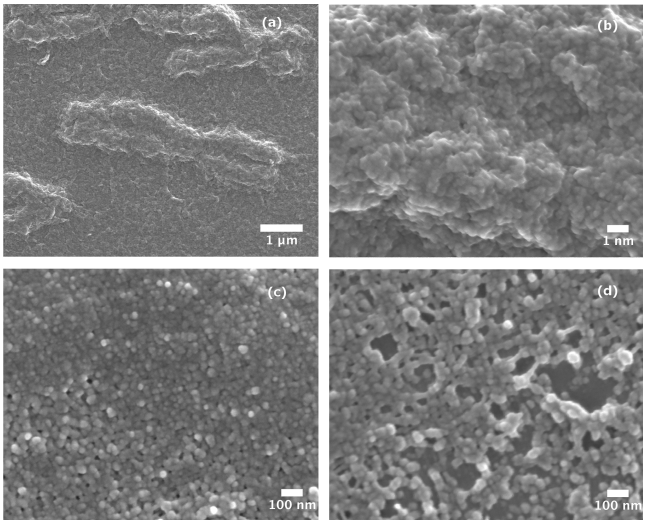

Figure 5.2: (a) Secondary electron image of a chromosome prepared without Cytoclear and the layer surrounding it. (b) Secondary electron image of chromosome in (a) at 80,000x magnification taken at a working distance of 6 mm. (c) Secondary electron images of a chromosome prepared with Cytoclear at 80,000x magnification at a working distance of 3 mm. (d) Secondary electron image of the mesh layer around the chromosome in (c) at 80,000x magnification working distance of 3 mm. Images taken at the Department of Anatomy, University College London

5.3.1.2 Imaging with a Scanning Electron Microscope

The slides were cut and mounted on 12.5 mm stubs. A 3-5 nm layer of carbon was evaporated onto the surface of the stubs to reduce charging effects. Images were taken with a JEOL Field Emission Gun SEM, model no. JSM-7401F at 1 kV accelerating voltage. Secondary Electron images were obtained using the gentle beam mode settings, with 3.6 mm working distance. Back-Scattered Electron images were obtained at an accelerating voltage of 3 kV at a working distance of 3.1 mm. The globule size was measured from the images by the following analysis. The images were first treated with a Gaussian filter to improve the sharpness over the edges of the globules. A threshold was applied to obtain just the contribution of the globules by removing the background. Measurements of the diameter of the globules were made from these thresholded images with ImageJ. This analysis was performed over different regions of interest in the image. Data from these regions was then combined to produce a histogram of globule size.

5.3.2 Sample Preparation effects on Chromosome Structure

Secondary electron (SE) and backscattered electron images (BSE) are used to identify the changes of structure by each step of the sample preparation. The SE images show the surface effects of the preparation and the BSE images study the effect of applying heavy metal stains.

The nucleoplasmic layer is observed in the SE images of chromosomes prepared with our modified drop-cryo protocol (fig. 5.2). This layer covers both the main body of the chromosome and

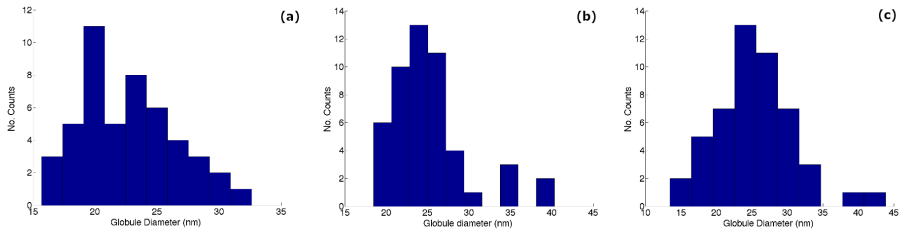

Figure 5.3: (a) Histogram of the globular subunit diameter of a chromosome prepared without Cytoclear (b) in a chromosome prepared with Cytoclear (c) in mesh layer surrounding the chromosome prepared with Cytoclear.

forms a mesh between the chromosomes in the spread (fig. 5.2(a).) It can be seen in the high magnification images of the chromosomes (fig. 5.2(b)-(c)), that the nucleoplasmic layer is made up of a globular size subunit, which has also been seen in the investigations mentioned in section 5.3. The application of HMDS in the protocol acts as a careful drying method preserving this subunit that would not be seen in air dried chromosomes.

The application of Cytoclear does not remove the nucleoplasmic layer however it appears to alter the density of the subunit. In the high magnification image of the nucleoplasmic layer over the main body of the chromosome prepared with Cytoclear (fig. 5.2(c)) the globular subunits that make up the layer appear more densely packed than in the preparation without Cytoclear (b). High magnification images of the mesh between the chromosomes prepared with Cytoclear reveal that the globular subunits are attached with fibres and do not form such a closely packed layer as over the main body of the chromosome (fig. 5.2(d)).

The globule subunit diameter was measured from the following images: chromosome body with a standard preparation (fig. 5.2(b)), chromosome body prepared with cytoclear (fig. 5.2(c)), and the mesh between chromosomes for the preparation with Cytoclear (fig. 5.2(d)). The globular diameters for these three cases are present in histograms , fig. 5.3(a), (b) and (c) respectively. The range of diameters of the globular unit is 15-30 nm in all cases with peaks at 25 nm for the cytoclear preparations and 20 nm for the standard preparation. This suggests that the addition of Cytoclear alters the globular substructure, increasing the diameter.

The BSE images show that the application of stain gives strong contrast to the signal from DNA in the BSE images (fig.5.4(c)). The winding of the DNA can be observed in the BSE image of the stained sample whereas the unstained sample shows just a dark region in the area of the chromosome (fig. 5.4(a)) showing that most of the signal is coming from the heavy metal ions of the stain and not the DNA fibre. Staining also gives a slight enhancement to the contrast seen in the SE image (fig. 5.4 (a) and (b)). As seen in [129], platinum blue is designed to increase the BSE signal from the chromosomes and therefore give information about the structure below the

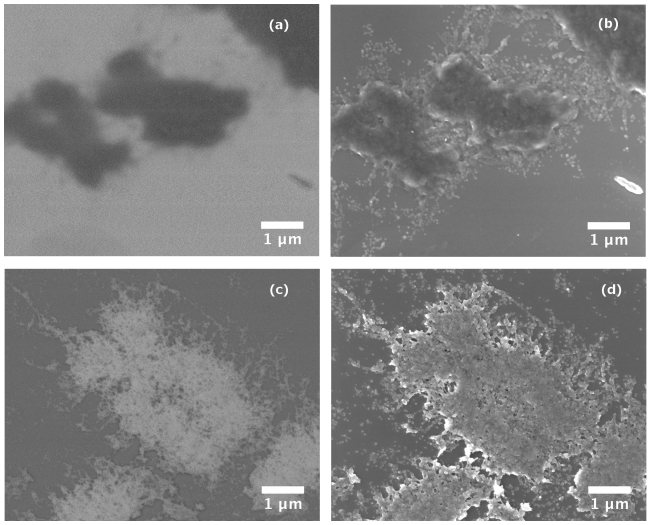

Figure 5.4: (a) BSE and (b) SE images of unstained chromosomes. (c) BSE and (d) SE images of chromosomes stained with Pt(terp)Cl. It can be seen in the BSE images that the contrast from the stain provides information on structure of the DNA inside the chromosome, in the unstained case no DNA structure is visible. The stain also provides some enhancement to the SE image in this case some finer details can be seen more clearly than the unstained case.

surface level.

5.3.3 Calculations of Phase Shift using SEM images

Like X-ray scattering, the BSE signal increases with atomic number therefore it is a useful diagnostic for looking at the potential contrast enhancement of the stains when applied to X-ray imaging. X-ray ptychography is a phase sensitive technique and the potential gain in phase shift from these staining methods can be directly calculated from the BSE images.

The relative phase shift $\Delta\phi$ is defined by the following:

$$\Delta\phi = \left(\frac{2\pi}{\lambda}\right)\delta z \tag{5.1}$$

where λ is the wavelength of the incoming X-rays, δ is the related to the refractive index by $\delta = 1-n$ assuming no absorption and z is the thickness of the material, (see section 2.1.3 for further details). Since we do not know the sample thickness, we can obtain it indirectly from the known mass of the chromosomes and their area, which can be measured from the SEM images. Thickness is related to area A by the following:

$$z = \frac{V}{A} = \frac{m}{\rho A} \tag{5.2}$$

where V is volume, ρ is the density and m is the mass of the chromosome. We have now

introduced the variables of mass and density which cannot be obtained from the images. The mass of the DNA in a chromosome can be calculated from its genome sequence length and the average molecular weight of a DNA base pair, 650 AMU. The density of the chromosomes does not have to be estimated because it is a constant factor in the calculation of δ. The value of delta can be found for an arbitrary value of density that will then be cancelled in the final calculation of phase shift using the following expression from eqs 5.1 and 5.2:

$$\phi = \frac{2\pi m}{\lambda A \rho}\delta \tag{5.3}$$

The area of the chromosome was measured from the images using the Measure tool in ImageJ. The mass of this chromosome was estimated from the number of sequenced base pairs of a chromosome of its size. Chromosomes are labelled by size, Chromosome 1 being the largest and Chromosome Y being the smallest. Compared to the others in the spread the chromosome was medium sized so would typically contain 140 Mbp [153]. This is a big underestimate of the mass of the chromosome because the calculation neglects the contributions of proteins and base pairs that are not sequenced. However the number of base pairs per chromosome provides an exact quantification of mass and can be used as a starting point in the calculations of phase shift.

For stained chromosomes the dye was modeled by platinum ions bound to the DNA. The mass of platinum inside the chromosome was estimated by the product of the number of base pairs multiplied by the binding ratio of the dye at 1 platinum ion per 2.5 base pairs [142]. The phase shift was calculated for stained and unstained chromosomes using fig. 5.4(c) for the area measurement. Phase shift from platinum stained chromosome with a 1:1 binding ratio is also calculated to provide a comparison.

The relative phase shift is plotted against energy, (fig. 5.5) for the following cases: unstained DNA (grey dashed line), DNA stained with Chloro(2,2:6,2-terpyridine)platinum(II) chloride (black dashed line) and DNA stained with a binding ratio of 1 platinum ion per base pair (solid black line). At energies between 2 -3 keV, the relative phase shift is 7 milliradians reducing to around 2 milliradians for higher. There is a steep decline in relative phase shift between 2 and 4 keV, whereas the change in relative phase shift between 6 and 8 keV is much less. Around 2 keV, the unstained chromosomes give greater phase shift than the stained chromosomes because of the absorption of the X-rays by platinum at these energies. Sharp drops in the phase shift of the stained cases can be seen at 2.1–2.2 keV resulting from the absorption edges of platinum.

The X-ray phase shift produced by chromosomes is a few milliradians, which is less than the current detection limit for X-ray ptychography [154]. For energies higher than 3 keV, the

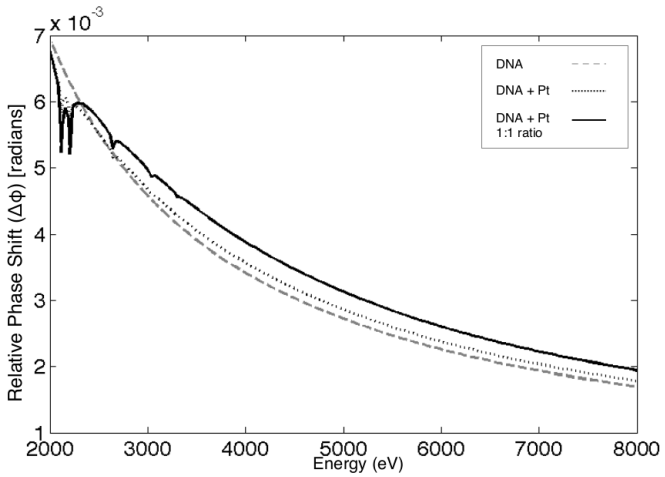

Figure 5.5: Phase shift from chromosome in fig. 5.4(c) unstained, stained with a platinum atoms based on the binding ratio of the NA specific stain Chloro(2,2´:6´,2˝-terpyridine)platinum(II) chloride. For comparison a stain with a binding ratio of one platinum ion per base-pair is plotted. Calculated with the CXRO online tool [39]

DNA stained with Pt(terp)Cl gave a marginally greater phase shift than the unstained case. The maximum difference in phase shift between the unstained (grey dashed line) and stained DNA (black dashed line) occurs between 4 and 5 keV and is 0.2 milliradians. The difference between unstained DNA and DNA stained with 1:1 binding ratio (solid black line) of platinum to base pair is 0.5 milliradians. At higher energies, the gain in phase shift from the application of stain decreases to 0.1 milliradians at 8 keV. The difference between the unstained case and the 1:1 binding ratio at this energy is 0.2 milliradians.

5.3.4 Discussion

SEM was used to investigate the sample preparation methods that can be applied to X-rays. This study focused on the changes to the surface structure and the uptake of heavy metal stains which cannot be observed with light or fluorescence microscopy. Sample preparation considerations of the two methods are similar, such as preventing radiation damage and drying samples, avoiding the evaporation of water, to preserve three-dimensional structure.

The addition of cytoclear to the cell culture did not remove the mesh-like layer. In all the examples studied, the globular structure was observed both in the layer and on the surface of the chromosomes. Globule size was found between 15 and 30 nm, with a characteristic diameter of around 20 nm, which does not correspond to any of the known structural units of a chromosome such as the nucleosome (11 nm) and the chromomere (200 nm). However, the measured size of the globules do correspond to the 30nm ribosome size observed by SAXS [122]. Despite not removing the layer, treatment with cytoclear changed the density and the size of the globules. It was observed

that the sub-units are more closely packed in chromosomes that had undergone treatment with cytoclear and had a larger diameter of 25 nm.

The measurement of the globule diameter is largely affected by the threshold applied to the images. SEM has a large depth of field from which surface topography can be seen as a change in greyscale. In the analysis of the images, regions of interest with a small greyscale difference were studied to try and ensure a consistent segmentation. The measurements of diameters had a range of 15–30 nm. Diameters above 30 nm where excluded as these large diameter values are often produced two globules that were not separated by the thresholding. A more accurate estimation of globular diameter could be found by applying segmentation techniques to the image. The diameter measurements are most likely to be an overestimation because of the contribution of the evaporated carbon layer (3–5 nm thick) to the diameter.

The BSE images (fig. 5.4) show that the platinum stain greatly increases the signal contrast. The internal structure of the DNA fibre can be clearly seen with the application of Pl(terp)Cl stain. Using this protocol could be used to increase signal in X-ray measurements as the uptake of heavy metal dyes by the DNA will increase the electron density of the chromosome. The nucleoplasmic layer covering the chromosomes also stains with platinum, therefore this structure would also be visible in X-ray images and may not be easily distinguishable from the main chromosome structure.

The contribution of platinum staining to X-ray signal is further investigated in the calculation of the relative phase shift. The calculated phase shifts are a few milliradians, just below the detection limit of ptychography. The behaviour of relative phase shift with energy and staining can provide useful information on the amplification of signal with stain and on the optimal energy to measure chromosomes. The maximum phase shift from the chromosome is at the lowest energy 2 keV however, here the difference between the stained and unstained chromosomes is owing to the absorption of X-rays by the platinum. At higher energies, the Pt(terp)Cl stain increases the phase shift given by the chromosomes but of the order of 0.2 milliradians. A 1:1 binding ratio of platinum ion to base pair increases this to 0.5 milliradians further indicating that by increasing the concentration of bound platinum will provide a gain in relative phase shift. The maximum gain from the platinum is in the energy range 4–5 keV at energies higher than this the gain form the platinum is negligible. The unstained chromosomes provide sufficient phase shift for measurement by ptychography at 2 keV but would require vacuum conditions.

Sample preparation modifications can be used to increase the phase shift as the area of the chromosome effects the phase shift (eq. 5.2). The numerical value of area for the phase shift calculation was taken from the BSE image in fig. 5.4 and was measured to be 12.3 μm^2. If the area of the chromosome was reduced to 1 μm^2, this would provide a phase shift of 70 milliradians

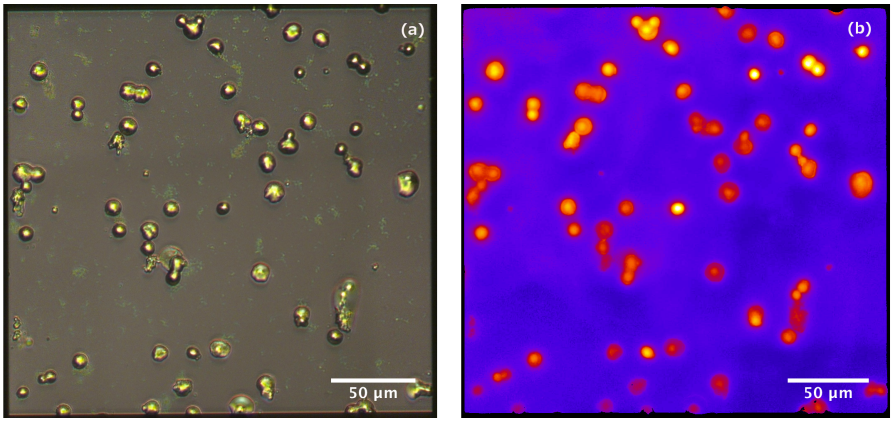

Figure 5.6: (a) Light microscopy map of the sample B59 measured during the experiment at 34-ID-C, (b) Map of the sample taken with fluorescence microscopy, the map is falsely coloured because of the stitching program used.

at 2 keV which is within the range to be measured by ptychography. Reducing the area of the chromosomes can be achieved in the preparation stages by using a polyamine buffer in the sample preparation step which results in smaller chromosomes than a methanol acetic acid suspension. This change in sample preparation will modify structure, however, it has been shown by light and EM that the in vivo structure of the chromosomes is preserved with polyamines [155]. The methanol acetic acid preparation is more widely used than polyamine in other chromosome imaging methods, which provide a base for comparison, therefore methanol acetic acid chromosomes were chosen for this study. The phase shift calculation only takes into account an estimated mass of the chromosome based on the sequenced DNA which is likely to give underestimate of the phase shift because contributions from the proteins and non-transcribing DNA have been omitted, therefore chromosomes imaged by ptychography are likely to give higher phase shift.

5.4 Sample Preparations for X-ray Imaging

5.4.1 Chromosome Preparation

All cell culture and chromosome sample preparations for X-ray experiments at I-13 beamline, Diamond Light Source, and 34-ID-C beamline Advanced Photon Source were produced by Mohammed Yusuf from protocols in section 5.5.1 and 5.5.3. The author characterized all samples with a light microscope before imaging with X-rays. Cytoclear was not used in the cell culture because of the evident changes it made to the structure of the chromosome. Chromosomes were fixed in 3:1 methanol acetic acid and then further fixed in glutaraldehyde in solution which protects the structure from radiation damage by cross linking the proteins. The chromosomes were isolated by spreading techniques onto a Silicon Nitride membranes 250 $\times$ 250 μm of thickness between

$100 - 250$ nm from Silson Ltd. The suspension of the sample could not be dropped from a height because this caused the thin membrane to shatter, however, chromosomes could be isolated by using a small drop of suspension (typically 2 μl) at close range to the membrane surface. It was found that chromosome prepared in methanol acetic acid fixative had less debris when spread on the membrane produce cleaner sample preparations than polyamine chromosomes. It was found that chromosomes prepared by methanol acetic acid also adhered more easily to the hydrophobic surface of the membrane than polyamine. The Silicon Nitride membranes are mounted on metal pieces designed with a hole as a sample window and a second mounting hole to screw the plate to the sample mount that will attach to the beamline (see section 6.3.1).

The samples were air-dried as the chemical drying method of hexmethyldisalizaine used for the SEM preparation was not comparable with the membranes surface and formed a layer visible in light microscopy. Critical point drying protocols were not established before the experimental set up but this would be the next step in improving the sample preparation.

The chromosomes were stained with heavy metal dyes and fluorescent dyes after the air drying step. As previously mentioned the heavy metal stain was applied to increase the phase shift produced by the DNA content of the chromosomes. The fluorescent dye was applied to check the quality and yield of the chromosomes in the fluorescence microscope. Maps of the sample were taken with light and fluorescence microscopy (fig. 5.6). Areas which contain DNA are shown in the fluorescence signal but complementary light microscopy images have to be taken to see debris. These maps are used to align the sample see section 6.2.1.2.

5.5 Methods and Materials

5.5.1 Cell culture protocol

Chromosomes were prepared from b-lymphocyte cells from a Yoruba cell line (GM18507) which were at passage 4. Cells were cultured in suspension in RPMI-1640 medium supplemented with 20% foetal bovine serum and 1% L-Glutamine at 37°C in a 5% CO2 incubator. For synchronization, thymidine was added to each culture at a final concentration of 0.3 mg mL^{-1} and incubated at 37°C for 17 hours. To obtain chromosomes at the mitotic stage, Colcemid (Invitrogen, UK) was added at a final concentration of 0.2 µg mL^{-1} for 16 hours. To separate the chromosomes from the cells they were centrifuged, resuspended in pre-warmed hypotonic solution (0.075 M potassium chloride) for 5 minutes and chromosomes were prepared after being fixed in three changes of 3:1 methanol acetic acid.

5.5.2 M-FISH Protocol

Karyotyping by multiplex fluorescence in situ hybridization (M-FISH) was performed as recommended by the 24XCyte mFISH probe kit manufacturer (MetaSystems, Germany, http://www.metasystems-international.com) and following previously published protocols [156]. The WCP probes are directly labeled with the five different fluorophores in a combinatorial labelling format to provide 24 distinct combinations. The hybridization of the probe with the cellular DNA site was visualized by means of fluorescence microscopy. M-FISH images were analyzed using the MetaSystems' Isis M-FISH software.

5.5.3 Isolation of chromosomes and preparation of membranes for X-ray imaging

Chromosomes were prepared for X-ray imaging according to a previously published protocol for chromosomes by Nishino et al, 2009 [70]. The chromosome sample was fixed in glutaraldehyde and placed onto a silicon nitride window containing 150 μM of SYBR. The sample was washed in water to remove residues of dye and then left to air dry. It has been seen in SEM studies that air drying can cause the chromosomes to flatten (see section 5.3.2). Chromosome preparations were verified by imaging using a Zeiss AxioZ2 fluorescence microscope with Isis software. Chromosomes on the same membrane were stained with Platinum blue 5 mM for 30 minutes and washed for 5, 10 and 15 minutes in water.

Chapter 6

Imaging of Chromosomes with ptychography

Coherent Imaging experiments were performed on chromosomes and nuclei prepared with sample techniques outlined in section 5.5.3. The two main experiments took place at the I-13 beamline at Diamond Light Source (Diamond), UK and the 34-ID-C beamline, Advanced Photon Source (APS), Argonne National Laboratory, USA. Both synchrotrons are 3rd Generation sources and provide the highly brilliant illumination (section 5.1) necessary for X-ray imaging methods. The I-13 and 34-ID-C beamlines have been established and developed for their coherent properties and have been used for lensless imaging experiments [8, 17]. The experimental work described in this chapter involved developing and testing a new ptychography set-up at these beamlines.

This chapter discusses some general aspects of synchrotron radiation and the implementation of a ptychography experiment. The chapter will outline the ptychography experiments at I-13 and 34-ID-C detailing the experimental set-up, data processing requirements and the reconstruction techniques used to obtain images. The resulting images are then analyzed and discussed. The results from related experiments performed at the cSAXS beamline, Swiss Light Source, Switzerland, and the TwinMic beamline, Elettra Sincrotrone Trieste, Italy, are also presented in this chapter and compared to the results of 34-ID-C and I-13. This chapter focusses on the performance of ptychography and its suitability as an imaging method for chromosomes and nuclei. The images of chromosomes and nuclei obtained from these images will be analyzed for structural information in Chapter 6.

6.1 Synchrotron Radiation

Synchrotron radiation is generated by changing the trajectory of high-speed electrons which produces radiation. The generation process in synchrotrons starts by producing bunches of electrons from a cathode ray tube. The bunches are then accelerated by a linear accelerator and injected into the booster synchrotron where they are further accelerated to an energy of a few GeV before being injected into the storage ring. The APS is a high energy storage ring that has a diameter of 1104 m and accelerates electrons to the energy of 7 GeV. Diamond operates at a lower energy of 3 GeV, therefore has a smaller diameter of 158 m. This process of accelerating with a LINAC into a booster synchrotron before injecting the bunches into a storage ring is called Top-up mode. The lifetime of the beam in this mode is approximately 20 hours at Diamond and 10 hours at APS. The lifetime of the beam is limited by collisions of electrons with residual gas causing the loss of electrons. After the lifetime has elapsed the beam is replenished from the booster synchrotron.

Synchrotron sources are used because they generate highly brilliant X-rays. Brilliance is a measure designed to compare X-ray sources in terms of the quality of the beam produced. The unit combines several characteristics of X-ray radiation from the output of the sources: the number of photons per second, the angular divergence or collimation of the source and its area. Brilliance, (sometimes referred to as Spectral Brightness) can be defined from units of these properties as :

$$\text{Brilliance} = \frac{\text{Photons/second}}{(\text{mrad})^2(\text{mm}^2\text{source area})(0.1\%\ \text{BW})} \tag{6.1}$$

The 0.1% BW term refers to the spectral bandwidth of the source. X-ray sources produce a variety of different spectra and in order to compare them it is convention to select the energy range as being 0.1% of the bandwidth. For synchrotron radiation the bandwidth is set by the characteristics of the ring and the Insertion Devices (see section 5.2). The high brilliance of synchrotron sources allow for many experiments to be performed that are unachievable with laboratory based sources. For a comparison, (see fig. 6.1) the brilliance of a synchrotron source is 10 orders of magnitude higher than a typical rotating anode laboratory based source.

6.1.1 Undulators

Synchrotron radiation is produced by accelerating electrons in the storage ring by Bending Magnets or Insertion Devices (ID). A Bending Magnet is situated in a section of the ring where the trajectory of the electrons is changed to produce a circular orbit. As the electrons accelerate through the curve of the Bending Magnet, radiation is released in a broad spectral range. This type of radiation is often used in spectroscopy but does not produce high energy X-rays and has less brilliance than

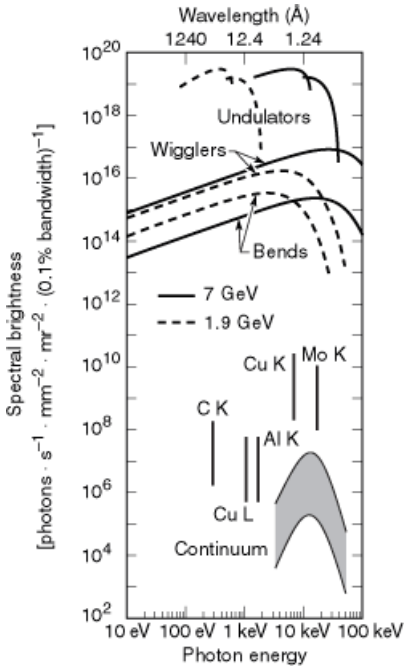

Figure 6.1: Comparison of spectral brightness for synchrotron radiation sources (Undulators, Wigglers and Bends), to lab based sources such as rotating anodes and stationary anodes. Stationary anodes have a spectral brightness in the low end of the range, and rotating anodes are in the middle range. There are 10 orders of magnitude brightness between synchrotron sources and stationary laboratory sources. Figure from [157]. Permission from author.

an ID.

We will be principally concerned with undulator radiation, which is a type of ID that is used in the straight sections of the ring. Most of the derivations on undulator radiation presented here follow closely to Soft X-rays and Extreme UltraViolet Radiation: Principles and Applications by D. Atwood [158]. An undulator is a series of magnets that create an alternating magnetic field. The alternating magnets have a period λ_u and the number of periods is given by N. As electrons travel through the undulator their trajectory is perturbed from the beam axis causing them to oscillate. As the electrons oscillate they release a cone of radiation which contains a spectral bandwidth of $\frac{\Delta\lambda}{\lambda} = \frac{1}{N}$. The half angle of the cone can be described in terms of the relativistic parameter γ and N which is the number of periods in the undulator:

$$\theta = \frac{1}{\gamma\sqrt{N}} \tag{6.2}$$

where θ is defined as containing radiation of the spectral bandwidth $\Delta\lambda/\lambda$. It is this bandwidth that is used to calculate the brilliance eq. 6.1, undulators are very bright sources partly due to the narrow bandwidth produced.

The amplitude of the electron oscillations in the undulator is governed by the dimensionless parameter K which is defined in terms of the undulator period λ_u:

Beamline	Energy	$d_{T,x}$ [m]	$d_{T,y}$ [m]
34-ID-C	5.5 keV	1.41×10^{-5}	2.76×10^{-4}
	7.0 keV	1.01×10^{-5}	1.97×10^{-4}
I-13	7.5 keV	9.0×10^{-5}	3.0×10^{-3}

Table 6.1: Coherence lengths produced by the undulator at the energies used in the experiments at 34-ID-C and I-13. The energies used at 34-ID-C were 5.5 keV and 7 keV and the energy used at I-13 was 7.5 keV. The coherence lengths produced by these undulators are greater in the y-direction than the x-direction

$$K = \frac{eB_0\lambda_u}{2\pi m_e c} \tag{6.3}$$

where B_0 is the magnetic field strength in the undulator and all other symbols have their usual meaning. From eq. 6.3 we can see that K can be changed by changing the magnetic field strength. In an undulator this is achieved by opening of closing the gap between the magnets.

As the electrons travel through the undulator at relativistic speeds the wavelength of the undulator is contracted. The resulting wavelength of the radiation, or the fundamental wavelength λ_l , is given in terms of λ_u, K, θ and γ by the following:

$$\lambda_l = \frac{\lambda_u}{2\gamma^2}(1 + \frac{K^2}{2} + (\gamma\theta)^2) \tag{6.4}$$

It can be seen from eq. 6.4 that undulators have a tunable wavelength. The K dependence in eq. 6.4 indicates that the wavelength will change with the magnetic field. Hence longer wavelengths are produced by increasing the B_0, which is achieved practically by opening the undulator gap.

An example a typical undulator has a period $\lambda_u = 1$ cm, and for electrons in a synchrotron $\gamma^{-2} \sim 10^{-8}$, this results in a fundamental wavelength $\lambda_l \sim 10^{-10}$ m which is in the X-ray regime.

It is assumed that the undulator does not alter the bunch structure of the electrons as they pass through, therefore, the beam size is the same as the bunch size. The bunch size can be modeled by a Gaussian, with its diameter in x and y given by the FWHM. The coherence of the beam is determined by the source size and source to observer distance, therefore a simple calculation of the transverse coherence of the beam coming from the undulator can be obtained with eq. 2.30. Top-up mode at the APS gives a beam size of $\sigma_x = 351$ μm and $\sigma_y = 18$ μm and the source to sample distance is 40 m. At Diamond the beam sizes is $\sigma_x = 230$ μm and $\sigma_y = 7$ μm and the source to sample distance is 250 m. The coherence lengths in the $x-$and $y-$directions of both beamlines are shown for the energies of 5.5 keV, 7.0 keV and 7.5 keV used in this experiment are tabulated in 6.1.

In a Coherent Imaging experiment a monochromatic source of X-rays is used. The radiation from the Undulator has a narrow spectrum but is not monochromatic as it also contains contributions

from higher harmonics. To get a monochromatic beam a mirror downstream of the undulator is used in conjunction with a monochromator. The mirror steers the beam in such a way as to remove the higher order harmonics. The beam then passes through a monochromator which filters out the correct wavelength using a crystal pair. The monochromator at 34-ID-C is a water cooled double crystal design operating in the energy range $6 - 15$ keV [159]. The monochromator at I-13 is a Quad Bounce Crystal (QCB) monochromator, which uses two crystal pairs to select the energy, however in the experiment presented in section 6.3.1 only one pair was used due to stability issues in the second pair.

6.2 Experimental Considerations for Ptychography

6.2.1 Practical implementation

To image non-crystalline samples with ptychography a transmission geometry set up is used (see fig. 2.8). In a ptychography experiment the beam is usually defined by a slit or a pinhole. Focussing optics, such as KB mirrors or zone plates are often used to increase the incident flux on the sample enhancing the weak scattering signal without destroying the transverse coherence [160].

Scattering from windows, beam-defining slits and air are problematic when measuring chromosomes because they provide background noise at the signal level of the sample. The noise from air scatter can be reduced practically by placing a vacuum tube between the sample stage and detector.

Scattering from the beam-defining slits can cause strong artifacts during the phase retrieval step therefore a second slit or pinhole is placed downstream of the beam defining aperture to block the scattering. The beam-defining slit and the second (or guard) slit need careful alignment to produce as little scattering as possible however there will always be some contribution from the slits seen in the diffraction pattern.

Windows are difficult to remove from the set-up without putting the experiment into a full vacuum chamber. Windows are made of X-ray transparent materials such as silicon nitride and kapton which produce a little scattering, however the scattering from these materials does increase with lower energies.

The requirements for the detector placement in a ptychography experiment are the detector has to be at a distance which is in the far-field that collects the largest scattering angle whilst remaining in the oversampling limit. In ptychography the distance needed for oversampling can be relaxed a little because the poor oversampling at the detector can be compensated for with a small scan step. For further explanation of the oversampling limit in ptychography, see section 2.4.

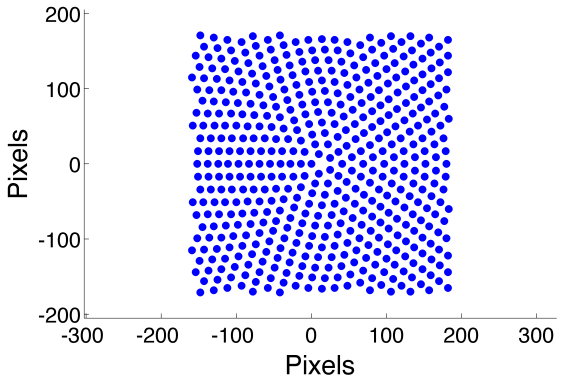

Figure 6.2: Schematic showing the motor positions in pixels of a Round Region of Interest (Round ROI) scan. The sample is scanned through the beam using this pattern. The scan pattern shown here has the following parameters: $N_\theta = 5$, $\Delta r = 14$ pixels, $n = 12$

Accurate knowledge of the probe position is critical in ptychography to get a successful reconstruction therefore motors with nanometer precision are used to scan the sample. In these experiments a Round ROI scan pattern was used (see fig. 6.2), which is defined by the following parametric equations:

$$\begin{aligned} x &= \Delta r.n \cos\left((m-1)\,\tfrac{2\pi}{N_\theta n}\right) \\ y &= \Delta r.n \sin\left((m-1)\,\tfrac{2\pi}{N_\theta n}\right) \end{aligned} \tag{6.5}$$

where x and y are the coordinates of the object position, Δr is the step size, n is the shell number, N_θ is the number of points in the first shell and m is the m^{th} point in the n^{th} shell. In the experiments discussed in this chapter $N_\theta = 5$. This scan pattern is used to avoid beam artifacts in the reconstructions that come from the strong symmetry of a raster grid, whilst still sampling the object evenly and with sufficient overlap [161]. One practical advantage of this scan is that the starting point is in the middle of the field of view.

Exposure times are of great consideration when imaging biological samples with ptychography. A large exposure time is needed to record the weak scattering signal but will lead to increased dose on the sample. Furthermore it is difficult to perform phase retrieval on data-sets taken over large time durations due to large probe drift during the scan, this will be discussed further in section 6.4.4.2. Experimentally, exposure times are reduced as much as possible whilst still maintaing a level of signal from weakly scattering samples.

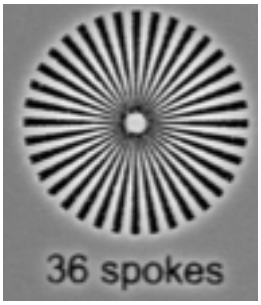

Figure 6.3: Scanning Electron Microscope image of the Siemens star test sample lithographed from 1.5 μm Tungsten. This test sample is designed to produce a 0.8π phase shift at 9 keV. The smallest feature on the test pattern is 82.9 nm.

Test Object	Transmission 5.5 keV	Transmission 7 keV	Phase Shift 5.5 keV	Phase Shift 7 keV
1.5 μm W	25%	50%	1.3π	π
150 nm W	87%	93%	0.13π	0.1π

Table 6.2: Transmission and phase shift characteristics of two Siemens Star test patterns at energies 5.5keV and 7keV. Transmission values from [39] The 1.5 μm test object was designed for use in the hard X-ray regime and the 150 nm thick object was designed for used in the soft X-ray regime.

6.2.1.1 Test Objects

Test objects are used firstly to test the reliability of the experimental set up and the phase retrieval algorithms. By reconstructing an object that is well known we can identify any artifacts in the image that may be caused by the experimental set-up or the phase retrieval algorithms. Secondly, the test pattern is used to give an initial estimate of the probe function that is then used as the starting probe guess when reconstructing images from data-sets of an unknown sample. We have found that it is very difficult to successfully reconstruct datasets from chromosome samples with a simulated probe.

A Siemens star, designed by Graeme Morrison and fabricated by Zone1plates Ltd, was used as a test object (fig. 6.3). Two test samples of different thicknesses of tungsten were designed to be used in different energy regimes. The soft X-ray test object is designed to have 25% intensity transmission and producing a 0.5π phase shift at 900 eV. This test sample was fabricated from 150 nm thick Tungsten on a 100 nm thick Silicon Nitride membrane. In hard X-ray experiments, a test sample of 1.5 μm thick Tungsten on a 1μm thick Silicon Nitride membrane was used. This is designed to produce a 70% intensity transmission and a +0.8π phase shift at 9keV. The characteristics of the test samples at the energies used in this experiment are displayed in table 6.2.

To better estimate the typical scattering from the chromosome sample the test object designed for 900 eV was used. This object produces phase shifts on the order of +0.13π at 5.5 keV.

6.2.1.2 Sample alignment

The samples were aligned from a map of the membrane produced with light and fluorescence microscopy (fig. 5.6). The corners of the membrane were used as fiduciary markers to find the coordinates of the membrane in terms of the beamline motor positions. These coordinates were then placed over the light map and motor positions of the sample could be recovered with in 5–10 μm error in position. The entire membrane was scanned with a raster pattern using very short exposures. By summing over regions of interest on the detector outside of the central maximum, a STXM type image could be built up rendering a low resolution map of the scattering points. Using this STXM in conjunction with the visible light and fluorescence maps the chromosomes could be found by looking at positions of scattering that match positions of fluorescence signal. The optical maps were used to check if the area around the scattering points was clear and there was no other biological debris that would cause scattering.

Software to calculate the STXM and align the coordinates of the map were developed by Jörg Schwenke. Due to the weak scattering nature of the object it is critical to use these mapping techniques in order to find the sample and verify that there is an object of interest in the beam.

6.2.2 Ptychography Algorithms

A ptychography experiment can be thought of as having two parts, the first is the collection of the diffraction data from the sample, explained in detail in the previous sections, the second part is to retrieve an image of the object from the diffraction patterns obtained. The phase retrieval algorithms used in ptychography are presented in section 2.5. The ptychography problem is briefly restated here. In order to retrieve the image from the diffraction pattern the phase problem must be solved (section 2.3) and to do this iterative algorithms that move between real and reciprocal space are used. These algorithms use constraints in each space in order to reach a solution. In reciprocal space the algorithms are constrained by the measured diffraction pattern, otherwise known as the modulus constraint (fig. 2.4). For ptychography the real space constraint is provided by the overlap of the data for which the redundancy allows the following equation to be solved:

$$\psi(\mathbf{r}) = P(\mathbf{r})O(\mathbf{r}) \tag{6.6}$$

where $\psi(\mathbf{r})$ is the exit wavefield, $P(\mathbf{r})$ is the probe function and $O(\mathbf{r})$ is the object function. The ptychography phase retrieval algorithms attempt to find a solution to eq. 6.6. Descriptions of the two algorithms used in ptychography, ePIE and Difference Map, and how they achieve a solution can be found in section 2.6, and a flow chart showing the actions of the algorithms are shown in

fig. 2.6. The following section discusses some finer details of implementing the algorithms.

There is no single protocol to achieve high quality reconstructions from every data set. Each data set has to be considered in turn and the success of the reconstructions can vary depending on the algorithms used and the constraints are applied. Currently there is no strong consensus on which situations one algorithm will outperform the other. During the phase retrieval stage there are many different combinations of algorithms, improvements and extra constraints that are used and often this recipe is not transferable between data sets. To test that the algorithms have reached the correct solution images are reconstructed from several different starting guess and should all reach the same solution. The images presented in this chapter are reconstructed to the best quality after trial and error. A concise summary of the phase retrieval processes for each image presented in this chapter is indicated in table 6.3. Outlined below are the following codes and extra constraints that are used in this work along with constraints and extra modifications.

6.2.2.1 Phase Retrieval codes

Firstly three different programs that perform phase retrieval were used in this work. The first is a modified version of Ptycho_Phasing_V2 written and developed by Jesse Clark, University College London which performs both DM and ePIE and can be used to switch between the algorithms. The second is a Difference Map code written by the cSAXS team at the Swiss Light Source, Villigen, Switzerland [21] modified to include some extra constraints needed for chromosome and nuclei reconstructions was used in some reconstructions. The third code was a version of ePIE written by Fucai Zhang, University College London. The method of Upsampling, was implemented in both ePIE and DM algorithm by Jörg Schwenke, University College London. In all of the codes the convergence of the algorithms is measured by the χ^2 error (eq. 2.38).

Further additions the DM and ePIE algorithm included in these codes are Upsampling and Position Correction. In ptychography knowledge of the probe position relative to the sample is critical for the success of the reconstructed algorithm. Experimentally it is difficult to know this precisely and often the real probe position differs from the recorded one. The position correction algorithm can find the correct positions of the probe by using the correlations of the retrieved diffraction patterns between successive iterations [162]. Another position correction algorithm uses a method of annealing where trial positions are given at every step of the algorithm and are accepted if they produce a diffraction pattern that better matches the measured diffraction [163]. The annealing method position correction was used in trying to improve the reconstructions but failed in the following experiments.

The method of Upsampling is used in some of the reconstructions shown in this chapter and is

an extension of the oversampling condition outlined in section 2.4. Based on an idea by Edo et al. [17] and developed by the Rodenburg group, this method was created to produce reconstructions from undersampled data by creating a "virtual detector" which has finer pixels than the those used in the experiment. The values of these pixels are then inferred at each step of the modulus constraint creating a finely sampled diffraction pattern. The Upsampling method is useful for data taken with very large probe sizes where the array size may limit the amount of space in which the probe to form. Increasing the array size allows for high frequency information in the probe to be reconstructed and therefore improves the quality of the reconstructed probe and image. Upsampling can only be performed when the step size of the scan pattern is small enough that oversampling as defined by eq. 2.35 is satisfied.

Binning the data can be used to increase the signal to noise ratio and this way improve the reconstruction. Binning takes a number of pixels and averages them into one pixel value. Binning can only be applied if the oversampling constraint is still valid after the operation.

6.2.2.2 Extra constraints

Extra constraints can be added to the algorithms to improve both the convergence and quality of the reconstructions. During the phase retrieval the probe intensity was found to move towards the corners of the array. This is an indication that the phase retrieval is not converging. In order to reconstruct the data successfully an extra constraint had to be applied to the probe. This is a real-space support constraint, like that applied in CDI, which only allows the probe to form in a certain area of space (see section 2.5 for more information on support constraints). In the following experiments two types of probe support were used. A strong support constraint of a circular aperture convolved with a Gaussian function with a diameter of 200 pixels in an array size of 256×256 pixels was used in some reconstructions where it was difficult to achieve convergence. For the chromosome and nuclei data a Butterworth filter was used as a support constraint to remove the strong edge of the circular support and hence producing as few artifacts in the Fourier Transform as possible. The Butterworth filter is a low pass filter that is designed to have a close to uniform sensitivity to the allowed frequencies [164]. The diameter of the support was also 200 pixels in a 256×256 array.

Further constraints can be put on the amplitude of the reconstructed object. As the object is not 100% transmissive, the amplitude should be less than one, therefore the amplitude values can be restricted to be between 0 and 1. Sometimes this constraint can reduce quality of the reconstructions because the amplitude retrieved is relative and not actual. On some occasions the resulting amplitude will be greater than 1 but the range of amplitudes present in the retrieved

image should still be equal to one.

6.2.2.3 Initial conditions

In both the experiments shown in this chapter it was very difficult to retrieve a reliable probe from the test object. In the I-13 experiment the probe was eventually successfully reconstructed from the test object and this was then used as a starting guess for the nuclei reconstructions.

The probe could not be reconstructed from a test object measured during the experiment at 34-ID-C using an initial guess of a simulated probe. The reconstruction of the probe and image from the test object was achieved by using an initial guess of a probe from a previous experiment at 34-ID-C. Despite the initial guess being measured on a different occasion and at a different energy the algorithms produced an image of the test patterns and a probe. The probe obtained from the reconstructions of the test sample was used to reconstruct the next scan.

In both experiments every scan was reconstructed from a probe taken from the previous scan. To further improve the reconstruction the phase retrieval was run a second time, using the reconstructed object and probe from the first phase retrieval as the initial object and initial probe guesses. The object was allowed to update from the first iteration and the probe was allowed to update after several iterations.

Experimental parameters of the wavelength, sample to detector distance, detector pixel size are used in the calculation to define the pixel size in real space. The motor positions are calculated from the scan parameters. The motor positions of the scan recorded during the experiment (the nexus file at I-13 or spec file at 34-ID-C) can be used as the scan parameters. Using the recorded motor positions over the calculated positions did not improve the performance of the algorithm in this case.

Table 6.3: Criteria used in the ptychography scans and phase retrieval algorithms to produce the images shown in this chapter. In the scan parameters column Field of View is abbreviated to FOV and the scan step size is written as dr. There is no single recipe that can be used in all data sets therefore each set of constraints and parameters are summarized here.

Object	Fig. & Scan no.	Scan Parameters, (incl. exposure per point)	Phase Retrieval Code	Iterations	Extra Constraints
Test Pattern	14765 Fig.6.6	FOV = 40 μm, dr = 2.5 μm, t = 15s	Modified DM	10	Probe Support - Circular aperture, Amplitude < 1
Nuclei	14932 Fig.6.7	FOV = 60 μm, dr = 4 μm, t = 40s	ePIE with Upsampling	300	Amplitude < 1
Nuclei	14939 Fig.6.8	FOV = 40 μm, dr = 4 μm, t = 40s	ePIE with Upsampling	300	Amplitude < 1
Test Pattern	S065 Fig.6.15(a)	FOV = 10 μm, dr = 0.4 μm, t =10s	Ptycho_Phasing_V2	10 ePIE, 180 DM, 10 ePIE	Probe support -Butterworth.
Test Pattern	S154 Fig.6.15(b)	FOV = 10 μm, dr = 0.4 μm, t = 1s	Ptycho_Phasing_V2	10 ePIE, 80 DM, 10 ePIE	Data binned - 4 pixels averaged to one pixel.
Test Pattern	S155 Fig.6.15(c)	FOV = 10 μm, dr = 0.4 μm, t = 2s	Ptycho_Phasing_V2	10 ePIE, 180 DM, 10 ePIE	Probe support -Butterworth.
Chromosome	S146 Fig.6.16	FOV = 4μm, dr = 0.25μm, t = 10s	Ptycho_Phasing_V2	10 ePIE, 450 DM, 20 ePIE	Probe support -Butterworth.
Chromosome	S150 Fig.6.17	FOV= 10 μm, dr = 0.4 μm, t = 10s	Ptycho_Phasing_V2	10 ePIE, 450 DM, 20 ePIE	Probe support -Butterworth.

Nucleus	S098 Fig.6.18(a)-(e)	FOV= 10 μm, dr = 0.4 μm, t = 12s	ePIE with Upsampling	300 iterations	Amplitude < 1
Nucleus	S099 Fig.6.18(g)-(h)	FOV= 12 μm, dr = 0.4 μm, t = 12s	Ptycho_Phasing_V2	10 ePIE, 450 DM, 20 ePIE	Probe support -Butterworth.

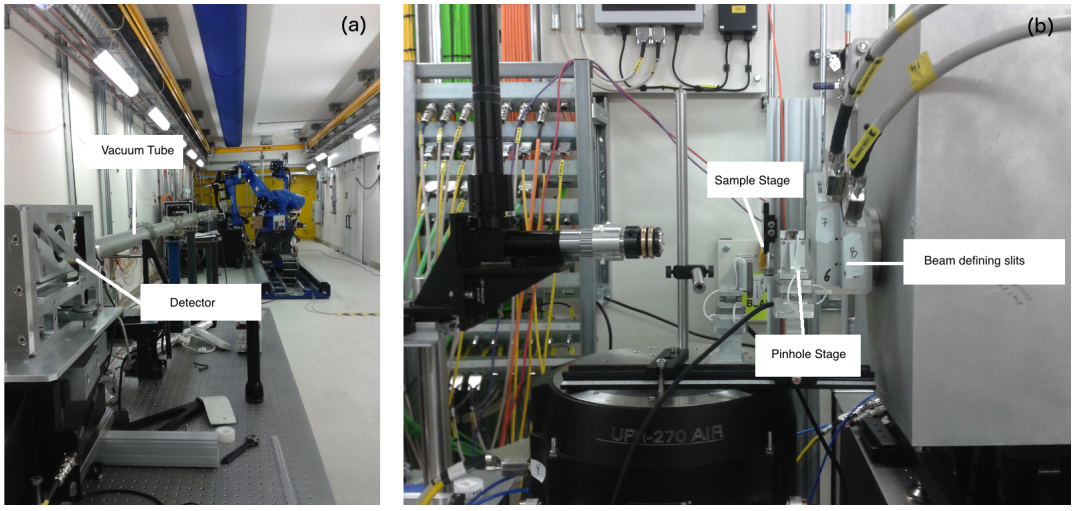

Figure 6.4: Photographs of the experimental hutch at I-13 (a) shows the detector at the far end of the 20 m hutch. The vacuum pipe extended towards the sample stage can be seen. (b) View of the sample stage at I-13, slits at the end of the silver K-B mirror box are used to reduce the scattering from aperture defining slits, producing the cleanest illumination possible. The piezo mount on the rotating stage is used to scan the sample through the beam.

6.3 Ptychography Experiment at I-13

6.3.1 Experimental Set-up at I-13

I-13 has a long experimental hutch allowing sample to detector distances of 15 m (fig. 6.5). The large obtainable transverse coherence lengths and the large sample to detector distance means that large objects can be still sufficiently oversampled to be imaged with CDI. Furthermore, due to the large probes size at this beamline the field of view for ptychography is greater than at many other beamlines, but for the largest fields of view the achievable resolution is less as the numerical aperture of the detector at the distances required for oversampling. We made use of the large probe size to increase the field of view of the ptychography scans without increasing the exposure time. We used a probe of approximately 25 μm diameter with a scanning range of 30 μm to give a maximum Field of View of 60 μm (see table 6.3).

The energy was set to 7.5 keV. The set-up was in transmission geometry with the detector placed 14.95 m downstream of the sample stage. A vacuum tube is placed between the sample and detector plane to reduce the air path to approximately 1 m around the sample. The beam was collimated in the vertical with Compound Refractive Lenses (CRL) , located 190 m upstream of the sample stage, to provide an increase in flux without using a strong focussing optic such as K-B mirrors or Fresnel Zone Plates (FZP). These focussing optics have given problems with stability in previous experiments. The beam was selected with a pair of slits placed 1.3 m upstream of the sample and closed to approximately 10×10 μm. This set-up was originally designed to do

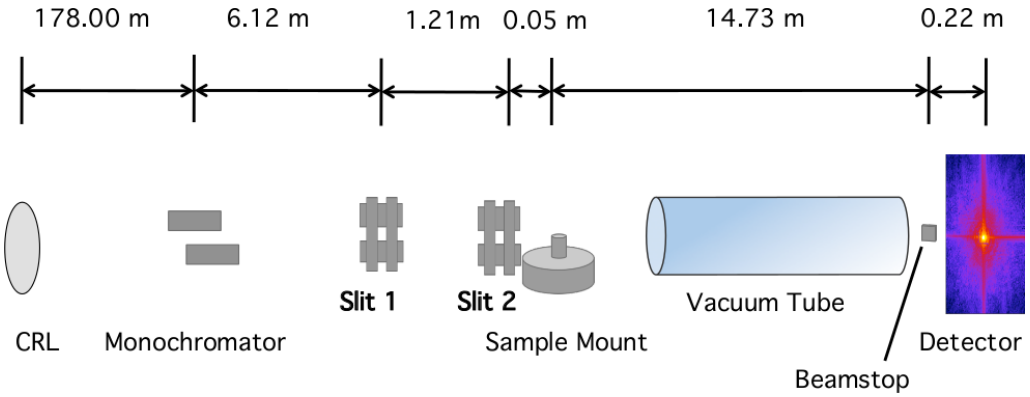

Figure 6.5: Schematic of the beamline set up at I-13. The beam is collimated in the vertical direction by Compound Refractive Lenses (CRL) which are 178 m upstream from the monochromator. After the monochromator the beam enters the experimental hutch. A part of the beam is then selected using Slit 1, the scattering from this slit is blocked by Slit 2, 1.21 m down stream. The sample is mounted on a piezo stage which scans the sample perpendicular to the beam. A vacuum tube is placed between the sample and the detector to reduce the air path. A Maxipix 2 (single photon counting) detector is placed after the vacuum tube and protected by a Cadmium beamstop.

CDI experiments however it was not possible to gain reconstructions from this set up therefore we changed to imaging with the more robust method of ptychography. A second pair of slits placed 1.21 m downstream of the first is used to suppress slit scattering from the first pairs producing a clean probe.

6.3.1.1 Detector

The detector used in this experiment was a Maxipix 2 [165] which is a single photon counting detector. The detector face is composed of four detector chips of 256×256 pixels with a size of 55 μm. The detector can be run in three different modes: Single Particle Counting, Time over Threshold (and/or event counting independently in each pixel) or Arrival Time mode. In this experiment Single Particle Counting mode was used. This mode can accept a count rate of particles arriving at 100 kHz. The dynamic range of the detector is 11810 counts. Each pixel can count cumulatively therefore exposure times can be arbitrary, but must be set under the saturation limit [166].

A beamstop of 25 μm Cadmium was used to protect the detector face. The beamstop 3.2% transmissivity at the experimental energy (data from [39]).

6.3.2 Data Processing

The first stage of the data preprocessing was to account for the use of the beamstop. The central region of the diffraction pattern was multiplied by the corresponding attenuation factor for the beamstop $\alpha = 315$. Multiplying the area covered by the beamstop recovers the suppressed intensity

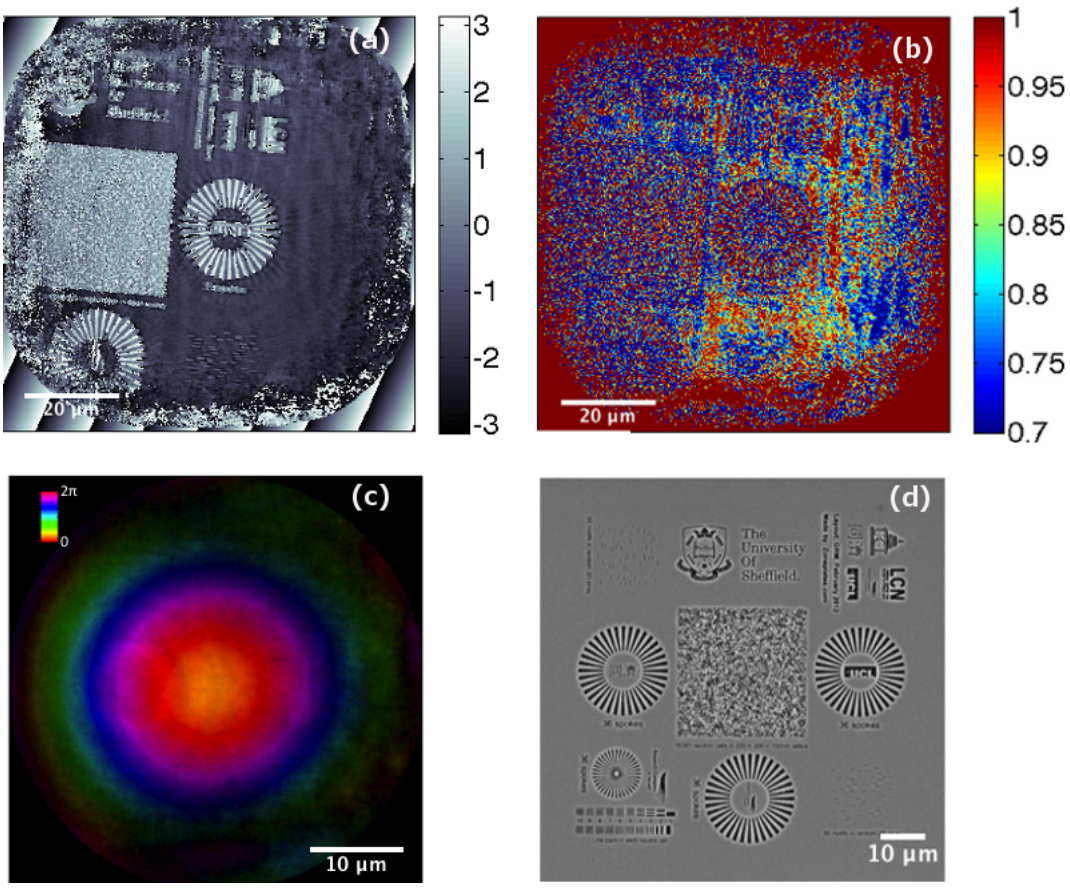

Figure 6.6: (a) Phase image and (b) amplitude image of the weakly scattering test object measured at 7.5 keV retrieved with the DM algorithm from scan 14765. (c) Retrieved probe with phase represented by colour and amplitude represented by intensity. A circular border can be seen around the probe coming from the support constraint. The real space pixel size in (a), (b) and (c) is 0.128 µm. (d) SEM image of the test sample showing Siemens star test objects, university logos and different types of phase gratings. The phase image shows some of the features of this text sample including lettering under the large features but the amplitude image suffers from strong artifacts and these details are difficult to see.

and forms a good match with the data outside of the beamstop area.

Window and air scattering from the experimental set up were at the level of the scattering from the biological objects reducing the SNR at high angles. The heavy scattering increased during the experiment and was due to a Silicon Nitride window in the the front of the experimental hutch which was damaged after too large exposure to the beam. It was difficult to remove this contribution from the data without losing signal from the sample.

6.3.3 Results from I-13

6.3.3.1 Test Object Reconstruction

The phase image of the test object (fig. 6.6(a)) shows good likeness to the the SEM image (fig. 6.6(d)) including details such as the letters and phase bars being reconstructed at low resolution.

The test object is made from a sheet of tungsten from which the features are lithographed. The features are holes on a flat tungsten background therefore there should only be two phase shifts present in the retrieved image, one corresponding to the background area and the other to the features. The phase between the spokes of the Siemens star and the empty areas inside letters of the logos is strongly positive but should have the same phase shift as the background. This positive phase is likely to be an artifact of the reconstruction. The features show an imprint in the background, for example shadows of spokes of the Siemens star can be seen in the area around the feature, these are likely to be caused by the large beam which will still have contribution from the Siemens star in an area of background.

The amplitude part (fig. 6.6(b)) reconstructed at low quality where only the outlines of the Siemens star and large random phase array can be seen. There are stripes of amplitude forming in the background and a cross-hatch effect seen on top of the amplitude reconstruction which is likely an artifact of the reconstruction. Again in the retrieved amplitude image there should only be two values of the amplitude one in the background from the less transmissive tungsten and the other from the feature, which is not represented in the image.

The probe (fig. 6.6(c)) obtained from the test pattern had a width of FWHM = 24.5 μm. Even with this large probe size the step size of the ptychography scans is sufficient to be in the oversampled regime defined by eq. 2.35. In order to successfully reconstruct the image the probe had to be constrained heavily using a circular aperture in real space. The probe shows a circular profile that would be expected from a beam collimated with a CRL. The illumination is only collimated in the vertical direction by the CRL, which is not evident in the reconstruction of the probe. The array size used in this reconstruction is too small to see the outer fringes which might display a stronger collimation in the vertical than in the horizontal, however, when Upsampling was attempted on this dataset it resulted in a reconstruction of poorer quality.

6.3.3.2 Nuclei Reconstructions

Images of clusters of nuclei, which have good resemblance to images of the same area taken with a visible light microscope (fig. 6.7(e)), were obtained using ptychography.

In the phase image (fig. 6.7(b)) fine details of the cluster can be seen such as different nuclei have different phase shifts. In some nuclei there is a variation in phase shift in the body of the nucleus, showing regions of greater density inside the nucleus. The image suffers from a striping artifact in the background which interferes with some of the phase shift coming from the nuclei near the bottom of the image, however, most of the nuclei in the cluster have a phase contrast above this effect.

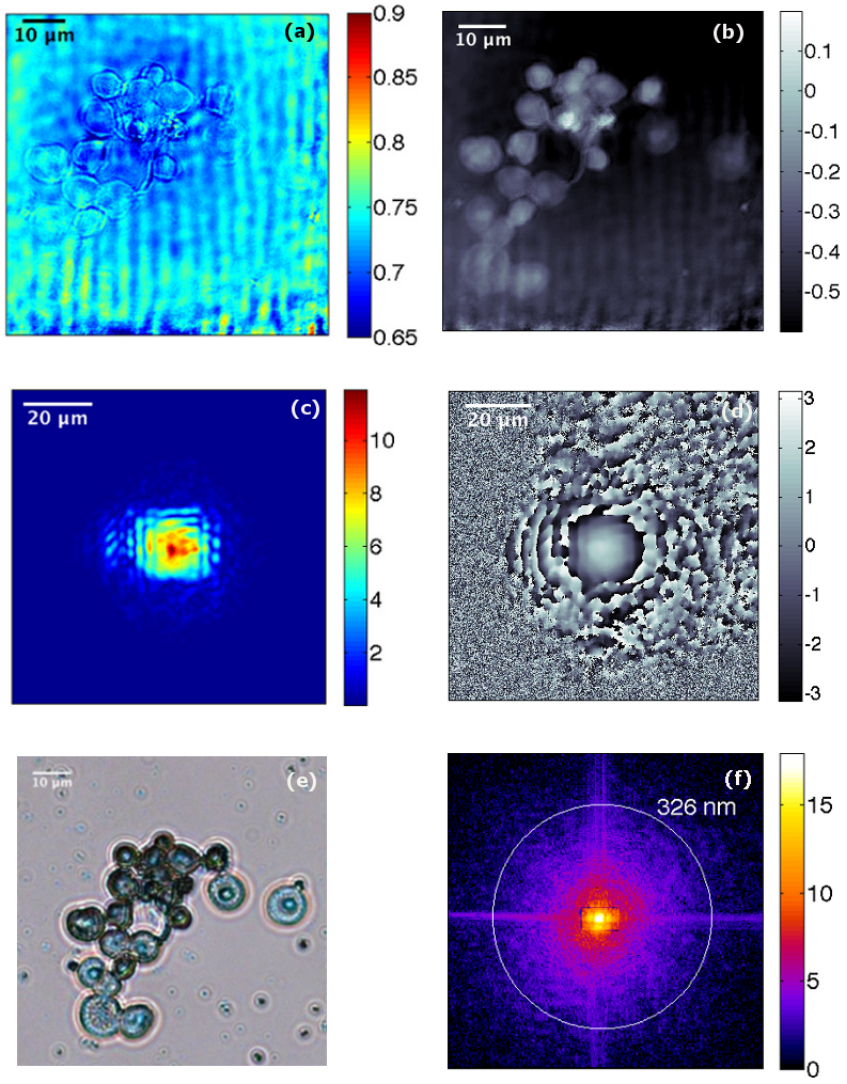

Figure 6.7: (a) Amplitude and (b) phase image of a nuclei cluster reconstructed with the ePIE algorithm with Upsampling from scan 14933 (c) amplitude and (d) phase of the retrieved probe. The round profile of the probe seen in the phase image comes from the CRL focussing but a square profile can be seen strongly in the amplitude image which is produced by the beam defining slit. (e) Visible light microscope image of the same nuclei cluster imaged with ptychography. It can be seen that ptychography reconstructions closely match the image taken with a visible light microscope. (f) The diffraction from the first frame of the ptychography dataset. The cross is the scattering from the slits and the speckles come from the nuclei and window scattering.

The reconstructed amplitude (fig. 6.7 (a)) shows strong contrast at the boundaries of the nuclei, but inside the amplitude value is little above the background. The striping artifact is greater in the amplitude image, in some places the striping is stronger than the nucleus border. There is a slight halo effect around the boundary of the nucleus which has the appearance of circles expanding out from the boundary.

The probe retrieved from this dataset is measured to be 23.4 μm at FWHM which is a similar to the probe reconstructed from the test sample. The probe is round in shape which is caused by the CRL focussing upstream however there is a straight edge from the slit that is strongly present in the amplitude image (fig. 6.7(c)). In the amplitude image the outer fringes have a straight edge as from a square slit but the fringes in the phase image shows a more speckled shape (fig. 6.7(d)). The probe does not have a very uniform distribution of phase in the centre or at the edges of the probe. Finer fringes can be observed in the horizontal more strongly than in the vertical direction. This is probably due to the vertical collimation of the CRL. It is likely that the probe changes considerably during the long scan times due to instabilities in the beamline, therefore the fringes occurring are due to the averaging of the probe over all the scan positions.

Similar phase and amplitude effects can be seen in another example of a nuclei cluster (fig. 6.8). The phase image clearly shows the shapes of the nuclei that agree with the light microscopy image. The phase shift though the nuclei in the ptychography image (fig. 6.8(b)) corresponds to the transmission through the nuclei in the light microscope image. Where phase shift appears brighter, hence stronger in the ptychography image the transmission appears darker in the light microscope image (fig. 6.8(d)). From the phase and visible light microscope images we can see there are a range of nuclei thicknesses present, giving a darker profile in the transmission of the light microscope image and a stronger phase shift in the ptychography image. The amplitude image (fig. 6.8(a)) shows the boundaries of the object but these are weaker than in fig. 6.7. In this example there is no striping artifact in the background but there are shadows of the beam causing phase shifts in the background. The probe, however, is not as well formed as the probe of the previous reconstruction (fig. 6.7(c)-(d)). The probe phase image (fig. 6.7(d)) shows outer fringes in the horizontal on the left hand side of the central maximum but speckled fringes on the right. The probe amplitude image (fig. 6.7(c)), again, shows the square profile coming from the slit.

This second example of a reconstructed nuclei cluster shows the limit of phase sensitivity of the experiment. The visible light microscope image of the nuclei cluster shows a chromosome which is marked with a red circle (fig. 6.8(e)). In the amplitude and phase images reconstructed by ptychography the chromosome cannot be easily visualized. The region where the chromosomes

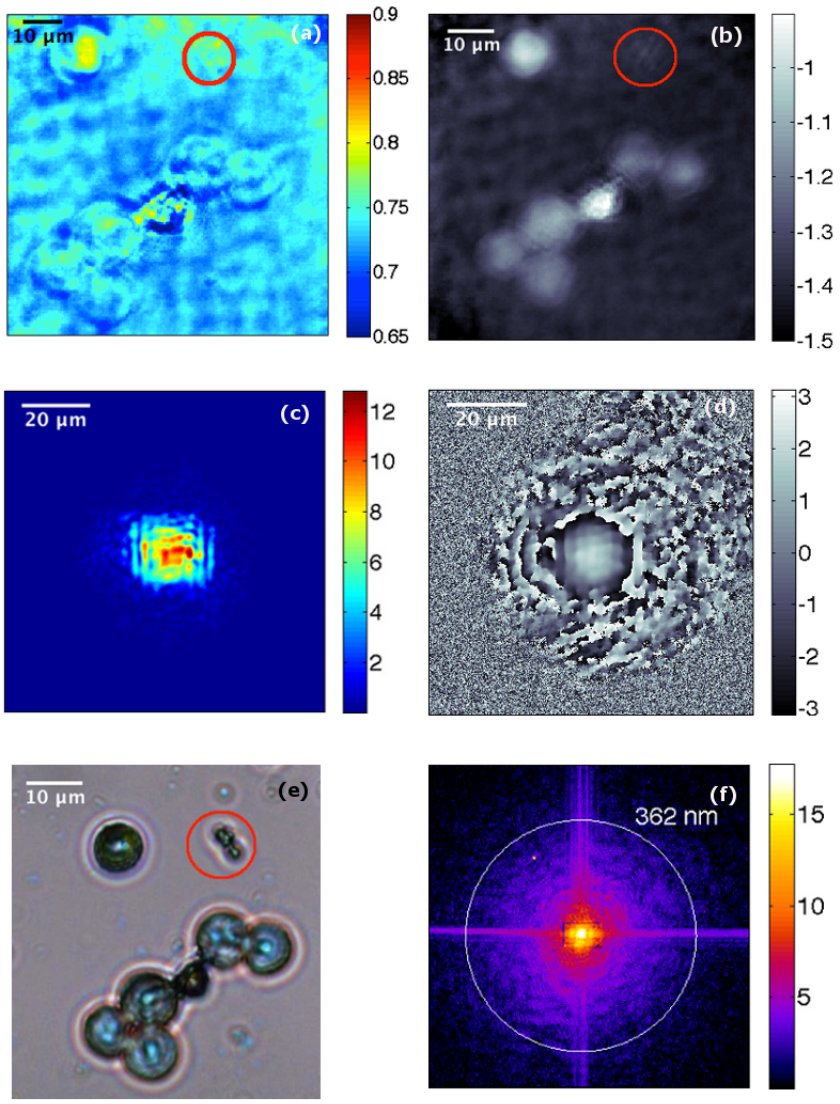

Figure 6.8: (a) Amplitude and (b) phase images of a second nuclei cluster reconstructed using the ePIE algorithm with Upsampling from scan 14939. (c) The probe amplitude showing a square profile from the beam defining slits (d) and phase showing a circular profile from the CRL focussing. (e) Corresponding visible light microscope image of the nuclei cluster. The red circle marks a cluster of chromosomes in the optical image. The phase and amplitude images from ptychography only show weak contrast from the chromosomes in the area marked by the red circle. (f) The diffraction pattern from the nuclei cluster with the estimated resolution shown by a white ring.

should be is marked with a red circle. The phase image shows a weak phase shift in that area, however no object that resembles the chromosome in the visible light microscope images can be observed. The amplitude image shows a small region of bright contrast but no strong boundary of an object.

The diffraction patterns from the nuclei shows a cross feature above the signal of the speckle. This is due to scattering from the slits used to define the beam (fig. 6.7(f) and fig.6.8(f)). The strong speckle from the nucleus can be observed above the noise at an angle equivalent to the spatial resolution of 362 nm. There is a large contribution of window scattering in this pattern that is at the signal level of the nuclei which is very difficult to remove. It is likely that the scattering from the sample extends to a higher angle, but cannot be observed above the level of window scattering.

6.3.4 Discussion

The method of Upsampling combined with ePIE greatly improved the reconstructions from these data sets. These images are comparable to visible light microscope images and show boundaries of the nuclei strongly, but are still poor in resolution. The phase image shows the varying phase shifts through the nuclei which gives information on the electron density of the nucleus, greater electron density produces greater phase shift. The phase shift can be compared to the absorption contrast in the light microscopy images, the nuclei that are very dark in the light microscopy images produce strong phase shifts. The thickness of the nucleus increase absorption contrast under light microscope in the same way it increases the phase shift in the ptychography images allowing for a direct, qualitative comparison.

The images of the nuclei clusters are a direct measure of the phase sensitivity of the ptychography set-up. The image of a nuclei cluster in fig. 6.8 shows that the current set up is not sensitive to detect the phase shift through chromosomes. The size of the chromosome feature is 6.4 μm (measured from the light microscopy image) which is as large as the small nucleus in the centre of the image, 5.7 μm, therefore is within the detectable spatial resolution. However the chromosome does not produce sufficient phase shift to be observed in this technique.

All the images show stronger artifacts in the amplitude than the phase. The low β of biological materials at this energy (see section 3.1) means that the absorption contrast from the chromosomes are very low compared to the phase contrast which is stronger and provides contrast above the level of the artifacts. Stripes of contrast (see fig.6.7) in the background could result from the beamstop edges visible in the diffraction data. The beamstop is 19 pixels in height and the median spacing of the stripes in the images is also 19 pixels, suggesting that this artifact is linked to the beamstop.

There is also the appearance of patches of amplitude in the background (see fig.6.8). These artifacts may be explained by the size and stability of the probe as instabilities in the illumination can cause artifacts. The ptychography algorithms retrieve one illumination function for all positions. There is an underlying assumption in ptychography that the probe is the same throughout the entire scan, therefore the probe retrieved by the algorithms is actually an average of the probe function over all the positions of the scan. The illumination is likely to change during the time of the scan, which in this experiment is a period of hours, therefore the illumination function is different at different positions in the scan. One way to avoid this drift is to split up the scan area into multiple fields of view to reduce the time over each scan [167].

The probe size is relatively large compared to those usually used in ptychography therefore scattering from a large area of the sample was included at each position. The large size of the probe causes the diffraction pattern to contain interference from parts of the sample far away in real space which the phase retrieval algorithm tries to resolve in the measured Field of View. This can be demonstrated with the test sample that shows shadows and imprints from the features of other parts of the test sample in the background of the object.

The implementation of Upsampling did not result in a better reconstruction in the case of the test object which was obtained using the Difference Map. The smallest feature observable in the phase image are the small phase gratings, at the bottom right of fig. 6.6(b), that are 1.4×0.3 μm in size. However the amplitude reconstruction only shows large scale details such as the general shape of the Siemens Star, 11.4 μm diameter and large square of the phase array.

6.4 Ptychography Experiment at 34-ID-C

6.4.1 Experimental set-up

At 34-ID-C, the beam is selected by slits and is focussed on the sample plane by a K-B mirror pair. It has been found by experimentation that the best working aperture for the ptychography set-up is 0.03×0.06 mm (fig. 6.9). This aperture gives a small source size which fulfills the oversampling criteria and therefore can be reconstructed easily. Larger probe sizes, produced by smaller slit settings, are at the limit of oversampling and it has been found that it is difficult to retrieve the probes using the ptychography algorithms. With our slit setting the K-B mirrors produce a focal spot with a radius of approximately 300 nm. The sample is positioned as close as possible to the focus of the KB mirrors so it is illuminated with the maximum flux. A guard pinhole of 40 μm is placed downstream near the sample plane and used to block the strong scattering from the slit flares without perturbing the beam shape , the pinhole to sample distance was 30 mm .

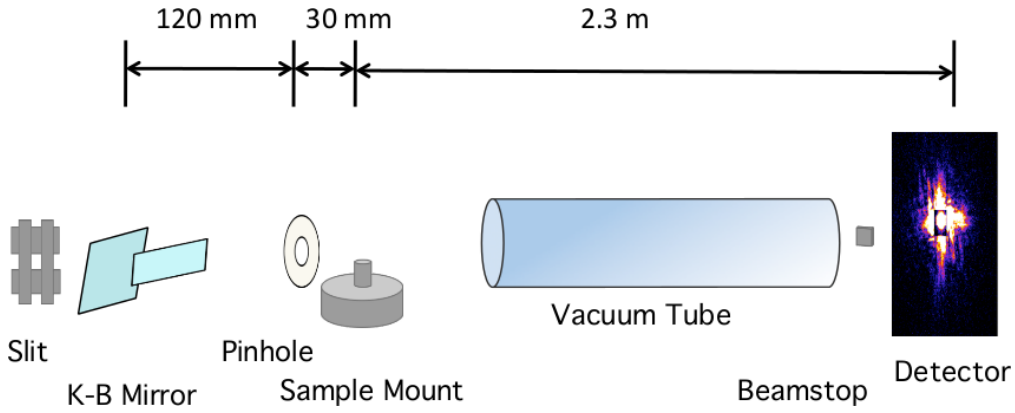

Figure 6.9: Schematic of experimental design used to perform ptychography experiments at 34-ID-C. The slit is used to define the aperture coming into the K-B mirrors focused at the sample plane. A 40 μm pinhole is used to block strong scattering from the beam defining slits. A sample mount is a 3D piezo stack with a magnetic mount to connect the sample. A vacuum tube runs between the sample stage and the detector to reduce the contribution of air scattering. A silicon beamstop is used to protect the detector from the direct beam. The detector is placed 2.3 m downstream of the sample.

The detector is placed 2.3 m from the sample stage and is protected from the direct beam by a beamstop. This geometry at the energies used provides an oversampling ratio (as defined by eq. 2.33) of $\sigma = 8$.

The sample stage consists of Piezo motors which can move in the plane of the beam face and along the beam axis, mounted on a motor stack used in other experiments fig. 6.10(a). This includes goniometers and rotation stages, and mounted on a diffractometer isolated from ground vibrations by an optical table providing a very stable base removed from vibrations. An Olympus confocal microscope is placed above the sample stage and its focus is aligned to the beam axis (fig. 6.10(b)). This installation is useful for performing experiments in reflection geometry as it allows the samples to be aligned quickly. In the chromosome experiments the confocal microscope was used to align the membrane with the beam axis and further alignment of the sample was achieved using the scattering signal from the sample.

Two energies were used in this experiment to look at the effect of lowering the energy on the quality of the reconstruction. Chromosomes have a larger cross-section at low energies therefore should produce a stronger phase shift. Some datasets of nuclei and test samples were obtained at an energy of 7 keV but no chromosomes could be found. The energy was reduced to 5.5 keV which is at the limit of the energy range of the beamline and chromosomes were measured at this energy.

6.4.1.1 Detector and beamstop

A Timepix detector from Amsterdam Scientific was used in this experiment. The Timepix detector is based on the same technology as the Maxipix detector described in section. The chip is an array

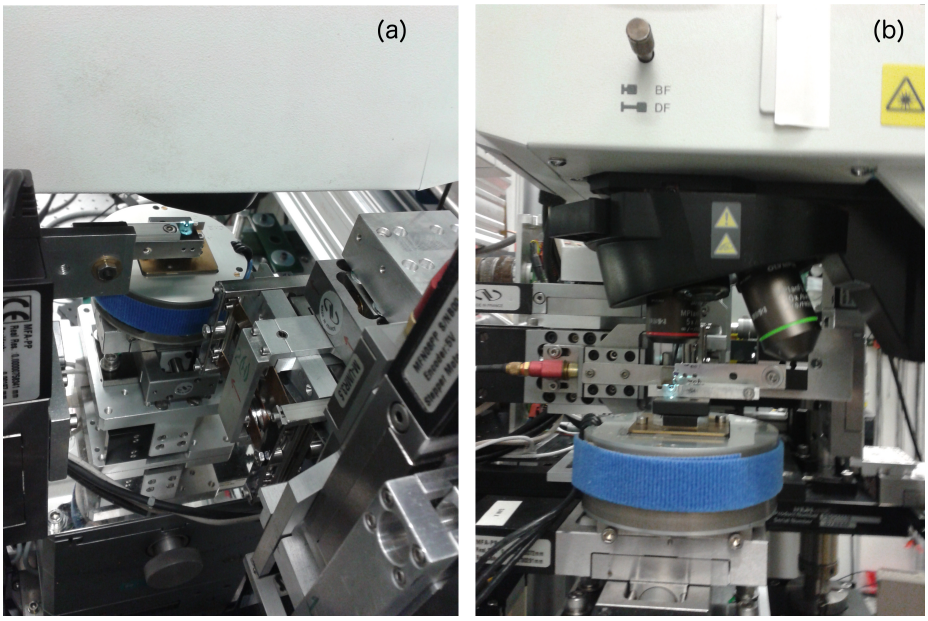

Figure 6.10: Photographs of the sample mounting at 34-ID-C (a) downstream view shows the pinhole set up mounted on Newport motor stages (b) upstream view shows the sample mount with the membrane mounted onto one of the holes in the metal plate. The confocal alignment microscope is seen at the top of the photographs. The sample is mounted on a magnetic mount that can reproduce sample positions faithfully allowing for samples to be changed easily. The motor stack shows a 3D piezo stack capable of movement along the beam axis and perpendicular to the beam.

of 256×256 pixels of size 55 μm.

In a previous experiment scattering from a Tungsten beamstop caused a visible powder ring on the detector. To avoid the detection of a powder ring the beamstop used in this experiment was a square of 200 μm thick Silicon that was designed for use at 9 keV. The Silicon beamstop has a transmissivity of 0.021% at 5.5 keV and 1.4% at 7 keV, values from [39].

6.4.2 Data Processing

6.4.2.1 Retrieval of Data behind the beamstop

To correct for the beamstop in the data collected at I-13 the attenuated area was simply multiplied with a factor derived from the transmission of the beamstop material at the experimental energy. For the data collected at 34-ID-C the attenuation factor had to be estimated from the data.

The transmission factors given in section 6.4.1.1 correspond to the following theoretical multiplication factors $\alpha = 71.43$ at 7 keV and $\alpha = 4756$ at 5.5 keV (data from CXRO online tool [39]). Multiplying the data under the beamstop with these factors gave an over-amplification of the region attenuated by the beamstop leading to artifacts in the reconstructions. The beamstop is carefully aligned in front of the detector face, however, there remain pixels which are partially covered by the beamstop. These pixels were set to zero and are not included in the modulus

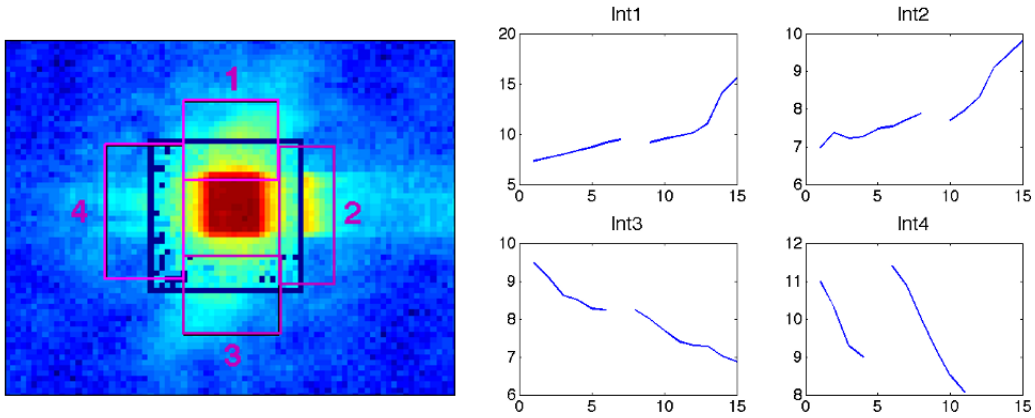

Figure 6.11: (a) Diffraction pattern from one frame of ptychography scan (S130) of a chromosome with the area under the beamstop corrected by multiplication with a constant factor $\alpha = 40.4$. Regions of interest over the four edges of the beamstop region are shown with red rectangles. The regions of interest were integrated parallel to the beamstop edge. (b) The integration profiles show the fit across the four sides of the beamstop. Across side 4 the line profile is disjointed this comes from low counts in this region giving a low integrated average.

constraint because the intensity has not been measured correctly in that area (fig. 6.11(a)).

The multiplication factor does not just depend on the transmission of the beamstop but also the transmission of the sample itself, therefore the multiplication factor determined from the whitefield was an under-amplification of the beamstop area in the frames where there was signal. The multiplication factors used for the Siemens star were $\alpha = 10$ at 5.5 keV and 110 at 7 keV. The nuclei and chromosome datasets typically used a factor between $\alpha = 40$ and $\alpha = 50$ at 5.5 keV. The multiplication factor at 5.5 keV is far lower than predicted from the transmission of the beamstop material at this energy. This could be caused by the presence of higher energies from high harmonic contamination as the beamline is working at the very end of its energy range (see section for further discussion). The multiplication factor at 7 keV was different approximately within $\pm 60\%$ of the predicted value but was not two orders of magnitude different as at 5.5 keV.

To choose a correct multiplication factor, a region of interest was integrated over the each side of the beamstop excluding the half pixels (see fig.6.11). These integrations profiles were taken for several frames at different points in the ptychography dataset. The integration shows that the profile does not fit over side 4 of the beamstop. This is due to the high number of zero counts in that area of the beamstop giving a low integrated average. The contribution from side 4 was ignored in choosing the correct multiplication factor. It can be seen there is a jump in the profile over side 2 which comes from the minimum between the strong flare and the first order that sits along the beamstop edge.

The beamstop has very low transmission at 5.5 keV, the energy at which the chromosomes and nuclei are measured. Despite the low transmission of this beamstop, short exposure times

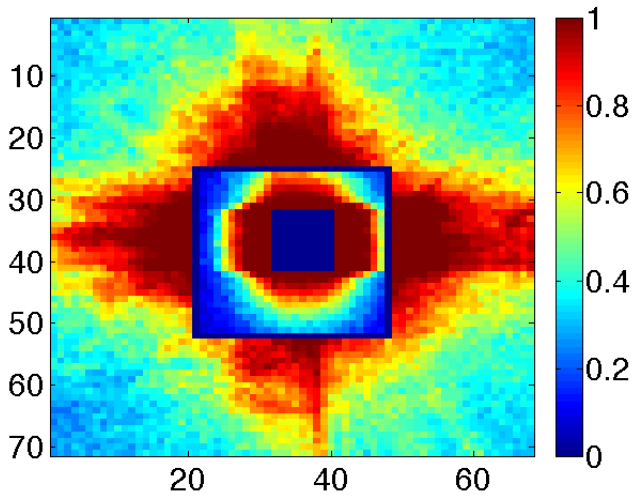

Figure 6.12: Average number of detected events in each pixel for every frame the ptychography dataset for the central region of the diffraction patterns covered by the beamstop and the region directly outside. The central beam is not taken into account for this measurement as there is a detected event in this region every frame of the dataset. The low statistics are in the corners of the beamstop the absences of counts in this area cause artifacts in the reconstructions. Axes give pixel numbers.

were accumulated over to avoid over-saturating the detector. Furthermore, the beamstop strongly attenuates the low resolution scattering from the chromosome leading to a low number of counts in the corners and near the edges of the beamstop and consequently a poor signal to noise ratio. Fig. 6.12 shows a representation of the average counts detected per pixel inside of the beamstop and in an area directly outside it for diffraction from a chromosome. This was calculated by counting the detected events in each pixel over all the ptychography projections and averaging. A detected event was defined as a pixel measuring a value above zero. It can be seen that the corners of the beamstop have significantly lower detected events than the area outside the beamstop and the centre indicating that much of the low resolution data is blocked by the beamstop. The poor fits in some of the integration profiles (fig. 6.11) is partly due to the poor statistics in the area near the edges of the beamstop.

In the phase retrieval algorithms pixels which have zero value are not updated by the modulus constraint. These values are left to float during the phase retrieval and over several iterations can find an intensity value that fits with the rest of the pattern. The area under the beamstop is filtered therefore some of the counts are going to be measured incorrectly and some will be blocked completely. By letting the area under the beamstop float in the algorithms improvements to the image could be made. However, not updating the central part of the diffraction pattern can lead to poor reconstructions and long convergence times therefore the centre of the pattern is updated by the modulus constraint for the first half of the iterations and is then left to float. This technique

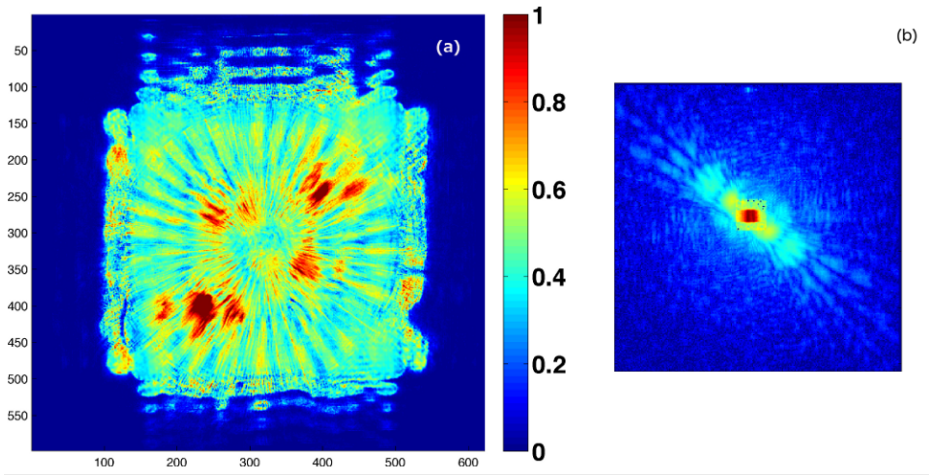

Figure 6.13: (a) Amplitude image of a Siemens star reconstructed from data where the beamstop has been corrected for every frame using a method of averaging the scaling factors inside and outside the beamstop. The patches of bright amplitude occurring along some spokes of the star are caused by the beamstop correction being over-amplified in certain frames. (b) The diffraction pattern from one frame of the ptychography dataset with and over-amplified central region. The multiplication factor used in this frame was calculated from the high counts in the lobes of the Siemens star passing over the edge of the beamstop which made the factor too large resulting in an overamplification. Dataset S065.

was applied in the reconstructions of the chromosomes and test objects measured at 5.5 keV. To further constrain the problem just the areas of the corners of the beamstop and the contribution from the central beam are left to float.

It was observed in the data from the Siemens star that a multiplication factor that provides a good fit for one frame of the dataset does not necessarily give a good fit for other frames in the same dataset. This could be due to low statistics at the beamstop edges which made the beamstop fit appear poor. In some frames, especially those that contained little scattering, the multiplied data inside the beamstop had a far greater intensity and the data outside the beamstop. One reason for the change in measured intensity could be the detector response at the energy of 5.5 keV. To try to produce the best beamstop fit on for every data frame a multiplication factor that varies from frame to frame was implemented.

This factor was calculated by taking the intensity ratio of pixels in at the inside edge of the beamstop and the first row of pixels outside the beamstop. The multiplication factor was calculated from an average of the intensity ratios. The variation of the multiplication factor produced artifacts in the amplitude part of the reconstructed image from datasets corrected in this way (fig. 6.13). The amplitude images show patches of strong amplitude or "hotspots" . The positions of these hotspots are related to positions in the dataset where the multiplication factor used to correct the beamstop was too great. The large multiplication factor was caused by strong first order diffraction lobes providing high counts across the beamstop edge making the average of the intensity ratios

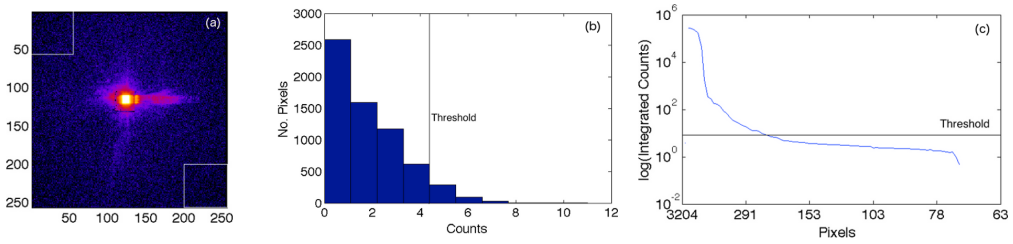

Figure 6.14: (a) Whitefield image from chromosome dataset with two rectangular regions marked. The counts in these regions were used to produce the histogram (b) which was used to decide the noise threshold. From the histogram the threshold value was taken to be 4.4. (c) Shows the radial integration of the average of the first 10 diffraction containing frames in the ptychography dataset . The solid line shows where the threshold level as decided from the histogram. From the radial integral it can be seen that the signal is at the level of the noise for high angles. Data from scan S145.

high and therefore α too large. To try and remove this error the average was weighted so that it did not include the high counts, however the reconstructed images still showed "hotspots" of amplitude. It was found that multiplying every frame by the same α value, hence using a constant beamstop correction, did not produce the bright spots in the amplitude image even though some data frames appear to have a poor fit between the beamstop are and the outer data. The central data should be corrected by a single multiplication factor as the transmission of the beamstop material should not change from frame to frame. The hotspots are caused by the overamplification of a changing multiplication factor. The appearance of poor fitting for the beamstop is not due to a poor detector response at this energy.

6.4.2.2 Thresholding and Noise

When imaging weak scattering samples taking account of the background noise becomes critically important as the Signal- to-Noise ratio can become very low. In the measurements there were many sources of noise including shot noise, detector noise, and scattering from air and windows. In the case of the chromosomes it is important to reduce window and air scattering as this can be at the same level as the scattering of the chromosomes. This was achieved in our experiments by using thin membranes of X-ray transparent material and vacuum flight paths. The read out noise from single photon counting detector is very low (section 6.3.1.1) therefore we only need to consider the shot noise which is governed by Poisson statistics therefore we can consider the standard deviation$\sqrt{N}$ where N is the number of the total counts per exposure. This standard deviation is equal to the Signal-To-Noise ratio, for the exposure of a single frame on a chromosome the SNR is approximately 5300 counts.

The most problematic source of noise in this experiment is the scattering from air, windows and the sample membrane because the scattering signal from these materials is at the level of the

signal from the chromosome, therefore reducing the SNR between chromosome and background scattering. Furthermore when measuring with coherent illumination scattering from background objects is coherently added to the signal therefore cannot be removed with a simple subtraction. Air scattering, however, is mostly diffuse scattering and can be counted as incoherent therefore can be removed by subtraction.

To attempt to find a background level from air and window scatter the whitefield frame was used. A position from the ptychography dataset that did not include any contribution from the sample was used as a whitefield. Two regions of interest of 50×50 pixels, were chosen at opposite corners of the detector to minimize the contribution from slit and pinhole scattering whilst capturing the background scattering (fig. 6.14(a)). A histogram of counts in these areas was used to determine a threshold level for the dataset (fig. 6.14(b)). It can be seen that most of the counts in the region of interest fall between $0-4$ counts, therefore the threshold level was taken to be 4.4 counts. Any counts below 4.4 were set to zero before being passed to the algorithm.

To look at the signal level over background, the first 10 frames of the dataset that contained scattering from the chromosome, were averaged and radially integrated over an angular range. The integration segment was chosen not to include contribution from the pinhole or slit scattering. There is a background level of 4 counts and the signal above this level drops off at a resolution of approximately 200 nm. At this point any signal from the chromosome cannot be distinguished above the background scattering. In applying the thresholding taken from the whitefield, some signal from the chromosome is subtracted too. However, we are no longer in a regime where the signal has enough statistical significance to contribute to the image and is lost in the noise.

6.4.3 Results from 34-ID-C

6.4.3.1 Test Pattern Reconstructions

During the experiment a scan of a test pattern was taken every few hours to test the performance of the experimental set up and provide a reliable reconstruction of the current probe. It was found during the run that the test pattern could only be reconstructed with the correct shape after the beamline was aligned at the energy of 7 keV. At the energy of 5.5 keV, images of the test object showed several different artifacts and in some cases failed to reconstruct to a significant quality, this could be due to the presence of high harmonics, (discussed further in section 6.4.4.1). Both the weak and strong test samples were imaged at 5.5 keV to check that the artifacts were not due to energy range being incompatible with the absorption characteristics of the test object at this energy. Both test objects are designed to produce certain phase shifts at a chosen energy (see table

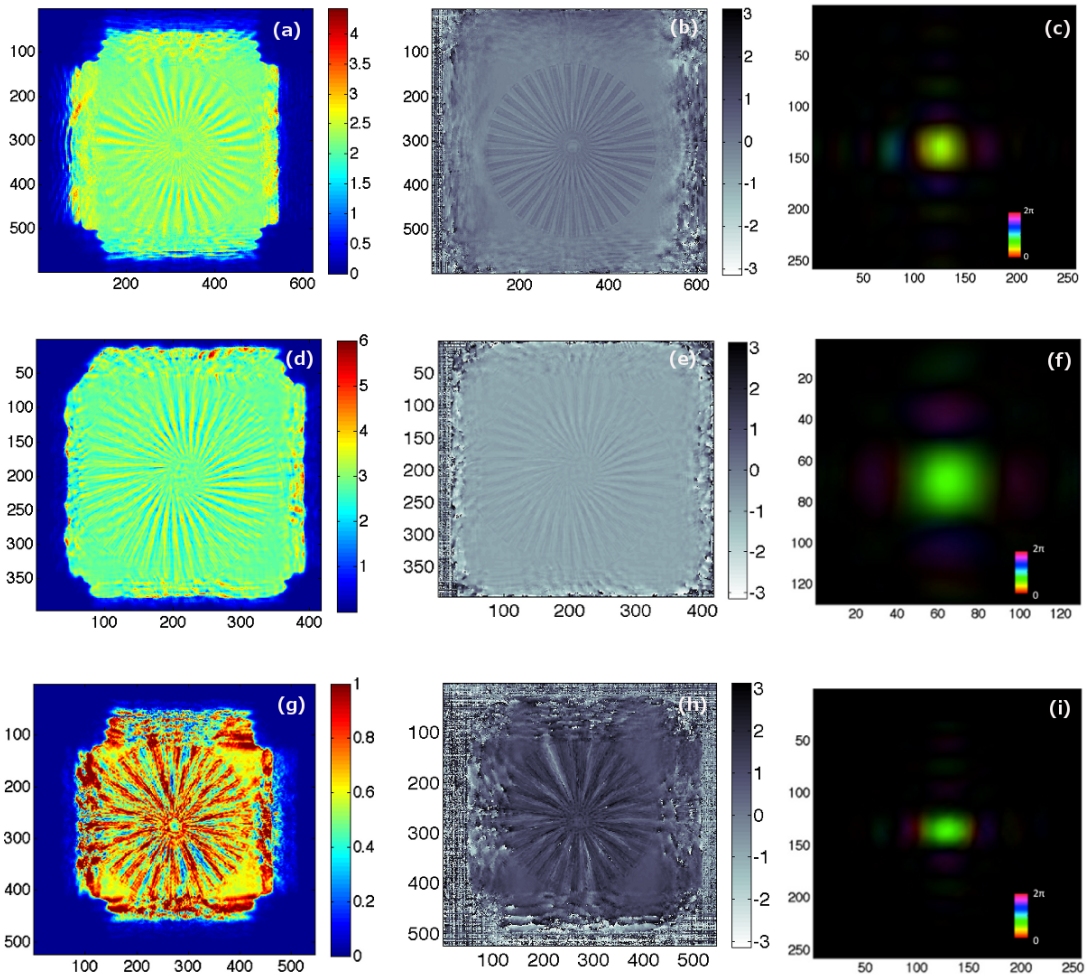

Figure 6.15: Reconstructions from test objects taken at 34-ID-C. The incident illumination was focussed with a KB set-up (a) Amplitude (b) phase and (c) probe reconstructions from the weak test object at 7 keV. Reconstructions from scan S065. (d) Amplitude (e) phase and (f) probe reconstructed images from the weak test object at 5.5 keV from scan S154. The dataset was binned to obtain this reconstruction therefore the array size is 128×128 pixels. (g) Amplitude (h) phase and (i) probe reconstructed images of the strong test object at 5.5 keV from scan S155. Strong asymmetry of the of the probe function appears in th case of the hard test object. The spokes of the Siemen star show loss in contrast and definition in the phase images taken at 5.5 keV whereas they are sharply defined at 7 keV. Axes show pixel numbers and probe is displayed with phase represented by colour and amplitude represented by intensity.

6.2), however when imaging these objects at an energy outside the designed range there may be strong absorption effects of the material if an absorption edge is near that range. In the case of high energies we are outside of the absorption edge effects but both objects where tested as they produce different phase shifts.

The individual spokes can be clearly distinguished in phase image of the weak test object measured at 7 keV, (fig. 6.15(a)), however there is a slight doubling effect that can be seen at their edges. In the amplitude image the spokes can be identified, however, the contrast between the spokes and the background is very low, which is expected for the absorption of the weak test object in this energy range. Patches of higher amplitude can be seen along the edge of some spokes in the star and the edges of the spokes are better defined towards the centre of the star than at the extremes. The reconstructed probe (fig. 6.15(c)), output in a colour scheme where the colour represents phase shift and the brightness of the colour represents amplitude, shows a 2-D sinc function profile, expected for a beam from a square aperture focussed by K-B mirrors.

At 5.5 keV the reconstructions of the weak and strong test objects show different artifacts. The phase and amplitude images of the weak test object shows a twisting of the spokes, spiralling out from the centre (fig. 6.15(d)-(e)). This twisting artifact cannot be removed in the reconstruction through position correction algorithms, or adding extra constraints on the allowed phase and amplitude ranges. To reconstruct the test pattern with sufficient quality to see the individual spokes of the Siemens star, the data was binned, therefore the probe and weak test object in (fig. 6.15(d)-(e)-(f)). look larger than the others shown but the pixel size in these reconstructions is in fact double the size of the other two. Despite the reconstruction from the Siemens star showing this effect, the retrieved probe shows the expected 2D sinc amplitude profile.

The strong test object measured at this energy does not display the twisting artifact of the weak test object and the spokes are visible and straight. In the phase image (fig. 6.15(h)), there are streaks of $-\pi$ phase radiating in the same direction of the spokes at the top of the image and diagonally opposite. This is reflected in the amplitude (fig. 6.15(g)) image where some spokes have different values across them than others, these regions correspond the streaks of $-\pi$ phase. In both the phase and the amplitude images the outline of the spokes shows very strongly a doubling effect especially towards the wider ends. The spokes in the bottom half of the star also appear shorter than the spokes in the top half. The probe reconstruction from this data set shows a central maximum that is stretched in the horizontal which is likely to be an indication that the algorithm has not converged. The probe shows strong first order fringes in the horizontal direction but not in the vertical direction.

It is clear from the reconstructions that the probes from these test objects measured at 5.5

keV can not be used as starting guesses as the object has not reconstructed in a reliable way. It is difficult to identify the cause of the twisting and phase streaks at 5.5 keV using the current data processing methods and algorithms available.

6.4.3.2 Chromosome Reconstructions

The amplitude and phase images both show the outline of a chromosome (fig. 6.16(a) and (b)) which agrees with the image of the same chromosome obtained with the Secondary Electron (SE) signal in SEM. The phase contrast between the object and background is very weak and the chromosome can only be identified due to the strong phase shift over its edge, there is no significant phase contrast inside of this boundary to distinguish the area from the background. The boundary itself is not continuous and is formed of pieces of negative phase surrounded by halos of positive phase. This jump between negative and positive phase continues out from the boundary of the object decreasing in amplitude like decaying oscillations. The disjointed boundary and ringing effect is not a feature of the chromosome but an artifact coming from the reconstruction which so far cannot be removed with our current ptychography methods.

The amplitude image also shows the same disjointed boundary seen in the phase and demonstrates a stronger ringing effect than the phase image. The amplitude contrast is very weak and the chromosomes can only be observed in the image due to the artifacts occurring in the boundary area. A weak amplitude contrast is expected because of the small value of β (see eq. 2.21) at the energy used.

These image of the chromosome obtained from the SE signal is a surface image of the chromosome rather than a 2-D projection through the object as obtained with ptychography. Due to the large depth of field of SEM, the images can be used to judge the 3D profile of the chromosome and qualitatively estimate what should be seen in the projection phase images taken by ptychography. In the SE images it can be seen that the chromosomes have a 3D profile and are not completely flat therefore we would expect to see some phase contrast across the whole body of the chromosome above the level of the background and not just at the edges. The ptychography phase images do not show any higher order information of the structure of the chromosomes, the chromatids nor the centromere can be identified. The separate chromatids can be seen in the SE images but due to the compact state of the chromosome there is no space between the chromosome arms that would correspond to a difference in phase shift in the ptychography image. The centromeres of the chromosomes are very wide and short and do not show a change in surface structure along them. It is unlikely that there would be a difference in phase shift between the centromere region and the rest of the chromosome which agrees with the observation seen with ptychography.

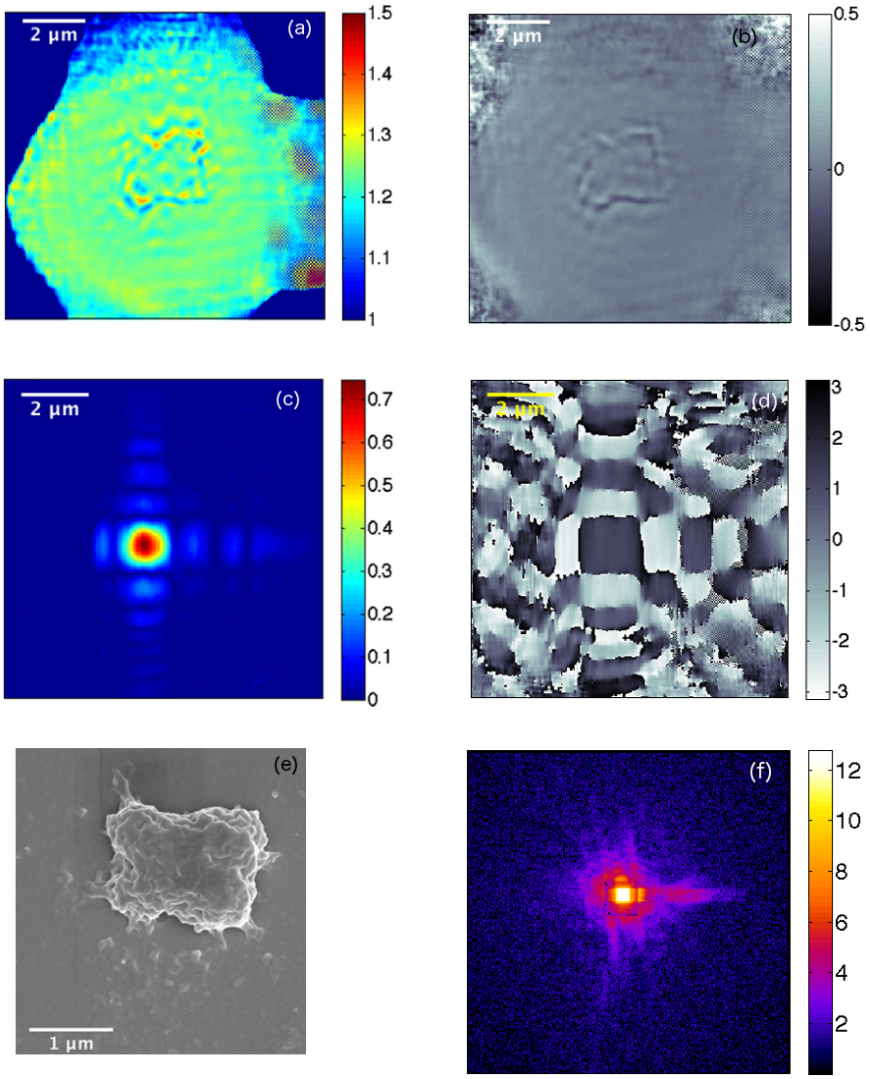

Figure 6.16: (a) Reconstructed amplitude and (b) phase of mitotic chromosomes using a combination of the ePIE and DM algorithm from scan S146. (c) Retrieved probe amplitude and (d) probe phase. The probe shows the 2D sinc profile expected from a KB-mirror source. (e) SEM image of the chromosome measured with ptychography from the Secondary Electron signal. The shape of the chromosome in the images retrieved by ptychography agrees with the shape observed in the SEM images. (f) Diffraction pattern from the chromosome displayed on a logarithmic scale. For analysis of the resolution of the diffraction see section 6.4.4.1.

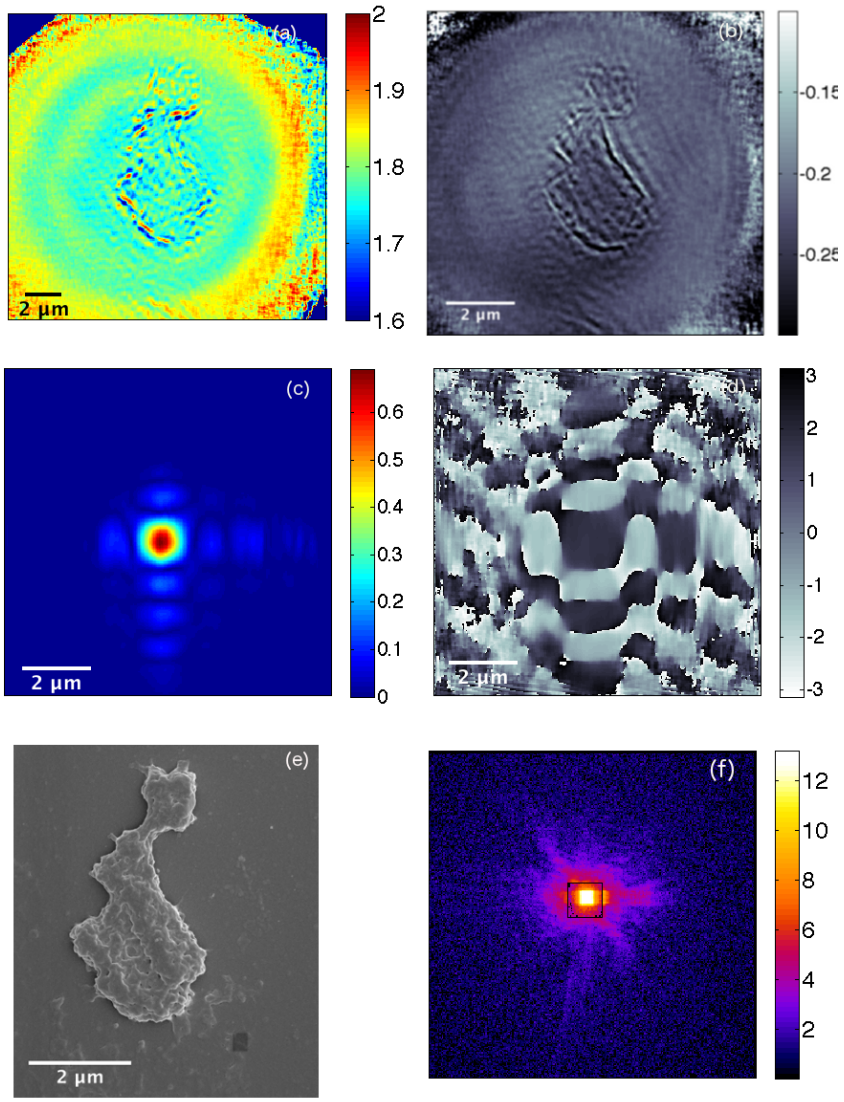

Figure 6.17: (a) Amplitude, (b) phase images from a chromosome cluster reconstructed using a combination of ePIE and DM algorithms from scan S143. (c) The retrieved probe amplitude and (d) phase. The probe shows strong outer fringes in the bottom and to the right hand side of the maximum. The horizontal fringes are poorly formed. (e) SEM image of a chromosome cluster of 3 chromosomes, imaged by ptychography. The image shows the three chromosomes that are grouped together in the scan area which appears as a single outline in the ptychography image. (f) The diffraction from the chromosome with the beamstop correction applied shown on a logarithmic scale.

A second example of ptychography shows a cluster of three chromosomes (fig. 6.17). Here the amplitude (fig. 6.17(a)) and phase (fig. 6.17(b)) images obtained with ptychography show the same disjointed boundary and low phase contrast across the body that is seen in fig. 6.16. The phase image shows a modulation over the body of the chromosomes. From the phase image and amplitude images it is difficult to distinguish the outline of the the three chromosomes which can be clearly seen in the corresponding SE image (fig. 6.17(e)). In the phase image only the outline of the three chromosomes is visible and it there is no boundary shown between them. The SE image clearly shows the chromatids and it appears that the largest chromosomes is partially covering the chromosome at the bottom righthand side of the image, this should correspond to an increase in phase shift in this area which is not seen in the phase image.

The background in the amplitude and phase images is not uniform as expected. It shows concentric rings of different phase and amplitude which follow the scan pattern. This is probably caused by the probe drift during the scan but could not be rectified with the position correction.

The retrieved probes in both the reconstructions shows the 2D sinc profile expected from a square aperture, however the outer fringes of the two probes are different. In fig. 6.16(c)-(d) the fringes on the left hand of the horizontal disappear in both the probe phase and probe amplitude images . In fig. 6.17(c)-(d) there is an absence of fringes in both the left hand side and above the central maximum. This shows a change in probe between the two scans which were taken several hours apart, this is further discussed in section 6.4.4.2.

The diffraction patterns from the chromosomes (fig. 6.16(f) and 6.17(f)) show a region of speckle from the chromosome and flares from the pinholes. The strong fringe on the right is caused by scattering from the aperture defining slits that could not effectively be blocked by the guard pinholes. The diffraction patterns shown here have not been thresholded and there is a level of background noise that comes from air and window scatter. The resolution of these diffraction patterns is further analyzed in section 6.4.4.1.

6.4.3.3 Nuclei Reconstructions

The phase images of the nuclei in fig. 6.18(a) and (d) show phase contrast over the body of the nucleus with a strong phase shift at the boundary. The boundary consists of two almost concentric rings, that are broken in places, therefore it is difficult to distinguish the edge of the object. The phase image of the nucleus in fig. 6.18(g) shows a modulating phase across the body very similar to the effects seen in the chromosome reconstructions (fig. 6.17).

In all the images a ringing effect can be seen in the background of the image which has also been observed in the chromosome images. This effect is the appearance of circles around the object that

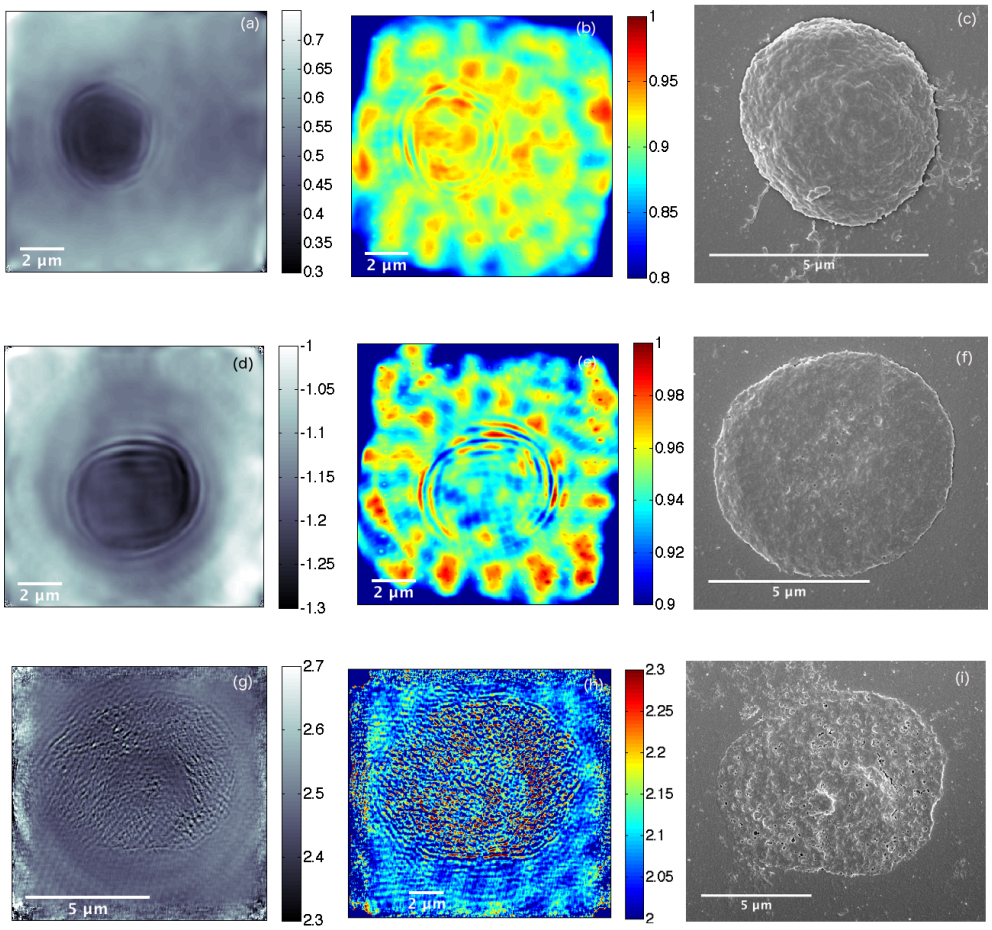

Figure 6.18: From scan S099: (a) phase and (b) amplitude images of a nucleus from b-lymphocyte cells reconstructed using ePIE with Upsampling. (c) SEM image of nucleus measured by ptychography. From scan S098 (d) phase and (e) amplitude images of a nucleus reconstructed with ePIE and Upsampling. (f) Corresponding SEM image. From scan S101: (g) phase and (h) amplitude images if a nucleus reconstructed using ePIE and DM. (i) Corresponding SEM image. The nuclei from S098 and S099 are intact whereas the nucleus from S101 has been broken. The phase images from the intact chromosome show a phase contrast over the body of the nucleus but the broken chromosome shows patches of phase. The difference between the intact and broken case is further supported by the SEM images of the same nuclei measured by ptychography.

fade with distance from the object. The amplitude of the object shows this effect more strongly than the phase image. The phase and amplitude regions do not show a uniform background, rather there are patches of different phase and amplitude values. This is an artifact that typically occurs from the uncertainty of the beam position and can be improved with position correction algorithms however the implementation of these algorithms was not successful in this case.

The SEM images confirm that reconstructed images give good agreement to the size and shape of the nuclei. The SEM images also show that the boundary of the nucleus is sharp and not doubled. This does not agree with the ptychography images all of which show a double boundary further suggesting that the doubling effect is an artifact of the reconstruction.

From ptychography images it is observed that the three nuclei all have different phase shifts and areas. This difference may be explained through the detail seen in the SE images. As explained in section 5.1 the cells are arrested in late prophase however not all the cells arrive at this stage in the cycle. When the nuclei are spread on the membrane those that are in interphase stay intact whereas those near late prophase, when the nuclear envelope is weak, burst to reveal the chromosomes. From the SE images which show the surface of each nucleus, it is observed that the nucleus in fig. 6.18(c) not as flat as the other two nuclei and covers a smaller area, typical of interphase nuclei. The nucleus shown in fig. 6.18(f) is flatter and covers a wider area but is still intact, this is again likely to be a nucleus in interphase. The phase images of these nuclei show a nearly flat phase profile across the body of the nucleus suggesting a uniform density of the contents indicating that the DNA inside the nucleus is distributed with uniform density which is most similar to the DNA compaction during interphase. The nucleus shown in fig. 6.18(i) and measured by SEM, is flat and covers a wide area. The layer over the nucleus also appears to be broken in some places, which could indicate this nucleus has entered prophase where the nuclear envelope starts to break down. The corresponding phase image fig. 6.18(h) of this nucleus shows patches of phase rather than a uniform phase. The layer of nuclear membrane covering the chromosomes in the SEM image prevents a further analysis to whether the patches of phase correspond to early forming chromosomes in the late G2 phase of the cell cycle. The artifacts in the phase image does not allow a deeper analysis of the phase patches.

6.4.4 Discussion

6.4.4.1 Resolution and Performance of Phase Retrieval

To assess the performance of the phase retrieval algorithms the Phase Retrieval Transfer Function (PRTF) was calculated. This measure is designed to look at the agreement of the reconstructed

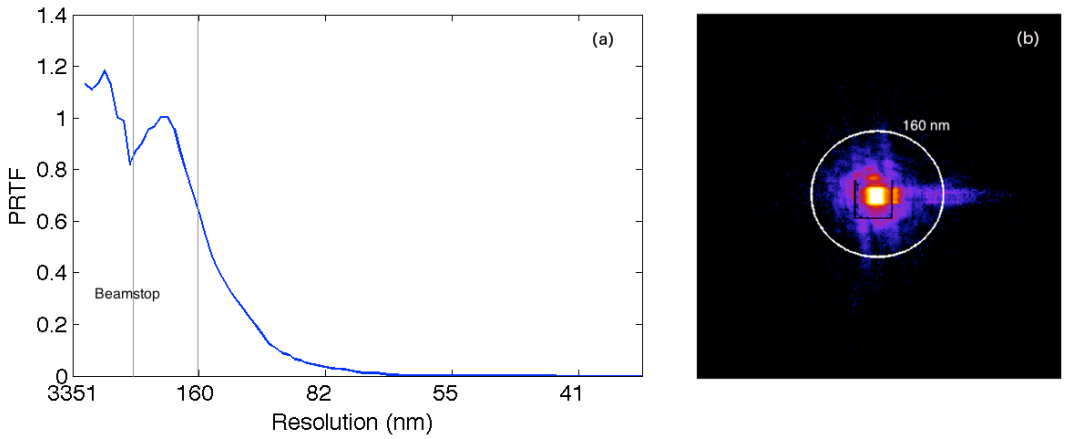

Figure 6.19: (a) Phase Retrieval Transfer Function for the chromosome reconstruction shown in fig. 6.16. The PRTF is averaged over the first ten ptychography frames and ten different random starts. Two grey lines indicate the position of the beamstop edge and the maximum measured resolution. (b) First frame of the diffraction from the chromosome, the maximum measured resolution as indicated by the PRTF is shown with a white circle. (Dataset scan S146)

data with the original data at a given resolution over a number of different random starts. The measure is designed to test both the convergence and the reproducibility of the solution at a given resolution (spatial frequency). The definition of the PRTF as designed for CDI (see eq.3.5) is modified for ptychography. Here the Fourier transform of the exit wave at the sample plane is used, which is the wave from the object multiplied by the wave of the probe. The PRTF was calculated by comparing reconstructions from 10 different random starts with the first frames of the data set which contain the strongest scattering signal (shown in fig. 6.19). The PRTF calculated for the chromosome in fig. 6.16, scan S146, and is shown in fig. 6.19.

The PRTF of the chromosome shows erratic behaviour inside the beamstop especially near the edges where the value drops to 0.8. The PRTF increases to 1 outside the beamstop and shows a good agreement with the data to a resolution of 160 nm before dropping below 60%. The resolution of the reconstructed images is therefore taken to be 160 nm, the scattering angle corresponding to this resolution is shown by a white ring on the diffraction pattern in fig. 6.19(b). The majority of the scattering falls inside the circle and the scattering outside is very close to the level of the noise. The resolution found here is very poor compared with the potential resolution of ptychography due to the weak scattering nature of the sample which does not provide sufficient SNR at high angles to achieve a high resolution reconstruction.

It can be seen from the comparison between the ptychography images and images taken with visible light microscopy and SEM, that there are many artifacts in the image coming from the phase retrieval algorithms. Propagating the retrieved exit wavefield to the detector plane shows that there is a lot of noise at high angles that does not match the data. This is further supported

by the low PRTF value at high angles.

The measured resolution of 160 nm is better than the resolution obtained with standard fluorescence microscopy but is still greater than most examples of biological objects measured by ptychography, which have been measured with a higher degree of resolution in 3D than seen here (see section 3.6 for more details). An example of mouse femur was imaged to 65 nm at cSAXS beamline, Swiss Light Source [46]. Other examples include the D. Radioranus bacteria which was measured in 2D by ptychography at 85 nm resolution [168] and then later in 3D at a resolution greater than 55 nm [7]. Whilst having significantly better resolution than measured here these samples can withstand a large radiation dose without being damaged. All the examples were measured at the cSAXS beamline which has a set-up that is optimized for 3D ptychography and has a detector with sufficient dynamic range to avoid using a beamstop.

The resolution obtained in this experiment is sufficient to see the gross morphology of the chromosome which agrees well with the optical microscopy image. It is likely that smaller spatial features seen in the phase are due to artifacts from the reconstructions as the PRTF indicates that agreement between the measured diffraction and the reconstruction diffraction are very low at high resolution.

The poor correction to the data under the beamstop also contributes to artifacts in the image. The beamstop acts as a high pass filter, therefore high frequency information is represented in the images. This can be seen in the chromosome images where there is the strong phase shift over the border of the objects but not over the main body of the chromosome. The use of the upsampling method on the nuclei data has reduced this filtering effect slightly but strong phase shift at the edges cannot be seen.

The convergence of the algorithms is measured by the error χ^2 (see eq. 2.38), this is calculated for each frame of the diffraction pattern and is simply a comparison of the reconstructed intensities to the measured intensities. The error metric is calculated for every position in the ptychography dataset and the average error metric is plotted in fig. 6.20. The error metric drops rapidly over the first few iterations and stabilizes when the probe starts to update. The DM algorithm stays stable and does not move through solutions indicating that the solutions does not change so much. There is a slight rise in the value of χ^2over the iterations of DM. The value of χ^2 drops rapidly again after the first 2 iterations of ePIE and then is stable for the following iterations. The value of χ^2 does not always correspond to the success of the algorithm, a poor reconstruction can still result in a low value of χ^2.

We could not retrieve reliable reconstructions of the test objects that were measured at 5.5 keV. Yet these were measured with a much higher resolution than the chromosomes and have a

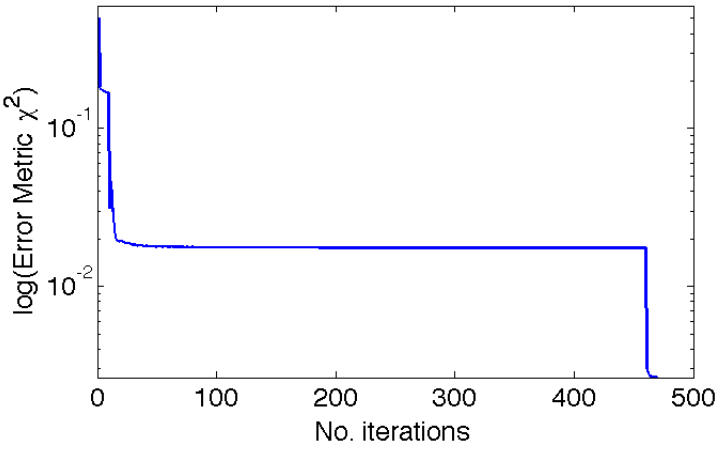

Figure 6.20: The change in average error metric of all the positions in a ptychography scan (S146) of a chromosome during the reconstruction. The iterations at which the different algorithms are switched is indicated. It can bee seen that there is a large change in the error metric during the first 10 iterations then does not change during the DM algorithm. The value of the metric decreases again when the algorithm is switched back to ePIE.

strong scattering information that comes from almost all spatial frequencies. The energy of 5.5 keV is at the limit of the beamline's energy range and due the alignment of the monochromator and mirror at this point there may be some contamination from higher harmonics in the images. The presence of two wavelengths in the source results in a doubling of features of the same frequencies at different positions in the image, therefore this is strongly observed in the case of the Siemens star. There is also evidence of this in the chromosome images where the border shows a rippling effect and the doubling of the border in the nuclei images.

6.4.4.2 Stability of the illumination

Probe instabilities could be responsible for the ringing artifacts of the chromosome and nuclei reconstructions, and the twisting artifacts in the reconstruction of the weak test object. To test the stability of the illumination during the scan phase retrieval was performed on a subset of scan positions taken close together in time. For example the phase retrieval was performed using only the positions 1-50 of the495 point round ROI scan which were taken in 30 minutes. Then phase retrieval was performed with positions 50 -100 of the scan, which again were taken over a 30 minute duration. Comparing the retrieved probes and the quality of the images from these two sets of positions from the same scan can demonstrate if there is any drift during the scan.

The test object measured at 7 keV was chosen for this test as it shows the truest image of the object so probes retrieved from this dataset can be taken to be the most accurate. The positions

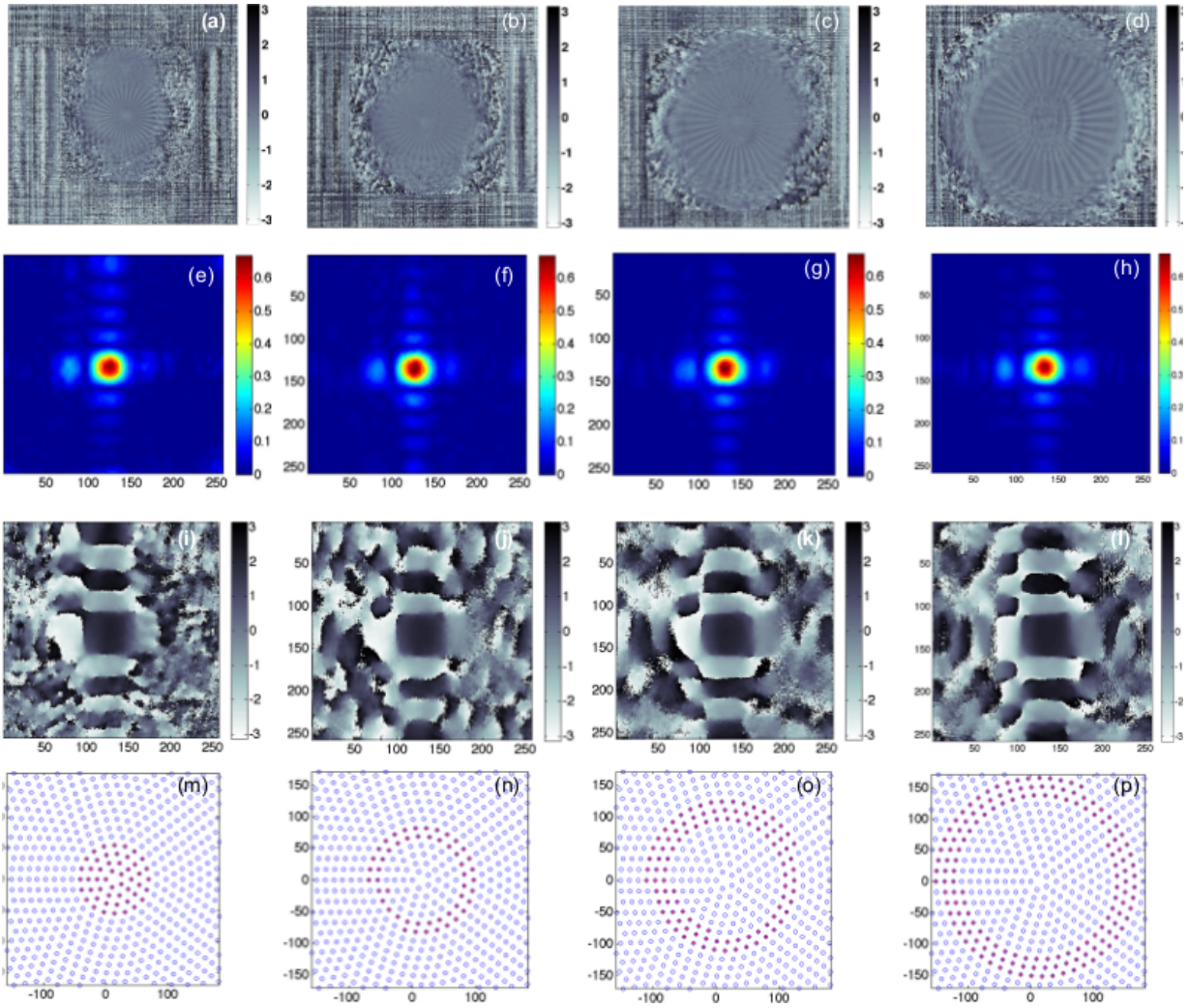

Figure 6.21: (a)-(d) Phase image of a reconstructed Siemens star using selected points in the scan (number S065) which chosen to be close in time. Reconstructed probe (e)-(h) amplitude and (i)-(l) phase from the selected points of the scan (m)-(p) The scan points used in the reconstruction are highlighted in red, the total positions recorded in the scan are are shown in blue. There is difference is both the shape and intensity of the outer fringes in the probe over the time of the scan. The instabilities in the probe can cause artifacts in the image if all the points are taken during the reconstructions because of these drifts.

used in each phase retrieval are marked in red (fig. 6.21) and resulting phase image of the object and phase and amplitude images are shown.

It can be seen in the phase and amplitude images that the probe centre remains in the centre of the image and does not change in shape over time (fig. 6.21(e)-(l)). The outer fringes of the probe are not stable in time and can be seen to change with the different positions used. For the first 50 positions the intensity of the probe appears in the corners of the array which suggests that the algorithms is not converging. The greatest change in the probe can be seen in the horizontal direction change the fringes move in space and change shape.

The best quality image for the probe and the phase is for the reconstruction from $200 - 350$ positions. This case has the longest exposure time and therefore suffers the most from probe instabilities, however, more data points are used in the phase retrieval algorithm which helps the convergence. From the scan patterns used in the reconstruction, (fig. 6.21(m)-(p)), it can be seen that in the case of the first 50 positions the overlap constraint is very strong as most positions are overlapped by their four closest neighbours. In the case of $50 - 100$ positions, fig. 6.21(n), and $100 - 200$ positions, fig. 6.21(o) each position is overlapped by 3 neighbours. The overlap of four nearest neighbours arrives again in the case of 200-300 which might suggest why this reconstructions is of better quality that the others. Furthermore the inner most spokes of the Siemens star scatter to the highest angles, therefore the first 50 positions has the largest amount of high frequency data which has not been measured with sufficient resolution to form an image.

This analysis was also tried with chromosome datasets however, these did not provide strong enough contrast in the phase of the object to check if the probe was reconstructing correctly using just a few points in the scan so a different method of monitoring probe drift was applied. Instead of using some points in the same scan to monitor the probe drift during the scan, probes retrieved from consecutive scans were compared. All the ptychography scans of chromosomes were taken consecutively over a period of several hours therefore it is possible to compare reconstructed probes from successive chromosome scans. These probes are retrieved from different datasets, however the objects imaged have similar optical properties so a comparison can be made. The probes shown in fig. 6.22 were reconstructed from chromosomes scan with the same parameters, algorithms and using the previous probe as an initial guess. A real space support constraint of a Butterworth filter, 200 pixels in diameter was used in each reconstruction. The probes retrieved from scans taken approximately 140 mins apart show several differences in maximum amplitude and fringe structure (fig. 6.22). Over the total time period the central maximum increases in amplitude and the point of maximum amplitude drifts from the centre after 670 mins. The phase images show that the formation of the outer fringes improves over time. In the early scans, the outer fringes

are very poorly formed and shift in position around the central maximum. Over time the probe shape stabilizes into a typical sinc shape that we would expect to see from a slit focussed by a K-B mirror pair.

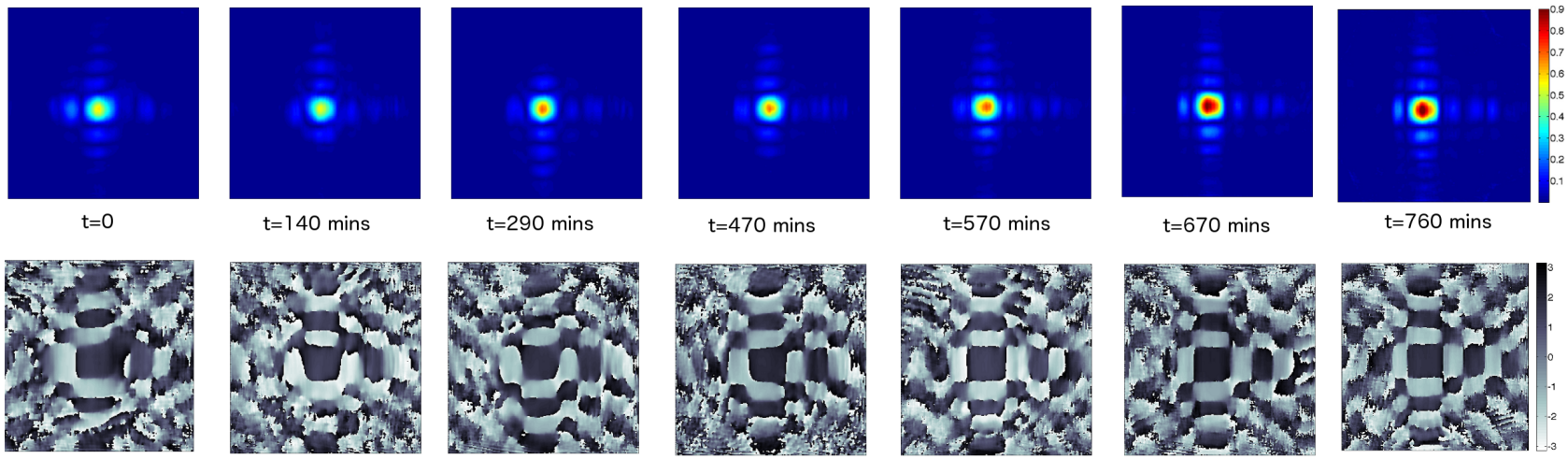

Figure 6.22: Probe drift during the chromosome scans. Chromosomes scans were taken consecutively over a period of hours, the retrieved probes from these datasets show large changes in their shape intensity and positions of the outer fringes. The amplitude and phase images of the retrieved probes shown over time. Probes reconstructed from the following scan numbers S139, S142, S143, S144, S145, S148 & S149. All images are outputted on the same colour scale to provide a direct comparison.

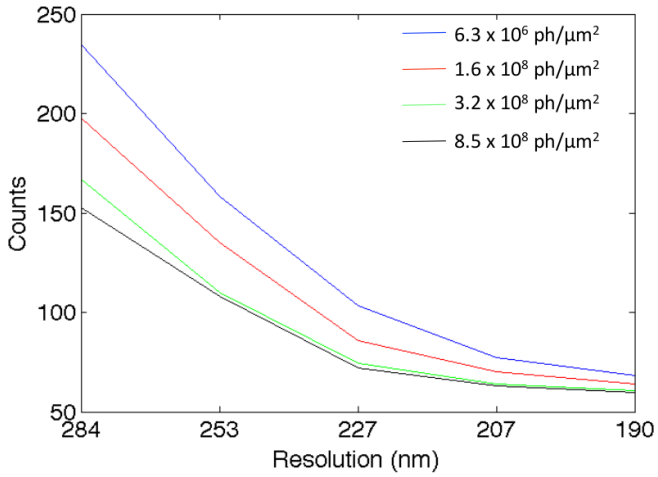

Figure 6.23: Radial integration over part of diffraction pattern showing scattering from the chromosome for successive dose applied. Each line represents the radial integration of the diffraction pattern after a number of photons is applied (shown in the legend). The intensity of the diffraction reduces at low resolution. The higher resolution data shows some collapse in angle. Data from S215b from 34-ID-C March 2013

For all probes shown in fig. 6.22 the reconstructed phase and amplitude images of the object contained artifacts. All the reconstructions, however, can be compared to visible light microscope and SEM images showing that the ptychography image has reconstructed somewhat faithfully. Due to the artifacts in the retrieved images we cannot be sure that the retrieved probes have been reconstructed very accurately however the changes in the probe shown are unlikely to be solely caused by the phase retrieval algorithms and are likely to be due to changes in the experimental set-up itself. It is not surprising to find drifts and changes in the illumination on a time scale of hours, however there are large scale changes to the shape and intensity of the probe would not be expected from such a ptychography set-up. These large drifts could be attributed to instabilities in the source or in the experimental set-up. Using a low energy for 34-ID-C, this can cause imperfections to build up on the K-B mirror surfaces as they are damaged more strongly at longer wavelengths. In this set-up the monochromator was being used at the very end of its range which could also result in instabilities and contributions from higher harmonics passing through.

6.4.4.3 Radiation Damage

Radiation damage has been seen in crystal diffraction by the gradual disappearance of diffraction spots with applied dose (see section 3.3.1). During the application of dose, diffraction spots disappeared from high scattering angles, until only the central spot remained (fig. 3.2). We applied the same method in a previous experiment at 34-ID-C, exposing a single area of a nucleus and observing the changes in the diffraction pattern over a time period. In order to see the changes in the pattern a radial integration was performed over a segment that did not include scattering from

slits or pinhole flares. The centre of the diffraction pattern which is suppressed by the beamstop was not included in the integration. The nucleus had previously been measured with ptychography therefore some damage would have occurred before the time scan was taken.

The dose applied is proportional to the incident flux on the sample. A single photon counting detector was used in this experiment therefore we can take an accurate measurement of the number of incident photons on the sample by summing the counts per frame. Here it is assumed that no incident counts are lost during the measurement. The flux is the number of photons per unit area. In the case of ptychography the unit area is the size of the beam and this can be measured from the reconstructed probe. An estimate of flux is calculated by simply dividing the total number of photons measured during the exposure by the area of the beam.

The time series was taken over a period of 40 minutes and was stopped when there was visible signs of change in the diffraction pattern. The integration profiles of the nucleus diffraction (fig. 6.23) show that there is a drop in intensity of the pattern over all scattering angles for increasing flux. At high-angles there is a small decrease in intensity over the time period. At scattering angles less than 227 nm the intensity drop occurs over the whole pattern simultaneously. There is a small disappearance of the high angle scattering first, as described by the crystallography experiment but it is not sufficient to make an estimate of damage at a length scale per unit dose.

The incident fluence on the sample during the 40 min period was 8.5×10^8 photons/μm^2 which is well below the Henderson limit, (described in section 3.3.1) of an incident fluence of 1.6×10^{10} photons/μm^2 causing an the diffraction intensity to drop by half. The intensity of the diffraction pattern seen here has fallen by less than one half which would be expected. As the nucleus had already been imaged by ptychography it has been exposed to a greater incident flux than measured here. The radiation damage occurs at high angles in the first few seconds of exposure therefore it is likely that we are not observing this damage because it has already occurred.

The chromosomes and nuclei undergo some fixation processes in the sample preparation stage however these may not withstand the large radiation damage. The Henderson limit is for frozen hydrated crystals, whereas the nuclei are measured dried and unfrozen. The samples undergo some fixation that is designed to withstand radiation damage but it is argued that freezing the sample gives greater protection from radiation damage [57].

6.5 Other Experiments

Samples produced by the methods outlined in section 5.1 have been measured at other beamlines as part of experiments developing coherent imaging methods. Nuclei have been measured with

ptychography at the cSAXS beamline, Swiss Light Source (SLS), by Ian Robinson and Fucai Zhang. Chromosomes and a clusters of nuclei have been measured using the technique of Scanning Transmission X-ray Microscopy (STXM) at the TwinMic Beamline, Elettra Sincrotrone, Italy by Graeme Morrison. The results will be briefly displayed in this section and discussed in comparison to the work presented from the 34-ID-C and I-13 beamlines.

6.5.1 Ptychography at cSAXS beamline

6.5.1.1 Description of Experiment

The experimental set-up was in transmission geometry, using a pinhole to define the illumination and with a sample to detector distance of 7.2 m. The energy used in this experiment was 6.2 keV which is the optimum energy for the beamline. A PILATUS detector, of 3 panels each consisting of a 487×192 array of 172 μm pixels, was used to record the diffraction patterns. This detector has sufficient dynamic range to measure the scattering from a nucleus without the need of a beamstop. A vacuum tube was placed between the sample and the detector to reduce air scattering. The illumination was unfocussed and selected by a pinhole of diameter 2 μm which was placed as close as possible to the sample plane (approximately 1 mm sample to pinhole distance). The sample was mounted on piezo stages that moved along the beam axis and perpendicular to the beam. A Round ROI scan pattern was used with a typical field of view of 40 μm with a step size of 1 μm.

The phase retrieval codes were written in-house by the team at cSAXS and use the Difference Map algorithm. They include a further improvement, the Maximum Likelihood (ML) refinement [24]. This refinement is designed to model the noise in the diffraction and apply a conjugate gradient method to reduce its impact on the reconstructions. It is applied as an optimization step after the DM algorithm.

A starting guess for the probe was taken from the reconstructions of the test object. The retrieved probe from the nucleus dataset is refined through propagation to the sample plane. It is often difficult to know where the sample is in comparison to the probe and the plane is not well defined by the phase retrieval. By simply propagating the probe function using Fresnel propagation the probe function can be estimated at the correct plane. This new estimate is then put back into the phase retrieval and the algorithm is run again to produce a better quality reconstruction.

6.5.1.2 Results from cSAXS

The diffraction from the pinhole and the nuclei filled more than one panel of the detector producing data at high angles. The phase retrieval performed using data from large scattering angles will

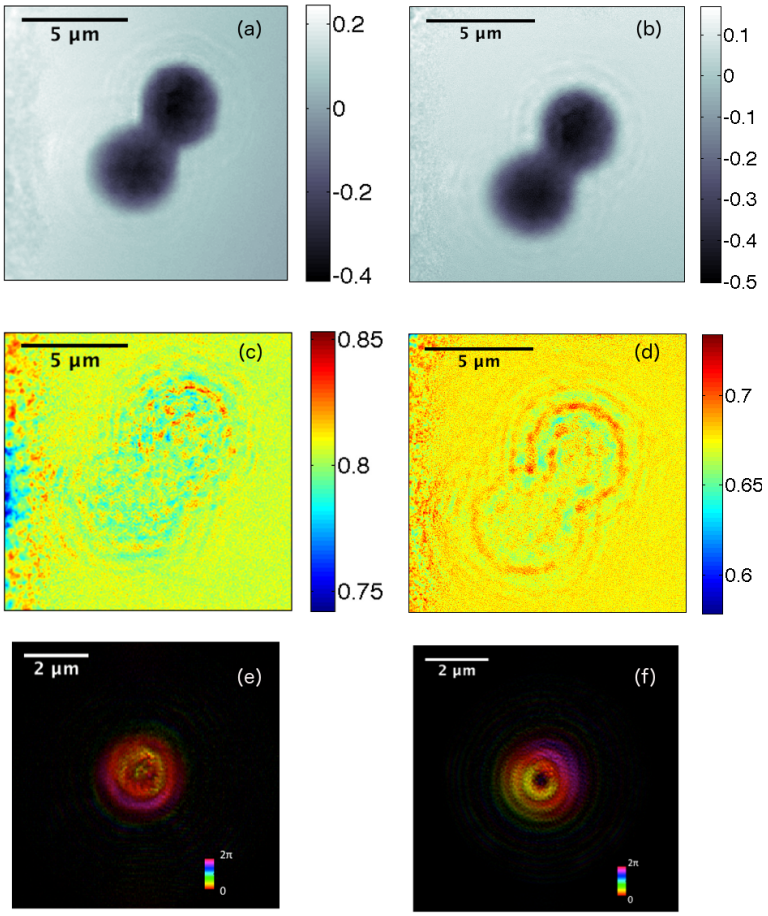

Figure 6.24: Reconstructions of nucleus data taken at the cSAXS beamline by Ian Robinson and Fucai Zhang. (a) Phase and (c) amplitude of two nuclei reconstructed from 192×192 array using DM started with an ML refinement and started with a propagated probe. From scan S00319 (e) Retrieved probe from this dataset with the phase shown by colour and the amplitude displayed as intensity. (b) Phase and (d) amplitude images of the same two nuclei reconstructed from 512×512 of the detector array. Scan number S00335 (f) Retrieved probe from this dataset. The images were reconstructed from the 512×512 using the DM algorithm.

result in the highest resolution image, however, there are benefits to performing phase retrieval on cropped data. The cropping improves signal to noise and has the practical consequence that using a smaller array increases the convergence and the rate of convergence. Cropping avoids having to take into account the missing data where the read out electronics between the panels are. In this experiment the missing data were obtained by recording two diffraction patterns at the same scan point with different detector positions. These two patterns are then used to update the modulus constraint of the algorithm therefore removing missing data.

The reconstructions shown in fig. 6.24(a)-(c)-(e) are from a 192×192 pixel array of the measured diffraction reconstructed using the DM algorithm with the ML refinement. The probe used in this data set was obtained by propagating the previously retrieved probe 1 mm to the sample plane. The reconstructions shown in fig. 6.24(b)-(d)-(f) are from a 512×512 pixel array of the measured diffraction data and are obtained using the DM algorithm.

The phase images of two nuclei retrieved from a 192×192 pixel array fig. 6.24(a) and a 512×512 pixel array fig. 6.24(b) show a sharp edge over the boundary expected from a nucleus. In both images the phase contrast is above the background across the whole body of the nuclei and is stronger in the centre of each nucleus and reduces towards the edges as would be expected from a projection image of a dome shaped object such as a nucleus. The two nuclei cannot easily be segmented as it is not apparent from the image where the boundary between them lies. In both images there is a slight ringing effect in the phase image can be seen as a ripple of phase outside the object. This effect is slightly less in the reconstruction from the 192×192 array (fig. 6.24(a)) where the probe has been propagated. Even when the probe is focussed the depth of focus can be large therefore even with the propagated probe it is difficult to place the object in the correct plane.

The corresponding amplitude images (fig. 6.24(c)-(d)) do not show a strong contrast over the bodies of the nuclei. The ringing effect is far more pronounced in the amplitude image than the phase and causes strong artifacts in the image. The reconstruction from the 512×512 pixel array fig. 6.24(d) shows a very strong amplitude contrast over the border of the image and shows a stronger ringing effect than in the phase image. The reconstruction from the 192×192 pixel array shows amplitude contrast below the level of the background over the bodies of the nuclei but has a strong ringing effect around the boundary and an artifact across the bodies of the nuclei that looks like the propagation effects of a wave. Having a contrast below the background implies that the nuclei are more transmissive than the background which is physically impossible and therefore most probably an artifact of the reconstruction.

The probes reconstruct (fig. 6.24(e)-(f)) to high resolution showing well defined circular fringes

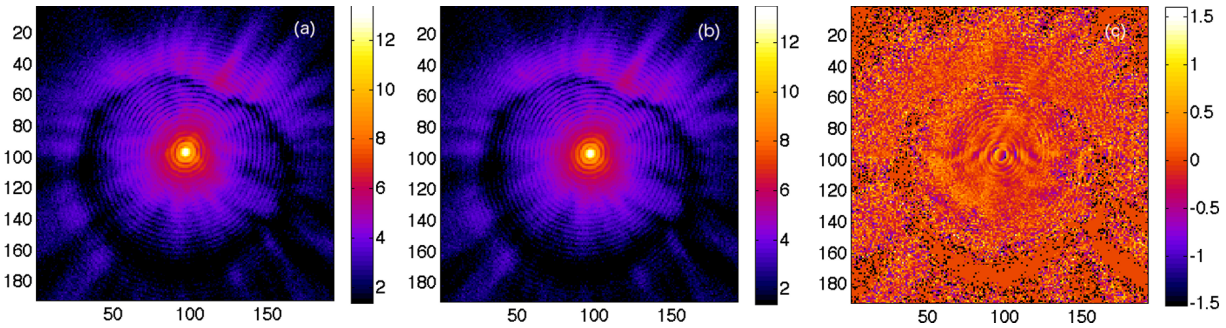

Figure 6.25: (a) Diffraction pattern of a nucleus from cSAXS (Scan S00335) and (b) the whitefield; scattering diffraction from the pinhole without contribution from the sample. The diffraction rings and the fringes are are from the pinhole and the nucleus scattering can be observed as a tiny modulation in the fringes. (c) The diffraction from the nucleus with the contribution from the whitefield divided out. The scattering from the nucleus can be seen as a fringe and a perturbation of the diffraction rings of the pinhole. Data taken by by Ian Robinson and Fucai Zhang.

as expected from a pinhole. The probe used in this experiment is highly diverse, which has been shown to increase resolution in ptychography [169]. The probe size was measured to be 2 μm FWHM in both cases. There is no strong difference between the propagated and non-propagated probe in terms of their shape and phase.

6.5.1.3 Discussion of Ptychography images

The estimation of the resolution of the scattering from the nuclei was difficult to establish because the signal from the nucleus was so much weaker than the signal of the probe it cannot be detected above the pinhole flares (fig. 6.25(a) and (b)). By dividing out the contribution from the whitefield, the pinhole scattering and diffraction, it can be seen that the scattering from the nucleus is a perturbation in the rings of the pinhole and has a single flare (fig. 6.25(c)). Another way is to subtract the intensities using an approach from [161]. An estimate of maximum resolution achieved in this experiment is taken from the maximum scattering of the flares pinhole at 52 nm. The resolution of the reconstruction can also be measured using the PRTF. This potential maximum resolution is higher than found at 34-ID-C and I-13. In the experiments at 34-ID-C and I-13 the flares from the pinholes and slits were measured to high angles however were not included in the estimate of the resolution because the scattering from the nucleus could easily be separated from them.

There is an argument that the stronger phase divergence in the probe can improve the resolution of the resulting reconstruction [169]. In the experiments at I-13 and 34-ID-C a highly diverse probe caused strong artifacts in the reconstruction therefore guard slits and pinholes had to be used to block the strong scattering from the aperture defining slit. In the experiment at cSAXS the pinhole scattering caused no such artifacts and the algorithms could accurately retrieve the probe function.

In the set-up at cSAXS the pinhole to sample distance was much smaller than in the experimental set-ups at I-13 and 34-ID-C. A large aperture to sample distance results in small instabilities in the illumination being magnified over the distance which probably results in the large artifacts seen at I-13 and 34-ID-C. For a high resolution reconstruction it maybe best to use a highly diverse probe very close to the sample plane.

The amplitude reconstructions for all the experiments show weak contrast and strong artifacts. It is expected that the object has weak amplitude because nuclei and chromosomes are highly transmissive objects but the source of the artifacts is not apparent. In all three images there is strong contrast from the border of the object which is the place where the amplitude changes rapidly, the method seems to have more sensitivity over these regions than in the others. The artifacts are similar they show strong halo effects that look like a convolution of an oscillating function and the shape of the object. In the amplitude images reconstructed with ePIE and Upsampling the area surrounding the nucleus is not uniform but shows patches of different amplitude. Chromosome images reconstructed with DM at 34-ID-C without Upsampling (fig. 6.16(a)) and the nuclei imaged at cSAXS (fig. 6.24(c)-(d)) do not have a patchy appearance, therefore it is likely that the patches of amplitude in the background come from either the ePIE algorithm or Upsampling method. The transmission from the objects is so large it may not give enough information to properly constrain the problem therefore the resulting amplitude image will always be of poor quality and contain artifacts. Such artifacts in weak data have been previously reported in [161].

The phase contrast observed in the reconstructions from the data taken at cSAXS is much greater than that at 34-ID-C . The slight ringing effect seen in the phase image (fig. 6.24(a)-(b)) does not interfere with phase in the body of the nucleus or break up the border as is seen in the retrieved images from 34- ID-C (fig. 6.18). The level of phase contrast seen at cSAXS is comparable to the reconstructed images from I-13 and the phase shifts through the object are further analyzed in section 7.1.

The area surrounding the nucleus in fig. 6.24(a) and (b) shows a flat phase which would be expected from the background. The images from 34-ID-C and I-13 show patches of phase in the background which look like shadows of the beam. This could be due to the probe drift over the sample resulting in a phase that belongs to the probe being put into the object function. At cSAXS the beam drift has been carefully documented so no scan takes place longer than the time the probe is stable on to achieve a high quality reconstruction. In this experiment the illumination selecting pinhole less than 1 mm from the sample plane whereas in the experiments performed at I-13 and 34-ID-C had sample to slit distances of a few centimeters and a metre. The instabilities of the beam are likely to be amplified over the source to sample distance therefore reducing this

distance can improve the reconstructions.

It is not evident when comparing the reconstructions what errors can be attributed to the role of the beamstop, as there are many differences between the retrieval and experimental factors which also contribute. It is clear that the reconstructed phase image from the nuclei taken at cSAXS show generally better defined phase contrast and features as well as a more accurate probe, than those taken at 34-ID-C and I-13, some of this success can be partially attributed to not using a beamstop however it is difficult to identify exactly what artifacts are caused by the addition of the beamstop.

The reconstructed probes of the experiment at cSAXS show the expected shape of a probe from a pinhole with good visibly in the higher order fringes. The probe is small in space compared to I-13 and stable therefore can be reconstructed to high accuracy. To further improve the images the reconstructed probe can be propagated to the sample plane and the reconstruction can be attempted with a new probe. A similar propagation step was attempted to improve the reconstructions from the 34-ID-C data however the starting probe was poorly reconstructed and propagating it produced a badly shape probe. The experiment at 34-ID-C was done at the very limits of the energies used and therefore there could be problems with the source illumination such as contributions from higher harmonics rather than the incorrect probe function at the sample plane.

6.5.2 Scanning Transmission X-ray Microscopy (STXM) of chromosomes

Scanning Transmission X-ray Microscopy is a lens-based imaging technique which normally uses absorption contrast to provide an image (see section 3.7). The STXM set-up involves an objective zone-plate which focusses the X-ray beam onto the sample. In STXM the sample is rastered through the beam and the signal is collected by a detector in the far-field. An image is built up from the contributions measured at each point.

Chromosomes were measured with STXM at the TwinMic beamline, Elettra Sincrotrone Trieste [170]. This beamline is designed to be operated in both a TXM and STXM mode an is operational in the soft energy regime. The chromosomes were measured using an energy of 500 eV and gave sufficient absorption contrast at this energy.

The resolution of the STXM is limited by the size of the focal spot produced by the zone-plate and the size of the scan step. The spot size of the zone-plate is characterized by the distance between the outer most zones. For the zone-plate at TwinMic the outermost zone width is 30 nm, however the focus spot is not diffraction limited. The scan parameters for the images of a nucleus cluster fig. 6.26(a) and a pair of chromosome fig. 6.26(b) are as follows.

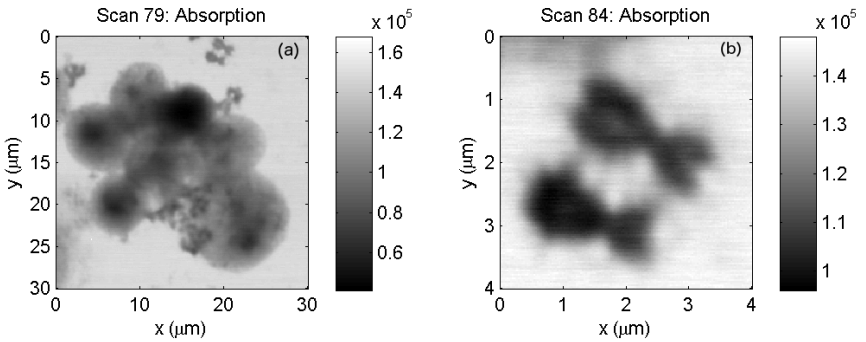

Figure 6.26: STXM images of chromosomes from the TwinMic beamline taken by Graeme Morrison (a) shows a cluster of nuclei with chromosomes at the periphery of the frame. (b) STXM of chromosomes in the top right corner of image (a). From scan 79. The images show absorption contrast form the chromosomes and nuclei and the axis show the field of view.

The nucleus cluster was taken with a raster grid of 250×250 points with a step size of 120 nm giving a 30 μm field of view. The non diffraction limited probe had a spot size of 150 nm and was dominated by the demagnifying of the x-ray source. The dwell time per step was 40 ms.

The chromosome pair were taken with a raster grid of 150×150 points with a step size of 30 nm giving a 4.5 μm field of view. The spot size was 50 nm, the size is increased due to convolution with the demagnified X-ray source. The dwell time per point was 140 ms.

6.5.2.1 STXM Results

Absorption images of a nuclei cluster show details of the difference in mass thicknesses across the cluster (fig. 6.26(a)). The resolution is sufficient to see individual chromosomes on the periphery of the cluster and a semi-formed spread of chromosomes near the bottom centre of the nucleus cluster. The thickness of some of the nuclei exceeded the depth of focus of the zone plate resulting in some parts of the image being out of focus. There is some sample debris that provides enough contrast at this energy to be resolved in the image.

The chromosome images clearly show the separate chromatids and have strong contrast (fig. 6.26(b)). Some tendrils can be seen at the edges of the chromosome which are similar to the nucleoplasmic layer seen in SEM. The STXM images have a greater spatial resolution than a visible light microscope and the measurements of chromosomes taken with ptychography which allows these small features to be seen.

The STXM image is far more detailed than any obtained with ptychography however there are small but evident artifacts in the images. Firstly there is evidence of striping the absorption contrast which is from the beam fluctuations. Secondly there is a small dot in the middle of the chromosome images from radiation damage as the unblanked beam was at rest in this position

before the scan took place. Neither of these artifacts disturb the information of interest in the images.

6.5.2.2 Discussion of STXM results

The resolution of the chromosome images from STXM is greater than our current attempt with ptychography. There are features such as chromatids and radially oriented fibres that can be readily distinguished in images taken from the STXM which cannot be seen in ptychography (fig. 6.16). The fibres outside of the chromosomes could be part of the nucleoplasmic layer as seen by SEM (section 5.3).

The contrast shown in the images taken from STXM is from absorption rather than phase, which is the contrast mechanism in ptychography, therefore the operation energy is lower in order to increase this contrast. The images produced by STXM at 500 eV show good absorption contrast over the bodies of the nuclei (fig. 6.26) and shows details such as dark patches in some of the nuclei which could be due to more dense regions of DNA.

The details of the chromosome image is currently better than what we have seen with ptychography. The nuclei measurements from STXM and ptychography show similar levels of detail. Comparing the nucleus cluster measured here with those measured at I-13 (fig.6.7 and 6.8) we can see different levels of contrast coming from the different nuclei and various changes in contrast over the body.

The absorption contrast of the STXM image, whilst showing similar levels of detail, cannot be used to calculate quantities such as electron density but can be related to mass thickness. Absorption contrast is far more useful in mapping chemical specificity of the object by scanning over a range of energies around the absorption edge of an element of interest. For chromosomes and nuclei which are mainly carbon with platinum staining we are more interested in the macroscopic structural information such as the density and thickness rather than the chemical specificity.

6.6 Summary

Synchrotron radiation provides a brilliant, partially coherent source which is critical to the technique of ptychography. Lensless imaging methods can be performed on beamlines that are optimized for their coherent properties and provide a stable source.

Ptychography experiments have been performed at the coherence beamlines I-13 and 34-ID-C. These experiments have produced images of chromosomes and nuclei where features seen in the images match information seen in light microscopy and SEM images of the same region of

interest. However, there are evident artifacts in the images produced by ptychography. These artifacts come both from the experimental set-up and the phase retrieval algorithms. Whilst it is difficult to ascertain what are the causes of the artifacts there are certain factors which are large contributors. The stability of the illumination causes artifacts in the probe and in the background of the images. The central area blocked by the beamstop has been seen to cause artifacts in the amplitude images if not corrected.

Extra constraints and adjustments are added to the basic algorithms in order to improve the solution and the requirements were different depending on the data. In performing the reconstructions we have found there is no single recipe for ptychography phase retrieval that works for every single data set. Despite the difference in the constraints used the images of chromosomes and nuclei show similar artifacts in the amplitude images of strong contrast over the border surrounded by halos. Phase shift can be seen over the body of the nuclei but in the chromosome reconstructions the phase contrast can only be seen at the boundary of the object.

The resolution of these experiments is not sufficient to see any higher order chromosome of nucleus structure above the gross morphology. The resolution was calculated to be 160 nm at 34-ID-C which is below standard fluorescence microscopy but not yet near the potential resolution of lensless imaging methods. The resolution at I-13 is estimated to be 326 nm, which is comparable to fluorescence microscopy. Scattering from the sample may have been measured to higher resolution, but was not detectable above the level of the window scattering.

In both experiments the test objects could not be fully reconstructed to a high resolution and contained several artifacts which were caused by problems in the experimental set-up. At 34-ID-C the test objects could not be reconstructed to sufficient quality at 5.5 keV therefore it can be assumed that any higher order structure effects seen in the chromosome and nuclei images are not caused by the sample. Many of the artifacts were solved in the experiment at cSAXS due to the stability of the set-up and the removal of the beamstop.

In terms of spatial resolution the ptychography methods have been out performed by Scanning Transmission X-ray Microscopy when applied to chromosomes. The energy range of this technique is sensitive to the absorption contrast than the phase contrast, but the absorption contrast showed details in the chromosomes so far unseen in the ptychography experiments. The ptychography performed at cSAXS gave promising phase contrast in imaging nuclei. The resolution at cSAXS was greater than previously seen at I-13 and 34-ID-C. The amplitude images showed several ringing artifacts but the phase and probe were reconstructed showing very few obvious artifacts.

A brief test of radiation damage shows that the diffraction pattern changes in energy with increased incident flux on the sample. The intensity at high angles decreases at a slightly more

rapid rate than low angles. The nucleus used in the radiation damage test had previously be imaged by ptychography therefore had already been exposed to damage, therefore it is unlikely that the extent of the damage effect on the pattern is seen in this experiment.

Chapter 7

Quantitative Ptychography of Nuclei and Chromosomes

The content of the nucleus changes during the cell cycle as the cell performs its function and prepares to divide. During the cycle the amount of DNA inside the nucleus is doubled and there are numerous transfers of proteins across‘ the nuclear membrane. It is difficult to obtain a precise measure of nuclear mass so it is not known if there is a large variation of mass between cells or cell divisions. Furthermore the environment, health of the cell and cell type may all affect the nuclear mass.

Fluorescent tagging can provide information on the presence and movements of specific proteins and the amount of DNA present. Cells can also be sorted by their volume using the technique of flow cytometry however neither of these methods give information on the nuclear mass. A 2D projection image taken with ptychography gives the phase shift through an object which provides a direct measurement of the mass density. Integrating the mass density over the nuclear area then gives a good estimate of the nuclear mass.

The mass is also a useful variable to monitor in the case of the chromosome. Comparing the mass of the chromosomes can be used to form a karyotype in a method similar to flow cytometry where the chromosomes are ordered by the total number of base pairs they contain, which is a mass argument (see section 4.3.2.1). Using mass to karyotype the chromosomes would take into account not only the sequenced and unsequenced DNA but also the protein contribution. Comparing the mass of the chromosomes to an estimate of the mass the DNA content from the flow cytometry measurements may give an indication of how much protein is in each chromosome. Producing a mass karyotype of human chromosomes has been achieved from electron microscopy [171].

This chapter discusses the measurements of phase shift through chromosomes and nuclei imaged by ptychography and makes an estimate of their volume and area. These measurements are compared to volumes measured of the same sample with confocal microscopy. A ptychography experiment using a laser source is performed on a spread of chromosomes to explore how mass calculations from a 2D projection image could be used to perform a karyotype. These measurements are a first step towards finding the structure of chromosomes by ptychography.

7.1 Quantifying the phase shift

The advantage of using ptychography as an imaging techniques is that quantitative phase information can be obtained. This phase information is related to the electron density in the material. The electron density is related to mass density, and when integrated over the area of an object can provide a good estimation of the mass.

The phase shift through a point (x, y) in a 2D projection image is related to the mass density $\frac{dm}{dxdy}$ by:

$$\phi(x,y) = \frac{2\pi\delta(\rho)}{\lambda\rho}\frac{dm}{dxdy} \tag{7.1}$$

The real part of the refractive index $\delta(\rho)$ is proportional to ρ so can be cancelled by the ρ in the denominator. In this case the refractive index can be calculated for an arbitrary density which is advantageous in the case of the nucleus where we can only estimate these two quantities. In order to obtain the mass of the nucleus from the image the phase shift is integrated across its area:

$$m = \int dm = \frac{\lambda\rho}{2\pi\delta(\rho)}\int\int \phi(x,y)dxdy \tag{7.2}$$

The image is discrete therefore the integral can be reduced to the following sum:

$$m = \frac{\lambda\rho}{2\pi\delta(\rho)}\sum \phi_n \times p \tag{7.3}$$

where p is the pixel area, ϕ_n is the phase shift per pixel.

The average phase shift can be found by normalizing the total phase shift across the total number of pixels in the area of the nucleus N:

$$\phi_{av} = \frac{\sum \phi_n}{N} \tag{7.4}$$

These quantities are calculated for the nuclei imaged with ptychography and compared as part

of a preliminary investigation into nuclear mass.

The mass of the chromosomes could not be obtained from the images taken at 34-ID-C because there was insufficient phase shift to be able to separate the chromosomes from the surroundings. There are also several artifacts in the images of chromosomes which are likely to affect the mass calculations. The images obtained at I-13 also show a weak phase shift in the presence of chromosomes, but again this is too weak to analyze and it is unknown whether it is a contribution from one or more chromosomes (see fig. 6.8). To attempt to measure the mass of chromosomes with ptychography an experiment was undertaken by Ephanielle Verbanis using a laser-source ptychography set-up. SHe also performed the confocal microscopy measurments. The aim of the experiment was to establish if measuring the mass of chromosomes was possible with laser-source ptychography and to provide a preliminary experiment to the X-ray set-up. All analysis of the results of the laser ptychography and confocal measurements was done by the author.

In using the visible light source there is a small change to eq. 7.1 to take into account the refractive index of the background n_0 :

$$\phi = \frac{2\pi(n - n_0)}{\lambda\rho}\frac{dm}{dxdy} \tag{7.5}$$

where n is the refractive index of the material. In our experiment the background is air, therefore $n_0 = 1$. In the case of visible light the excess density, i.e the difference between the density of the material and the background, is proportional to $n - n_0$. For the case of an object in air the density of the material will be proportional to $n - 1$ allowing this to be cancelled by the density in the denominator. As in the case of x-rays the mass of the chromosomes is found by integrating the phase shift over the area (see eq. 7.2).

In order to calculated the absolute mass for these materials an estimate of the density and the refractive index is made. Even though these two quantities are proportional the proportionality factor is still used in finding the mass. In the case of X-rays the δ can be calculated for an arbitrary density from the Henke tables, using the CXRO online tool [39]. In the case of visible light an estimate of the refractive index is taken from an experiment DNA microfilms of $0.5-5$ μm thickness [172]. We use this experiment to provide an estimate of the refractive index for chromosomes by estimating them as totally composed of DNA and to be approximately 1-2 μm thick. The value of refractive index for a film of 1.5 μm thick was $n = 1.54$ and was used as our estimation of refractive index for chromosomes. This refractive index was measured using a wavelength of 632.8 nm. In order to karyotype the chromosomes we are principally concerned with their relative mass and not absolute mass, therefore the estimates of refractive index and density do not need to be considered

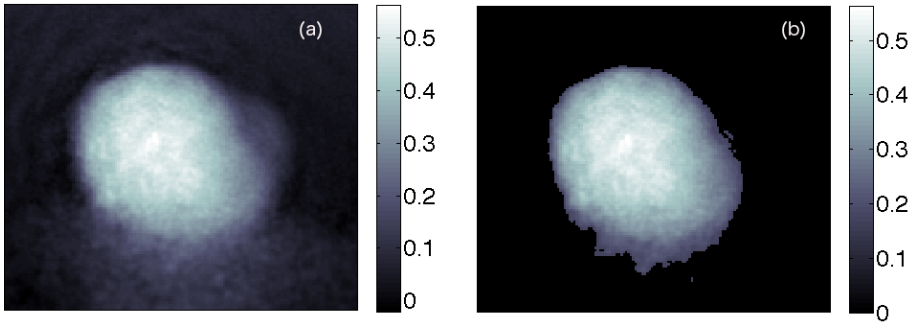

Figure 7.1: (a) A cropped area of a phase reconstruction from cSAXS showing a single nucleus from scan S000335 (b) The nucleus isolated from the background after the threshold was applied. The phase shift through the nucleus was then integrated over its area. An estimate of the volume of the nucleus was calculated from the integrated phase shift.

because they are constant factors.

7.2 Phase Analysis Nucleus

Phase shifts were measured through isolated nuclei from images obtained at I-13, 34-ID-C and cSAXS, some examples of which are shown in Chapter 5. The images used in this analysis contained a nucleus that had sufficient phase shift across the body to be separated from the background. It was not possible to perform this separation on chromosome reconstructions from 34-ID-C which only showed strong contrast at the boundary of the object. All phase measurements were done on a single nucleus except for some of the reconstructed images from cSAXS that show a pair of nuclei clustered together (see fig. 6.24). As the nuclei were difficult to separate by segmentation the mass and phase shift was calculated for the pair.

The phase shift measured by ptychography is relative to the background, therefore in order to gain an absolute measurement the background contribution must be subtracted. The background level is decided by taking a histogram of the phase in the image and fitting a Gaussian to it using the Curve Fitting Toolbox in MATLAB. The mean value of the phase taken from the Gaussian fit was used as the background phase. After the background subtraction, the body of the nucleus was separated from the surrounding area by setting the phase values under a threshold to zero. This threshold was chosen as the limit to clearly separate the nucleus body from the surroundings. The δ is calculated for stained DNA from the Henke tables, using the CXRO online tool [39]. For simplicity the nucleus was considered to be entirely stained DNA for which an empirical formula was estimated. The empirical formula for DNA was taken from the literature to be $H_{16}C_6N_4O_{10}P$ [173], to which a contribution from the Platinum dye is added. The dye used in the following experiments was PtBlue which stains through minor groove binding. The binding ratio of this dye

is not known therefore to approximate the binding of PtBlue we use the known binding ration of Pt(terp)Cl which has a similar chemical structure as a monomer of PtBlue (see section 5.2). The dyes have an approximate binding ratio of 1 Pt atom per 2.5 base pairs, therefore stained DNA is about 40% Pt atoms. The δ of the stain was calculated using the CXRO online tool using an empirical formula of $H_{16}C_6N_4O_{10}PPt_{0.4}$[39].

Uncertainty in the measurement were calculated by changing the threshold values by $\pm 1\%$ and looking at the change in the area considered for integrating the phase shift over. This error in the integrated phase was then taken through the calculation to give an error on the mass measurement.

Table 7.1: Measurements of area, average phase shift and mass of nuclei measured with ptychography at 34-ID-C, I-13 and cSAXS. A * marks measurements from twin nuclei, these values contain the contribution from both. Measurements from confocal and standard light microscopy are compared where possible.

Beamline	Scan no.	Pixel size [μm^2]	Area [μm^2]	Average Phase Shift [rad]	Mass [pg]	Area with LM [μm^2]
34-ID-C	S098	1.4×10^{-3}	25.414 ± 1.06	0.0766 ± 0.002	10.4 ± 0.2	38 ± 2
	S099		13.340 ± 0.63	0.1232 ± 0.001	8.7 ± 0.2	15.7 ± 0.6
I-13	14933	3.6×10^{-2}	23.6 ± 0.3	0.2929 ± 0.004	67 ± 2	37 ± 3
	14939		42.1 ± 2.4	0.2530 ± 0.008	104 ± 3	58 ± 2
	14948- area 1		49.6 ± 3.9	0.1070 ± 0.004	54 ± 2	63 ± 3
	14948- area 2		37.5 ± 2.1	0.1362 ± 0.004	48 ± 1	55 ± 2
cSAXS- 192×192	S00319	1.9×10^{-3}	23.8 ± 0.8 *	0.3481 ± 0.006*	48.9 ± 0.7*	-
	S00325-area 1		26.0 ± 4.2 *	0.3799 ± 0.010*	60.3 ± 0.2*	-
	S00325-area 2		10.1 ± 0.6	0.3607 ± 0.011	21.4 ± 0.2	-
	S00335		23.7 ± 0.7 *	0.3391 ± 0.006*	47.4 ± 0.7*	-
cSAXS- 512×512	S00319	2.7×10^{-4}	22.2 ± 0.3 *	0.3711 ± 0.007*	48 ± 1*	-
	S00325-area 1		26.0 ± 1.6*	0.3382 ± 0.010*	47 ± 2*	-
	S00325-area 2		8.8 ± 0.6	0.3547 ± 0.011	16.8 ± 0.8	-
	S00335		23.5 ± 0.8*	0.3562 ± 0.006*	49.7 ± 0.8*	-

7.2.1 Results- Phase Analysis of Nuclei

The area, average phase shift and mass are shown for nuclei measured by ptychography on the three different experiments at 34-ID-C, I-13 and cSAXS in table 7.1. For the images taken at cSAXS where the nuclei could not be separated with segmentation, the area, phase shift and mass calculations are taken over both the nuclei and are denoted with a (*). The measured average phase shifts through the individual nuclei are in the range of $0.08 - 0.29$ rad, and the twin nuclei show a phase shift in the range $0.34 - 0.38$ rad which is a approximately double the average phase shift through a single nucleus. All the measurements of the different beamlines fall near the same value, and can be measured by ptychography independently of the experimental set-up.

The mass of sequenced DNA gives 3.5×10^9 bp in the entire genome. During the G2 step of interphase and mitosis there are four copies of the DNA giving the total number of base pairs in the nucleus by 14×10^9 bp. A single basepair has the mass of 650 a.m.u., therefore the total weight of the DNA inside the nucleus can be approximated to $14 \times 10^9 \times 650 \times 1.67 \times 10^{-24}$g which gives 15.2 pg. With the addition of the mass of water and proteins this number is comparable to the masses calculated in table 7.1.

Compared to the other experiments, nuclei measured at 34-ID-C have an integrated phase shift and mass in the low end of the previously stated range. There is a large difference between phase shifts and areas of the two nuclei measured at 34-ID-C, with the phase shift of nucleus S098 has approximately half of the phase shift and double the area of S099. The observations of phase shift and area further support the idea that S098 is less thick and more spread out than S099 which matches images taken with SEM (discussed in section 6.4.3.3). The calculated masses show good agreement, however due the ringing artifacts in the ptychography images these results should not be considered and are included in the table for completeness.

The phase shifts through the nuclei measured at I-13 are at the high end of the range of phase shifts for an individual nucleus. They are also more than twice as large in area and mass than nuclei measured at the other beamlines. Even though the sample preparations are all made from the standard protocols (see section 5.1) and cell culture, the cells used in I-13 were not taken from the same cell culture batch as 34-ID-C and cSAXS, which would account for the difference in area and mass between these nuclei and those measured at the other beamlines.

The area measured by ptychography was validated by comparison to measurements taken from visible light microscope images for I-13 and confocal images at 34-ID-C. The measurements of area from these images are larger than the measurements obtained with ptychography. The areas found by visible light and confocal microscopy are larger than the X-ray determined values for the same

nuclei.

There are no light or confocal microscope images to verify the mass and area calculations from images taken with ptychography at cSAXS however measurements of phase are repeated over the same nuclei in reconstructions from a 192×192 array and 512×512 array. The data entries in table 7.1 marked with a star show twin nuclei which have approximately double the area and volume of the single nucleus. Scans S00319 and S00335 are of the same nucleus and the measurements resulting from these images show good agreement in area, mass and average phase shift. The reconstructions from cSAXS had the largest average phase shift of any measurements taken. The calculated mass also agrees between different reconstructions. However, there is a large discrepancy in the measurements of S00325 from a 192×192 array and a 512×512 array which is not seen for S00319 and S00335. This discrepancy in the measurement could be caused by the ringing effect in this image obscuring the boundary of the nucleus. In the high resolution image from the 512×512 array, the boundary between nucleus and background is better defined than in the 192×192 array case resulting in a more accurate measurement of mass.

7.2.2 Discussion

All the nuclei measured were prepared by the same sample preparation protocol. The nuclei measured at cSAXS and 34-ID-C come from the same cell culture batch but the samples measured at I-13 come from a different cell culture batch. It is expected that the nuclei measured at cSAXS and 34-ID-C will have similar morphology. The disagreement in mass and area measurements between images taken at the two beamlines is caused by the poor quality reconstructions from 34-ID-C. These reconstructions have weak phase contrast and include many artifacts which will affect the measurements of mass and area.

The areas measured by light microscopy methods are much larger than the areas measured by ptychography, even taking into account measurement errors. This might be explained by an over-estimation due to the halo effect in the visible light images. The confocal microscope does not produce such a halo in the images and still measures an area larger than seen by ptychography. It would be expected that a 2D projection image taken by ptychography would give the same area as those taken with confocal or visible light microscopy. This disagreement in measured area could partially to be due to the edges of the nuclei being very thin and therefore not causing enough phase shift to be registered above the background which would result in a loss of measured area. In some reconstructions the broken boundaries regions make it difficult to set an area to measure over resulting in an underestimate of area.

The nuclei measured at I-13 have much larger areas and mass than seen at cSAXS and 34-ID-C.

The light microscope images of the nuclei measured at I-13 give an area approximately 1.5 times bigger than the ptychography experiments. The expansion of the nuclei could be caused by the drying step in the sample preparation protocol (see section 5.1). Humidity can effect the spreading of chromosomes, therefore it is likely that this has an effect on the nuclei that are produced by this preparation [141].

The nuclei will contain some quantity of water. In measuring the nuclei a dried state only the contribution of DNA and proteins will be counted. The sample preparations used air drying so there is still likely to be an unknown quantity of water that will contribute in the mass measurement. In future preparations careful drying methods such as critical point drying and freeze drying may be used to remove the water content however a complete dehydration may not be possible.

During the cell cycle the nucleus goes through many changes where components are lost, such as the disappearance of the nuclear membrane, and parts are added, such as the replication of the DNA (see section 4.2). These changes may appear at the macroscopic structural level as a change in mass therefore there is a potential for using ptychography to monitor the progress of a nuclei through the cell cycle. We have seen that ptychography is sensitive to changes in phase shift through the nucleus and a mass can be calculated from this. From the range of masses we have measured here it is likely that the sensitivity of the technique should be sufficient to see the doubling of DNA that would occur at the replication stage but the quality of the reconstructions would have to be improved significantly in order to detect small changes to the volumes. Currently we do not have enough examples of nuclei measured in the same experiment to establish the level of mass variation between the states. An example of quantitative analysis of phase shift has been used with a visible light ptychography microscope to see the division of cancer cells [174]. It was found in this study that the phase shift from the cell increases as the cell is about to divide. This is due to the this increases in cell thickness as the cell undergoes division, (here the area of the cell reduces but the volume remains constant), and therefore produces a greater phase shift. The structural changes in the nucleus during the time of division could be observed with X-ray ptychography.

7.3 Phase Analysis of Chromosomes

The laser-based ptychography set-up was successful in generating an image of a spread of chromosomes with sufficient resolution to see isolated chromosomes. We aim to produce a karyotype from the mass of the isolated chromosomes which can be verified by using two further imaging methods of Multicolour Fluorescence in-situ hybridization and confocal microscopy. M-FISH is a

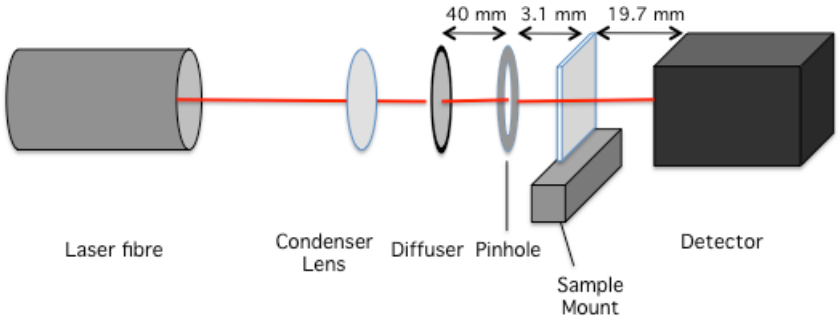

Figure 7.2: Ptychography with a laser source. A laser of 409 nm produces a beam incident on a diffuser used to increase the numerical aperture providing higher resolution. A condenser lens is used to focus the light onto a diffuser which is used to increase the numerical aperture of the system. A 1 mm pinhole is used to select out a region of the diffused beam. The sample is placed on a mount that can scan perpendicular to the beam face. The diffraction patterns were collected by sCMOS detector.

fluorescence microscopy method to identify the individual chromosomes in the spread measured by ptychography. The chromosome spread is then imaged by confocal microscopy and the volumes can be compared to the estimated mass. The chromosomes are sorted in terms of mass and are compared to a karyotype of human chromosomes produced by flow cytometry taken from the literature.

7.3.1 Ptychography using laser light

In order to perform ptychography the source must be coherent and able to penetrate the sample, therefore for thin, semi-transparent samples, ptychography can be performed with a laser source. Using a laser source for ptychography has the advantage that the source illumination is extremely stable, and is fully spatially and temporally coherent. The resolution of ptychography is wavelength limited therefore the achievable resolution with laser light is less than X-ray ptychography. Practically, the largest constraint on the obtainable resolution with laser ptychography is the numerical aperture given by the detector.

Ptychography was performed on chromosomes using the following set-up, a laser source of wavelength $\lambda = 409$ nm was incident on a diffuser of one degree, from Thorlabs, placed before a 1 mm pinhole (fig. 7.2). The diffuser was used to increase the numerical aperture by extending the angular divergence of the beam and therefore increase the obtainable resolution. The probe was selected with a 0.5 mm diameter pinhole placed 40 mm downstream of the diffuser. The sample was placed 3.1 mm from the pinhole, on Newport translation stages that scanned perpendicular to the beam. A Round ROI scan was used with a field of view of 1 mm and step size of 0.1 mm. The detector was an sCMOS CCD produced by Andor, with a chip of 2048×2048 pixels, each of size 6.5 μm^2 and was placed 19.7 mm downstream of the sample.

The probe could not be reconstructed directly from the chromosome sample therefore a test

object of tissue was used to retrieve the probe. This probe was then used as a starting guess for the chromosome reconstructions. The code used to retrieve the phases was written by Fucai Zhang and performs the ePIE algorithm. The algorithm converged after 100 iterations and no extra constraints were used. To calculate the mass of the chromosome from the retrieved image, the isolated chromosome was cropped from the spread. The background phase is subtracted from the cropped area. A threshold was applied to separate the chromosome from the surroundings. The phase was then summed over the area of the nucleus and the mass was calculated from this value using eq. 7.5.

The chromosomes were prepared from standard cell culture techniques described in section 5.5.1. A drop of methanol acetic acid suspension was dropped on to a glass slide and allowed to air dry. The chromosomes were stained with 0.1 μg/l DAPI and the quality and density of the chromosome spreads was checked with a Zeiss Axio-Z2 fluorescence microscope. Fluorescence microscopy was used to find the location of spreads of chromosomes which contained the most isolated chromosomes. The positions of these spreads was recorded with the fluorescence microscope. The translation stage of the ptychography set up was calibrated to the stage of the fluorescence microscope so the positions of the chromosomes spreads could be retrieved and these spreads to be imaged with ptychography.

7.3.2 Multicolour Fluorescence in-situ hybridization (M-FISH)

M-FISH was performed on the sample to identify the chromosomes in the spread. The M-FISH protocol used in this experiment can be found in section 5.5.2.

A detailled explanation of M-FISH can be found in section 4.3.2.1 but using this method to karyotype chromosomes is briefly restated here. Fluorescent dyes are covalently attached to fragments of sequence extracted from the chromosomal DNA which are then hybridized to the spread. These dyes have an affinity to different genetic sequences so each chromosome is labelled with a different combination of paints. The dyes are excited by and fluoresce at different wavelengths. The fluorescence from chromosome spread is viewed through a series of wavelengths and each chromosome has a unique fluorescence pattern from the dyes that mark it. The chromosomes are sorted into a karyotype from this fluorescence code. This method is sometimes referred to as spectral karyotyping.

7.3.3 Confocal Microscopy

The volumes and areas of the chromosomes were measured with an Olympus LEXT-OLS4000. The volumes of the chromosomes were measured in two ways, the first, which will be referred to as Confocal method 1, used the software package from the microscope to threshold an area from the background by height and then measure the volume in that region. The second method, which will be referred to as Confocal method 2, integrates the measured height over the area of the chromosome.

7.3.4 Flow Cytometry

Flow cytometry is discussed in detail in section 4.3.2.1 and will be briefly stated here. The flow cytometry method the chromosomes are stained by two dyes that fluoresce at different wavelengths. Chromosomes are streamed in a buffer under a laser source that excites the dyes, and a detector which measures the amount of fluorescence. The measured fluorescence is used to calculate the number of base pairs the chromosomes contain. The number of base-pairs is then used to sort the chromosomes into a karyotype. The number of base-pairs is a mass argument and can provide a comparison to the mass measured by ptychography. This technique is referred to as Fluorescence Activated Cell Sorting (FACS).

7.4 Results

7.4.1 Ptychography images

The phase and amplitude images show the spread at sufficient resolution to be able to distinguish isolated chromosomes on the edges of the spread (fig. 7.3(a)-(b)). There is contrast between the chromosome and the background of the image in both the phase and the amplitude. There is a slightly higher background of phase around the chromosomes that may be due to the phase shift coming from the nucleoplasmic layer (see section 5.3). This is further supported by the confocal microscopy image in fig. 7.5. The amplitude image has slightly more contrast at the borders of the object than in the centre. The chromosomes appear larger in the amplitude image than in the phase and some halo effect can be seen around the image. Unlike an X-ray source, where the phase contrast is much stronger than the amplitude contrast, a chromosome provides about equal amplitude and phase contrast from a laser source. In the ptychography images there is no strong artifacts or weak contrast over the body of the chromosomes in the amplitude images as is seen for X-rays (see section 6.4.3.2).

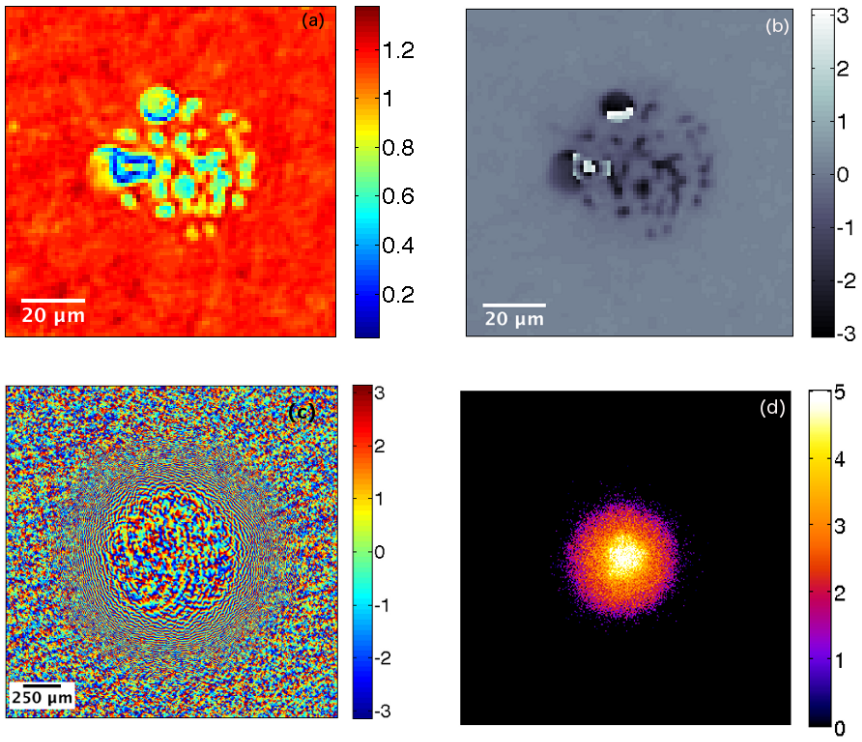

Figure 7.3: (a) Amplitude and (b) phase image of a chromosome spread reconstructed using the ePIE algorithm from a ptychography dataset produced by a laser source. (c) The phase of the reconstructed probe . (d) The diffraction pattern from the sample and the diffuser shown on a logarithmic scale. The pixel size in this image is 0.6 microns.

The probe shows the individual speckles from the diffused laser light (fig. 7.3(c)). The complexity of the probe does not limit the reconstruction as the images do not contain artifacts coming from the probe. The source is stable therefore there are no illumination drifts during the scan that can produce artifacts in the image. The probe is much larger than the spread shown which has been cropped from the full field of view. Despite the size of the probe the oversampling is sufficient to be able to retrieve the image using ptychography.

The maximum resolution of the set-up is comparable to the size of the chromosomes. Due to the resolution limit the area covered by the isolated chromosomes in the final reconstructions is only four or five pixels in size and where the chromosomes are close together it is difficult to distinguish between individuals. The small area from the few isolated chromosomes is sufficient to calculate the phase shift through the chromosomes.

7.4.2 M-FISH Images

In the M-FISH images (fig. 7.4) the colour of the individual chromosomes is computer generated. from a coding scheme that involves various pairs of five dyes. As each chromosome pair has a different colour under this coding, it can be used to produce the karyotype. In the karyotype

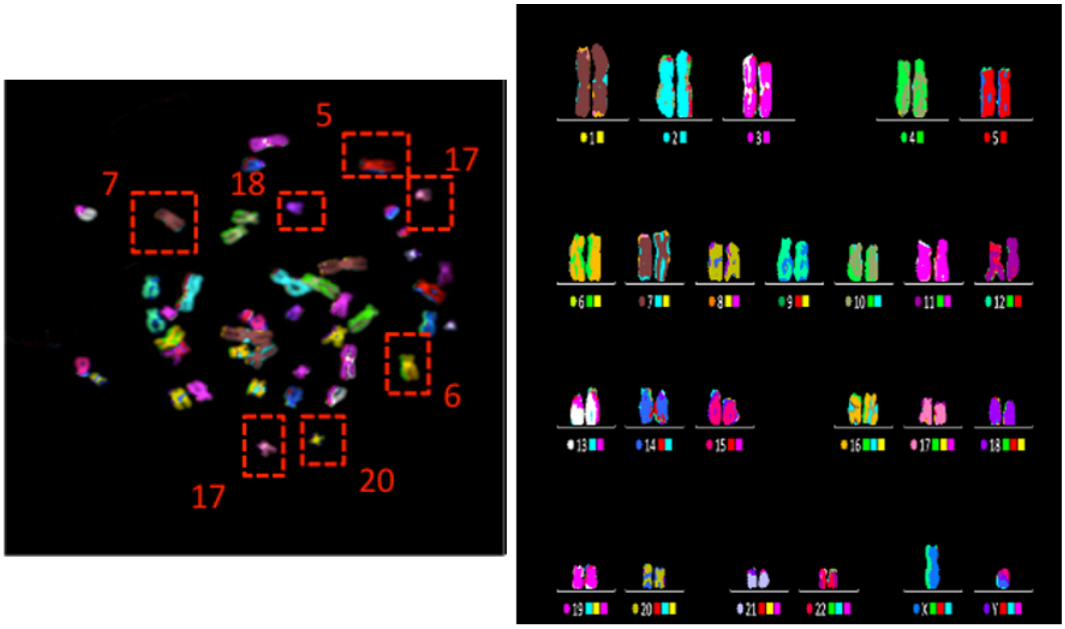

Figure 7.4: (a) M-FISH image of the spread measured by ptychography. The colours of the chromosomes represent the fluorescence pattern from the multiple dyes that label each chromosome. Each chromosome has a unique colour which allows them to be sorted into a karyotype. (b) The karyotype shows the pairs of chromosomes and their number. The dot on the left hand side of the number represents the colour of the chromosomes and the coloured squares represent the fluorescence combination observed to obtain that colour.

the chromosome number is shown under the chromosome pair, and on the left of the number, a coloured spot indicates the expected result for this chromosome after M-FISH has been applied (fig. 7.4). As described in section 7.3.2, the resulting colour is a combination of the fluorescence of several dyes, the squares on the right of the number indicate the colours that are used to make up the colour on the right. For example chromosome 9 has a green circle on the left which matches the colour of the resulting chromosomes, on the right of the number there is a red and yellow square which represent the fluorescence of the two dyes used to make this colour.

The M-FISH was only partially successful as chromosomes 1 and 12 do not show their expected colour. The incorrect colouring can be caused by the bleeding of the multiple dyes used in M-FISH. A second factor is the performance of the hybridization step which can impeded by the proximity between chromosomes. These chromosomes were stained with DAPI before the M-FISH was performed which could result in the blocking of binding sites therefore the hybridization could not bind well.

The karyotype is represented faithfully as the majority of expected colours were present. The chromosomes where the dyes did not give the correct colour are positioned in the karyotype by their size, chromosome 1 is always the largest chromosome, leaving the other gap to be filled by chromosome 12. The isolated chromosomes in the ptychography image are indicated with a red

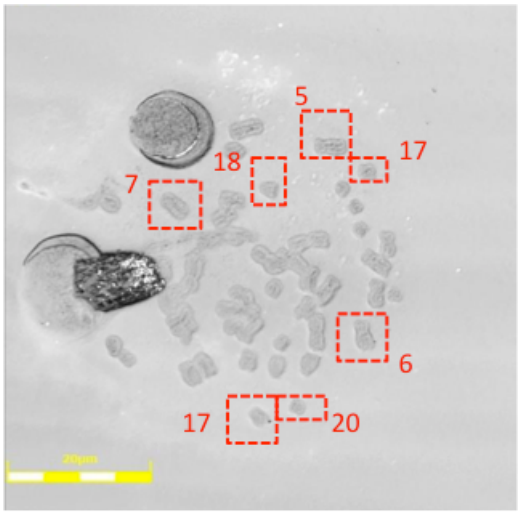

Figure 7.5: Confocal microscope image of the same spread imaged by ptychography. The chromosomes identified by M-FISH and isolated in the ptychography image are identified in red boxes. The volumes and areas of the chromosomes were measured with confocal microscopy and compared to the volume measurements calculated by ptychography .

box and their number, did give the expected colours therefore can be assumed to be correctly identified.

7.4.3 Confocal Microscope Images

The confocal image of the same chromosome spread (fig. 7.5) imaged with ptychography shows the individual chromosomes with sufficient resolution to see details such as the chromatids and nucleoplasmic layer. The chromosomes isolated in the ptychography image are shown in red boxes with their chromosome number as identified by M-FISH.

7.4.4 Phase analysis of Chromosomes

The mass of chromosomes measured by ptychography are given in table 7.2. Due to the small area which the mass calculation the choice of threshold and background values must be carefully made as the addition of a single pixel to the selected area can dramatically change the mass estimation. To take this into account the mass are calculated by taking the mean of the mass calculated for a $\pm 1\%$ change in threshold value.

The value of the absolute mass is highly dependent on the value of the refractive index used. The value of the refractive index, $n = 1.54$, was experimentally found using a wavelength of 638 nm [172]. These value is dependent on the wavelength of the incident light therefore the DNA is likely to have a different refractive index at the wavelength used in this experiment of 409 nm. Early studies on DNA films by Inagaki et al. show that the refractive index of DNA at 621 nm is $n = 1.61$

Chr no.	FACS	Mol. Weight (Mbp)	Ptychography mass [pg]	Confocal Vol 1 [μm^3]	Confocal Vol 2 [μm^3]
5	0.621	181	6.0 ± 0.3	0.9 ± 0.2	3.6 ± 0.4
6	0.593	171	5.1 ± 0.3	1.1 ± 0.2	4.1 ± 0.4
7	0.549	159	7 ± 1	1.1 ± 0.2	4.5 ± 0.5
17	0.294	81	3.7 ± 0.2	0.36 ± 0.08	1.9 ± 0.3
17	0.294	81	2.3 ± 0.3	0.42 ± 0.09	1.9 ± 0.2
18	0.283	78	4 ± 1	0.43 ± 0.09	2.0 ± 0.3
20	0.231	63	2.68 ± 0.09	0.31 ± 0.08	1.6 ± 0.2

Table 7.2: Chromosome mass found with ptychography, and the volume found confocal microscopy methods are compared with the numbers for these chromosomes found from flow cytometry. FACS refers tot he relative fluorescences measured by flow cytometry. The number of base pairs from sequencing is shown in the column Molecular weight. The values of molecular weight are from reference [153]. The chromosome numbers are shown in the first column and are identified from the chromosomes measured by M-FISH

and the refractive index at 414 nm is $n = 1.59$, which is a small change over this wavelength regime [175]. However, there is a difference between the refractive inex values found by Inagaki et al. and Samoc et al. at around $\lambda \approx 600$ nm possibly due to the difference is DNA preparations and thicknesses. This suggests that the refractive index of DNA is experimentally difficult to ascertain, therefore the mass calculations performed here are likely to be an approximation of the actual mass.

The masses calculated from ptychography are compared to values of the fluorescence from specific chromosomes measured by flow cytometry. As these measurements can be directly related to the number of base pairs in a chromosome they are related to a mass measurement. The relative fluorescence as measured by the flow cytometry experiment shown table 7.2 under the title FACS. The values of fluorescence from FACS for chromosomes from a human female are taken from [176].

The volumes in column Confocal 1 and Confocal 2 refer to the volumes measured by confocal microscopy using the two different methods (section 7.3.3). As volume is linear related to mass we can treat this measurement again as a mass-related measurement. The two methods of measuring the volumes by confocal microscopy disagree strongly in value, with the method of confocal 1 being approximately 4 times smaller than confocal 2. However, the relative volumes of the chromosomes agree between the two methods, for example, in both methods chromosome 6 and 7 are measured to be larger than chromosome 5. The volumes found by ptychography again do not agree with the volumes taken by either of the confocal methods, however this measurement is heavily dependent on the value of refractive index used which is unknown for a chromosome therefore, it is more important to look at the relative volumes of chromosomes measured by this technique.

In order to compare the 5 sets of mass values from the fluorescent dyes, ptychography and confocal measurements, the masses for each method are scaled to chromosomes 5. The chromosomes

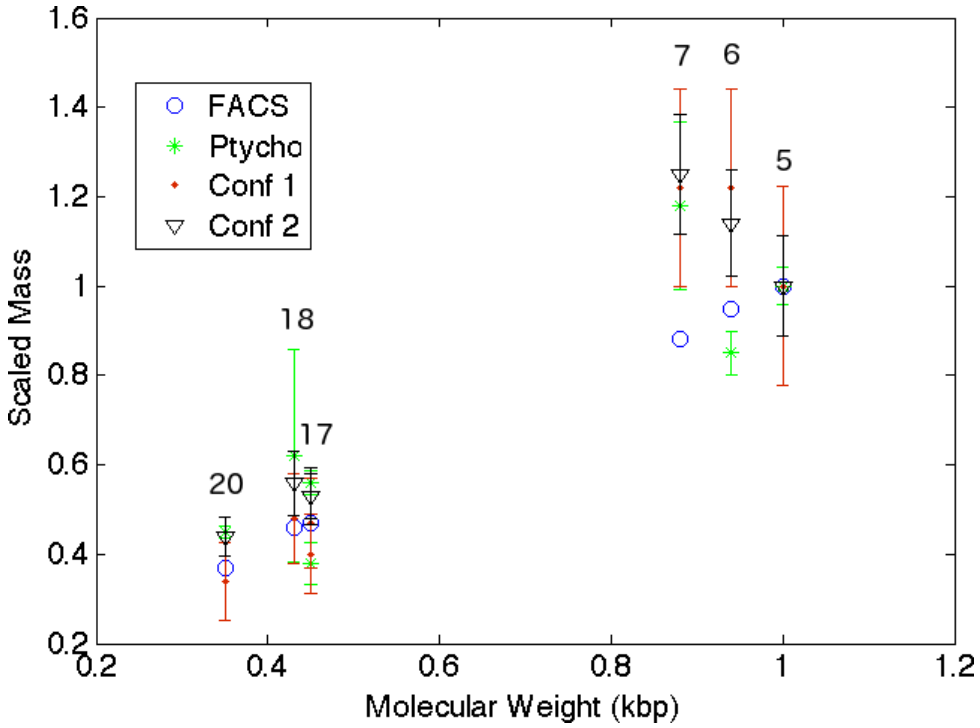

Figure 7.6: The mass-related values found by the various methods outlined in table7.2 are shown against chromosome number. These masses are scaled relative to the mass of chromosome 5, the largest chromosome measured. The blue circles show the scaled fluorescence of FACS. Scaled mass results from ptychography are shown by green stars. The scaled volumes from the confocal methods 1 and 2 are shown by the filled red dots and black triangles respectively.

are traditionally karyotyped in order of length with chromosome 1 being the largest and the Y sex chromosome being the smallest, therefore the masses of the chromosomes can be scaled relative to the largest one.

These masses are compared to the molecular weight of chromosomes, which is the number base-pairs in a chromosome found by sequencing methods, measured in a unit of kilo base pairs (kbp), where one base pair weighs approximately 650 a.m.u. The values are taken from a data based developed by the Wellcome Trust Sanger Institute [153]. The molecular weight provides a reference to compare the measurements of the mass because it is a well documented mass argument from which chromosomes can be accurately identified. As the chromosomes measured by ptychography and confocal microscopy have been sorted using M-FISH, a mass measurement for a particular chromosome can be compared to its known molecular weight. The comparison of the relative volumes for the chromosomes measured in table 7.2 is shown in fig. 7.6.

The flow cytometry experiment has been used to karyotype the entire 46 human female chromosomes, however, fig.7.6 shows only the values for the chromosomes that were measured in the ptychography experiments. The information from flow cytometry can be used successfully perform a karyotype, therefore we can use it as a guideline to compare the measurements of mass taken

with ptychography and confocal microscopy respectively.

The mass measured in the confocal and in the ptychography experiment show that mass decreases with decreasing molecular weight. For the chromosomes with the lowest molecular weights, numbers 17, 18 and 20, the measurements of mass show the strongest agreement with the mass measured by flow cytometry. For example the range of relative masses of chromosome 20 across all methods is 0.08. For the larger chromosomes, numbers 6, 7, the range of relative masses is much larger at 0.29. The volumes found for the larger chromosomes do not show as good an agreement with the flow cytometry results as chromosome 7 is measured to have a larger mass than chromosome 5 by all of the methods. Chromosome 6 is measured to be larger than chromosome 5 by the confocal methods but not by ptychography. Without any data for chromosomes between $7-17$ we cannot assume that mass decreases linearly with molecular weight.

In the spread studied here, two isolated chromosomes, identified as chromosome 17 were measured. The mass measured by ptychography and confocal microscopy show a large difference between the two members of the chromosome pair. However, the average of these masses has good agreement with flow cytometry.

7.5 Discussion

There is a general agreement among all the methods that the mass decreases with molecular weight however there is too little information to verify a linear trend. In [176] a strong linear trend is shown from the flow cytometry, however without any data for chromosomes between $7-17$ we cannot assume the trend is linear for the other measurement techniques. For the smaller molecular weights the mass measured with ptychography and confocal microscopy show a better agreement to the flow cytometry results than for larger molecular weights. In order to continue this study most chromosomes in a spread must be measured in order to establish a full karyotype. In order to verify the trend several complete spreads would need to be imaged by ptychography and confocal microscopy.

In the identified measured chromosomes there were two chromosome number 17. The measurements of mass of the two chromosomes 17 did not show good agreement which does not show good repeatability of the measurement. A factor causing the difference between these two measurements could be due to the spatial resolution of the confocal and ptychography techniques as the size of the smaller chromosomes are at the limits of resolution of each of these imaging techniques. At the limits of spatial resolution the size of the chromosomes becomes difficult to measure accurately and this can cause the discrepancy between the two values of chromosome 17.

The limitation to both ptychography and confocal microscopy, or indeed any imaging technique, is the achievable resolution. For ptychography the spatial resolution is optimal for this particular laser source set-up, but it is difficult to see isolated chromosomes at this resolution. The chromosomes only appear as a few pixels of phase making it difficult to establish boundaries of the object which are needed for measuring mass.

In confocal microscopy the limitation of resolution is in the measurement of the height through optical slices, with only 60 nm slice being able to be resolved, which can introduce high levels of error on a volume measurement of an object that is only a few hundred nanometers thick. Ptychography is advantageous because it measures phase shift, hence thickness, with an accuracy of milliradians.

These first results show promise that ptychography could be applied to karyotyping, however further work must be done to increase spatial resolution firstly by repeating this experiment with an X-ray source. Spreading methods need to be refined so that each spread contains chromosomes isolated in a large area allowing for all 46 to be imaged. One way to improve spreading over a larger area is to control the humidity of the environment in which spreading is performed [141]. From these measurements it may be possible to see the effect of protein content of the chromosomes on the karyotype. As we know the DNA content of the euchromatin by sequencing we can estimate the mass of DNA in each chromosome.

In this study we have compared mass to molecular weights obtained from sequencing. The molecular weights will only take into account only the DNA in the euchromatin compared to the mass established by flow cytometry, that take into account non-sequenced and sequenced DNA. The measurements of ptychography and confocal microscopy take into account the entire volume of the chromosome, not just the volume of DNA, therefore it could be possible that the protein contribution of the chromosomes could change their position karyotype or whether the trend is still linear indicating that chromosomes contain a similar amount of protein to DNA.

7.6 Summary

First attempts of using ptychography have been successful in yielding macroscopic structural information, (shape and mass) of chromosomes and nuclei. There is potential to apply these measurements to mapping macroscopic structural changes through the cell cycle. The X-ray images of nuclei show sufficient phase contrast to calculate mass however the reconstruction techniques need to be improved to remove artifacts to provide a more accurate measurement of the phase. In future sample preparations the drying methods need to be improved to remove as much of the

water content as possible.

The mass of the chromosomes has also been calculated from ptychography images taken with a laser source. Whilst the chromosomes are on the spatial resolution of this set-up, isolated chromosomes can be identified. The mass calculated from the phase shift is sufficient to begin sorting the chromosomes by their relative masses, however a full spread needs to be measured in order to verify this method can be used to produce a karyotype. Improvement of the X-ray ptychography methods would allow the chromosome spreads to be imaged with greater spatial resolution, therefore giving a more accurate value for mass.

Chapter 8

Conclusions and Future Outlooks

The aim of this study was to observe the coiling of the DNA that makes up the human mitotic chromosome using the lensless imaging techniques of Coherent Diffraction Imaging and Ptychography. The wavelength limited resolution and large penetration depth of these techniques give the potential to access the 30 nm length scale in 3D without staining or performing sectioning. In this work ptychography has been used to image nuclei clusters, individual nuclei and chromosomes in two dimensions, using a number of beamlines and sources.

Ptychography was quickly adopted as a favoured imaging method over CDI as the high degeneracy of the data results in far more robust phase retrieval algorithms. The I-13 beamline is the only beamline that will allow an experimental set-up where the oversampling is sufficient to image a chromosome with CDI. Early experiments at this beamline found it was difficult to perform phase retrieval. Ptychography was performed at several beamlines with different experimental set-up all of which produced images of nuclei. The images from the different set-ups are of varying quality and show different levels of phase contrast and artifacts. It was difficult to establish the cause of some of the artifacts through analysis of the images, convergence of phase retrieval and comparison between the set-ups. One of the biggest factors to the quality of the reconstructions is the stability of the illumination. The fundamental assumption in ptychography implies that the probe function is constant in all positions of the scan. Fluctuations in the probe appear in the object function and the solution of the probe function is averaged across all positions. One way to improve the stability of the illumination is to move the aperture defining pinhole very close to the sample. The experiment at cSAXS had an aperture to sample distance of 1 mm and the scan time was limited to the known duration of the stability of the beam. It can be seen that the phase contrast in these images was significantly higher than in the set-ups at other beamlines where the aperture to sample distance was several centimeters away.

Using a beamstop to block the central region of the data causes problems in the phase retrieval. As discussed in section 3.5, the phase retrieval algorithms are very sensitive to missing or incorrect data in the centre of the diffraction pattern. In order to solve this problem a semi-transparent beamstop was used to cover the central part of the beam. This allowed some information through that could be then recovered using a multiplication factor. The central part of the diffraction pattern was successfully recovered at I-13 but this technique did not work well at 34-ID-C. This was partly due to the low number of counts being recorded in the corners of the beamstop during this experiment leading to regions of low signal to noise in the centre of the diffraction patterns. The experiment at cSAXS did not use a beamstop which is the most desirable case, however it was difficult to tell by direct comparison between the three images the artifacts that were caused by incorrect multiplication of the central region.

Phase retrieval was performed on diffraction data taken with these set-ups using a variety of algorithms and programs. As presented in section 6.2.2.1 there is no single recipe for ptychography. In many cases images could only be obtained through a specific set of conditions. It can be argued that the failure of the phase retrieval could be caused by the poor stability of illumination and diffraction data. Even for the most stable set-up at cSAXS, the amplitude images produced by Difference Map with a Maximum Likelihood correction contained several artifacts in the amplitude part of the images. This was true of all images that phase image contained less artifacts than the amplitude image. Due to the weak β values of biological molecules at these energies it is expected the the amplitude contrast would be considerably weaker than the phase contrast. It was seen in all images that there the strongest amplitude contrast at the boundaries of the objects but the amplitude inside was indistinguishable from the background.

The structural information that could be found in the images was limited because only two dimensional projection images were taken. In projection all the information of helicity and chirality that would be of interest in higher order structures is lost, however projection information is still useful for looking at density changes in the sample. In the images of the nucleus we can see phase information in projection that corresponds to the absorbance seen in the optical images. In the nuclei taken at 34-ID-C we can see difference in the phase of the more intact nuclei and one that is ready to break. The patches of phase in the broken nucleus could be linked to the chromosomes that have started to condense inside but it is difficult to observe this in the image.

The images of chromosomes taken with X-ray ptychography show phase contrast at the boundaries but none across the body of the chromosome. The chromosome 2D projections taken with ptychography by Nishino et al. shown in chapter 3 (fig. 4.14), show higher electron densities in the chromatids and the centromeres showing that phase retrieval methods have the sensitivity to

be able to identify different regions of the chromosome by their electron density. In the case of the ptychography performed at 34-ID-C the errors in the image come from the experimental set-up as this beamline was performing at the limits of its energy range. From images of nuclei taken at cSAXS, with small changes to the experimental set-up at 34-ID-C, such as a close pinhole providing the illumination would provide better images of chromosomes.

The absorption contrast images from the STXM image shows a uniform mass thickness over the chromatids and centromeres. Clearly reducing the energy can provide greater contrast in both amplitude and phase from the chromosomes. Measurements of phase from visible light ptychography provide enough phase shift to be analyzed for mass. It is very difficult to increase the resolution of the technique but this does show that imaging chromosomes with ptychography is possible. It may be beneficial to measure chromosomes in the ranges of 500-2000 eV with ptychography where the phase contrast is quite strong. As discussed in chapter 2 there have been some promising imaging of biological samples with the ptychography in the small energy regime.

As discussed in section 3.3, measuring at lower energies will increase the dose on the sample as dose is proportional to λ^{-4} . In our brief study of radiation damage we saw minor effects, a drop in intensity over the diffraction pattern and a small decrease in angular resolution (section 6.4.4.3). The study was insufficient to find a damage rate. The damage could happen very rapidly in which case it would severely limit the resolution that was achievable by ptychography because of the large exposure time needed to sufficiently measure all positions. The discussion of resolution and damage in chapter 2 is calculated for CDI which is a single shot method. Applying the dose fractionation theorem allows for the dose needed to achieve a 2D image can be split amongst the projections in 3D. In ptychography the dose needed to obtain an image is increased because of the overlap condition. The maximum dose limited resolution for CDI is 10 nm, due to the overlap effect in ptychography it is likely that the maximum resolution would be greater. An advantage to measuring with lower energies is the gain in phase contrast, which is beneficial for the determination of mass of the chromosomes and nuclei.

In chapter 2 the flux required to get an image was discussed in terms of material refractive index. For a weak refractive index a greater flux is required to provide a statistically relevant signal. In this study we have tried to increase the scattering signal from the chromosomes with the application of platinum based stains. Heavy metals increase the refractive index of the chromosomes therefore should increase the phase shift from the DNA the part that we are principally interested in. A preliminary calculation of the increased phase shift from staining was obtained from the SEM images (see section 5.5). These calculations showed that the application of stain only increases the phase shift by a few milliradians. In the experiments with X-rays no images

have been reconstructed from unstained material, so no comparison between the two cases has been made. Another way to improve the signal from the chromosomes is to try and remove some of the background noise content. We have seen that the signal from the chromosomes descends to the noise level at scattering angles corresponding to approximately 200 nm. In order to reduce signal from windows and air the chromosomes could be imaged in full vacuum this might improve the resolution.

In this thesis the technique of ptychography was applied to imaging both nuclei and mitotic chromosomes. Whilst there have been examples of ptychographic imaging in biology that have imaged useful 3D structure at resolutions of tens of nanometers we have not been able to replicate such good images in the case of the chromosomes. We have been unable to measure in 3D but the promising 2D projection images from cSAXS suggest that we have the potential to be able to measure in 3D in the near future. We did not manage to take images of chromosomes with sufficient quality to make out more than their shape. The shape agreed with images taken by electron microscopy. From this study we have managed to find some of the causes of the poor ptychography images from chromosomes and if we were to repeat the experiment making these changes we could potentially obtain better images of chromosomes.

The quality of the images from I-13, Diamond Light Source and cSAXS at the Swiss Light Source allowed the phase shift to be measured and the structural feature of mass was obtained. These results are the first measurements of their kind and resolution must be increased and artefacts in the image must be reduced to make the results more reliable. The mass is a macroscopic quantity that could be potentially used to track changes in nuclear behaviour through the cell cycle if the mass measurements had sufficient sensitivity. By using ptychography to measure cells prepared so they were in different phases of the cell cycle an average mass for each stage could be determined and in this way documenting the changes in the cell cycle. In visible light ptychography the measurements of phase shift had enough sensitivity to be able to sort chromosomes by mass. This preliminary study indicates that ptychography has the potential for karyotyping chromosomes by mass which can be calculated from the integrated phase shift. A karyotype performed by absolute mass would have contributions from both the DNA and protein content of chromosomes. Flow cytometry is another method that karyotypes using mass arguments and has been shown in this work to be comparable to ptychography.

8.1 Future outlooks

This study has shown promising preliminary images of nuclei from X-ray ptychography that have shown details such as varying electron density that can be analyzed for mass. From the ptychography of the nuclei, and the visible light and STXM images of the chromosomes it is reasonable to believe that we can get good ptychography images for the chromosomes if changes to the experimental set- up were made. We have seen in a recent experiment at I-13 huge improvements in the quality of the data and reconstructions just by using a pinhole at 1 mm distance from the sample to define the probe. In these images it has been also possible to see chromosomes which is again an improvement on previous images taken with I-13.

This study provides the ground work for imaging higher order structure of chromosomes with ptychography. All the beamlines used to measure the chromosomes and nuclei have the ability to perform measurements in 3D. In order to do this rotating the sample must be implemented which is a technical challenge but has been performed successfully at cSAXS. According to the dose fractionation theorem imaging in 3D requires no extra dose than the 2D projection.

The onset of radiation damage could be prevented by moving to a frozen state. This presents a huge technical challenge but there has been a great body of work both in TEM and STXM which looks at preparing frozen samples for imaging. We can use this work as a starting point to design both sample stages and preparation protocols for measuring in a frozen state.

Imaging the 3D structure of the chromosome is a huge technical effort but could provide some promising results in structure such as the existence of the hypothesized 30 nm chromatin fibre [116]. From this images we have seen here and the ongoing improvements to the experimental set-ups it is a promising next step.

A second direction for this work is to continue the mass measurements of chromosomes and nuclei. From the visible light ptychography we have a preliminary karyotype of chromosomes and with better images and measuring more chromosomes spreads this can be easily improved. Karyotyping by mass may give some insight into the protein to DNA content of the chromosomes and how this changes with chromosome size. Identifying chromosomes by flow cytometry already takes into account the entire DNA contribution so comparing these two measurements we may learn something about protein contents. It would be useful to couple karyotyping by ptychography with general G-banding to see how the mass changes with insertions and deletions of genes in diseased chromosomes. Similarly the nuclear mass found by ptychography could be used to monitor changes in the protein and DNA content during the cell cycle.

Bibliography

[1] R. E. Franklin and R. G. Gosling. Evidence for 2-chain helix in crystalline structure of sodium deoxyribonucleate. *Nature*, 172:156–157, 1953.

[2] J. D. Watson, F. H.C. Crick, et al. Molecular structure of nucleic acids. *Nature*, 171(4356):737–738, 1953.

[3] C. L. Woodcock and R. P Ghosh. Chromatin higher-order structure and dynamics. *Cold Spring Harbor perspectives in biology*, 2(5), 2010.

[4] C. Flors and W.C. Earnshaw. Super-resolution fluorescence microscopy as a tool to study the nanoscale organization of chromosomes. *Current Opinion in Chemical Biology*, 15:838Ð844, 2011.

[5] J. M. Rodenburg and H.M.L Faulkner. A phase retrieval algorithm for shifting illumination. *Appl. Phys. Lett.*, 85:4795–4797, 2004.

[6] J. Miao, P. Charambolous, J. Kirz, and D. Sayre. Extending the methodology of x-ray crystallography to allow imaging of micrometre-sized non-crystaliine specimens. *Nature*, 400, 1999.

[7] R. N. Wilke, M. Priebe, M. Bartels, K. Giewekemeyer, A. Diaz, P. Karvinen, and T. Salditt. Hard X-ray imaging of bacterial cells: nano-diffraction and ptychographic reconstruction. *Opt. Express*, 20(17):19232–19254, 2012.

[8] R. Harder, M. Liang., Y. Sun, Y. Xia, and I. K. Robinson. Imaging of complex density in silver nanocubes by coherent x-ray diffraction. *New Journal of Physics*, 12:035019, 2010.

[9] B. Chen, M. Guizar-Sicairos, G. Xiong, L. Shemilt, A. Diaz, J. Nutter, N. Burdet, S. Huo, J. Mancuso, A. Monteith, F. Vergeer, A. Burgess, and I. Robinson. Three-dimensional structure analysis and percolation properties of a barrier marine coating. *Sci. Rep.*, 3:1177, 2013.

[10] J. Als-Nielsen and D. McMorrow. *Elements of Modern X-ray Physcis*. John Wiley and Sons, Ltd., 2011.

[11] J. Baruchel, J-L. Hodaeau, M. S. Lehmann, J-R. Regnard, and C. Schlenker, editors. *Neutron and Synchrotron radiation for condensed matter studies*. Springer-Verlag, 1993.

[12] S. J. Leake, M.C. Newton, R. Harder, and I.K. Robinson. Longitudinal coherence function in x-ray imaging of crystals. *Opt. Express*, 12:15853–15859, 2009.

[13] D. Sayre. Some implications of a theorem due to Shannon. *Acta Crystallographica*, 5(6):843, 1952.

[14] H. Nyquist. Certain topics in telegraph transmission theory. *Trans. AIEE*, 47:617–644, 1928.

[15] R. H. T. Bates and W. R. Fright. Composite two-dimensional phase-restoration procedure. *J. Opt. Soc. Am.*, 73(3):358–362, 1983.

[16] J. Miao and H. N. Chapman. Phase retrieval from the magnitude of the fourier transforms of nonperiodic objects. *J. Opt. Soc. Am.*, 15, 1998.

[17] T. B. Edo, D. J. Batey, A. M. Maiden, C. Rau, U. Wagner, Z. D. Pešić, T. A. Waigh, and J. M. Rodenburg. Sampling in x-ray ptychography. *Phys. Rev. A*, 87:053850, 2013.

[18] J. R. Fienup. Phase retrieval algorithms: a comparison. *Appl. Opt.*, 21(15):2758–2769, 1982.

[19] S. Marchensini. A unified evaluation of iterative projection algorithms for phase retrieval. *Rev. Sci. Instr.*, 78:011301–011309, 2007.

[20] G.J. Williams, M.A. Pfeifer, I.A. Vartanyants, and I.K. Robinson. Three-dimensional imaging of microstructure in au nanocrystals. *Physical review letters*, 90(17):175501, 2003.

[21] P. Thibault, M. Dierolf, O. Menzel, A.and Bunk, and F. David, C.and Pfeiffer. High-resolution scanning x-ray diffraction microscopy. *Science*, 321:379, 2008.

[22] J. M. Rodenburg and R. H. T. Bates. The theory of super-resolution electron microscopy via wigner-distribution deconvolution. *Phil. Trans. R. Soc. Lond. A*, 339:521, 1992.

[23] M. Guizar-Sicairos and J. R Fienup. Measurement of coherent x-ray focused beams by phase retrieval with transverse translation diversity. *Opt. Express*, 17(4):2670–2685, 2009.

[24] P. Thibault and M. Guizar-Sicairos. Maximum-likelihood refinement for coherent diffractive imaging. *New Journal of Physics*, 14(6):063004, 2012.

[25] A. Maiden and J. M. Rodenburg. An improved ptychographical phase retrieval algorithm for diffractive imaging. *Ultramicroscopy*, 109:1256–1262, 2009.

[26] V. Elser. Phase retrieval by iterated projections. *J. Opt. Soc. Am. A*, 20(1):40–55, Jan 2003.

[27] A. Levi and H. Stark. Signal restoration from phase by projections onto convex sets. *J. Opt. Soc. Am.*, 73:810–822, 1982.

[28] V. S. Chamard, J. Stangl, G. Carbone, A. Diaz, G. Chen, C. Alfonso, C. Mocuta, and T. H. Metzger. Three-dimensional x-ray fourier transform holography: The bragg case. *Phys. Rev. Lett.*, 104 165501:165501, 2010.

[29] S.O. Hruszkewycz, M. V. Holt, A. Tripathi, J. Maser, and P. H. Fuoss. Framework for three-dimensional coherent diffraction imaging by focused beam x-ray bragg ptychography. *Opt. Lett.*, 36(12):2227–2229, 2011.

[30] M. Guizar-Sicairos, A. Diaz, M. Holler, M.S. Lucas, A. Menzel, R.A. Wepf, and O. Bunk. Phase tomography from x-ray coherent diffractive imaging projections. *Opt. Express*, 19(22):21345–7, 2011.

[31] H. Jiang, C. Song, C.C. Chen, R. Xu, K. S. Raines, B. P. Fahimian, C-H. Lu, T-K Lee, A Nakashima, J. Urano, T. Ishikawa, F Tamanoi, and J. Miao. Quantitative 3D imaging of whole, unstained cells by using x-ray diffraction microscopy. *Proc. Natl. Acad. Sci.*, 107:11234–11239, 2010.

[32] M. C. Newton, S. J. Leake, R. Harder, and I. K. Robinson. Three-dimensional imaging of strain in a single ZnO nanorod. *Nat. Mater.*, 9(2):120–124, 2010.

[33] Benjamin R. Arenkiel and Michael D. Ehlers. Molecular genetics and imaging technologies for circuit-based neuroanatomy. *Nature*, 461:900–907, 2009.

[34] M. A. Pfeifer, G. J. Williams, I. A. Vartanyants, R. Harder, and I. K. Robinson. Three-dimensional mapping of a deformation field inside a nanocrystal. *Nature*, 442(7098):63–66, 2006.

[35] B. Chen, F. Zhang, F. Berenguer, R. J. Bean, C. M. Kewish, J. Vila-Comamala, Y.S. Chu, J.M. Rodenburg, and I. K. Robinson. Coherent x-ray diffraction imaging of paint pigment particles by scanning a phase plate modulator. *New Journal of Physics*, 13:103022, 2011.

[36] X. Shi, G. Xiong, X. Huang, R. Harder, and I. Robinson. Radiation-induced bending of silicon-on-insulator nanowires probed by coherent x-ray diffractive imaging. *New Journal of Physics*, 14(6):063029, 2012.

[37] Jessica Sullivan-Brown, Margaret E Bisher, and Rebecca D Burdine. Embedding, serial sectioning and staining of zebrafish embryos using JB-4 resin. *Nature protocols*, 6(1):46–55, 2011.

[38] J. Kirz, C Jacobsen, and M. Howells. Soft x-ray microscopes and their biological application. *Q. Rev. Biophys.*, 28:33–130, 1995.

[39] B.L. Henke, E.M. Gullikson, and J.C. Davis. X-ray optical constants data from http://henke.lbl.gov/optical_constants/ from x-ray interactions: photoabsorption, scattering, transmission, and reflection at e=50-30000 ev, z=1-92, atomic data and nuclear data tables vol. 54 (no.2), 181-342 ., 1996.

[40] K. Giewekemeyer, M. Beckers, T. Gorniak, M. Grunze, T. Salditt, and A. Rosenhahn. Ptychogrphic coherent x-ray diffractive imaging in the water window. *Opt. Express*, 19(2):1037–1050., 2011.

[41] R. M. Glaeser. Limitations to significant information in biological electron microscopy as a result of radiation damage. *Journal of Ultrastructure Research*, 36(3-4):466 – 482, 1971.

[42] D. Sayre, J. Kirz, R. Feder, D.M. Kim, and E. Spiller. Transmission microscopy of unmodified biological materials. comparative radiation dosages with electrons and ultrasoft x-ray photons. *Ultramicroscopy*, 2(0):337 – 349, 1976-1977.

[43] A. Rose. *Television pick up tubes and the problem of vision*, volume 1 of *Advances In Electronics*. Academic Press, New York, 1948.

[44] J. Miao, K. O. Hodgson, T. Ishikawa, C. A. Larabell, M. A. LeGros, and Y. Nishino. Imaging whole Escherichia coli bacteria by using single-particle x-ray diffraction. *Proc Natl Acad Sci*, 100(1):110–112, 2003.

[45] A.M. Maiden, G.R. Morrison, B. Kaulich, A. Gianoncelli, and J.M. Rodenburg. Soft x-ray spectromicroscopy using ptychography with randomly phased illumination. *Nat. Comms.*, 4:1669, 2013.

[46] M. Dierolf, A. Menzel, P. Thibault, P. Schneider, C. Kewish, R. Wepf, O. Bunk, and F. Pfeiffer. Ptychographic x-ray computed tomography at the nanoscale. *Nature*, 467:436–439, 2010.

[47] M. Holler, A. Diaz, M. Guizar-Sicairos, P. Karvinen, Elina Färm, Emma Härkönen, Mikko Ritala, A. Menzel, J. Raabe, and O. Bunk. X-ray ptychographic computed tomography at 16 nm isotropic 3d resolution. *Sci. Rep.*, 4:–, January 2014.

[48] H. N. Chapman, A. Barty, S. Marchesini, A. Noy, S. P. Hau-Riege, C. Cui, M. R. Howells, R. Rosen, H. He, J. C. H. Spence, U. Weierstall, T. Beetz, C. Jacobsen, and D. Shapiro. High-resolution ab initio three-dimensional x-ray diffraction microscopy. *J. Opt. Soc. Am. A*, 23(5):1179–1200, May 2006.

[49] Joan Vila-Comamala, Sergey Gorelick, Elina Färm, Cameron M Kewish, Ana Diaz, Ray Barrett, Vitaliy A Guzenko, Mikko Ritala, and Christian David. Ultra-high resolution zone-doubled diffractive x-ray optics for the multi-kev regime. *Opti. Express*, 19(1):175–184, 2011.

[50] WO Saxton and W_ Baumeister. The correlation averaging of a regularly arranged bacterial cell envelope protein. *Journal of Microscopy*, 127(2):127–138, 1982.

[51] D. Starodub, P. Rez, G. Hembree, M. Howells, D. Shapiro, H. N. Chapman, P. Fromme, K. Schmidt, U. Weierstall, R. B. Doak, and J. C. H. Spence. Dose, exposure time and resolution in serial X-ray crystallography. *Journal of Synchrotron Radiation*, 15(1):62–73, 2008.

[52] Q. Shen, I. Bazarov, and P. Thibault. Diffractive imaging of nonperiodic materials with future coherent X-ray sources. *Journal of Synchrotron Radiation*, 11(5):432–438, 2004.

[53] M.R. Howells, T. Beetz, H.N. Chapman, C. Cui, J.M. Holton, C. J. Jacobsen, J Kirz, E. Lima, S. Marchesini, H Miao, D. Sayre, D.A. Shapiro, J.C.H. Spence, and D. Starodub. An assessment of the resolution limitation due to radiation-damage in x-ray diffraction microscopy. *J. Elec. Spec. Rel. Phen.*, 170:4–12, 2009.

[54] T.W. Ford, G. F. Foster A. M. Page, and A.D Stead. *Soft X-ray Microscopy by Jacobsen and Trebes*, chapter Effects of soft x-ray irradiation on cell ultrastructure, pages 325–332. Society of Photo-Optical Instrument Engineers, 1992.

[55] P. M. Bennet, G. F. Foster, C.J. Buckley, and R.E. Burge. The effect of soft x-radiation on myofibrils. *Journal of Microscopy*, 172:109–119, 1993.

[56] M. K. Lamvik. Radiation damage in dry and frozen hydrated organic material. *Journal of Microscopy*, 161:171–181, 1991.

[57] S. Williams, X. Zhang, C. Jacobsen, J. Kirz, S. Lindaas, J. Van't Hof, and S. S. Lamm. Measurements of wet metaphase chromosomes in the scanning transmission X-ray microscope. *Journal of Microscopy*, 170(2):155–165, 1993.

[58] R. Henderson. Cryo-protection of protein crystals against radiation damage in electron and x-ray diffraction. *Proceedings: Biological Sciences*, 241(1300):pp. 6–8, 1990.

[59] R. Neutze, R. Wouts, D. van der Spoel, E. Weckert, and J. Hajdu. Potential for biomolecular imaging with femtosecond X-ray pulses. *Nature*, 406(6797):752–757, 2000.

[60] A. M. Maiden, M. J. Humphry, F. Zhang, and J. M. Rodenburg. Superresolution imaging via ptychography. *J. Opt. Soc. Am. A*, 28(4):604–612, 2011.

[61] A. M. Maiden, M. J. Humphry, and J. M. Rodenburg. Ptychographic transmission microscopy in three dimensions using a multi-slice approach. *J. Opt. Soc. Am. A*, 29(8):1606–1614, 2012.

[62] A. Schropp and C. G. Schroer. Dose requirements for resolving a given feature in an object by coherent x-ray diffraction imaging. *New Journal of Physics*, 12(3):035016, 2010.

[63] H. M. Quiney and K. A. Nugent. Biomolecular imaging and electronic damage using x-ray free-electron lasers. *Nat. Phys.*, 7(2):142–146, 2011.

[64] W. Hoppe and R. Hegerl. Some remarks concerning the influence of electron noise on 3D reconstruction. *Ultramicroscopy*, 6(2):205–206, 1981.

[65] B.E.H. Saxberg and W.O. Saxton. Quantum noise in 2D projections and 3D reconstructions. *Ultramicroscopy*, 6:85–90, 1981.

[66] W. Hoppe, B. Grill, R. Gruehn, and W. Mertin. 3-Dimensional electron microscopy of inorganic crystals. *Z. Kristallogr.*, 174(1-4):87–88, 1986.

[67] B. F. McEwen, K. H. Downing, and R. M. Glaeser. The relevance of dose-fractionation in tomography of radiation-sensitive specimens. *Ultramicroscopy*, 60(3):357 – 373, 1995.

[68] Specifications of pilatus detector capabilities. https://www.dectris.com/pilatus features.html, 2013.

[69] X. Huang, J. Nelson, J Steinbrener, J Kirz, J. J. Turner, and C Jacobsen. Incorrect support and missing center tolerances of phasing algorithms. *Opt. Express*, 18:26441–26449, 2010.

[70] Y. Nishino, Y. Takahashi, N. Imamoto, T. Ishikawa, and K. Maeshima. Three-dimensional visualization of a human chromosome using coherent x-ray diffraction. *Phys. Rev. Lett.*, 102:018101, 2009.

[71] R. N. Wilke, M. Vassholz, and T. Salditt. Semi-transparent central stop in high-resolution X-ray ptychography using Kirkpatrick–Baez focusing. *Acta Crystallographica Section A*, 69(5):490–497, Sep 2013.

[72] P. Thibault, V. Elser, C. Jacobsen, D. Shapiro, and D. Sayre. Reconstruction of a yeast cell from X-ray diffraction data. *Acta Crystallographica Section A*, 62(4):248–261, Jul 2006.

[73] D. Shapiro, P. Thibault, T. Beetz, V. Elser, M. Howells, C. Jacobsen, J. Kirz, E. Lima, H. Miao, A. M. Neiman, and D. Sayre. Biological imaging by soft x-ray diffraction microscopy. *Proc Natl Acad Sci*, 102(43):15343–15346, 2005.

[74] Johanna L. Höög, Cindi Schwartz, Angela T. Noon, Eileen T. O'Toole, David N. Mastronarde, J. Richard McIntosh, and Claude Antony. Organization of interphase microtubules in fission yeast analyzed by electron tomography. *Developmental Cell*, 12(3):349–361.

[75] S. Levin-Zaidman, J. Englander, E. Shimoni, A.K. Sharma, K. W. Minton, and A. Minsky. Ringlike structure of the Deinococcus radiodurans genome: A key to radioresistance? *Science*, 299:254–256, 2003.

[76] K. W. Urban. Studying atomic structures by aberration-corrected transmission electron microscopy. *Science*, 321(5888):506–510, 2008.

[77] Y. Takahashi, Y. Nishino, R. Tsutsumi, H. Kubo, H. Furukawa, H. Mimura, S. Matsuyama, N. Zettsu, E. Matsubara, T. Ishikawa, and K. Yamauchi. High-resolution diffraction microscopy using the plane-wave field of a nearly diffraction limited focused x-ray beam. *Phys. Rev. B*, 80:054103, Aug 2009.

[78] O. Medalia, I. Weber, A. S. Frangakis, D. Nicastro, G. Gerisch, and W. Baumeister. Macromolecular architecture in eukaryotic cells visualized by cryoelectron tomography. *Science*, 298(5596):1209–1213, 2002.

[79] J. Mayer, L. A. Giannuzzi, T. Kamino, and J. Michael. TEM sample preparation and fib-induced damage. *MRS Bulletin*, 32(05):400–407, 2007.

[80] Kfir Ben-Harush, Tal Maimon, Israel Patla, Elizabeth Villa, and Ohad Medalia. Visualizing cellular processes at the molecular level by cryo-electron tomography. *Journal of cell science*, 123(1):7–12, 2010.

[81] M. J. Rust, M. Bates, and X. Zhuang. Sub-diffraction-limit imaging by stochastic optical reconstruction microscopy (STORM). *Nat Meth*, 3(10):793–796, 2006.

[82] S. W. Hell. Microscopy and its focal switch. *Nat Meth*, 6(1):24–32, January 2009.

[83] J. S. Biteen, M. A. Thompson, N. K. Tselentis, G. R. Bowman, L. Shapiro, and W. E. Moerner. Super-resolution imaging in live caulobacter crescentus cells using photoswitchable EYFP. *Nat Meth*, 5(11):947–949, 2008.

[84] J. Folling, M. Bossi, H. Bock, R. Medda, C. A. Wurm, B. Hein, S. Jakobs, C. Eggeling, and S. W. Hell. Fluorescence nanoscopy by ground-state depletion and single-molecule return. *Nat Meth*, 5(11):943–945, 2008.

[85] Putman C.A.J. De Grooth, B.G. High resolution imaging of chromosomes related structures by atomic force microscopy. *Journal of Microscopy*, 168:239Ð24239Ð247, 1992.

[86] T. Ushiki, O. Hoshi, K. Iwai, E. Kimura, and M. Shigeno. The structure of human metaphase chromosomes: Its histological perspective and new horizons by atomic force microscopy. *Archives of Histology and Cytology*, 65(5):377–390, 2002.

[87] S. Thalhammer, U. Koehler, R.W. Stark, and W.M. Heckl. GTG banding pattern on human metaphase chromosomes revealed by high resolution atomic-force microscopy. *Journal of Microscopy*, 202:46–47., 2001.

[88] W. Kalle and P. Strappe. Atomic force microscopy on chromosomes, chromatin and DNA: a review. *Micron*, 43(12):1224–1231, 2012.

[89] R.W. Stark, F.J. Rubio-Sierra, S. Thalhammer, and W.M. Heckl. Combined nanomanipulation by atomic force microscopy and UV-laser ablation for chromosomal dissection. *European Biophysics Journal*, 32:33–39, 2003.

[90] G. McDermott, D. M. Fox, L. Epperly, M. Wetzler, A. E. Barron, M. A. Le Gros, and C. A. Larabell. Visualizing and quantifying cell phenotype using soft x-ray tomography. *Bioessays*, 34(4):320–327, 2012.

[91] M. Uchida, G. McDermott, M. Wetzler, M. A. Le Gros, M. Myllys, C. Knoechel, A. E. Barron, and C. A. Larabell. Soft x-ray tomography of phenotypic switching and the cellular response to antifungal peptoids in Candida albicans. *Proc Natl Acad Sci*, 106(46):19375–19380, 2009.

[92] G. Schneider. Cryo x-ray microscopy with high spatial resolution in amplitude and phase contrast. *Ultramicroscopy*, 75(2):85 – 104, 1998.

[93] C. A. Larabell and K. A. Nugent. Imaging cellular architecture with x-rays. *Current Opinion in Structural Biology*, 20(5):623 – 631, 2010.

[94] B. Kaulich, D. Bacescu, J. Susini, C. David, E. di Fabrizio, G. R. Morrison, P. S. Charalambous, J. Thieme, T. Wilhein, J. Kovac, D. Cocco, M. Salomé, O. Dhez, T. Weitkamp, S. Cabrini, D. Cojoc, A. Gianoncelli, U. Vogt, M. Podnar, M. Zangrando, M. Zacchigna, and M. Kiskinova. TwinMic – a European twin x-ray microscopy station commissioned at ELETTRA. pages 22–25, 2006.

[95] Mark A Le Gros, Gerry McDermott, and Carolyn A Larabell. X-ray tomography of whole cells. *Current Opinion in Structural Biology*, 15(5):593–600, 2005.

[96] W. S. Klug, M. R. Cummings, C. A. Spencer, and M. A. Palladino. *Essentials of Genetics*. Pearson, 2010.

[97] M.A. Sunderland. *The Cell: A Molecular Approach. 2nd edition*. Sinauer Associates, 2000.

[98] Nature Education. Essentials of cell biology. unit 5: How do cells know when to divide: http://www.nature.com/scitable/topicpage/mitosis-14046258, 2013.

[99] A.A. Azari S. Glushakova G. Zhang J. Zimmerberg R.D. Leapman M.F. Hohmann-Marriott, A.A. Sousa. Nanoscale 3d cellular imaging by axial scanning transmission electron tomography. *Nat. Methods*, 6:729Ð731, 2009.

[100] MW Hess. Of plants and other pets: practical aspects of freeze-substitution and resin embedding. *Journal of microscopy*, 212(1):44–52, 2003.

[101] T Nagata. Three-dimensional high voltage electron microscopy of thick biological specimens. *Micron*, 32(4):387–404, 2000.

[102] D. Woodward. Biology 110 - basic concepts and biodiversity , DNA and replication. https://wikispaces.psu.edu/display/BIOL110Su2013/DNA+Replication, 2013.

[103] Nature Education. The double helical structure of dna, http://www.nature.com/scitable/content/the-double-helical-structure-of-dna-104944953, 2013.

[104] J. C. Venter, M. D. Adams, G. G. Sutton, A. R. Kerlavage, H. O. Smith, and M. Hunkapiller. Shotgun sequencing of the human genome. *Science*, pages 1540–1541, 1998.

[105] R. A. Hoskins, C. D. Smith, J. W. Carlson, A. B. Carvalh, A. Halpern, J. S. Kaminker, and C. Kennedy et al. Heterochromatic sequences in a drosophila whole-genome shotgun assembly. *Genome Biol*, 3:0081–0085, 2002.

[106] Dorland's Medical Dictionary for Health Consumers by Saunders, an imprint of Elsevier. http://medical-dictionary.thefreedictionary.com/_/viewer.aspx?path=dorland&name=centromere.jpg, 2007.

[107] A. L. Boyle, S. G. Ballard, and D. C. Ward. Differential distribution of long and short interspersed element sequences in the mouse genome: chromosome karyotyping by fluorescence in situ hybridization. *Proceedings of the National Academy of Sciences*, 87(19):7757–7761, 1990.

[108] G. Wanner and H. Formanek. Imaging of dna in human and plant chromosomes by high-resolution scanning electron microscopy. *Chromosome Research,*, 3:368–374, 1995.

[109] J. J. Yunis and O. Sanchez. G-banding and chromosome structure. *Chromosoma*, 44(1):15–23, 1973.

[110] J Bayani and JA Squire. Advances in the detection of chromosomal aberrations using spectral karyotyping. *Clinical genetics*, 59(2):65–73, 2001.

[111] Kenneth R Castleman. Concepts in imaging and microscopy: color image processing for microscopy. *Biological Bulletin*, pages 100–107, 1998.

[112] R. G. Langlois, L. C. Yu, J. W. Gray, and A. V. Carrano. Quantitative karyotyping of human chromosomes by dual beam flow cytometry. *Proceedings of the National Academy of Sciences*, 79(24):7876–7880, 1982.

[113] F. Kasai, P.C.M. O'Brien, and M.A. Ferguson-Smith. Reassessment of genome size in turtle and crocodile based on chromosome measurement by flow karyotyping: close similarity to chicken. *Biology Letters*, 8(4):631–635, 2012.

[114] A. L. Olins and D. E. Olins. Spheroid chromatin units (ν bodies). *Science*, 183(4122):330–332, 1974.

[115] K. Luger, A. W. Mäder, R. K. Richmond, D. F. Sargent, and T. J. Richmond. Crystal structure of the nucleosome core particle at 2.8 Å resolution. *Nature*, 389(6648):251–260, 1997.

[116] C. L. Woodcock. A milestone in the odyssey of higher-order chromatin structure. *Nat. Struc. Mol. Biol.*, 12(8):639–640, 2005.

[117] S. Ohta, L. Wood, J. C. Bukowski-Wills, J. Rappsilber, and W. C. Earnshaw. Building mitotic chromosomes. *Current Opinion in Cell Biology*, 23(1):114 – 121, 2011.

[118] H. Takata, S. Uchiyama, N. Nakamura, S. Nakashima, S. Kobayashi, T. Sone, S. Kimura, S. Lahmers, H. Granzier, S. Labeit, S. Matsunaga, and K. Fukui. A comparative proteome analysis of human metaphase chromosomes isolated from two different cell lines reveals a set of conserved chromosome-associated proteins. *Genes to Cells*, 12(3):269–284, 2007.

[119] Philipp Oberdoerffer & David A. Sinclair. The role of nuclear architecture in genomic instability and ageing. *Nature Reviews Molecular Cell Biology*, 8:692–702, 2007.

[120] P.J.J. Robinson and D. Rhodes. Structure of the "30 nm" chromatin fibre: A key role for the linker histone. *Current Opinion in Structural Biology*, 16:336Ð–343, 2006.

[121] S.A. Grigoryev, G. Arya, S. Correll, C.L. Woodcock, and T. Schlick. Evidence for heteromorphic chromatin fibers from analysis of nucleosome interactions. *Proc Natl Acad Sci*, 106:13317–22, 2009.

[122] Y. Nishino, M. Eltsov, Y. Joti, K. Ito, H. Takata, Y. Takahashi, S. Hihara, A. S. Frangakis, N. Imamoto, T. Ishikawa, and K. Maeshima. Human mitotic chromosomes consist predominantly of irregularly folded nucleosome fibres without a 30-nm chromatin structure. *EMBO J*, 31(7):1644–1653, 2012.

[123] T. Schalch, S. Duda, D. F. Sargent, and T. J. Richmond. X-ray structure of a tetranucleosome and its implications for the chromatin fibre. *Nature*, 436:138–141, 2005.

[124] Y. Fan, T. Nikitina, E.M. Morin-Kensicki, J. Zhao, T.R. Magnuson, C.L. Woodcock, and A.I. Skoultchi. H1 linker histones are essential for mouse development and affect nucleosome spacing in vivo. *Mol Cell Biol*, 23:4559–72., 2003.

[125] T.J. Maresca and R. Heald. The long and the short of it: Linker histone H1 is required for metaphase chromosome compaction. *Cell Cycle*, 5:589–91, 2006.

[126] X. Lu, S. N. Wontakal, A. V. Emelyanov, P. Morcillo, A. Y. Konev, D. V. Fyodorov, and A. I. Skoultchi. Linker histone H1 is essential for drosophila development, the establishment of pericentric heterochromatin, and a normal polytene chromosome structure. *Genes & development*, 23(4):452–465, 2009.

[127] R. Kaufmann, C. Cremer, and J. G. Gall. Superresolution imaging of transcription units on newt lampbrush chromosomes. *Chromosome Research*, 20(8):1009–1015, 2012.

[128] Christopher L Woodcock and Stefan Dimitrov. Higher-order structure of chromatin and chromosomes. *Current Opinion in Genetics & Development*, 11:130–135, 2001.

[129] G. Wanner and H. Formanek. A new chromosome model. *Journal of Structural Biology*, 132(2):147 – 161, 2000.

[130] L.S. Shopland, C.R. Lynch, K.A. Peterson, K. Thornton, N. Kepper, J. Hase, S. Stein, S. Vincent, K.R. Molloy, and G. Kreth. Folding and organization of a contiguous chromosome region according to the gene distribution pattern in primary genomic sequence. *J Cell Biol*, 174:27–38, 2006.

[131] J. Dekker, K. Rippe, M. Dekker, and N. Kleckner. Capturing chromosome conformation. *Science*, 295(5558):1306–1311, 2002.

[132] E. de Wit and W. de Laat. A decade of 3C technologies: insights into nuclear organization. *Genes & development*, 26(1):11–24, 2012.

[133] T. Nagano, Y. Lubling, T. J. Stevens, S. Schoenfelder, E. Yaffe, W. Dean, E. D. Laue, A. Tanay, and P. Fraser. Single-cell Hi-C reveals cell-to-cell variability in chromosome structure. *Nature*, 502(7469):59–64, 2013.

[134] W. C Earnshaw and U. K. Laemelli. Architecture of metaphase chromosomes and chromosome scaffolds. *The Journal of cell biology*, 96(1):84–93, 1983.

[135] K.A. Hagstrom and Meyer B.J. Condensin and cohesin: More than chromosome compactor and glue. *Nat Rev Genet*, 4:520–534, 2003.

[136] A. Losada and T. Hirano. Shaping the metaphase chromosome: coordination of cohesion and condensation. *Bioessays*, 23(10):924–935, 2001.

[137] Michael G Poirier and John F Marko. Mitotic chromosomes are chromatin networks without a mechanically contiguous protein scaffold. *Proceedings of the National Academy of Sciences*, 99(24):15393–15397, 2002.

[138] Karolin Luger, Mekonnen L Dechassa, and David J Tremethick. New insights into nucleosome and chromatin structure: an ordered state or a disordered affair? *Nature reviews Molecular cell biology*, 13(7):436–447, 2012.

[139] Allen TD Harris R. Harrison CJ, Jack EM. Light and scanning electron microscopy of the same human metaphase chromosomes. *J Cell Sci.*, 77:143–53, 1985.

[140] K. Maeshima and U. K. Laemmli. A two-step scaffolding model for mitotic chromosome assembly. *Developmental cell*, 4(4):467–480, 2003.

[141] W. Deng, S. W. Tsao, J Lucas, C.S. Leung, and L. M Cheung. A new method for improving metaphase chromosome spreading. *Cytometry Part A*, 51A:46–51, 2003.

[142] K. W. Jennette, S. J. Lippard, G. A. Vassiliades, and W. R. Bauer. Metallointercalation reagents. 2-hydroxyethanethiolato(2,2',2"-terpyridine)-platinum(ii) monocation binds strongly to dna by intercalation. *Proceedings of the National Academy of Sciences*, 71(10):3839–3843, 1974.

[143] D.B. Brown, R.D. Burbank, and M.B. Robin. Platinblau. *Journal of the American Chemical Society*, 91:111, 1969.

[144] D.L Ma and C.M. Che. A biofunctional platinum(ii) complex capable of intercalation and hydrogen-bonding interactions with DNA: binding studies and cytotoxicity. *Chemistry - a European Journal*, 9:6133–6144, 2003.

[145] C. J. Harrison, T. D. Allen, M. Britch, and R. Harris. High resolution scanning electron microscopy of human metaphase chromosomes. *J. Cell Sci.*, 56:409–422, 1982.

[146] A. T. Sumner. Scanning electron microscopy of mammalian chromosomes from prophase to telophase. *Chromosoma*, 100:410–418, 1991.

[147] T. Sone, M. Iwano, S. Kobayashi, T. Ishihara, N. Hori, H. Takata, T. Ushiki, S. Uchiyama, and K. Fukui. Changes in chromosomal surface structure by different isolation conditions. *Archives of Histology and Cytology*, 65(5):445–455, 2002.

[148] V. Wigglesworth. Union of protein and nucleic acid in living cell and its demonstration by osmium staining. *Quaterly Jornal of Microscopical Science*, 105:113–122, 1964.

[149] G. Wanner, H. Formanek, R. Martin, and R.G. Herrmann. High resolution scanning electron microscopy of plant chromosomes. *Chromosoma*, 100:103–109, 1991.

[150] E. Schroeder-Reiter. *High resolution analysis of mitotic metaphase chromosomes with scanning electron microscopy: Localizing histone H3 modifications with immunogold labeling in barley (Hordeum vulgare).* PhD thesis, Ludwig-Maximillians-Universität München, 2004.

[151] T. Gautier, C. Masson, C. Quintana, J. Arnoult, and D. Hernandez-Verdun. The ultrastructure of the chromosome periphery in human cell lines. *Chromosoma*, 101(8):502–510, 1992.

[152] F. Braet, R. De Zanger, and E. Wisse. Drying cells for SEM, AFM and TEM by hexamethyldisilazane: a study on hepatic endothelial cells. *Journal of Microscopy*, 186(1):84–87, 1997.

[153] Developed by Wellcome Trust Sanger Institute E, the European Bioinformatics Institute. From database release 72. http://www.ensembl.org/Homo_sapiens/Location/Chromosome?r=9;., June 2013.

[154] A. Diaz, P. Trtik, M. Guizar-Sicairos, A. Menzel, P. Thibault, and O. Bunk. Quantitative x-ray phase nanotomography. *Phys. Rev. B.*, 85:020104(R), 2012.

[155] J. Sedat and L. Manuelidis. A direct approach to the structure of eukaryotic chromosomes. *Cold Spring Harb Symp Quant Biol.*, 42 Pt 1:331–50, 1978;.

[156] M. Yusuf, K. Leung, K. J. Morris, and E. Volpi. Comprehensive cytogenomic profile of the in vitro neuronal model sh-sy5y. *neurogenetics*, 14(1):63–70, 2013.

[157] A. C. Thompson and D. (Eds.) Vaughan. *X-ray data booklet.* Lawrence Berkeley National Laboratory, University of California Berkeley, CA, 2001.

[158] D.T. Attwood. *Soft x-rays and extreme ultraviolet radiation: principles and applications.* Cambridge University Press, 2000.

[159] T. Kupp, B. Blank, A. Deyhim, C. Benson, I. Robinson, and P. Fuoss. Development of a double crystal monochromator. In *AIP Conference Proceedings*, volume 705, page 651, 2004.

[160] I. K Robinson, F. Pfeiffer, I. A. Vartanyants, Y. Sun, and Y. Xia. Enhancement of coherent x-ray diffraction from nanocrystals by introduction of x-ray optics. *Opt. Express*, 11(19):2329–2334, 2003.

[161] M. Dierolf, P. Thibault, A. Menzel, C. M Kewish, K. Jefimovs, I. Schlichting, K. von König, O. Bunk, and F. Pfeiffer. Ptychographic coherent diffractive imaging of weakly scattering specimens. *New Journal of Physics*, 12(3):035017, 2010.

[162] F. Zhang, I. Peterson, J. Vila-Comamala, A. Diaz, F. Berenguer, R. Bean, B. Chen, A. Menzel, I. K. Robinson, and J. M. Rodenburg. Translation position determination in ptychographic coherent diffraction imaging. *Opt. Express*, 21(11):13592–13606, Jun 2013.

[163] A.M. Maiden, M.J. Humphry, M.C. Sarahan, B. Kraus, and J.M. Rodenburg. An annealing algorithm to correct positioning errors in ptychography. *Ultramicroscopy*, 120(0):64 – 72, 2012.

[164] S. Butterworth. On the theory of filter amplifiers. *Wireless Engineer*, 7:536–541, 1930.

[165] C Ponchut, JM Rigal, J Clément, E Papillon, A Homs, and S Petitdemange. Maxipix, a fast readout photon-counting x-ray area detector for synchrotron applications. *Journal of Instrumentation*, 6(01):C01069, 2011.

[166] X. Llopart, R. Ballabriga, M. Campbell, L. Tlustos, and W. Wong. Timepix, a 65k programmable pixel readout chip for arrival time, energy and/or photon counting measurements. *Nuclear Instruments and Methods in Physics Research Section A: Accelerators, Spectrometers, Detectors and Associated Equipment*, 581:485–494, 2007.

[167] M. Guizar-Sicairos, I. Johnson, A. Diaz, M. Holler, P. Karvinen, H.-C. Stadler, R. Dinapoli, O. Bunk, and A. Menzel. High-throughput ptychography using eiger-scanning x-ray nanoimaging of extended regions. *Optics express*, 22(12):14859–14870, 2014.

[168] K. Giewekemeyer, P. Thibault, S. Kalbfleisch, A. Beerlink, C.M Kewish, M Dierolf, F Pfeiffer, and T Salditt. Quantitative biological imaging by ptychographic x-ray diffraction microscopy. *Proc. Natl. Acad. Sci.*, 107(2):529–534, 2010.

[169] M. Guizar-Sicairos, M. Holler, A. Diaz, J. Vila-Comamala, O. Bunk, and A. Menzel. Role of the illumination spatial-frequency spectrum for ptychography. *Phys. Rev. B*, 86:100103, 2012.

[170] A. Gianoncelli, G. R. Morrison, B. Kaulich, D. Bacescu, and J. Kovac. Scanning transmission x-ray microscopy with a configurable detector. *Appl. Phys. Lett.*, 89(25):251117, 2006.

[171] G. F. Bahr and H. M. Golomb. Karyotyping of single human chromosomes from dry mass determined by electron microscopy. *Proc. Nat. Acad. Sci. USA*, 68(4):726–730, 1971.

[172] A. Samoc, A. Miniewicz, M. Samoc, and J.G. Grote. Refractive-index anisotropy and optical dispersion in films of deoxyribonucleic acid. *Journal of Applied Polymer Science*, 105(1):236–245, 2007.

[173] D. Rudolph and G. Schmahl. *X-ray Microscopy in Biology and Medicine*. Japan Scientific Societies Press, Springer-Verlag, 1990.

[174] J. Marrison, L. Raty, P. Marriott, and P. O'Toole. Ptychography - a label free, high-contrast imaging technique for live cells using quantitative phase information. *Sci. Rep.*, 3:–, 2013.

[175] T. Iganaki, R.N. Hamm, and E.T. Arakawa. Optical and dielectric properties of dna in the extreme ultraviolet. *J. Chem. Phys*, 61:4264, 1974.

[176] E.S. Tobias, M. Connor, and M. Ferguson-Smith. *Essential Medical Genetics*. Essentials. Wiley, 2011.